Dipartimento di Ingegneria Meccanica e Industriale (DIMI)

Dottorato di Ricerca in Ingegneria Meccanica

ICAR/08 Scienza delle Costruzioni

Ciclo XXXVII

Modeling and simulations for the future generation of sodium-ion batteries

Marzieh Bastanfar

Supervisor: Prof. Alberto Salvadori

To my family,
for their sacrifices.

Acknowledgments

This work was carried out within a research project co-financed by the European Union under the **PON** R&I 2014–2020 Programme, FSE REACT-EU resources, Action IV.5 “Doctorates on Green topics”.

This work has been financed by the Research Fund for the Italian Electrical System under the Three-Year Research Plan 2022–2024 (DM MITE n. 337, 15.09.2022) in compliance with the Decree from 16 April 2018.

I acknowledge SOLEIL for the provision of synchrotron radiation facilities, and I would like to thank Timm Weitkamp for assistance in using beamline Anatomix under proposal 20231869.

I owe my gratitude to my supervisor, **Prof. Alberto Salvadori** whose guidance, high standards, and encouragement shaped this thesis from the very first idea to the final page.

I am sincerely grateful to **Dr. Mattia Serpelloni** for his insightful advice, generous availability, and clear direction at crucial moments. His guidance helped me find my way when the path was not obvious.

My heartfelt thanks to **Manuel Berlato**, a true friend throughout my PhD. His support made the hard days lighter and the good days even better.

I would like to express my deep appreciation to **Hossein Khalilnasl**, whose constant help and motivation have been invaluable during this journey.

Contents

List of Figures

List of Tables

Sommario

Le batterie agli ioni di sodio (SIB) rappresentano un'alternativa promettente ai sistemi agli ioni di litio per l'accumulo su larga scala integrato con le fonti rinnovabili, grazie all'abbondanza del sodio e alla maggiore resilienza della catena di approvvigionamento. Tra gli elettrodi negativi per SIB, le leghe di stagno (Sn) offrono bassi potenziali di inserzione e alte capacità teoriche, ma subiscono ampie variazioni di volume indotte dalla (de)sodiazione che innescano frammentazione, formazione di vuoti e perdita di contatto elettrico. Questa tesi combina esperimenti multimodali con una modellazione termodinamicamente coerente per comprendere e mitigare tali meccanismi di degradazione chemo–meccanica negli anodi a base di Sn.

Sul piano sperimentale, abbiamo sintetizzato e valutato elettrodi di Sn e studiato gli effetti della scelta del legante e dei collettori di corrente su stabilità e prestazioni di velocità (rate capability). La voltammetria ciclica, i test galvanostatici, la microscopia elettronica a scansione con contrasto in elettroni retrodiffusi (SEM/BSE), la spettroscopia EDX, la diffrazione a raggi X (XRD) e la microtomografia a raggi X da sincrotrone mettono in evidenza i legami tra morfologia e prestazioni: capacità intorno a $350\,\mathrm{mAh\,g^{-1}}$ a C/10 sono riproducibili, mentre le immagini mostrano frammentazione, parziale densificazione e formazione di cavità. Architetture che confinano lo Sn in reti ricche di carbonio limitano l'espansione macroscopica e sostengono meglio la rate capability rispetto a configurazioni "a spugna" spesse e limitate dal trasporto ionico.

Dal punto di vista modellistico, sviluppiamo un quadro continuo e multifisico di tipo phase-field in grado di catturare segregazione di fase, moto dell'interfaccia e generazione di tensioni durante la (de)sodiazione. Vengono avanzate due formulazioni complementari: (i) un modello di Cahn–Hilliard basato sulla concentrazione, accoppiato all'elasticità e stabilizzato mediante uno operator splitting penalizzato; (ii) una formulazione a frazioni di volume che traccia esplicitamente più fasi intermetalliche, con cinetiche di reazione descritte dalla legge d'azione di massa e mappatura "a strato sottile" delle reazioni interfacciali. Analisi parametriche chiariscono come diffusività, energia di interfaccia (di gradiente), intensità di interazione e accoppiamento

meccanico governino stabilità, larghezza dell'interfaccia e robustezza numerica; controlli di bilancio di massa ed energia validano l'implementazione.

Nel complesso, i risultati forniscono indicazioni progettuali ancorate all'evidenza sperimentale per anodi SIB durevoli: il confinamento dello Sn entro matrici carboniose conformi e conduttive è preferibile, mentre le architetture a spugna spesse sono soggette a un decadimento precoce guidato dai limiti di trasporto. Il quadro di modellazione concilia fedeltà fisica (vincoli di limitatezza, conservazione, stechiometria) e praticità numerica, offrendo una base calibrata per futuri studi tridimensionali, e abilitati alla descrizione del danneggiamento.

Abstract

Sodium-ion batteries (SIBs) are a promising alternative to lithium-ion systems for large-scale, renewable-integrated storage due to sodium's abundance and supply-chain resilience. Among SIB negative electrodes, tin (Sn) alloys offer low insertion potentials and high theoretical capacities but suffer from large (de)sodiation-induced volume changes that drive fragmentation, voiding, and loss of electrical contact. This thesis combines multimodal experiments with thermodynamically consistent modeling to understand and mitigate these chemo–mechanical degradation mechanisms in Sn-based anodes.

Experimentally, we synthesize and evaluate Sn electrodes and study the effects of binder choice and current collectors on stability and rate performance. Cyclic voltammetry, galvanostatic testing, SEM/BSE, EDX, XRD, and synchrotron X-ray microtomography reveal morphology–performance links: capacities around $350\,\mathrm{mAh\,g^{-1}}$ at C/10 are reproducible, while imaging shows fragmentation, partial densification, and void formation. Architectures that confine Sn in carbon-rich networks limit macroscopic expansion and sustain rate capability better than thick, transport-limited sponge designs.

Modeling-wise, we develop a continuum, multiphysics phase-field framework that captures phase segregation, interface motion, and stress generation during (de)sodiation. Two complementary formulations are advanced: (i) a concentration-based Cahn–Hilliard model coupled to elasticity stabilized by a penalty-based operator splitting, and (ii) a volume-fraction formulation that explicitly tracks multiple intermetallic phases with mass-action reaction kinetics and thin-layer mapping of interfacial reactions. Parametric sweeps clarify how diffusivity, gradient (interfacial) energy, interaction strength, and mechanical coupling govern stability, interface width, and numerical robustness; mass/energy checks validate the implementation.

Together, the results deliver experimentally anchored design guidance for durable SIB anodes: confining Sn within compliant, conductive carbon matrices is favored, whereas thick sponge architectures are prone to early, transport-driven fade. By ensuring boundedness, conservation, and stoichiometric consistency while remaining numerically practical, the framework offers a calibrated basis for future 3D and damage-focused work.

Chapter 1

Introduction

Modern power systems increasingly rely on intermittent renewable sources, which makes affordable, durable, and scalable energy storage indispensable [1]. Lithium-ion batteries (LIBs) dominate today's applications, but concerns around long-term resource availability and cost motivate the exploration of alternatives. Among these, sodium-ion batteries (SIBs) have emerged as particularly compelling due to sodium's abundance and supply-chain resilience. While SIB operation parallels LIBs, with Na^+ shuttling between positive and negative electrodes during charge and discharge [2], the chemistry of the negative electrode is different: graphite does not reliably intercalate Na^+ under practical conditions, which rules out the canonical LIB anode material [3]. As a result, research has focused on carbonaceous anodes (hard carbons and related graphitic derivatives) produced via high-temperature carbonization of organic precursors, including industrial by-products. In these systems, high capacity depends on carefully engineered disorder and nanoporosity in the carbon matrix, often requiring templating/porogens and synthesis temperatures above 1000°C [4].

In parallel with the historical evolution of LIBs, from carbonaceous to alloying anodes, there is intense interest in alloy anodes for SIBs. Elements that form low-potential Na alloys (< 1 V vs. Na/Na^+) provide attractive theoretical capacities, spanning $\sim$300 to $>$1000 mAh g^{-1} depending on the alloy system [5]. This thesis concentrates on tin (Sn) as an active anode material because it combines a low average insertion potential with high theoretical capacity and industrially tractable chemistry. The central challenge, however, is the substantial volumetric expansion and contraction during (de)sodiation, which can induce particle fracture, interfacial delamination, loss of electrical contact, and rapid performance fade [6]. Modeling this chemo–mechanical coupling, where transport, phase transformation, and stress evolution are inseparably linked, is the core scientific problem tackled in this work.

Experimentally, we synthesized and evaluated Sn-based alloy anodes to identify processing–structure–performance relationships germane to sodium storage. Reproducible electrochemical behavior was achieved, including capacities around 350 mAh g^{-1} at C/10 for representative electrodes. We systematically probed the role of binders and current collectors on performance and stability, recognizing that polymer mechanics, adhesion, and electronic pathways critically shape the electrode response. To observe how the active material and architecture evolve during cycling, we employed a multimodal characterization program combining cyclic voltammetry (CV), galvanostatic charge–discharge (GCD), scanning electron microscopy with backscattered imaging (SEM/BSE), energy-dispersive X-ray spectroscopy (EDX), X-ray diffraction (XRD), and synchrotron X-ray microtomography. These complementary techniques reveal the onset of fragmentation, void formation, and partial densification; they also show that confining Sn within carbon-rich matrices tends to mitigate macroscopic expansion relative to thicker, transport-limited designs. The tomographic measurements, in particular, provide direct evidence of volumetric and morphological changes that any credible model must capture, offering critical validation targets and parameter bounds for simulation.

To explain and ultimately guide mitigation of expansion-driven degradation, we developed a thermodynamically consistent computational framework that couples transport, interfacial energetics, and mechanics. At its foundation is a phase-field description in which the free energy collects chemical thermodynamics (solid solution and two-phase regions), gradient energy (which sets interfacial width and penalty), and elastic energy from coherency strains. In the simplest setting, a conserved order parameter evolves by a Cahn–Hilliard (CH) equation, while structural variables, if required, are treated by Allen–Cahn kinetics, enabling diffusion, reaction, and structural transformation to be handled within a single variational framework [7, 8]. For computational tractability with standard finite elements, we adopt a penalty-operator approach [9, 10] that splits the fourth-order CH equation into coupled second-order problems while penalizing inconsistency between the split fields. This modification retains the correct physics, reduces implementation barriers, and improves robustness in stiff regimes (high effective diffusivity, strong gradient penalties, and fine meshes).

While much of the battery modeling literature uses concentration variables, multistep Na–Sn intermetallic formation with sharp stoichiometries and large swelling motivates a transition to phase volume fractions $\phi^\alpha \in [0, 1]$ (e.g., Sn, $NaSn_3$, Na_9Sn_4, $Na_{15}Sn_4$), which naturally enforce boundedness, local filling, and phase coexistence [11, 12]. Within this representation, we derive bulk reaction rates from mass action written directly in ϕ^α so that stoichiometry is honored at the level of phase transfer. Interfacial

electrochemical reactions are mapped to thin volumetric layers embedded in the finite-element mesh, which ensures that boundary fluxes match the volumetric sources/sinks and avoids numerical discontinuities, while the coupling to mechanics, via the chemo–mechanical component of the chemical potential, captures how stress and deformation feed back on both diffusion and reaction kinetics. The resulting framework supports explicit or implicit time integration with Newton–Raphson linearization for the tightly coupled fields; salient dimensionless groups (scaled diffusivity, interfacial length, and penalty parameters) illuminate stability and mesh-resolution requirements. Throughout, we verify mass conservation and decompose the Helmholtz free energy into entropic, interaction, interfacial, and mechanical parts to diagnose driving forces during charging and post-charge relaxation.

Taken together, the combined experimental and modeling results provide design guidance for durable Sn-based SIB anodes. Architectures that confine the active Sn within compliant, conductive carbon networks reduce macroscopic expansion and better sustain rate capability, whereas thick, transport-limited structures are prone to early capacity loss. Simulations reproduce segregation fronts and compressive-stress patterns consistent with observed densification and voiding, while the penalty-stabilized operator splitting extends convergence across demanding parameter regimes. Finally, the volume-fraction and reaction-kinetics formulation reconciles physical constraints (boundedness, conservation, stoichiometry) with numerical practicality, positioning the framework for future calibration and upscaling.

Chapter 2

Background

In this chapter, fundamental concepts and parameters of battery technology are established. These definitions are important for a comprehensive understanding of the discussions and analyses presented in the subsequent chapters.

2.1 Internal resistance

The internal resistance of a cell, expressed in ohms (Ω), represents the impedance to the flow of current within the cell and is an important metric of its performance. A lower internal resistance enables the battery to deliver a high current with minimal voltage loss, whereas a higher internal resistance limits the cell's ability to supply large currents and results in a greater voltage drop. Various factors contribute to internal resistance, including the type and composition of the electrode, the cell's temperature, and its state of charge. The discharge rate also affects internal resistance, with higher rates typically leading to increased resistance. Assessing a battery cell's internal resistance evaluates its performance and detects any potential problems [13].

2.2 Open-circuit voltage, state of charge, and state of health

The open-circuit voltage (OCV) represents the potential difference between the cathode and anode under equilibrium conditions, where no current flows. The OCV observed during active charge or discharge cycles differs due to kinetic effects, such as mass transport. Through the use of a galvanostatic intermittent titration technique (GITT), the OCV across various states of charge can be accurately determined by measuring the potential at the end

of sufficient relaxation periods.

Dynamic battery models depend on the relationship between OCV and cell capacity to accurately estimate internal states such as state of charge (SOC) and state of health (SOH). SOC, expressed as a percentage, indicates the remaining charge relative to the cell's maximum capacity, while SOH assesses the degradation in cell performance over time, affected by factors like capacity fade and internal resistance increases.

Battery models often incorporate OCV as a function of cell capacity or SOC for easy implementation and reliable initial performance. However, as cells degrade and the relationship between OCV and capacity shifts due to capacity fade, these models require updates to maintain accuracy. Changes in the OCV curve shape, indicative of electrode SOH, are generally overlooked but are considerable in assessing the health of the cell. Physical OCV models, which integrate thermodynamic data from the electrode materials, account for phase transitions and lithium intercalation during charging and discharging. These models help to identify the main degradation mechanisms and predicting the cell's lifecycle but are often complex and difficult to integrate with standard dynamic battery models due to the extensive physical parameters required. To capture the OCV characteristics over the lifespan of the cell effectively, there is a need for an OCV model with simpler, identifiable parameters [14, 15].

2.3 C-rate

The C-rate is a measure that describes the charge or discharge current of a battery in relation to its nominal capacity, expressed in Ampere-hours. This parameter denotes the speed at which a battery depletes its charge. Expressed as C/R, where R represents the hours needed to fully deplete the battery, a C-rate of C/10 for a 5 Ah cell implies a discharge duration of 10 hours and a corresponding current of 0.5 A, while a C/5 rate would result in a 1 A discharge current. While C-rates are commonly detailed in experiments assessing cells or electrodes, they may not remain constant in practical scenarios. For instance, with primarily resistive loads, the current may reduce as the battery's output voltage declines, thereby altering the C-rate during discharge. It is important, however, to consider the C-rate when evaluating the performance of different materials, electrodes, or complete battery cells. The influence of the C-rate extends beyond just the average voltage or the charge output; it significantly affects the total energy available from the battery, as indicated by the area under the discharge curve, which varies with changes in the C-rate [16, 17].

2.4 Cutoff voltage

The cut-off voltage marks the point at which a battery is deemed fully discharged. Selecting an appropriate charging cut-off voltage is a key factor influencing electrochemical performance and the long-term stability of electrode materials. Operating at excessively high cut-off voltages can trigger irreversible phase transitions in layered oxide cathodes, leading to changes in cell volume and localized stress accumulation. Such effects may result in the collapse of the layered structure, as well as the formation of intergranular and intracrystalline cracks, ultimately degrading structural integrity. High cut-off voltages also intensify interfacial reactions between the electrolyte and electrodes, promoting the formation of an unstable SEI, which consumes electrolyte, increases interfacial resistance, and reduces charge–discharge efficiency. Moreover, elevated cut-off voltages can induce oxygen release, accelerating crystal structure deterioration and posing safety risks. They also facilitate the migration of transition metal ions into the alkali metal layer, blocking sodium-ion transport pathways. In contrast, a cut-off voltage set too low reduces the accessible energy output [18].

2.5 Thermodynamics and kinetics of electrode reactions

To understand how these operational limits arise, it is necessary to review the fundamental electrochemical principles governing electrode reactions.

Oxidation–reduction (redox) reactions are chemical processes in which electrons are transferred between species. Oxidation refers to the process where a molecule loses electrons or its oxidation state increases. The electrons released during oxidation are accepted by another molecule, which undergoes reduction as a result [19].

Electrode reactions differ from standard chemical reactions because they involve the production or consumption of electrons. A general electrode reaction can be written as:

$$O + ne^- \rightleftharpoons R \tag{2.1}$$

where O is the oxidant, R is the reductant, and n is the number of transferred electrons [20]. When the electrode potential changes from ϕ_0 to ϕ, the Gibbs free energy of the reaction also changes as:

$$\Delta G_o = -nF(\phi - \phi_0) \tag{2.2}$$

where F is the Faraday constant. This expression highlights that the electrode potential directly controls the driving force of the electrochemical reaction.

For an electrochemical reaction to proceed, electrons must overcome an activation barrier. The activation energies for reduction and oxidation shift with the electrode potential:

$$\Delta E_{a,o} = \Delta E_{a,r} - nF(\phi - \phi_0) \tag{2.3}$$

This relation shows that decreasing the electrode potential ($\phi < \phi_0$) facilitates the reduction reaction by lowering its activation energy, while the oxidation pathway becomes less favorable. To describe how the energy change is distributed between the reduction and oxidation barriers, the asymmetric charge-transfer coefficient α is introduced:

$$\alpha = \frac{|\Delta E_{a,r}|}{|\Delta G_o|}, \qquad 1 - \alpha = \frac{|\Delta E_{a,o}|}{|\Delta G_o|} \tag{2.4}$$

with $0 < \alpha < 1$. This coefficient quantifies how much of the energy change contributes to the forward (reduction) versus the backward (oxidation) process. Figure 2.1 shows the energy diagram illustrating Gibbs free energy versus reaction coordinate, with activation barriers for reduction and oxidation. It also illustrates how a change in electrode potential modifies the activation energies.

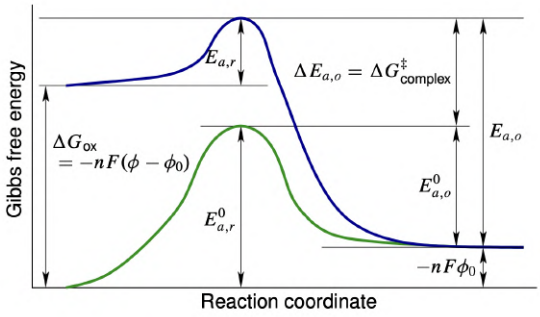

Figure 2.1: Energy diagram of electrode reactions, showing Gibbs free energy and activation barriers for reduction and oxidation [20].

2.5.1 Interface kinetics vs. bulk transport

The insertion and extraction of lithium/sodium ions in alloying or intercalation electrodes is controlled by two coupled processes: (i) electrochemical reaction kinetics at the electrode–electrolyte interface, and (ii) bulk transport of sodium inside the active material. This coupling can be expressed through a boundary condition that links the Butler–Volmer kinetics to the diffusion equation inside the particle.

2.5.2 General reaction rate

For a chemical reaction of the type

$$\text{Reactants} \longrightarrow \text{Products},$$

the reaction rate is defined as

$$r = \frac{d}{dt} \prod_i c_{\text{product},i} = k \prod_i c_{\text{reactant},i}, \tag{2.5}$$

with k the reaction rate constant, which typically follows an Arrhenius relation:

$$k = k_0 \exp\left(-\frac{E_a}{RT}\right), \tag{2.6}$$

where E_a is the activation energy, R is the ideal gas constant, and T is the temperature

2.5.3 Rate of reduction and oxidation

Introducing the asymmetric charge-transfer coefficient α:

$$r_f = k_0 c_o \exp\left(-\frac{E^0_{a,r} - \alpha n F(\phi - \phi_0)}{RT}\right), \tag{2.7}$$

$$r_o = k_0 c_r \exp\left(-\frac{E^0_{a,o} - (1-\alpha) n F(\phi - \phi_0)}{RT}\right). \tag{2.8}$$

2.5.4 Butler–Volmer equation

Summing the anodic and cathodic contributions yields the total current density:

$$i = i_0 \left[\exp\left(\frac{(1-\alpha) n F \eta}{RT}\right) - \exp\left(-\frac{\alpha n F \eta}{RT}\right)\right], \tag{2.9}$$

where η is overpotential. With the exchange current density defined as

$$i_0 = n F k_0 c_r^{\alpha} c_o^{1-\alpha}. \tag{2.10}$$

At equilibrium, no net current, $\phi = \phi_0$, so $i = 0$, which corresponds to the open-circuit voltage (OCV), while at finite overpotential, the kinetics are activated and the flux i drives Li/Na insertion or extraction [21].

2.5.5 Flux balance at the interface

The surface flux obtained from Butler–Volmer provides the boundary condition for the bulk transport equation:

$$-D\frac{\partial c}{\partial n}\bigg|_{\text{surface}} = \frac{i}{nF}. \tag{2.11}$$

The current density i can be converted into a molar flux of sodium ions through Faraday's law:

$$N_{\text{interface}} = \frac{i}{nF}, \tag{2.12}$$

where $N_{\text{interface}}$ has units of $\text{mol}\,\text{m}^{-2}\,\text{s}^{-1}$. Inside the active material, lithium/sodium transport is described by a diffusion or phase-field equation. In the case of Fickian transport, the molar flux is:

$$N_{\text{bulk}} = -D\nabla c, \tag{2.13}$$

where D is the diffusivity and c the lithium/sodium concentration. At the particle surface, the flux normal to the boundary reads:

$$N_{\text{bulk}} = -D\frac{\partial c}{\partial n}\bigg|_{\text{surface}}. \tag{2.14}$$

2.5.6 Relation between reaction rate and current density

In electrochemical systems, the molar reaction rate per unit area, r $[\text{mol}\,\text{m}^{-2}\,\text{s}^{-1}]$, is directly related to the current density i $[\text{A}\,\text{m}^{-2}]$ through Faraday's law:

$$i = nFr, \tag{2.15}$$

Thus, the Butler–Volmer equation can be understood as the electrochemical extension of the classical Arrhenius rate law, with the current density i representing the rate of the interfacial redox reaction expressed in electrical units.

In practice, GITT experiments provide a direct way to determine kinetic parameters by relating the measured current response to the overpotential, allowing extraction of i_0 and the charge-transfer resistance.

2.6 Volumetric energy density and gravimetric energy density

Volumetric energy density is defined as the amount of energy stored per unit volume. This metric assesses the space efficiency of fuel, which is

particularly important in real-world applications. For example, in electric vehicles, a higher volumetric energy density means the vehicle can cover a greater distance with a battery pack of the same size. Gravimetric energy density measures the energy stored per unit mass and is an indicator of energy efficiency in both fuels and batteries. A higher gravimetric energy density, or specific energy, is beneficial in applications requiring lightweight solutions, such as in the case of mobile phones using lithium-ion batteries. The volumetric energy density of a battery is a remarkable factor in determining its suitability as an energy source. The relatively high volumetric energy density of lithium-ion batteries contributes significantly to their widespread adoption across various sectors.

While gravimetric energy density, which measures how much energy a battery can hold relative to its weight, is important for applications where devices need to operate for long durations without becoming cumbersome, it often takes a backseat to volumetric energy density in many practical uses. Although the theoretical gravimetric energy densities for lithium-ion batteries are quite high, practical values are generally lower due to the safety concerns associated with high gravimetric densities [22].

2.7 Cycle life

The cycle life indicates the number of recharge cycles a device can undergo before its performance (such as capacity or output kinetics), significantly deteriorates, affecting the longevity and sustainability of energy devices [17]. High stability of electrodes during cycling contributes to an extended service life for energy storage systems. This stability for large-scale energy storage applications helps lower the costs associated with frequent replacements or maintenance [23].

2.8 Coulombic efficeincy

Coulombic efficiency (CE) is defined as the ratio of the discharge capacity to the charge capacity of a given electrode within a battery. Since the overall capacity of LIBs is typically limited by the cathode, CE reflects the ratio of Li^+ ions or electrons that return to the cathode compared to those that leave the cathode in a complete cycle.

CE is commonly utilized to predict the cycling life of lithium-ion batteries because it indicates the loss of Li^+ ions during each cycle. While CE is often used to assess the cycle life of lithium metal batteries (LMB), it does not gauge the longevity of LMBs. Variability in CE measurements across different

research groups is notable, stemming from the absence of a standardized protocol that aligns with the practical conditions of high-energy LMBs [24].

2.9 Solid electrolyte interphase

The solid electrolyte interphase (SEI) is a considerable layer that develops on the anode surface in all alkali metal ion batteries using liquid electrolytes. This layer serves as an electronic insulator and ion conductor. However, its formation leads to irreversible capacity loss. In high-capacity anodes used in SIBs, repeated cycling causes the SEI to rupture, thereby exposing new anode surface areas to electrolyte reduction [25].

2.10 Thermal runaway

Thermal runaway represents a severe form of thermal failure in batteries, marked by a rapid escalation in temperature due to the exothermic decomposition of battery components. This condition results in a heat release rate that exceeds the capacity for effective dissipation into the surroundings, making it impossible to maintain temperatures within safe limits. Such heat generation can lead to a domino effect, where one cell's thermal failure triggers adjacent cells, potentially resulting in a disastrous chain reaction that may cause the battery to catch fire or explode [26].

Thermal runaway can be triggered under extreme conditions such as overcharging , excessive heating, or severe mechanical damage like extrusion and puncture. These scenarios underscore the risks and severe consequences associated with such incidents [27].

2.11 Galvanostatic test

Galvanostatic Charge/Discharge (GCD) testing is a technique used to assess the performance of energy storage devices, such as those found in electrochemical capacitors. It entails consistently applying specific current levels to charge and discharge the system within defined potential boundaries, typically over repeated cycles. Through GCD analysis, one can discern the capacitive behavior, detect irreversible Faradaic processes, and calculate performance metrics, including capacitance, storage capacity, energy, and power [28].

2.12 Cyclic voltammetery

Cyclic Voltammetry (CV) is an electroanalytical technique to assess the kinetic aspects of electrochemical redox processes. In this method, an electrode's potential is swept between two limits while the resulting current is recorded, revealing information about the electrochemical behavior. CV is characterized by its ability to elucidate the redox potential, charge transfer kinetics, redox species concentration, and diffusion coefficients [29]. This technique yields insights into various electrochemical dynamics, including the inherent potential linked to the standard reduction potential in redox systems, the kinetics associated with electron transfer processes, redox species concentrations, elucidation of chemical reaction pathways, and determination of diffusion coefficients for redox-active species [30]. It also provides insights into chemical reaction mechanisms, enabling a comprehensive understanding of the system under study. The technique's versatility makes it indispensable in investigating materials and systems related to energy conversion and storage.

2.13 Transmission electron microscopy

Transmission electron microscopy (TEM) is a technique in electron microscopy where an electron beam is transmitted through an ultra-thin specimen to produce high-resolution images and provide detailed chemical insights at atomic dimensions, with spatial resolutions of less than 1 nanometer ($<$1nm) [31].

2.14 Scanning electron microscopy

Understanding the relationship between a battery's microstructure and its electrochemistry enhances battery performance. While optical microscopy has yielded limited insights at the microscale during cycling processes, scanning electron microscopy (SEM), including Environmental SEM, has facilitated in situ observations. Such studies have focused on the surface behaviors of anode and cathode materials during cycling, contributing to a deeper understanding of their operational dynamics.

In the case of a SEM, two types of electrons are detected: backscattered electrons (BSEs) and secondary electrons (SEs). BSEs reflect back following elastic interactions with the sample, whereas SEs come from the atoms of the sample due to inelastic interactions with the electron beam. BSEs emerge from deeper within the sample, while SEs come from the surface areas. Consequently, each type provides different information. BSE images

reveal variations in atomic number, with materials of higher atomic numbers appearing brighter. SE imaging offers detailed information about the surface [32].

2.15 X-ray diffraction

Operando X-ray diffraction (XRD) has emerged as a powerful analytical method, enabling real-time investigation of phase transitions and alterations in the crystal structure of electrodes. XRD stands as a non-destructive investigative method, discerning the crystallographic configuration, chemical composition, and material characteristics in electrochemical cells [33, 34]. This technique is valued for its ability to detect changes in phase transitions, lattice constants, and crystal structures. Such changes are integral to understanding the electrochemical behavior of electrodes during charging and discharging cycles, often triggered by redox reactions within the electrodes [35].

2.16 Electron diffraction

Electron diffraction, a technique similar to XRD, utilizes a beam of electrons instead of X-rays to create a diffraction pattern from the analyzed sample. This method is typically conducted using a TEM, where electrons traverse a thin film of the material under study. The emerging diffraction pattern is captured on a fluorescent screen, photographic film, imaging plates, or by a CCD camera. By tilting the sample relative to the incoming electron beam, diffraction patterns from various crystal orientations can be obtained, enabling 3D mapping of the crystal structure.

For effective electron diffraction in TEM, the sample thickness must not exceed 100 nm to ensure electron transparency. Preparing specimens is meticulous and time-consuming, and there is a risk of causing damage the thin sample sections with the electron beam during analysis. Although electron diffraction offers highly accurate crystallographic structural information, achieving the right experimental conditions and interpreting the results are complex and typically not routine.

Consequently, XRD is often preferred for determining lattice parameters and atomic positions in surface analysis at the microscale due to its relative ease and reliability [36]. Diffraction patterns yield detailed crystallographic data that can be traced back to their specific locations on the specimen. The analysis and indexing of these patterns are generally automated, producing outputs in various statistical and visual formats [37].

2.17 Energy dispersive X-ray

Energy Dispersive X-ray (EDX) microanalysis is a technique in material science, often utilized alongside SEM to determine the elemental composition of materials. This technique capitalizes on the the phenomenon of emitting characteristic X-rays from a specimen when it is bombarded with an electron beam. These X-rays provide insights into the types and quantities of elements present, particularly near the surface of the sample. EDX analysis facilitates the mapping of these elements, allowing researchers to estimate elemental proportions across different regions of the sample.

The operational principle of EDX involves directing an electron beam, usually between 10–20 keV, onto a conductive sample. This interaction induces the emission of X-rays, the energies of which are indicative of the sample's elemental makeup. The technique provides depth profiling up to about 2 microns below the surface, offering a semi-quantitative analysis that is invaluable for studying the surface and near-surface regions.

Although EDX is not a surface analysis tool, its ability to identify and quantify heavy metals in nanoparticles, such as silver, gold, and palladium, makes it particularly useful for investigating materials where these elements are prevalent. However, the technique has limitations, such as difficulty in detecting elements with low atomic numbers due to their faint X-ray emissions.

In conjunction with EDX, other X-ray characterization techniques such as XRD, X-ray photoelectron spectroscopy, and X-ray absorption fine structure are employed to offer a comprehensive insight of a material's composition and structure. These methods complement EDX by offering detailed insights into the material's crystallography, electronic state, and atomic arrangements, which are notable for developing advanced materials and enhancing their applications in various fields [38].

2.18 Synchrotron X-ray tomography

Understanding the dynamics of electrode materials in their three-dimensional configurations during battery operation advances rechargeable battery technologies. Synchrotron X-ray tomography emerges as a tool for this purpose, offering non-destructive, multi-scale, three-dimensional visualization of electrode components throughout battery operation. This technique surpasses traditional laboratory X-ray tomography by providing higher spatial and temporal resolutions, thanks to advancements in third-generation synchrotron light sources. Such capabilities are instrumental for in situ or operando analysis of commercial batteries, allowing detailed characterization of com-

plex electrochemical phenomena at the microscale, including microstructure evolution, phase transitions, and ion transport pathways. Detailed tomo-

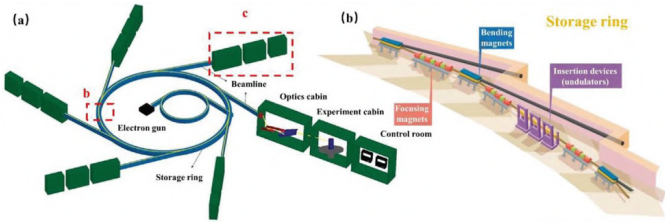

Figure 2.2: a) Diagrammatic representation of a synchrotron radiation facility. b) A depiction of a curved segment of a storage ring that includes a bending magnet coupled with an insertion unit used for generating X-rays [39].

graphic studies reveal the deformation processes and damage mechanisms at the microstructural level. These include crack formation and growth, particle fracturing, and other degradation phenomena that can adversely affect battery performance [40, 41]. Figure 2.2 diagrammatically depicts the production of synchrotron X-rays.

3D Synchrotron X-ray imaging involves reconstructing 3D tomography data from over a thousand 2D radiographic images obtained at different angles, using techniques based on the Radon transform, Figure 2.3. Two main classes of reconstruction algorithms are utilized: analytic and iterative methods, with filtered back projection being the most common analytic method. This method involves smearing projection line profiles back along their acquisition lines to reconstruct an object-resembling image, which is refined with increasing numbers of projections and mathematical filtering to reduce edge blurring. The reconstructed 3D images, made up of voxels indicating X-ray beam attenuation, can be displayed through various rendering algorithms, facilitating the quantification of morphological characteristics and enhancing the understanding of internal battery mechanisms. This imaging approach bridges the gap between macroscopic battery performance and the microscopic electrode processes, unveiling the real-time, dynamic reactions within operating batteries [39].

2.19 Density functional theory

Density Functional Theory (DFT) is recognized as a ab initio method employed across the energy storage and conversion sectors for the exploration of new materials and structures that exhibit exceptional performance. Within the realm of energy storage, DFT calculations are instrumental in examining electrode characteristics such as capacity, voltage, and ion diffusion.

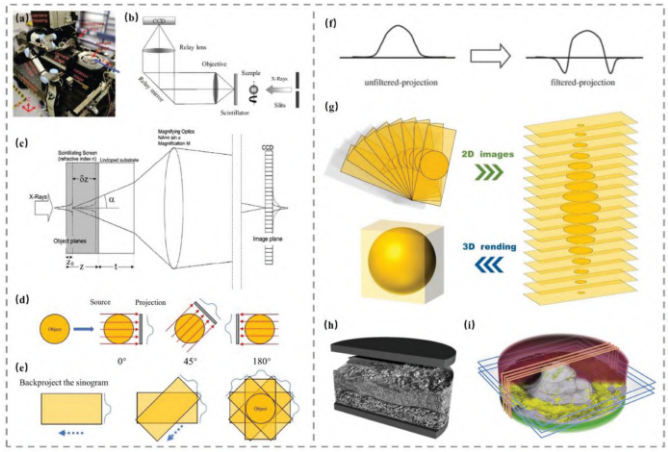

Figure 2.3: a) An image capturing the P05 beamline setup, highlighting various spatial motion platforms. This image also features the sample changer and a slit system, located at DESY. b) A diagram representing the arrangement of microscope optics observed at SLS. c) A conceptual drawing of scintillating screens connected optically to CCD cameras. d) A series of illustrations depicting the process of acquiring synchrotron X-ray 2D images from multiple angles. e) Visuals demonstrating the reconstruction of an object utilizing the back-projection technique from 2D images. f) A diagram outlining the process of applying filters during the reconstruction phase. g) A depiction of how 3D rendering is achieved from the amalgamation of reconstructed 2D slices. h) A rendering showing a 3D volume of a cycled lithium-sulfur (Li-S) battery. i) A visualization of a 3D volume rendering highlighting the segmented parts of a Li symmetrical cell following internal short circuit [39].

These calculations also facilitate the analysis of ion intercalation structures, revealing the fundamental mechanisms behind energy storage. For energy conversion applications, advanced DFT techniques like free energy diagrams and volcano plots are utilized to assess the efficacy of electrochemical reactions [42]; moreover, DFT is utilized to determine the thermodynamic properties, electronic structures, reaction kinetics, and pathways for ion transport in battery electrodes and electrolytes [43].

Chapter 3

Literature review

This chapter reviews recent advancements in energy storage technologies, with a focus on the shift from lithium-ion to sodium-ion batteries. It covers both experimental studies and computational modeling, including experimental protocols and macroscopic/microscopic modeling techniques.

3.1 Advancements in energy storage technologies: the shift from lithium-ion to sodium-ion batteries

With rising global energy demand and increasing penetration of intermittent renewables, large stationary storage has become essential. As a result, grid-scale systems, electric vehicles, and portable devices rely increasingly on rechargeable batteries with high energy density, long cycle life, low cost, and abundant materials. Lithium-ion batteries (LIBs) dominate today's market; however, their raw-material constraints challenge long-term sustainability. Sodium-ion batteries (SIBs) have emerged as a promising alternative [44]. The operation of SIBs is analogous to LIBs: charge and discharge proceed by insertion/extraction of Na^+ between positive and negative electrodes. During charging, Na^+ is removed from the cathode and inserted into the anode through the electrolyte; during discharging, Na^+ is extracted from the anode and inserted into the cathode [2] (Fig. 3.1).

Table 3.1 summarizes key Li/Na properties relevant to battery design. The standard reduction potentials differ (Li^+/Li: -3.04 V; Na^+/Na: -2.71 V), implying anodes in SIBs typically operate at slightly higher potentials than in LIBs. Although LIBs generally offer higher gravimetric and volumetric energy densities, SIBs are attractive due to lower cost and resource abundance [2].

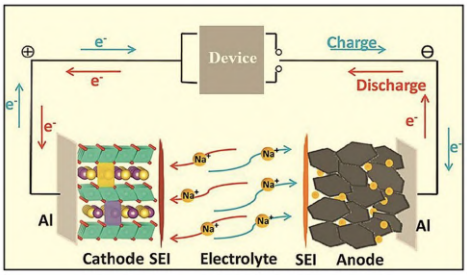

Figure 3.1: The operation of SIBs [45].

Property	Li	Na
Atomic mass $[g/mol]$	6.94	22.99
Electron configuration	[He] $2s^1$	[Ne] $3s^1$
Cationic radius [Å]	0.76	1.02
Standard electrode potential $[V]$	–3.04	–2.71
Melting point $[^oC]$	180.5	97.7
Density $[gc/m^3]$	0.971	0.534
First ionization energy $[kJ/mol]$	520.2	495.8
Theoretical gravimetric capacity $[mAh/g]$	3861	1165
Theoretical volumetric capacity $[mAh/cm^3]$	2062	1131
Coordination preference	Octahedral-tetrahedral	Octahedral-prismatic
Cost, carbonates	\$5000/ton	\$150/ton

Table 3.1: Lithium and sodium physical characteristics [2].

Sodium is widely available in the Earth's crust ($\sim 2.83\%$), whereas lithium is less abundant ($\sim 0.01\%$) and unevenly distributed [44, 46] (Fig. 3.2). This abundance underpins the cost advantage of SIBs. SIBs also benefit from aluminum current collectors at both electrodes, unlike LIBs which typically require copper at the negative and aluminum at the positive, reducing material and manufacturing costs [47]. In addition, SIB cells using Al collectors can be shipped and stored fully discharged (0 V), simplifying logistics [48].

Anodes play a key role in battery performance, influencing capacity, cyclability, and stability [52]. Unlike LIBs, graphite is generally ineffective as an anode for SIBs. Therefore, there has been intensive work to develop

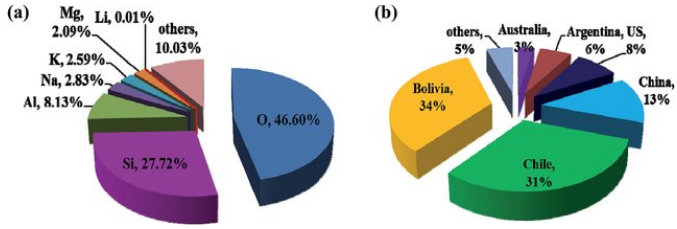

Figure 3.2: (a) The amount of the major elements in the crust of the Earth, (b) the uneven spread of lithium [46].

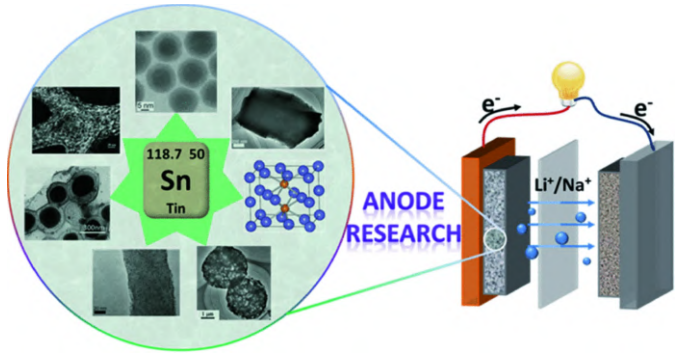

Figure 3.3: Sn as a promising anode for SIBs [49].

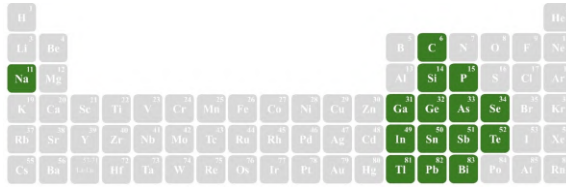

Figure 3.4: The periodic table illustrating elements from various chemical groups, excluding transition metals, that are capable of forming alloys with Na through deposition for Na and adsorption/intercalation for C [50].

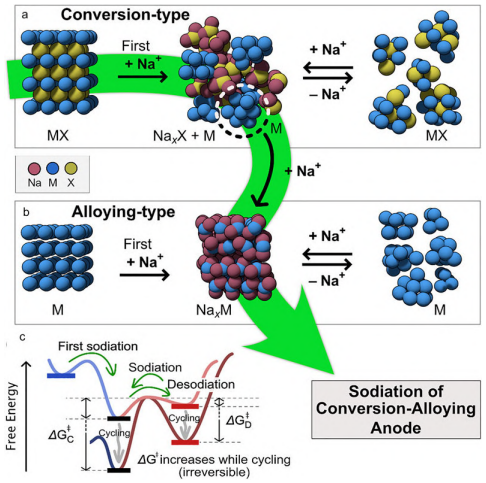

Figure 3.5: Schematic illustration of (a) conversion-, (b) alloying-, and (a+b) conversion-alloying-type reaction modes; and (c) high free energy barrier by the cycling-induced disorder. The first sodiation process of the conversion-alloying anode is highlighted in green [51].

durable anodes with high specific capacity and long cycle life [53].

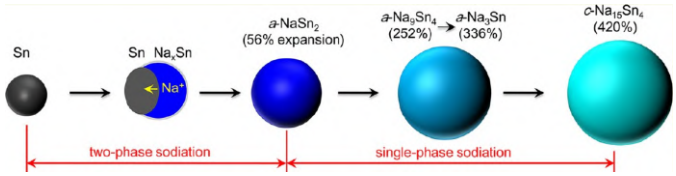

Figure 3.6: Progressive stages of electrochemical sodiation in tin nanoparticles, illustrating the transformation from crystalline Sn to various Na–Sn alloy phases with associated volumetric expansions, captured via in situ transmission electron microscopy [54].

SIBs anode materials are classified into three types, based on the reaction mechanism: intercalation (carbonaceous materials and titanium-based materials); conversion, which involves a chemical reaction [56] (metal oxides, sulphides, and selenides); and alloying [57] (phosphorus, tin, antimony and bismuth).

Large gravimetric capacities of alloying materials, such as Sn-based materials, Fig. 3.3 and Table 3.2, are of particular interest. Moreover, metallic Sn alloy-based anodes due to their high theoretical capacity, safe reaction potential and electrical conductivity have grown, while Carbonaceous materials are limited by their low theoretical capabilities. A central challenge

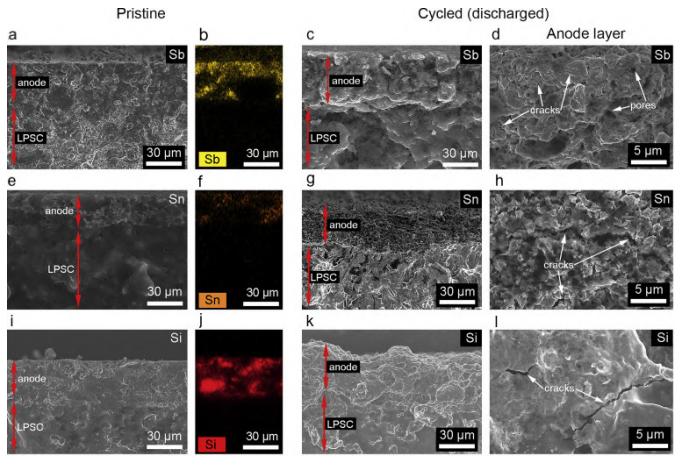

Figure 3.7: Alloy-anode composite morphology before and after cycling; (a-l) Cross-sectional SEM images show pristine anode composites in cells (a, b, e, f, i, j) and after five cycles (c, d, g, h, k, l) across three materials: Sb (a-d), Sn (e–h), and Si (i–l). Initial low-magnification and EDS map images are contrasted with post-cycling images at varying magnifications. The LPSC and alloy composite anodes underwent cycling at C/10 (0.25 to 0.29 $mAcm^{-2}$) at 60 °C [55].

of Sn-based anodes is the drastic volume expansion, up to $\sim$ 420%, that accompanies the formation of Na–Sn alloys during sodiation [56, 58]. This originates from the larger ionic radius of Na^+ compared to Li^+, which also slows reaction kinetics. Such expansion induces severe mechanical stress, leading to cracking, pulverization, and loss of electrical contact in the electrode. As later studies demonstrate (Figs. 3.6, 3.8, 3.17), this structural instability is the key limitation to the long-term cyclability of Sn anodes.

Thanks to the high theoretical capacity, 847 $mAhg^{-1}$ [61], and low sodiation potential, several elements from Group IIIA, IVA (for example Sn) and VA (such as Sb) and VIA have been investigated as anode materials for SIBs [50, 56]. Alloying- and conversion-based anodes can store sodium ions by forming Na-rich metallic compounds such as $Na_{15}Sn_4$, and Na_3Sb through alloying or conversion reactions Fig. 3.5. These processes proceed through intermediate crystalline or metastable Na–Sn phases, as illustrated by the free-energy diagrams in Fig. 3.5c, where repeated cycling increases hysteresis and energy loss.

The application of Sn anodes in batteries was first reported in 2011, with theoretical studies on the Na–Sn system predicting various phase transformations during battery operation. These phases include $NaSn_5$, NaSn, Na_9Sn_4, and $Na_{15}Sn_4$. In 2012, TEM studies showed that Sn nanoparticles undergo

Material	**Synthesis method**	**Rate property** $(mAh/g - A/g)$	**Cycling stability** $(mAh/g - A/g)$
$Sn_{0.9}Cu_{0.1}$ nanoparticles	Wet chemistry	126-1.694	420-0.169-100
Ni_3Sn_2 porous micro cages	Solvothermal	276-10C	270-1C-300
Sn@spherical carbon network	Aerosol spray pyrolysis	349-4	415-1-500
Sn NDs@PNC nanofibers	Electrospinning/Annealing	450-10	483-2-1300
Yolk–shell Sn@C eggette-like nanostructure	Solvothermal/pyrolysis	160-5	200-1-1000
Sn-N-doped carbon microcages	NaCl-templating method	149-5	332-0.05-300
Sn@N-doped carbon nanofibers	Electrospinning and annealing	190-4.24	390-0.847-1000
TiO_2–Sn@carbon nanofibers	Electrospin and atomic layer depos.	—	413-0.1-400
Multi-layered 2D Sn nanodendrites	One-step electrodeposition	412.84-4.24	757.38-0.1-300
Sn@SNC foam Hydrogel	Freeze-drying/Annealing	0.6 mAh/cm^2-4.0 mA/cm^2	1.0 mAh/cm^2-3.0 mAh/cm^2-700
Sn@N-doped carbon nanotub	Hydrothermal method	124.1-2	398.4-0.1-150
SnNGnP	Ball-milling	253-2	290-1-1000
3D Sn-NS-CNFs@RGO	Electrospin, filtration and calcination	189-10	373-1-5000

Table 3.2: An overview of sodium storage behavior and preparation techniques for different metallic Sn-based electrode materials [62].

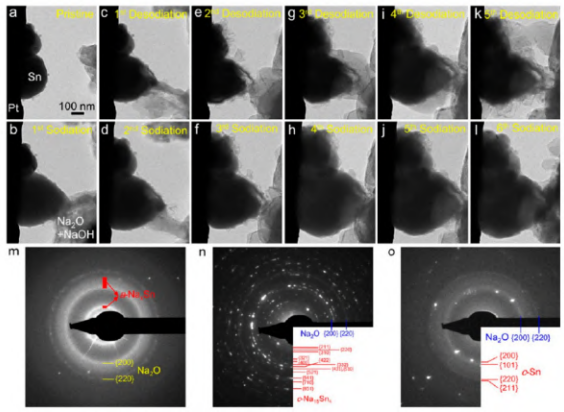

Figure 3.8: In situ TEM investigations of alloying electrode materials throughout (de)sodiation cycles. This includes the microstructural changes of Sn nanoparticles [59].

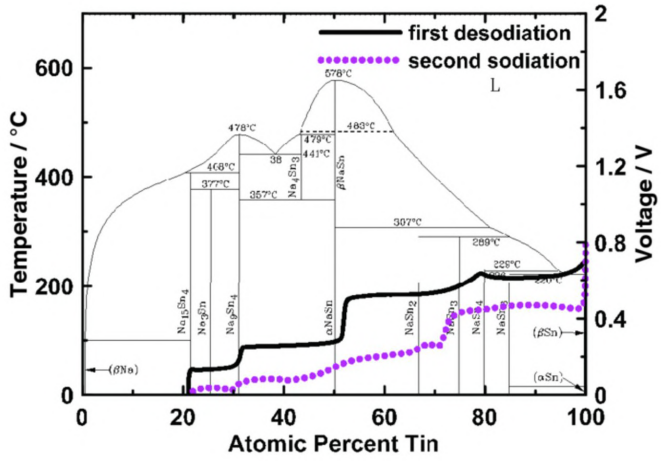

Figure 3.9: Voltage profiles for the first desodiation and second sodiation of sputtered tin, overlaid on the binary phase diagram of Na–Sn [58].

a series of phase transformations during the sodiation process. Additional experimental findings reported in subsequent years further detailed the formation of other Na–Sn compounds, enhancing understanding of the reaction pathways and structural changes [63].

The study by Wang et al. [54] delves into the microstructural changes and phase transformations of tin nanoparticles during electrochemical sodiation, using in situ transmission electron microscopy. The sodiation of Sn occurs through four distinct stages, each marked by specific biphasic reactions.

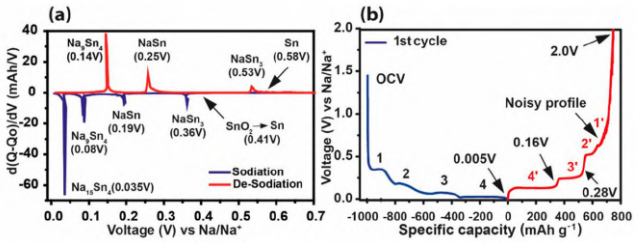

Figure 3.10: Differential capacity graph derived from the galvanostatic charge/discharge cycle, revealing clear peaks corresponding to different phases that emerge through sodiation and desodiation processes. (b) Galvanostatic charge/discharge curve of the newly prepared Sn film (with a mass loading of 0.9 mg/cm^2) cycled at 20 μA. Black arrows in part b show the electrochemical potentials where SEM images were captured [60].

Initially, crystalline Sn nanoparticles undergo a two-phase transformation, where sodium ions diffuse into the tin matrix, host material, forming a Na-poor, amorphous Na_xSn alloy at the interface. This stage results in a volume expansion of approximately 60%. As sodiation progresses, the transformation transitions into a single-phase process, eventually leading to the formation of multiple Na-rich amorphous phases, Fig. 3.6. Dewen et al. [59] further demonstrated reversible sodiation/desodiation of Sn nanoparticles across multiple cycles, including transient Na precipitation on particle surfaces (Fig. 3.8), which was reabsorbed in subsequent cycles. Complete sodiation yielded crystalline $Na_{15}Sn_4$ with robust cyclability.

The study by Stratford et al. [61] offers insights into the sodium storage mechanisms in tin anodes; sodium insertion into tin initially transforms crystalline tin into a layered structure with mixed Na/Sn occupancy, identified as approximately $NaSn_3$. Subsequent transformations lead to the formation of $NaSn_2$, a phase predicted to be thermodynamically stable, characterized by hexagonal layers without intermediate tin atoms. Further sodium interaction breaks $NaSn_2$ into an amorphous phase ($Na_{1.2}Sn$), predominantly consisting of tin chains. The process evolves to form structures with Sn-Sn dumbbells that change via a solid-solution mechanism into $Na_{5-x}Sn_2$, ultimately leading to $Na_{15}Sn_4$, which can incorporate extra sodium, forming an off-stoichiometric phase similar to $Li_{15}Si_4$ observed in lithium-silicon systems. The study of Li [64] explores the phase transformations and performance characteristics of tin and its compounds in SIBs. It illustrates that during the sodiation of metallic tin, the process does not strictly follow the equilibrium series of phase transformations as predicted by the phase diagram. Sodiation occurs through a series of metastable crystalline and amorphous

structures before finally reaching the terminal equilibrium phase of $Na_{15}Sn_4$ [65]. Fig. 3.9 overlays voltage profiles onto the Na–Sn binary phase diagram, demonstrating the link between electrochemical potentials and phase transitions at different compositions. Fig. 3.10 shows differential capacity and charge/discharge curves, with distinct peaks corresponding to sequential Na–Sn phase transitions. While generally aligning with DFT predictions, deviations due to polarization and side reactions were observed, sometimes causing rapid capacity fade [60].

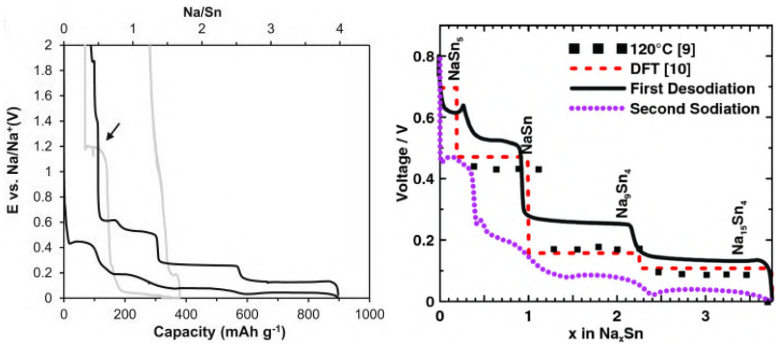

(a) (b)

Figure 3.11: (a) Electrochemical potential profiles for the first (black) and second (gray) cycles of a 2 μm-thick micro-weighted Sn film electrode cycled between 0.005 and 2 V. The first cycle was recorded at a discharge current of 15.79 μA cm^{-2} (C/70) and a charge current of 7.89 μA cm^{-2} (C/130), with the second cycle representing typical subsequent behavior [58]. (b) Voltage profiles for the first desodiation and second sodiation of sputtered Sn, overlaid with the DFT-predicted voltage curve and the 120 °C open-circuit measurements [66].

In-situ XRD by Ellis et al. [58] confirmed that $Na_{15}Sn_4$ is the only equilibrium sodiated phase, while intermediate compositions ($NaSn_3$, NaSn, Na_9Sn_4) often appear as amorphous or metastable states. Baggetto et al. [66] extended these findings, identifying a transient Na_5Sn_2 (R-3m) phase and correlating electrochemical plateaus with structural evolution. Their analysis also revealed that surface oxidation of Sn accelerates electrolyte decomposition at higher potentials, underscoring the importance of interfacial stability.

Additionally, sodiation of Sn leads to a significant mechanical softening, with both Young's and shear modulus reduced by about 75% as weaker Na–Sn bonds replace stronger Sn–Sn bonds [67]. A complementary study on binder- and carbon-free thin film Sn electrodes (Fig. 3.12) showed that, unlike lithiation where pore formation occurs mainly during delithiation, Na

insertion induces pronounced surface swelling and pore generation already during sodiation. Upon desodiation up to 0.28 V, cracks developed laterally across the electrode, fragmenting it into islands of active material [60].

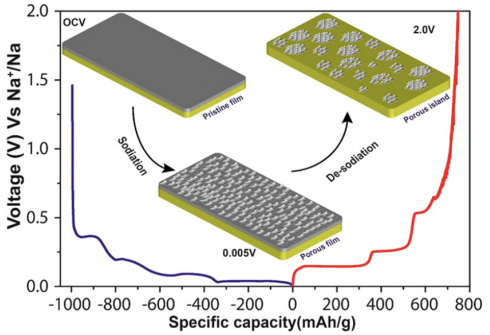

Figure 3.12: Sodiation and desodiation mechanism inside the active material [60].

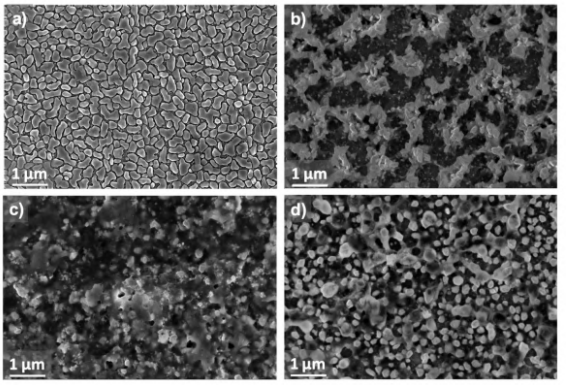

Figure 3.13: Images from a scanning electron microscope of atomic Sn film electrodes. a) as-prepared, and after 50 cycles at desodiation cutoff voltages of b) at 0.8 V, c) at 0.8 V with a current limit of $20mA/g$ and d) at 1 V [68].

The structures of Sn anodes before and after cycling are shown in Fig. 3.13. Cycling at 0.8–1 V for 50 cycles transforms the granular as-deposited film into a porous, coral-like structure [68]. A related study reported a self-healing Sn anode with 99.8% capacity retention over 5000 cycles at 10C, enabled by nanometer-sized Sn particles reconstructing into a stable 3D porous framework (Fig. 3.15) [69]. This morphology accommodates repeated volume changes while preserving electrical connectivity, further enhanced by conductive carbon nanotube additives.

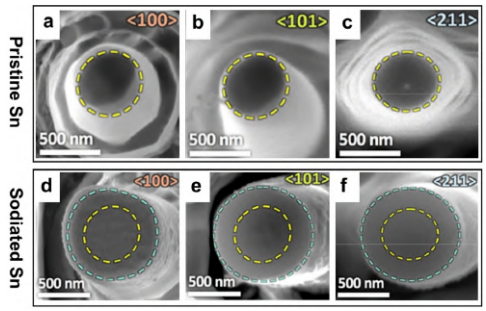

Figure 3.14: Cross-sectional morphologies of pristine and sodiated Sn nanopillars with different crystallographic orientations: (a, d) ⟨100⟩, (b, e) ⟨101⟩, and (c, f) ⟨211⟩[50].

For Sn nanopillars, isotropic expansion during sodiation has been observed across multiple crystallographic orientations (Fig. 3.14), consistent with prior reports. By contrast, Sb pillars exhibit anisotropic swelling, and lithiation of Si and Al also proceeds anisotropically [50].

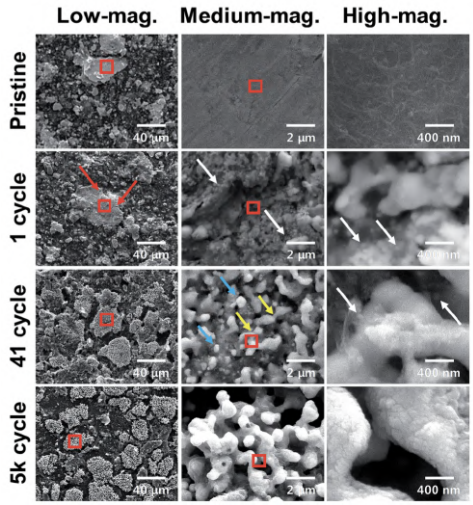

Figure 3.15: SEM images of the Sn anode throughout various cycling stages. The arrows indicate: red for cracks, white for spherical particles of tens of nanometers in size, blue for Sn spheres under a micrometer in size, and yellow for ligamental-shaped Sn particles [69].

Li et al. [60] showed that Sn thin films become highly porous during sodiation, with pore sizes of 0.2–1.8 µm, and develop cracks during desodiation, leading to isolated islands of active material (Fig. 3.16). These findings were supported by impedance spectroscopy measurements of Na diffusion.

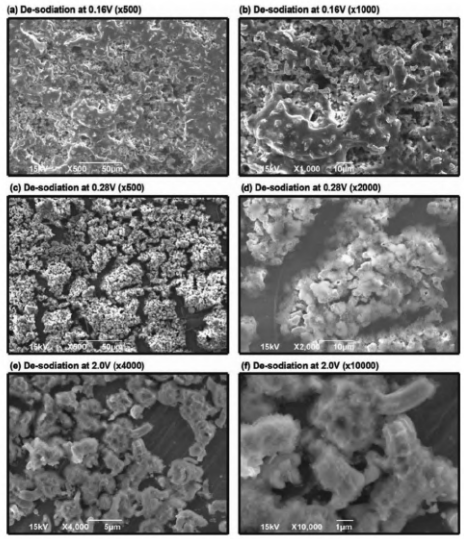

Figure 3.16: SEM images depict Sn thin film electrodes during various phases of the initial desodiation cycle up to 2.0 V: (a, b) captured at 0.16 V; (c, d) taken at 0.28 V; (e, f) recorded at 2.0 V [60].

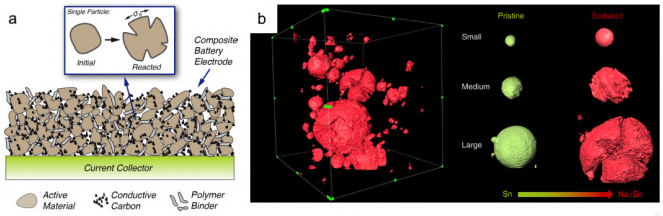

Figure 3.17: (a) shows the graphic of a composite battery electrode made up of granular active material, conductive carbon, and polymer binder; it is also shown a single active material particle both before and after reacting with an alkali ion Na^+. Volume expansion and stress generation during reaction have caused cracks to form. (b) illustrates X-ray tomographic pictures of Sn particles before and after sodiation, including a multi-particle electrode after sodiation and individual particles of varying sizes before and after the sodiation [70].

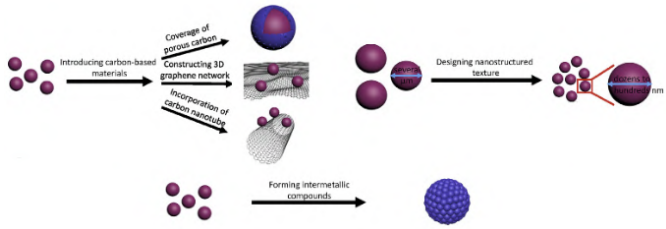

Figure 3.18: Methods for improving anode electrochemical performance in alloying and conversion-based materials [56].

Binder and microstructure effects are illustrated in Fig. 3.17, where cracks form as expansion disrupts particle–binder contacts [70]. In situ X-ray tomography of SnO (Fig. 3.19) further revealed crack propagation and structural disorder, highlighting the importance of mitigating chemo-mechanical degradation [71].

Mitigation strategies focus on nanostructuring and compositing (Fig. 3.18). Hollow, porous, and core–shell architectures, together with carbon matrices, shorten Na^+ diffusion paths, buffer stresses, and prevent direct Sn–electrolyte contact, thereby improving conductivity, coulombic efficiency (Section 2.8), and cycling stability [62, 72–74]. Additional approaches include intricate interface designs, heteroatom doping (e.g., N or S), and the formation of intermetallic M–Sn compounds (M being an active or inactive metal for Na-ion storage), which further enhance rate performance and long-term durability [56].

In situ studies of SnSb thin films also revealed fast amorphization under bias, enhancing Na^+ transport but eventually limited by stress accumulation [75].

Finally, advances in 3D current collectors help suppress dendrite formation. Porous Al foils and Ni scaffolds provide homogeneous current distribution, achieving stable cycling for over 1000 cycles with near-100% Coulombic efficiency [76].

Because both Si-Li and Sn-Na operate as alloying anodes, the governing physics is strikingly parallel: multi-step formation of intermetallic phases at near-flat potentials, colossal volumetric expansion during (de)sodiation/(de)lithiation, loss of electronic percolation, SEI instability, and consequent chemo–mechanical degradation (cracking/pulverization). Obrovac & Chevrier's landmark review on alloy negative electrodes for Li-ion batteries codifies these generic alloy-anode behaviors (thermodynamics of phase formation, capacity-expansion trade-offs, failure modes, and mitigation via nano-structuring, buffering matrices, and binder engineering) largely independent of the specific active element—providing a modeling playbook

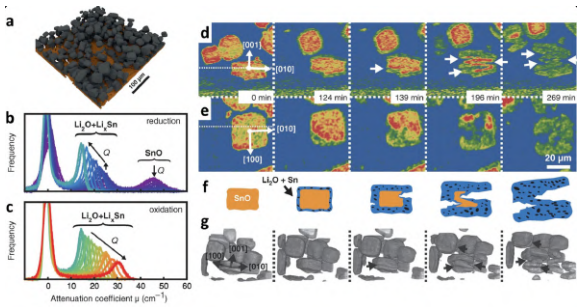

Figure 3.19: In situ X-ray tomography of SnO during battery operation. (a) The 3D renderings of X-ray tomograms of SnO captured during battery operation. Histograms of the X-ray attenuation coefficient during electrochemical (b) reduction and (c) oxidation phases, with colors indicating changes over time. Q denotes capacity. (d) Coronal and (e) transverse cross sections of a particle during electrochemical reduction are shown. Horizontal dotted white lines in the cross-sections indicate the planes of sectioning at 0 min. Crystallographic orientations are identified and marked. White arrows highlight locations of cracks; (f) A schematic illustrating the particle phase changes and crack development leading to a zig-zag morphology; (g) 3D rendering of a subvolume showing the zig-zag morphology across multiple particles. Black arrows point to fractures [71].

(mass conservation with moving phase fronts, stress–diffusion coupling, and architecture-based strain accommodation) that is directly reusable beyond Si-Li [77]. Complementing this, Mou et al. survey Sn anodes across both Li-ion and Na-ion systems, explicitly emphasizing that the same root causes-huge volume change upon Li^+/Na^+ insertion-extraction-drive irreversible capacity loss and short cycle life, and that the same remedies (nanostructuring, conductive/elastic matrices, pre-alloying, and interface control) translate across chemistries [78]. Taken together, these two sources justify importing Si-Li alloy-anode modeling strategies (e.g., phase-fraction or two-phase formulations with stress coupling and SEI-aware boundary conditions) to Sn-Na, while only swapping material parameters and phase equilibria; in other words, the framework is shared, the constants differ.

3.2 Modeling sodium-ion batteries

Even though experimental findings pave the way for the creation and optimization of cell architecture, simulation and analysis may help fully comprehend all the aspects of a cell. Computational simulations can be useful allowing to select constituents and tailoring architectures, providing meaningful insights on the evolution of ionic concentrations during working and predicting restricting elements together with material deterioration in charge/discharge processes. Extensive modeling literature exists for LIBs, ranging from 1D to 3D, where the latter reconstructs electrode microstructures. These results are fundamental when the mechanical response of the battery can be a limiting factor. For SIBs the large expansion within the porous electrodes due to sodiation has a strong impact on the behaviour of the cell, so theoretical frameworks specialized to model the problem of the reactions inside the electrodes are necessary [79].

To have an understanding of the electrochemical processes such as the current distribution, the electrode state of charge, and the electrode evolution inside the battery, different theoretical studies can use models developed for LIBs [80–82].

3.2.1 Macroscopic modeling

In the work of Chayambuka et al. [83] an experimental investigation is done to understand the individual electrode behavior and further elucidate relevant parameters for physics-based models. This study presents experimental characterizations of the SIB electrodes based on $Na_3V_2(PO_4)_2F_3$ (NVPF) cathode and hard carbon (HC) anode. As a consequence, geometric, thermodynamic, and kinetic characteristics are derived from the SIB electrodes. In addition, diffusion mass transport restrictions and Ohmic losses are found for both electrodes according to investigations of Na/NVPF and Na/HC half-cells.

Marangon et al. (2025) analyzed commercial 18650-type sodium-ion cells and highlighted the kinetic limitations of hard carbon anodes compared to layered $Na_xNi_yFe_zMn_{1-y-z}O_2$ cathodes [84]. Hard carbon exhibited sluggish Na-ion insertion due to its disordered structure and limited interlayer spacing, whereas the layered oxide cathodes showed fast and reversible Na-ion diffusion. Electrochemical impedance spectroscopy confirmed this contrast, with hard carbon showing much higher resistance ($\sim$2300 Ω at OCV, decreasing to 1400 Ω after cycling) compared to the cathode ($\sim$5 Ω). Functional electrolyte additives in carbonate solvents (EC, PC, DMC, EMC) were also identified as contributors to interfacial stability and SEI formation, helping extend cycle life. However, at higher C-rates (>1C), capacity retention dropped

significantly, suggesting Na plating and transport limitations in the hard carbon anode. These results underline the need for improved anode structures (e.g., graphitized hard carbon or composites) and electrolyte engineering to enable fast charging and long-term stability in commercial SIBs.

In the second work of Chayambuka et al. [85], a physics-based, pseudo-two-dimensional (P2D) model of a full-cell SIB is presented to optimize the design and performance of these batteries in various applications. The model is based on NVPF and HC as positive and negative electrodes, respectively and uses a coupled set of partial differential equations for the current and concentration profiles.

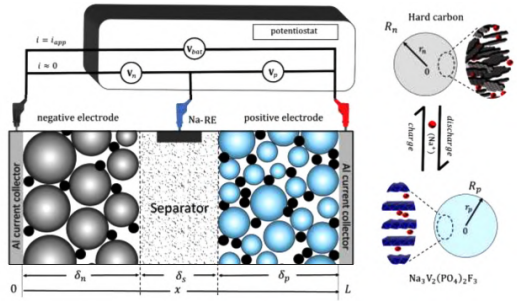

Figure 3.20: HC/NVPF full cell configuration (de)sodiation mechanism inside the active material [85].

The active particles are assumed to be spherical, Fig. 3.20, homogeneous, and represented by an average radius. The electric potential, the current, and the Na concentration are the model's variables. As a result, the voltage profiles for negative and positive electrodes were found at various C-rates and showed good agreement with experimental voltage profiles. It has been demonstrated that the poor mass transfer in the HC and NVPF electrodes as well as in the electrolyte limits the high C-rate performance of the electrodes. Reducing the particle sizes can enhance mass transfer in HC electrodes; however, for NVPF particles, the limiting factor is a low diffusion coefficient.

In [44], based on the single particle assumption, Garapati et al. [44] propose a reduced order model for SIBs, validating with experimental data and the predictions of a pseudo-two-dimensional (P2D) model. Due to the difficulty of solving coupled differential-algebraic equations, P2D models are computationally costly. Reduced-order models are simplified electrochemical approaches offering fast alternatives to P2D. Numerous reduced-order models for LIBs have been put forth over the years. Authors favor the single particle model (SPM), which is methodically drawn from the P2D model.

The model considers an HC anode and NVPF cathode separated by $NaPF_6$-based electrolyte. Each electrode is represented by a single spherical

particle. The single particle model (SPM) makes the assumption that, as shown in Fig. 3.21, one particle from each electrode depicts the behavior of all the particles of that electrode. The diffusion of sodium-ion in a spherical electrode particle is expressed by Fick's second law. The Butler-Volmer equation can be used to calculate the kinetic reaction flux results from the intercalation reaction at the particle surface. It is essential for linking concentration and potentials of the solid phase with those of the electrolyte. The SPM accurately predicts voltage across a range of discharge currents,

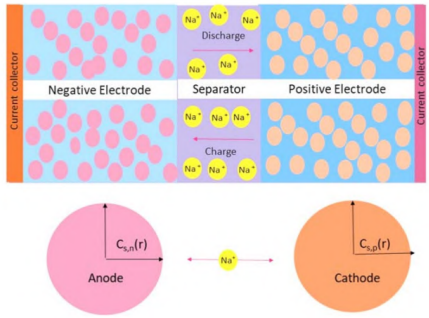

Figure 3.21: Schematic representation of SPM. An electrode containing electrolyte solution is represented by each sphere [44].

despite its simplifying assumptions.

3.2.2 Microscopic modeling

In modeling tin-based sodium-ion batteries, understanding microscopic behaviors such as phase transformations, stress development, and chemo–mechanical coupling is crucial. Various theoretical and computational frameworks have been developed, ranging from thermodynamically consistent continuum models to phase-field formulations. While not all are directly applied to Na–Sn anodes, they provide essential insights into the mechanics–transport interplay that underpins phase-field modeling.

3.2.2.1 Continuum and variational frameworks

Anand [86] unified Cahn–Hilliard-type diffusion with large elastic–plastic deformations in a thermodynamically consistent setting. Salvadori et al. [87] developed a small-strain framework with trapping, later extended by Arricca et al. [88] to large strains via multiplicative decomposition to capture swelling, shrinking, elastic and inelastic effects. For conversion electrodes with sharp reaction fronts, Afshar et al. [89] proposed a gradient theory of diffusion–reaction–deformation and demonstrated stress-driven front blunting in FeS_2

(see Fig. 3.22). These works highlight strong coupling between diffusion, reactions, and mechanics that informs the design of phase-field models for Na–Sn.

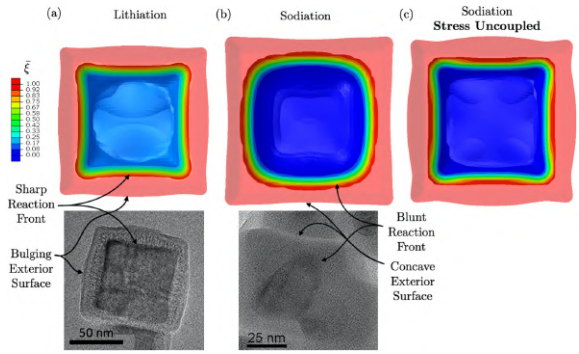

Figure 3.22: Reaction front morphology in FeS_2: (a) lithiation, (b) sodiation with stress-coupling, and (c) sodiation without stress effect. Stress coupling leads to a blunter front during sodiation [89].

Bower et al. [90] derived closed-form fields for concentration, chemical potential, and stress in spherical particles with a moving phase boundary (Fig. 3.23), clarifying the mechanics–chemistry balance at sharp interfaces. Pohjonen [91] introduced a diffuse-interface description of solid–solid transformations linking advection/front kinetics to Allen–Cahn dynamics, offering a bridge between sharp- and diffuse-front pictures. In his simulations, the framework was applied to the austenite–ferrite transformation, where the diffuse-interface model successfully reproduced isotropic growth of a homogeneously nucleated ferrite domain within austenite (see Fig. 3.24). This result highlights how the model captures interface propagation and transformation strains in a manner consistent with both classical sharp-interface kinetics and phase-field approaches.

3.2.2.2 Phase-field and interface methods

Gomez et al. [92] reviewed interface-capturing (phase-field) and interface-tracking (level set) strategies for phase transitions, emphasizing adaptive mesh refinement and time-stepping for efficiency and accuracy.

For battery cathodes, Zhang and Kamlah [93] coupled Cahn–Hilliard diffusion with finite-deformation elasticity to model phase segregation in Na_xFePO_4; the framework was refined to include stress-assisted diffusion and multiwell thermodynamics [94], and later extended with anisotropic elasticity and diffusion channels from first principles [95]. Together, these studies show how segregation, stress, and crystallographic anisotropy dictate

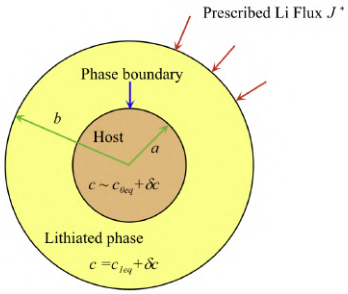

Figure 3.23: Schematic of a spherical particle with an advancing phase boundary [90].

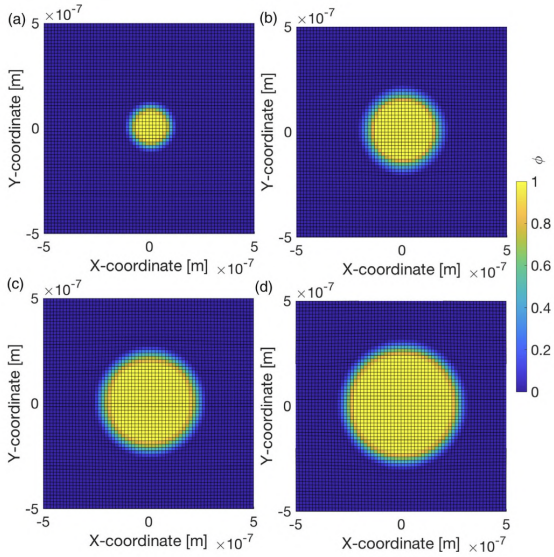

Figure 3.24: Simulation of isotropic growth of a ferrite region homogeneously nucleated within austenite. The ferrite eigenstrains were set as $\epsilon^{00}_{xx} = 0.05 = \epsilon^{00}_{yy}$. Snapshots are shown at time steps: (a) 2.587×10^{-4} s, (b) 0.0290 s, (c) 0.0482 s, and (d) 0.0646 s [91].

microstructure evolution and integrity.

For electrochemical alloying, Hofmann et al. [96] coupled Cahn–Hilliard transport to Butler–Volmer interfacial kinetics in porous electrodes. Their simulations revealed the onset of spinodal decomposition in the cathode, where lithium segregates into Li-rich and Li-poor phases once a critical state of charge is exceeded (Fig. 3.25). Zhao et al. [97] incorporated elastic coupling and large deformations in a CH framework using isogeometric FEM, demonstrating stress effects on segregation and interface thickness. Their

results showed that Li-rich regions generally experienced compressive stresses while Li-poor regions were subject to tensile stresses, leading to higher overall stresses than predicted by dilute-solution models. Moreover, they found that particle geometry strongly influenced phase segregation: spherical particles developed core–shell structures, whereas spheroidal particles displayed anisotropic segregation patterns and distinct stress distributions.

For tin systems, Hulikal et al. [98] calibrated a CH phase-field for Li–Sn thin films against potentiostatic/galvanostatic data, identifying free energies, diffusivities, exchange currents, and finite interface mobility, a transferable blueprint for Na–Sn. They demonstrated that the diffusivity of Li in Li_2Sn_5 ($\sim 10^{-12}$ cm^2s^{-1}) is orders of magnitude larger than in Sn ($\sim 10^{-16}$ cm^2s^{-1}), and that the exchange current density of Li_2Sn_5 (~ 60 μA cm^{-2}) far exceeds that of Sn (~ 0.3 μA cm^{-2}).

Bazant [99] unified reaction kinetics with CH thermodynamics (CHR), generalizing Butler–Volmer/Marcus laws for concentrated solids with coherency strain. The theory predicted that phase separation in $LiFePO_4$ nanoparticles is suppressed above a critical current and below a critical size, leading to homogeneous filling instead of two-phase coexistence. A recent review by Andrews and Thornton [100] surveys such phase-field electrochemical models and their integration with realistic thermodynamics, kinetics, and microstructure. They emphasized how multiscale simulations, parameterized with data from atomistics and experiments, can capture complex interactions among transport, reaction, and morphology in electrodes. Two case studies, $LiFePO_4$ intercalation and Li–Cu–TiS_2 displacement reactions, were highlighted, illustrating how particle size, microstructure, and free-energy landscapes govern phase separation, reaction pathways, and degradation.

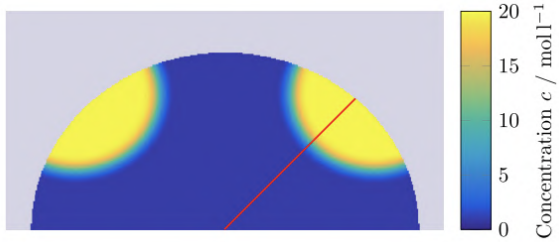

Figure 3.25: Spinodal decomposition in a semi-circular cathode particle during charging, showing nucleation of Li-rich regions and the development of phase interfaces (adapted from Hofmann et al. [96]).

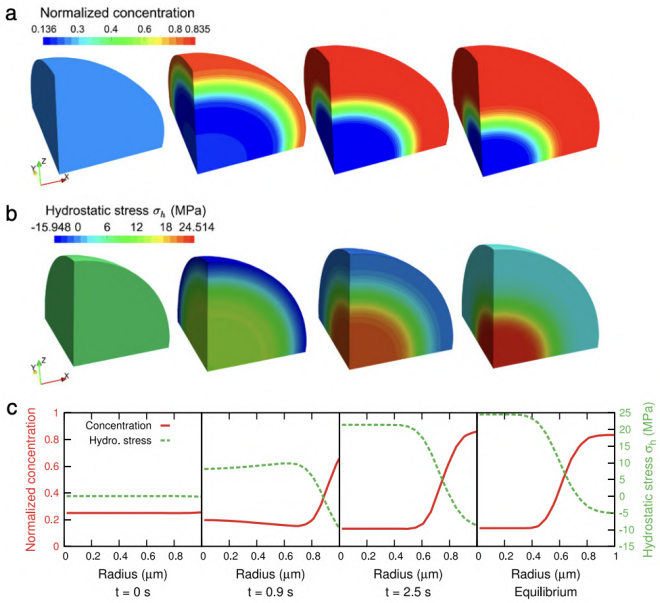

Figure 3.26: Snapshots of concentration (a) and hydrostatic stress distribution (b) in a spherical particle at different times, illustrating the formation of a Li-rich shell and tensile stresses in the core (adapted from Zhao et al. [97]).

3.2.2.3 Transition to multiphase-field formulations

To initially describe Na–Sn alloying, a single-order-parameter Cahn–Hilliard (CH) framework was adopted to capture spinodal segregation and interface evolution, calibrated to experimental sodiation data [98]. However, tin-based anodes exhibit multiple intermetallic phases (e.g., NaSn, Na_9Sn_4, $Na_{15}Sn_4$) with distinct stoichiometries and molar volumes, which cannot be explicitly represented in a single CH variable. To overcome this limitation, the modeling framework was extended to a multiphase-field formulation based on volume fractions. In this approach, each phase α is associated with a local volume fraction field ϕ^α, subject to the natural filling constraint $\sum_\alpha \phi^\alpha = 1$, thereby ensuring volumetric consistency and preventing voids or overlaps. This enables direct tracking of nucleation, growth, and coexistence of multiple solid phases during sodiation (Fig. 3.27).

Daubner et al. [101] demonstrated the advantages of this strategy by comparing a CH concentration model with a multiphase Allen–Cahn plus grand-potential formulation for $NaFePO_4$ cathodes. Their results showed that faster in-plane diffusion promotes phase separation, while coherency strain and higher C-rates can suppress it. Importantly, they highlighted how polycrystalline morphology leads to nucleation at triple junctions and

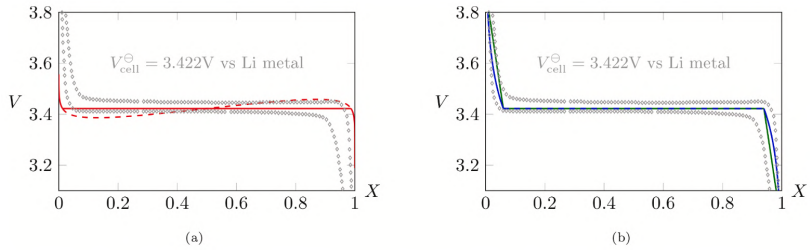

Figure 3.27: Open circuit potential V_{OCV} as a function of the filling fraction X in Li_xFePO_4. (a) Regular solution fit for a Cahn–Hilliard formulation. (b) Quadratic (green) and logarithmic (blue) chemical energy fits for the Allen–Cahn multiphase-field framework, illustrating improved ability to represent discrete phase transitions [101].

grain-by-grain filling, phenomena naturally captured by volume-fraction fields.

At the methodological level, Steinbach and Pezzolla [102] introduced a reformulation in terms of pairwise interface fields, which resolved pathologies at triple points and recovered Young's law in the sharp-interface limit. This is crucial for modeling systems such as Na–Sn, where three or more phases frequently meet and interact mechanically and chemically. Finally, Nestler et al. [103] derived the governing equations for multicomponent, multiphase systems from a thermodynamically consistent entropy functional, providing practical formulations for interfacial anisotropy, multiwell bulk potentials, and the suppression of spurious third-phase formation at two-phase boundaries. Together, these developments motivated the multiphase-field framework adopted in this thesis, enabling realistic simulation of the discrete Na–Sn intermetallic phases and their chemo–mechanical interactions during sodiation.

Building on prior advances in continuum thermodynamics [86–89], sharp- and diffuse-front analyses [90, 91], numerical interface-capturing methods [92], phase-field studies of cathodes [93–95], and alloying-electrode formulations [96–100], this thesis develops a multiphase-field model for Na–Sn anodes that captures phase segregation, reaction kinetics, and chemo–mechanical coupling, with parameters tailored to sodiation in tin.

The resulting multiphase-field framework not only generalizes the CH description to multiple intermetallic phases but also naturally incorporates mechanical interactions, interfacial energies, and reaction kinetics into a single thermodynamically consistent setting. In the remainder of this thesis, this formulation is specialized to the Na–Sn system, where experimentally motivated parameters and boundary conditions are employed to study phase nucleation,

growth dynamics, and stress development during sodiation–desodiation cycles. This provides a unified tool to analyze chemo–mechanical degradation mechanisms in tin-based sodium-ion batteries, bridging the gap between microstructural evolution and electrochemical performance.

Chapter 4

Experimental insights of fabrication and electrochemical performance of tin-based anodes for sodium-ion batteries

This chapter presents the experimental analysis carried out to investigate phase transformations, morphological changes, and performance characteristics of different tin-based anodes before and after sodiation. The study employed a combination of cyclic voltammetry (CV), galvanostatic charge/discharge tests, scanning electron microscopy (SEM), energy-dispersive X-ray spectroscopy (EDX), X-ray diffraction (XRD), and synchrotron X-ray tomography. The results from these complementary techniques provide insights into the structural and electrochemical behavior of the anodes, highlighting their potential applications in sodium-ion batteries.

4.1 Electrode fabrication and cell assembly

Tin-based anodes are promising candidates for sodium-ion battery technology. Metallic Sn can alloy with up to 3.75 Na atoms per Sn atom to form $Na_{15}Sn_4$, corresponding to a theoretical specific capacity of 847 mAh/g. This alloy is electrochemically active between 0.05 and 1.5 V vs. Na. However, full sodiation leads to a substantial volumetric expansion of up to 420% relative to the pristine material [53, 104].

4.1.1 Structural and morphological characterization of Sn powder

Commercially available Sn powder with a nominal particle size of 5 μm was employed for electrode fabrication.

XRD analysis of the pristine material revealed no secondary phases or impurities (Fig. 4.1). Prior to electrode preparation, the powder was also characterized morphologically by SEM. As shown in Fig. 4.2, the powder consists of compact grains, generally rounded in shape, but with a wide size distribution. Most particle diameters ranged between 1.64 and 24.19 μm, although both smaller and larger grains were present.

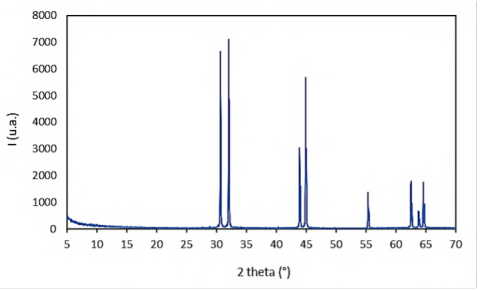

Figure 4.1: X-ray diffractogram of the commercial Sn powder, showing the absence of impurities.

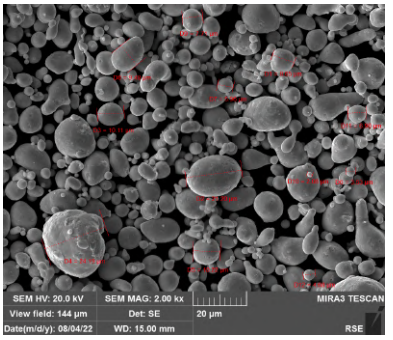

Figure 4.2: SEM images of commercial Sn powder. Grain size distribution spans from 1.64 μm to 24.19 μm, with smaller and larger particles also present.

4.1.2 Electrode production

The electrodes were prepared by slurry casting on aluminum foil current collectors. The ink formulation consisted of 70% active materials (Sn +

carbon nanofibers, CNF; Fig. 4.6b), 20% conductive carbon black (C_{65}), and 10% binder. Two binder–current collector combinations were tested (Table 4.1): PVDF dissolved in NMP with Al, and CMC dissolved in water with Al coated with carbon (Al+C).

After mixing, the slurry was cast using a doctor blade and dried overnight. To remove residual solvent, the electrodes were further dried in a vacuum oven at 60–70 °C for 2 h, followed by calendering (Fig. 4.5). The final electrode thickness was approximately 90 μm.

Calendering is critical for improving electrical contact between the active material and the current collector. Increasing compaction pressure decreases electrode thickness and increases density, which reduces porosity and increases tortuosity. High compaction also alters particle aspect ratios, enabling tighter packing. Moderate compaction has been reported to minimize capacity loss [105]. SEM images before cycles and before and after calendering for PVDF or CMC have been shown in Fig. 4.3 and Fig. 4.4, respectively.

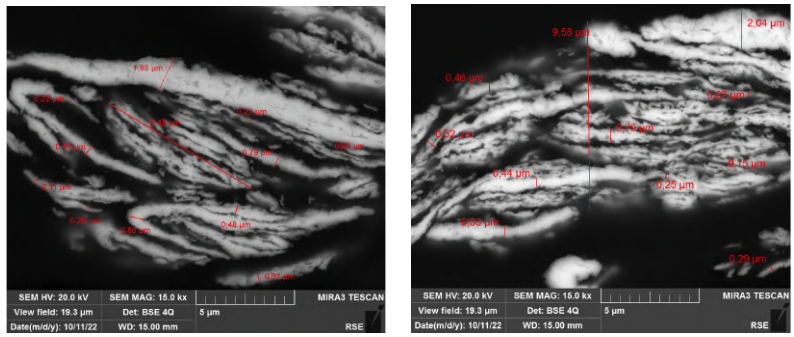

(a) (b)

Figure 4.3: SEM images of active material particles, C_{65} and PVDF in the electrode: (a) uncalendered, (b) calendered.

Areal loading and areal capacity. For completeness, we recall the per-area metrics often used to compare electrodes:

$$L_{\text{areal}} = \frac{m_{\text{active}}}{A}\ [\text{mg cm}^{-2}], \qquad C_{\text{areal}} = L_{\text{areal}}\,\hat{C}_{\text{sp}}\ [\text{mA h cm}^{-2}],$$

where m_{active} is the mass of electrochemically active solids, A is the geometric electrode area, and $\hat{C}_{\text{sp}}$ is the specific capacity (mA h g^{-1}).

Note: Areal metrics best serve planar, high-loading electrodes used for device-level comparisons. Because this study centers on half-cell, materials-screening tests with nonuniform architectures (including sponges) and variable active fractions, mAh cm^{-2} *would not improve interpretability. In addition,*

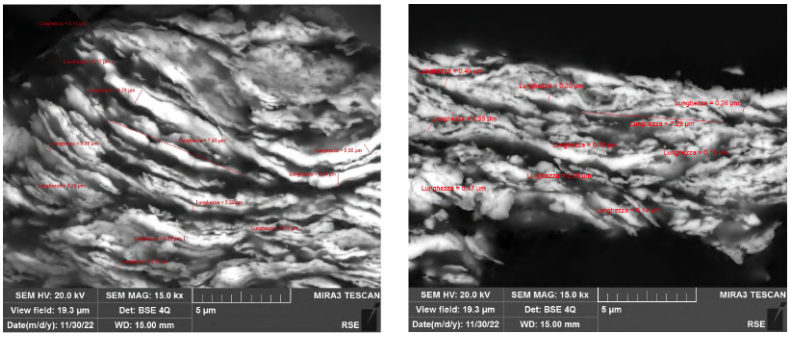

(a) (b)

Figure 4.4: SEM images of active material particles, C_{65} and CMC in the electrode: (a) uncalendered, (b) calendered.

the experimental records do not provide reliable retrospective coating masses, so I refrain from calculating areal values to avoid potential errors. Capacities are therefore reported in $\mathrm{mAh\,g^{-1}}$*, together with explicit notes on transport limitations and morphology.*

The electrolyte used was 1 M $NaPF_6$ in EC:DEC (1:1 v/v), with a glass microfiber filter paper separator and sodium metal counter electrode.

Cell assembly was carried out in an Ar-filled glovebox (O_2 and H_2O < 0.1 ppm) to prevent Na oxidation and electrolyte degradation. The electrode and separator were placed in Swagelok-type cells, filled with electrolyte, and sealed.

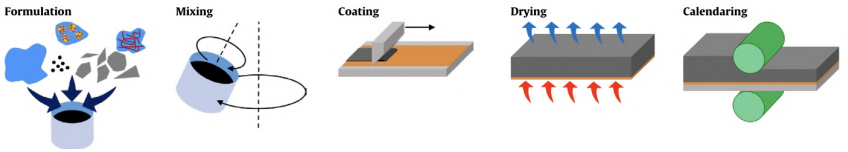

Figure 4.5: Schematic summary of the electrode manufacturing process [106].

Binder/solvent	**Acronym**	**Current collector**	**Abbreviation**
Polyvinylidene fluoride / N-methyl-2-pyrrolidone	PVDF	Aluminum	Al
Carboxymethyl cellulose / water	CMC	Carbon-coated aluminum	Al+C

Table 4.1: Binder–collector combinations tested for Sn-based electrodes.

Electrodes with CMC binder showed poor homogeneity due to segregation

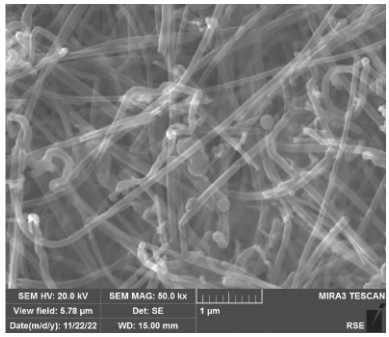

(a) Carbon nanofibers (CNF).

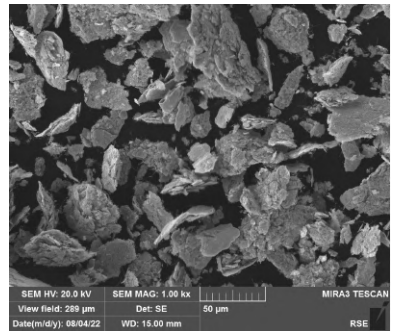

(b) Sn–CNF active material mixture.

Figure 4.6: SEM images of (a) CNFs and (b) Sn + CNF active material mixture.

of dense Sn particles during slurry deposition, leading to non-uniform films. In contrast, PVDF binder yielded more homogeneous coatings and improved adhesion to the Al current collector. For subsequent electrochemical testing, PVDF with Al foil was selected as the optimized combination.

4.1.3 Electrochemical characterization

Electrodes with an active area of 1 cm^2 were evaluated using CV and galvanostatic charge–discharge cycling.

CV involves imposing a potential sweep and measuring the corresponding current response relative to a reference electrode. Charge–discharge tests, instead, record the potential as a function of applied current, using two-electrode configurations. Electrochemical tests were conducted in Swagelok-

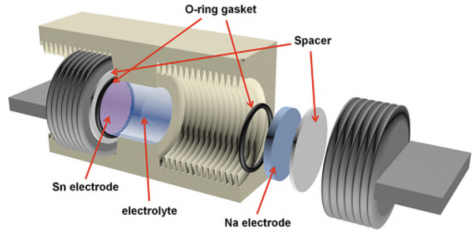

Figure 4.7: Schematic of a Swagelok-type half-cell, featuring a Sn working electrode and Na counter electrode, each with an area of 1 cm^2 [65].

type half-cells (Fig. 4.7) containing the Sn-based working electrode, Na counter electrode, a Whatman G/D glass fiber separator soaked in electrolyte, and, when required, a Na reference electrode. Two electrolyte formulations

were investigated (Table 4.2). CV performed in $NaPF_6$ EC:DEC electrolyte

Solvent(s)	**Salt**	**Composition**	**Abbreviation**
Ethylene carbonate (EC) + diethyl carbonate (DEC)	$NaPF_6$	1 M $NaPF_6$ in EC:DEC (1:1 v/v)	$NaPF_6$ EC:DEC
Ethylene carbonate (EC) + diethyl carbonate (DEC)	$NaClO_4$	1 M $NaClO_4$ in EC:DEC (1:1 v/v)	$NaClO_4$ EC:DEC

Table 4.2: Electrolytes tested for Sn-based electrodes.

(Fig. 4.8) indicated alloying and dealloying reactions between 1.5 and 0.1 V. Below 0.1 V, sodium plating dominated. Subsequent charge–discharge

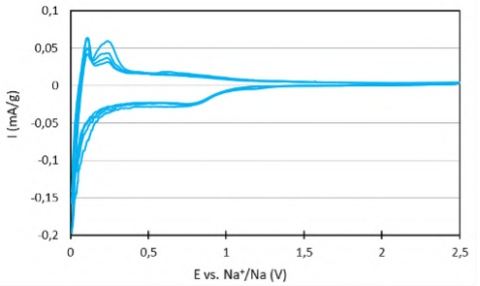

Figure 4.8: Cyclic voltammogram (Section 2.12) of Sn electrode in 1 M $NaPF_6$ EC:DEC electrolyte at 0.1 mV/s scan rate.

cycling (Fig. 4.9) confirmed poor electrochemical performance, with low specific capacities observed for both electrolytes. Slightly better results were obtained with $NaPF_6$ EC:DEC.

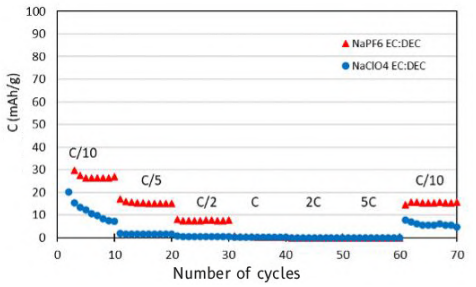

Figure 4.9: Comparison of discharge profiles for Sn-based electrodes cycled in $NaPF_6$ EC:DEC (red triangles) and $NaClO_4$ EC:DEC (blue circles) electrolytes at different C-rates.

4.1.4 Conclusions

The broad grain size distribution of commercial Sn powder hindered the formation of homogeneous electrodes and limited Na diffusion into the particles, resulting in poor electrochemical performance. Among the tested electrolytes, $NaPF_6$ EC:DEC was found to yield marginally superior results and was therefore selected for subsequent experiments.

4.2 Sn in solid mixture with carbon nanofibers

Literature often highlights the importance of the interaction between the active material and carbon. This is because suitable carbonaceous materials can cushion the chemical expansion of the active material during alloy formation, preventing the active material grains from mechanically impacting the binder and current collector, which could lead to cracking and detachment. Generally, from the literature, it is observed that alloy anodes, regardless of the element considered, benefit from being synthesized in conjunction with carbon structures such as nanowires, nanotubes, nanofibers, etc [62, 104, 107].

4.2.1 Synthesis

A mechanical mixture of tin and carbon nanofibers (CNF, Sigma-Aldrich) was prepared by grinding 1 g of commercial Sn powder with 0.2 g of CNF in a vibratory mill. Milling was performed in a tungsten carbide jar with a 15 mm diameter ball at 15 Hz for 10 minutes.

4.2.2 Structural and morphological characterization of the active material

XRD (Section 2.15) of the Sn+CNF mixture (Fig. 4.10) shows altered relative peak intensities compared to pristine Sn (Fig. 4.1) and the appearance of a broad feature at $2\theta = 26.6°$, attributable to carbon nanofibers. These changes suggest a partial reduction of Sn crystallinity due to mechanical mixing.

SEM imaging (Fig. 4.11) revealed that the powder forms large agglomerates composed of exfoliated flakes of Sn and CNF. The surfaces of the grains appear covered by nanofibers, which promote a flake-like morphology with thicknesses between 0.8 and 3.5 μm.

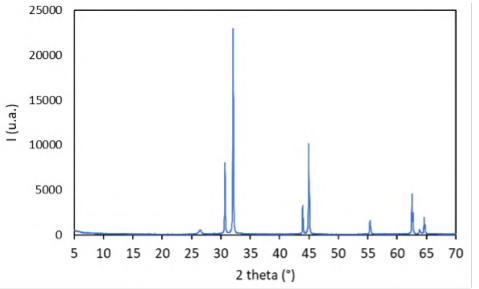

Figure 4.10: XRD pattern of the mechanical Sn+CNF mixture.

4.2.3 Electrode production

Electrodes were fabricated by mixing the Sn+CNF powder with conductive carbon (C_{65}) and a binder in a turbula mixer, followed by slurry casting onto a current collector. Two binders were tested: PVDF and CMC.

Since PVDF dissolved in NMP showed poor adhesion on Al+C collectors in earlier trials, an alternative binder was evaluated: PVDF Solvay Solef® 75130, soluble in acetone. This aimed to improve adhesion while retaining compatibility with Al+C collectors. The additional carbon ensured electronic percolation and minimized insulating regions.

The electrode preparation process followed that described in Section 4.1.2. Each electrode was divided into two parts, with one part subjected to hot pressing, enabling evaluation of binder type and pressing effects on electrochemical and morphological properties.

4.2.4 Morphological and electrochemical characterization of the electrode

SEM analysis was performed to assess surface and cross-sectional morphologies before and after pressing (Fig. 4.12 and Fig. 4.13). To prepare polished cross-sections, the electrodes were embedded in resin, cut, and graphite-coated.

Calendered electrodes exhibited thinner, broader grains compared to non-calendered samples. Image analysis indicated an average grain height of $\sim$14 μm for calendered samples versus $\sim$22 μm for non-calendered ones. This difference arises mainly from reduced interlayer spacing of Sn grains rather than thinning of individual grains. In BSE images, the lighter Sn phase is clearly distinguished from darker CNF, and calendered electrodes showed reduced Sn–Al separation.

Interestingly, in PVDF-based electrodes a carbon-rich interfacial layer between Al and the active material was visible (Fig. 4.12), whereas in

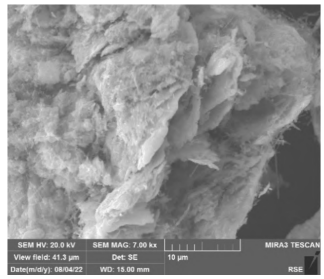

(a) Sn+CNF after vibratory milling (SE)

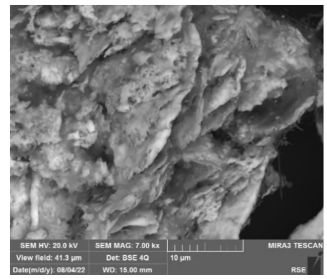

(b) Sn+CNF after vibratory milling (BSE)

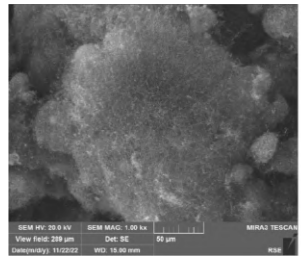

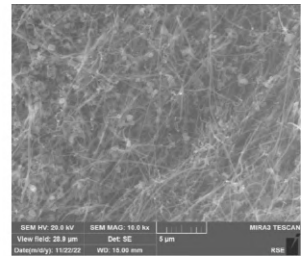

(c) Commercial CNF reference(SE)

Figure 4.11: SEM micrographs at different magnifications in SE and BSE mode of (a, b) Sn+CNF mixture and (c) pristine CNF.

CMC-based samples this interlayer was absent (Fig. 4.13), likely due to binder–solvent interactions. However, no significant morphological changes due to pressing were otherwise observed.

Electrochemical testing was performed in $NaPF_6$ EC:DEC electrolyte. CV measurements (Fig. 4.14) showed that both PVDF- and CMC-based electrodes exhibited sharper alloying/dealloying peaks compared to commercial Sn (Fig. 4.8). The CMC electrode displayed a greater number of peaks, consistent with literature reports [61], suggesting improved phase transitions.

Charge–discharge tests (Fig. 4.15, Fig. 4.16) showed that electrodes with CMC binder were less sensitive to pressing, whereas PVDF-based electrodes performed better when calendered. Despite overall low capacity values, the CMC electrodes consistently outperformed PVDF ones, particularly at low C-rates (Section 2.3).

4.2.5 Conclusions

Although overall electrochemical performance remained limited, this study clarified key aspects of electrode preparation with Sn+CNF composites. The combination of CMC binder and Al+C current collector yielded the most consistent performance, while PVDF electrodes showed improvements only

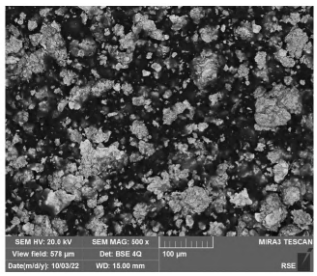

(a) Non-calendered surface (BSE).

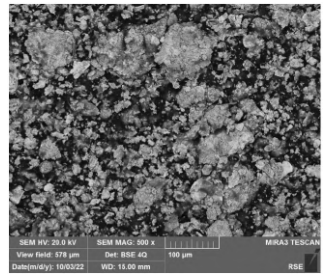

(b) Calendered surface (BSE).

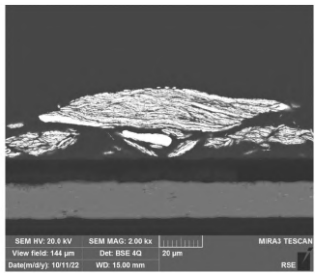

(c) Non-calendered cross-section.

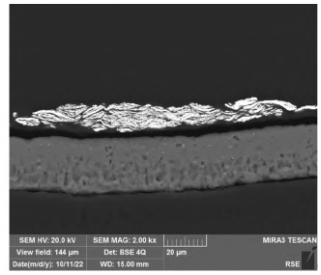

(d) Calendered cross-section.

Figure 4.12: SEM images of Sn+CNF electrodes with PVDF binder: (a, c) non-calendered and (b, d) calendered.

under pressing. These results highlight the importance of binder–collector compatibility in the design of alloy anodes.

4.3 Tin-based electrodes synthesized with sodium alginate as chelator (Sn+SA)

Chelating agents are negatively charged molecules that coordinate with metal cations, forming complexes of varying stability depending on the charge and coordination environment. In this work, sodium alginate (SA) was employed as a chelator for Sn^{2+} ions.

4.3.1 Synthesis

Sodium alginate (SA) was employed as a chelating agent for Sn^{2+}. SA, the sodium salt of alginic acid, contains negatively charged functional groups that stably coordinate divalent cations. A 0.2 M SA solution in water was mixed with conductive carbon (C_{65}) at a 2:1 weight ratio. This dispersion was then added dropwise to a 0.1 M aqueous solution of $SnCl_2$. Upon contact,

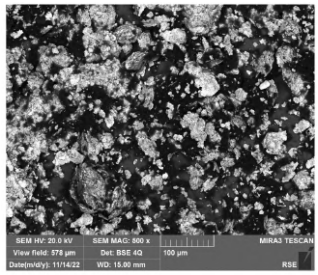

(a) Non-calendered surface.

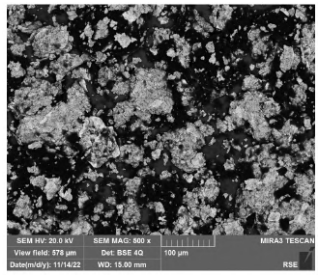

(b) Non-calendered cross-section.

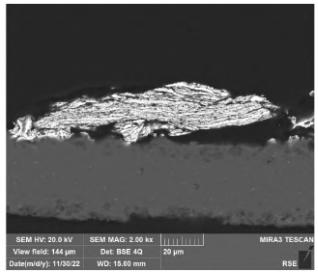

(c) Calendered surface.

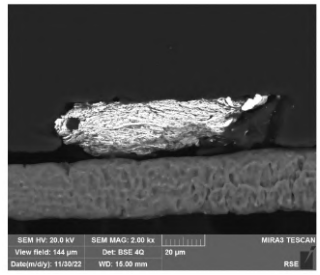

(d) Calendered cross-section.

Figure 4.13: SEM images of Sn+CNF electrodes with CMC binder, comparing non-calendered (a, b) and calendered (c, d) samples.

Sn^{2+} ions were coordinated by the alginate, forming gelatinous droplets that simultaneously trapped carbon particles.

The droplets were repeatedly washed with distilled water to remove residual chlorine or unreacted components, dried overnight in a vacuum oven at 60°C, and subsequently calcined in a quartz reactor at 210°C for 12 h under flowing argon (5°C/min heating ramp). The calcination temperature was selected to decompose alginate chains without melting metallic Sn (232°C).

4.3.2 Structural and morphological characterization

XRD (Fig. 4.17) revealed a broad peak characteristic of amorphous material, along with faint reflections corresponding to metallic Sn, suggesting a weakly crystalline tin phase.

SEM images (Fig. 4.18) show Sn grains uniformly coated with a carbon layer derived from both C_{65} and partial combustion of alginate. BSE images indicate that beneath this carbon shell, Sn grains are porous, composed of smaller fused blocks and cavities.

EDX microanalysis (Fig. 4.19) confirmed the presence of Sn and carbon,

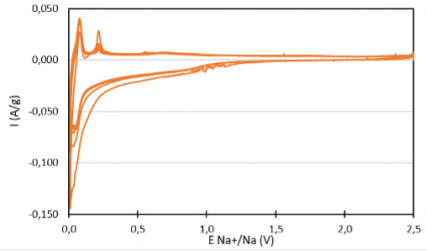

(a) PVDF binder.

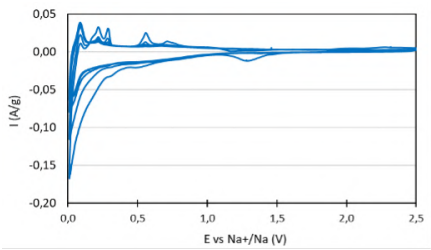

(b) CMC binder.

Figure 4.14: Cyclic voltammograms of Sn+CNF electrodes with PVDF and CMC binders (calendered samples).

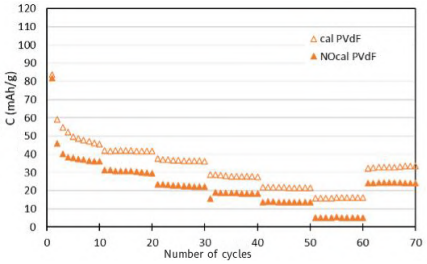

(a) PVDF binder.

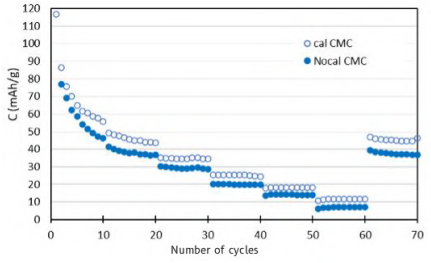

(b) CMC binder.

Figure 4.15: Charge–discharge cycles of Sn+CNF electrodes with PVDF (triangles) and CMC (circles). Filled symbols: non-calendered; hollow symbols: calendered.

with only minor sodium residues from the chelator. No chlorine traces from the precursor salt were detected, indicating effective washing.

4.3.3 Electrochemical and morphological characterization

Electrodes were prepared by mixing the Sn+SA active material with CMC binder (90:10 wt.%), without additional conductive carbon. This composition was motivated by EDX, which estimated that ∼20% of the sample was Sn while the remainder was carbonaceous. The slurry was cast on graphite-coated aluminum foil, and half-cells were assembled with $NaPF_6$ (1 M EC:DEC) electrolyte and sodium counter electrodes.

CV measurements (Fig. 4.20) displayed no discernible alloying peaks, likely due to the limited Sn content. However, galvanostatic cycling showed higher specific capacity than all previous Sn-based samples, although at high currents (> 1C) capacity remained below 100 mAh/g (Fig. 4.21). Capacity fluctuations were partially attributed to external interruptions in

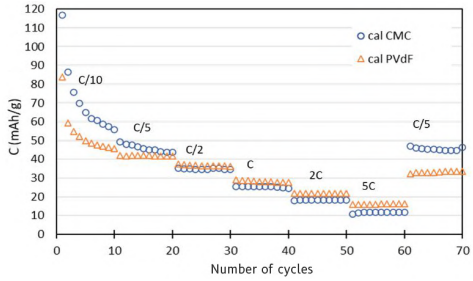

Figure 4.16: Charge–discharge cycling of calendered Sn+CNF electrodes with PVDF (triangles) and CMC (circles).

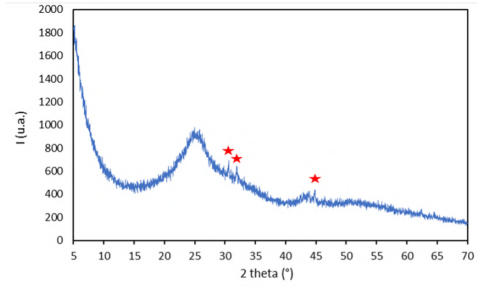

Figure 4.17: XRD pattern of the Sn+SA sample after calcination. Red stars mark the main diffraction peaks of metallic Sn.

instrumentation.

To examine whether poor electrode compression contributed to variability, the electrode was also tested in a Hohsen cell (Fig. 4.22), which applies constant spring pressure. In this configuration, capacity improved markedly: > 300 mAh/g at C/10 and $\sim$110 mAh/g at 2C (Fig. 4.23). Capacity recovered to initial values upon returning to C/10, confirming stability after high-rate cycling.

Long-term cycling at C/10 (Fig. 4.24) showed a gradual decline from $\sim$350 to $\sim$300 mAh/g after 31 cycles, partly linked to power interruptions and possibly lab temperature variations. The average operating potential ranged from 0.66 V (C/10) to 0.70 V (2C).

SEM cross-sections revealed that uncycled electrodes had Sn grains embedded in and sometimes encapsulated by carbon (Fig. 4.25). After cycling (Fig. 4.26), the structure became less compact, with increased porosity and reduced Sn grain definition. BSE contrast suggested formation of mixed Sn–Na phases.

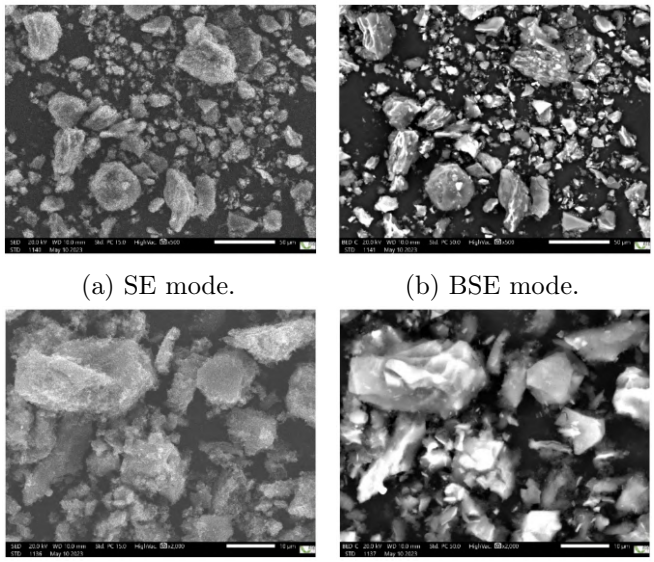

(a) SE mode. (b) BSE mode.

(c) SE mode. (d) BSE mode.

Figure 4.18: SEM micrographs of Sn+SA powder after calcination, showing carbon-coated Sn grains with internal porosity.

4.3.4 Conclusions

The Sn+SA synthesis route produced highly carbon-coated, weakly crystalline Sn particles. Despite low Sn content, electrodes displayed enhanced specific capacity compared to commercial Sn powders, particularly under controlled compression in Hohsen cells. Cycling stability and morphological changes indicate partial Sn–Na phase formation within a porous carbon matrix. Further synchrotron tomography is needed to quantify volume changes and refine mechanistic understanding.

4.4 Sn from aqueous solutions

Inspired by reports on the deposition of fine particulates capable of alloying with sodium onto carbon substrates [104], we explored the use of graphitic sponges (3 mm thick) as both current collectors and growth substrates for Sn-based electrodes.

4.4.1 Synthesis

Graphitic sponges were infused with a 1 M aqueous solution of tin acetate by syringe, using 1 cm diameter rods. After air drying, the sponges were

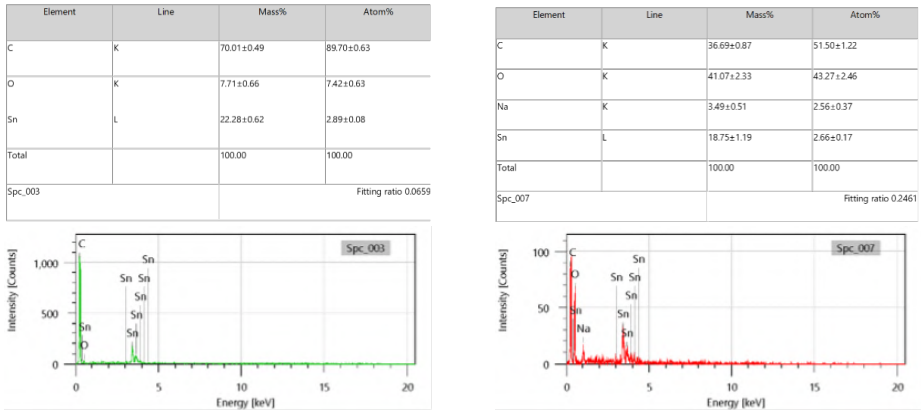

(a) Point without Na. (b) Point with residual Na.

Figure 4.19: Representative EDX spectra from different points of the Sn+SA sample.

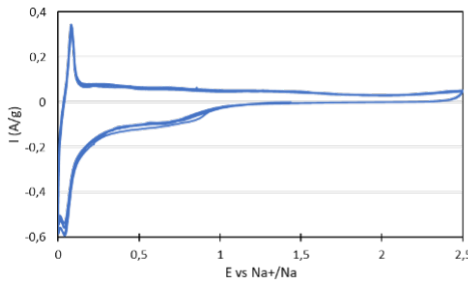

Figure 4.20: Cyclic voltammogram of the Sn+SA electrode (scan rate 0.1 mV/s).

calcined at 210°C under flowing Ar (5°C/min heating rate), then cooled to room temperature. Calcination served to carbonize organic residues and fix Sn particles onto the graphite fibers.

4.4.2 Morphological and electrochemical characterization

This method produced electrodes directly, enabling immediate SEM/EDX verification.

SEM images before calcination (Fig. 4.27) show Sn acetate distributed across the sponge surface and within its bulk, with higher accumulation in regions of dense fiber networks or on the resting face. After calcination (Fig. 4.28), Sn crystallites appeared predominantly as acicular structures of varying sizes, with agglomeration evident in fiber intersections.

For electrochemical testing, electrodes were pre-soaked in electrolyte

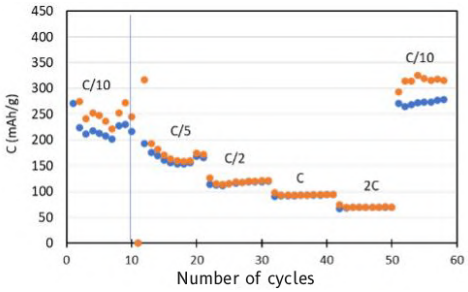

Figure 4.21: Charge/discharge profiles of the Sn+SA electrode at different C-rates. The blue line marks a measurement interruption.

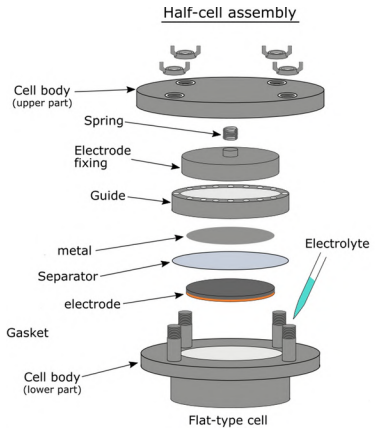

Figure 4.22: Schematic of a Hohsen cell, composed of a Sn electrode sheet and Na counter electrode [108].

overnight to improve wetting. Cycling was performed in both Swagelok- and Hohsen-type cells (Fig. 4.29).

In Swagelok cells, minimal pressure led to poor interfacial contact and capacity collapsed within the first ten cycles, with no recovery. In contrast, Hohsen cells, which apply constant spring pressure, exhibited higher capacities: stable values around 500–600 mAh/g at C/10, albeit with significant variability at low rates. At C/2, capacities stabilized, but at C-rate they dropped to zero. Upon returning to C/10, partial recovery occurred, though a power interruption during the 57th cycle interrupted testing.

These results suggest that poor high-rate performance originates from the electrode's large thickness, which limits Na-ion transport through the sponge.

Average operating potentials ranged from 0.44 V vs. Na/Na^+ at C/10 to 0.46 V at C/2.

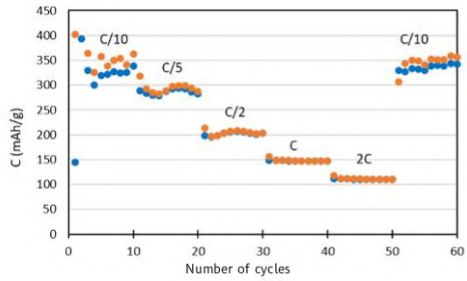

Figure 4.23: Charge/discharge curves of the Sn+SA electrode cycled in a Hohsen cell at various C-rates.

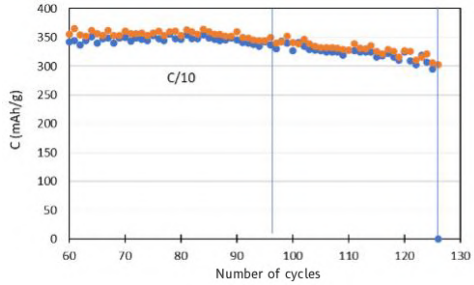

Figure 4.24: Extended C/10 cycling of Sn+SA electrode. Blue lines mark power interruptions.

Post-cycling SEM (Fig. 4.30) showed that distinct acicular grains fused into compact agglomerates, consistent with alloying. BSE contrast changes suggest the incorporation of Na into Sn grains. EDX analysis (Fig. 4.31) confirmed residual $NaPF_6$ despite washing, with an average post-cycling Na:Sn atomic ratio of ∼13.4:3.8, close to that expected for $Na_{15}Sn_4$.

4.4.3 Conclusions

The aqueous infiltration approach enables direct growth of Sn particles on conductive carbon sponges, producing electrodes with promising specific capacities (∼500–600 mAh/g at C/10) and average working potentials below 0.5 V vs. Na/Na^+. However, performance remains unstable at higher currents due to poor Na-ion transport in thick electrodes. Morphological and compositional analyses confirmed Na incorporation into Sn grains, consistent with the formation of $Na_{15}Sn_4$. Further optimization of electrode thickness and architecture is needed to improve rate capability and cycling stability.

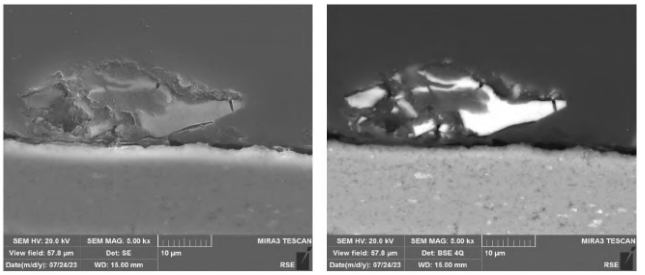

(a) SE mode. (b) BSE mode.

Figure 4.25: SEM cross-section of pristine Sn+SA electrode.

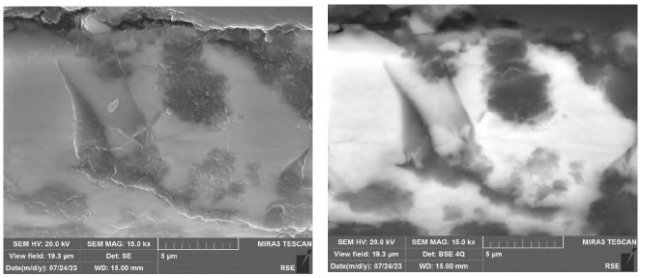

(a) SE mode. (b) BSE mode.

Figure 4.26: SEM cross-section of Sn+SA electrode after 60 cycles at different C-rates.

4.5 Synchrotron X-ray tomographic analysis

In situ synchrotron X-ray tomography (Section 2.18) was performed to investigate the morphological evolution of two representative Sn–C electrodes under cycling. The two samples differ significantly in their synthesis route: one consisted of tin micrometric particles dispersed within carbon sponges, while the other used a chelation strategy in which Sn particles were embedded within a carbonaceous matrix. Both approaches were designed to buffer the large (∼400%) volumetric expansion associated with Sn sodiation, which typically leads to loss of electrical contact and electrode degradation.

Measurements were conducted at the ANATOMIX beamline using specialized in situ electrochemical cells, enabling continuous μCT scanning during cycling. The high spatial resolution of synchrotron μCT is essential to distinguish phases and detect void formation, particle cracking, and morphological rearrangements. Coupling structural information with chronoamperometry allowed correlation of microstructural changes with specific alloying/dealloying steps, providing a deeper understanding of electrode degradation

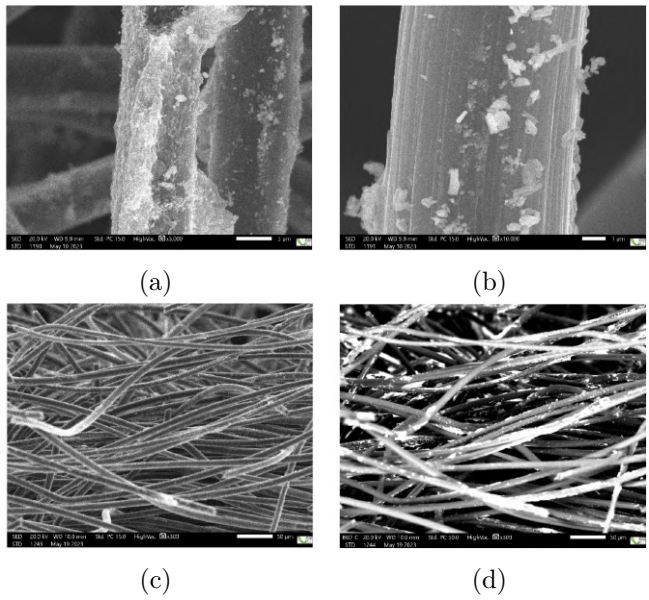

Figure 4.27: SEM images of the dried, non-calcined electrode: (a–c) SE mode, (d) BSE mode.

mechanisms.

The acquired 3D datasets also provide the basis for chemo-mechanical models, enabling advanced multiphysics simulations to predict performance and optimize electrode design.

4.5.1 Design and orientation of the cell

The cell body was built from high-pressure PEEK fittings (25 mm height, 6.35 mm external diameter, 3 mm internal diameter). A central narrowing created a through-hole of 0.50 mm diameter for electrode placement.

Electrical connections were established using two steel rods (30 mm × 0.8 mm) acting as current collectors, secured by PEEK nuts and ferrules. The active material was positioned within the through-hole, with the separator and Na counter-electrode placed adjacent to it. For sponge electrodes, ∼0.2 mg of material was compressed into the cavity, leaving a portion exposed for electrical contact. For the chelated Sn sample, the steel rods were immersed directly in the active material ink.

The cell was mounted on a 3D-printed stage fixed to a SEM stub and goniometer head, ensuring vertical alignment with the beam path (Fig. 4.32).

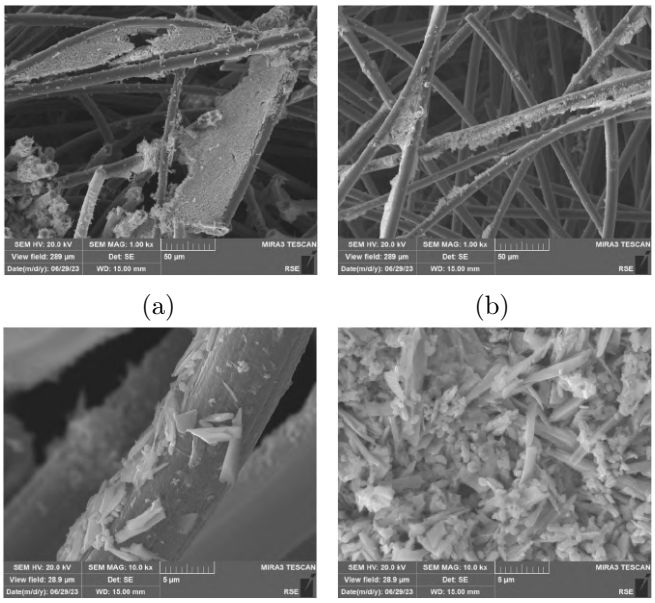

Figure 4.28: SEM images of the electrode after calcination at 210°C in Ar, SE mode at different magnifications.

4.5.2 Tin-based electrode synthesized with sodium alginate as chelator

Electrodes were prepared as in Section 4.3 (Sn+SA with CMC binder, 90:10). The cell contained 1 M $NaPF_6$ in EC:DEC (1:1 v/v), a Na counter electrode, and a Whatman separator placed on the counter electrode side only.

4.5.2.1 Conclusions

SEM analysis of the pristine electrode showed Sn grains embedded and partially encapsulated by carbon, occasionally forming tin "veins" within the carbon matrix (Fig. 4.25d). After cycling, SEM revealed a porous, less compact structure, with fewer distinct Sn grains but more extended veins (Fig. 4.26b).

Synchrotron tomography confirmed these observations: voxel intensity profiles (Dragonfly software) showed density loss (red arrows, Fig. 4.33), cracks (white arrows), and fractures (black arrows), while some intact Sn particles remained (yellow arrows). Phase evolution and crack-induced hollow morphologies closely matched SEM results, though overall volume changes appeared limited due to confinement of Sn within the carbon–binder matrix.

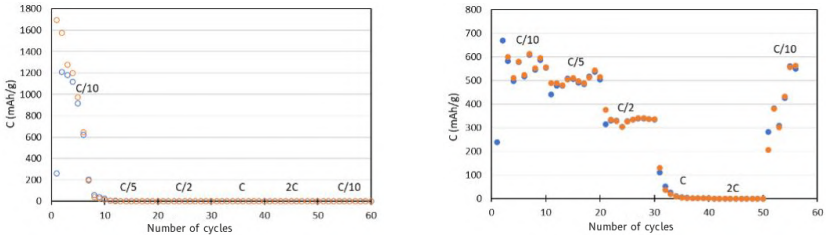

(a) Swagelok cell. (b) Hohsen cell.

Figure 4.29: Charge–discharge curves of Sn-infiltrated graphite sponge electrodes in (a) Swagelok and (b) Hohsen cells.

Step	Reaction	Voltage (V)
SEI formation	—	0.75
Reduction	$SnO_2 \rightarrow Sn$	0.41
Alloying I	$Sn \rightarrow NaSn_3$	0.36
Alloying II	$NaSn_3 \rightarrow NaSn$	0.19
Alloying III	$NaSn \rightarrow Na_9Sn_4$	0.08–0.06
Final alloy	$Na_9Sn_4 \rightarrow Na_{15}Sn_4$	0.035

Table 4.3: Electrochemical transformations during sodiation of Sn+SA electrode.

Electrochemical analysis (Table 4.3) showed sequential transformations: SEI formation (∼0.75 V), SnO_2 reduction (∼0.41 V), and alloying through $NaSn_3$ (0.36 V), NaSn (0.19 V), Na_9Sn_4 (0.08–0.06 V), and finally $Na_{15}Sn_4$ (0.035 V). The progressive current decrease indicated rising resistance due to evolving microstructural damage.

4.5.3 Tin-based electrode from aqueous solutions

Electrodes were prepared as in Section 4.4 (Sn acetate infiltrated in carbon sponges). The cell configuration was identical, with $NaPF_6$ electrolyte and Na counter electrode.

4.5.3.1 Conclusions

SEM and tomography both showed morphological degradation upon cycling. Initially, Sn acetate was uniformly dispersed throughout the sponge, with local accumulations at fiber intersections (Figures 4.28, 4.30). After cycling, acicular Sn grains fused into compact agglomerates, while tomography revealed hollowing and void formation (Fig. 4.34b).

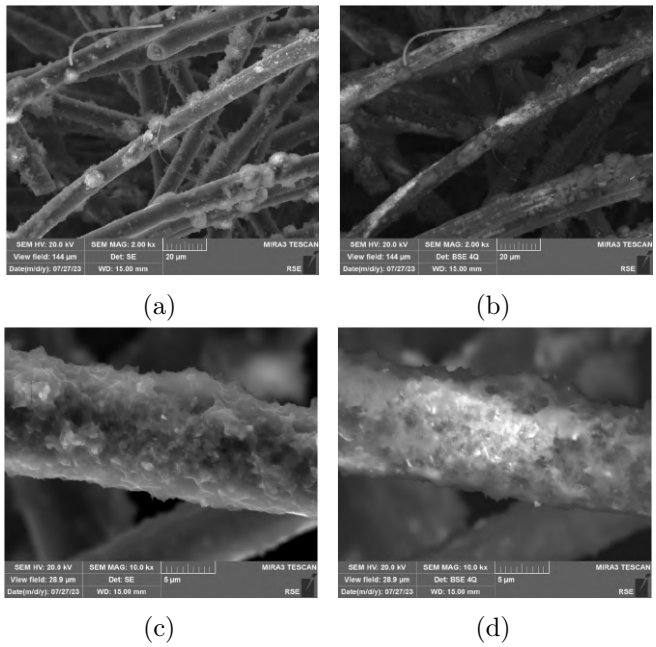

Figure 4.30: SEM images of the electrode after 60 cycles in a Swagelok cell: (a, c) SE mode; (b, d) BSE mode.

BSE imaging indicated reduced Sn contrast, consistent with Na incorporation. EDX confirmed residual Na and $NaPF_6$, with an average Na:Sn ratio ($\sim$13.4:3.8) consistent with the $Na_{15}Sn_4$ alloy (Fig. 4.31).

Synchrotron tomography revealed complementary insights to SEM/EDX: both chelation-derived and sponge-infiltrated Sn electrodes undergo fragmentation, void formation, and partial densification upon cycling. However, confinement within a carbon-rich matrix (Sn+SA) limited macroscopic volume expansion compared to sponge electrodes, where transport limitations led to capacity loss at higher rates.

4.6 Overview of electrode variants

We investigated three Sn-based electrode variants; their rationale and high-level outcomes are summarized in Table 4.4. Detailed syntheses and results follow in Sections 4.2, 4.3, and 4.4.

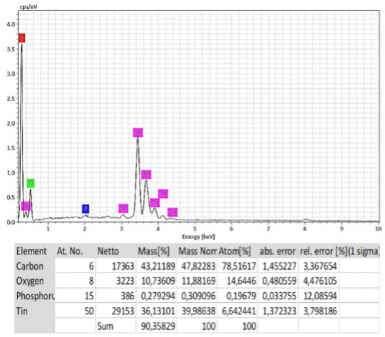

Element	At. No.	Netto	Mass[%]	Mass Norm	Atom[%]	abs. error	rel. error [%]	(1 sigma
Carbon	6	17363	43,21189	47,82283	78,51617	1,455227	3,367654	
Oxygen	8	3223	10,73609	11,88169	14,6446	0,480559	4,476105	
Phosphoru	15	386	0,279294	0,309096	0,19679	0,033755	12,08594	
Tin	50	29153	36,13101	39,98638	6,642441	1,372323	3,798186	
		Sum	90,35829	100	100			

(a) Before cycling.

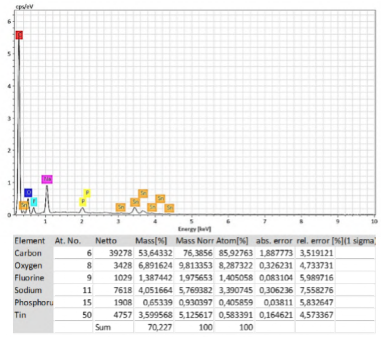

Element	At. No.	Netto	Mass[%]	Mass Norm	Atom[%]	abs. error	rel. error [%]	(1 sigma
Carbon	6	39278	53,64332	76,3856	85,92763	1,887773	3,519121	
Oxygen	8	3428	6,891624	9,813353	8,287322	0,326231	4,733731	
Fluorine	9	1029	1,387442	1,975653	1,405058	0,083104	5,989716	
Sodium	11	7618	4,051664	5,769382	3,390745	0,306236	7,558276	
Phosphoru	15	1908	0,65339	0,930397	0,405859	0,03811	5,832647	
Tin	50	4757	3,599568	5,125617	0,583391	0,164621	4,573367	
		Sum	70,227	100	100			

(b) After cycling.

Figure 4.31: Representative EDX spectra of Sn-infiltrated sponge electrode before and after cycling.

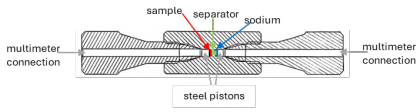

(a)

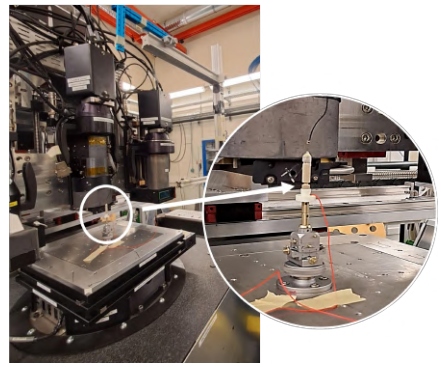

(b)

Figure 4.32: (a) Schematic of the in situ electrochemical cell configuration, (b) Experimental setup for in situ synchrotron X-ray tomography.

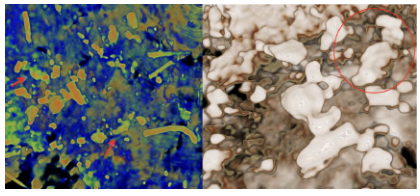

(a) Non-cycled electrode.

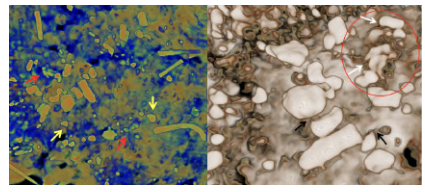

(b) Cycled, fully sodiated electrode.

Figure 4.33: Synchrotron X-ray tomography of Sn+SA electrode before (a) and after (b) cycling.

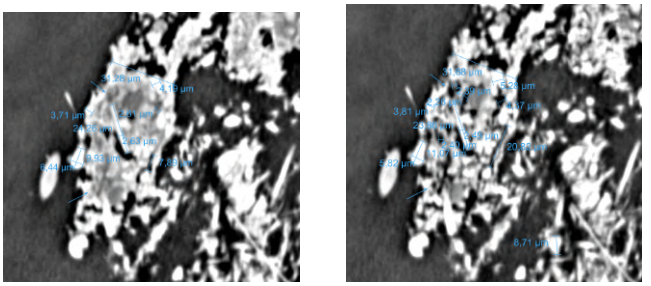

(a) Pristine electrode. (b) Cycled electrode.

Figure 4.34: Synchrotron tomography of sponge-type electrode: (a) before cycling, (b) after full sodiation.

Variant	**Motivation / change**	**Outcome (electrochem + morphology)**
Sn + CNF (PVDF vs CMC; calendered/non-calendered)	Binder mechanics/adhesion; electron pathways	CMC + Al+C most consistent; PVDF improves with pressing; overall low capacities, but CMC > PVDF at low C-rates; clearer alloying peaks in CV; reduced Sn–Al separation when calendered.
Sn + sodium alginate (chelation + calcination)	Carbon coating + better Sn dispersion; confinement	Higher specific capacity than commercial Sn; in Hohsen cell $> 300\,\mathrm{mAh\,g^{-1}}$ at C/10 and $\sim 110\,\mathrm{mAh\,g^{-1}}$ at 2C; weakly crystalline Sn under carbon; post-cycling porosity/veins consistent with partial Na–Sn alloying.
Sn infiltrated in graphite sponge	Architected 3D current collector; direct growth	$\sim$ 500–600 $\mathrm{mAh\,g^{-1}}$ at C/10 in Hohsen; strong rate limitations at higher current due to thickness/-transport; acicular Sn fuses into agglomerates; tomography shows hollowing/voids.

Table 4.4: Electrode variants, motivations, and outcomes.

Chapter 5

Phase-field methodology for chemo–mechanical coupling

This chapter introduces the phase-field method as a rigorous framework for modeling microstructural evolution and chemo–mechanical coupling in materials. We first contrast sharp- and diffuse-interface descriptions, then summarize the variational foundations of phase-field models (order parameters, free energies, and kinetic laws), and finally specialize to rechargeable batteries, where the approach captures phase separation, interface motion, and stress generation during ion insertion/extraction.

The insights developed here—drawing on formulations originally conceived and validated for Li-ion electrodes (Anand [86]; Afshar et al. [89])—underpin our later comparison of these two continuum frameworks and guide the Na–Sn multiphase-field modeling proposed in this thesis.

5.1 Phase-field fundamentals: from sharp to diffuse interfaces

Classical sharp-interface models treat phase boundaries as zero-thickness surfaces separating bulk PDEs, closed with interfacial jump conditions (e.g., Stefan condition for energy balance, Gibbs–Thomson curvature effects). While physically transparent, they are cumbersome for complex morphologies, topology changes, and strong coupling to transport and mechanics.

Phase-field (diffuse-interface) models replace the sharp boundary with a thin but finite transition region, described by one or more continuous order parameters $\phi(x,t)$. Interfaces are encoded as narrow zones of steep but smooth variation in ϕ, removing the need to explicitly track the interface. The formalism follows classical irreversible thermodynamics and, under asymptotic analysis as the interface thickness tends to zero, recovers the sharp-interface

limit with the correct interfacial physics [109]. This makes phase-field models well suited to solidification, spinodal decomposition, dendritic growth, solid-state transformations, grain evolution, and multiphase flows.

5.2 Core phase-field theory

A total free energy functional penalizes bulk thermodynamics and interfacial gradients,

$$\mathcal{F}[\phi, \nabla\phi, \ldots] \;=\; \int_{\Omega} \big(f_{\text{chem}}(\phi, \ldots) \;+\; f_{\text{grad}}(\nabla\phi) \;+\; f_{\text{elas}}(\phi, \boldsymbol{E}, \ldots) \big)\, \mathrm{d}V,$$

with f_{chem} encoding phase thermodynamics (e.g., double-well or CALPHAD-based), $f_{\text{grad}} \propto |\nabla\phi|^2$ setting interfacial energy/width, and f_{elas} accounting for composition-dependent elasticity and coherency strains. Kinetics arise from variational dissipation principles:

- Allen–Cahn (AC) for non-conserved order parameters ϕ: $\partial_t \phi = -L_\phi \, \delta\mathcal{F}/\delta\phi$, where L_ϕ is a kinetic coefficient.

- Cahn–Hilliard (CH) for conserved fields (e.g., composition c): $\partial_t c = \nabla\cdot\big(M(c)\,\nabla\mu\big)$, with $M(c)$ the mobility and $\mu = \delta\mathcal{F}/\delta c$ the chemical potential.

Coupled AC/CH systems naturally represent nucleation/growth, spinodal decomposition, interface curvature effects, and stress-assisted segregation. Phase-field handles complex geometries and topological changes with minimal additional machinery, at the cost of introducing a numerically resolved interface thickness that must remain small relative to microstructural scales [110].

5.3 Phase-field modeling in rechargeable batteries

In batteries, the order parameters typically represent local composition (Li/Na fraction) and, where needed, structural/phase indicators. The free energy collects: (i) chemical thermodynamics (solid solution + two-phase regions), (ii) gradient energy (interfacial penalty and width), (iii) elastic energy (coherency strains from lattice mismatch), and, when appropriate, (iv) electrostatic contributions (electrical potential and charge carriers).

Combining CH for conserved composition with AC for structural variables enables diffusion, reaction, and structural transformation in one variational framework. This captures: (i) nucleation and growth during (de)sodiation, (ii) anisotropic phase-boundary motion (orientation and elasticity effects), (iii) stress generation, softening, and fracture due to large volume change, (iv) metastable intermediates that modulate kinetics, (v) degradation modes such as particle pulverization and loss of contact. Because the driving forces and constraints (transport, reactions, mechanics, fields) are treated consistently,

phase-field models have become central to material design, microstructure optimization, and lifetime prediction in electrodes [7, 8].

5.4 Comparative frameworks: Anand vs. Afshar

Building on the general principles of phase-field modeling in batteries, we now compare two thermodynamically consistent chemo–mechanical frameworks that are particularly relevant for diffusion–reaction–deformation problems. Anand [86] couples Cahn–Hilliard-type diffusion with elastic–plastic deformation and swelling, while Afshar et al. [89] extend the formulation by incorporating reaction-driven sharp interfaces and stress-sensitive kinetics. This comparison clarifies the modeling choices, state variables, driving forces, and coupling strategies, that inform our Na–Sn multiphase-field model.

5.4.1 Mass balance

Anand [86] formulates mass balance in terms of species diffusion driven by chemical potential gradients and mobility, without explicit reactions. The governing equation is

$$\dot{c}_R = -\mathrm{Div}\, j_R, \tag{5.1}$$

where $\dot{c}_R$ is the rate of concentration change and $\mathrm{Div}\, j_R$ denotes the divergence of the flux. This expression simply tracks concentration evolution due to diffusion.

In contrast, Afshar et al. [89] extend the balance law to include chemical reactions, reflecting the behavior of conversion-type electrodes:

$$\dot{c}_R = -\mathrm{Div}\, j_R - \dot{\xi}. \tag{5.2}$$

Here, $\dot{\xi}$ is the reaction rate per unit reference volume, representing the consumption of species C as it reacts with host A to form a new compound B (Fig. 5.1). Importantly, the reaction coordinate ξ is defined independently of the concentration in either unreacted or reacted phases. This distinction allows the reacted phase to still accommodate diffusing species, while ξ specifically tracks the amount that has chemically transformed. Accordingly, Afshar introduces two independent capacity parameters: $c^R_{\max}$, the maximum concentration that can react to form a new compound, and $c^D_{\max}$, the maximum concentration that can be hosted in unreacted or reacted phases. This separation enables a rigorous treatment of simultaneous diffusion and reaction in deforming solids.

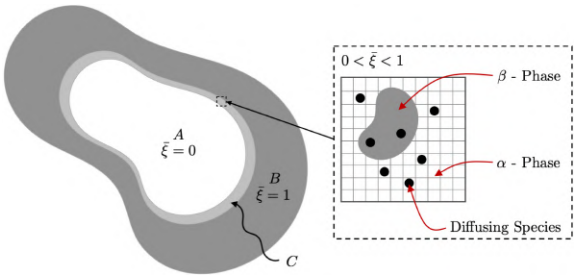

Figure 5.1: Definition of reaction extent $\bar{\xi} = \xi / c^R_{\max}$, showing that $\bar{\xi} = 1$ corresponds to complete consumption of $c^R_{\max}$ moles of species. The parameter $c^R_{\max}$ is determined by the stoichiometry of the specific reaction and defines the maximum reactable amount of diffusing species [89].

5.4.2 Kinematics

Both Anand [86] and Afshar et al. [89] adopt a kinematic framework based on the deformation gradient, velocity, and velocity gradient. These are defined as

$$\boldsymbol{F} = \nabla \chi, \quad v = \dot{\chi}, \quad L = \nabla v = \dot{\boldsymbol{F}} \boldsymbol{F}^{-1}. \tag{5.3}$$

Their key difference lies in how F is multiplicatively decomposed to represent different distortion mechanisms.

Anand [86] decomposes the deformation gradient into swelling, plastic, and elastic parts (in the order adopted by his formulation):

$$\boldsymbol{F} = \boldsymbol{F}^e \boldsymbol{F}^p \boldsymbol{F}^s, \tag{5.4}$$

where $\boldsymbol{F}^s$ captures volumetric swelling due to chemical insertion, $\boldsymbol{F}^p$ accounts for irreversible plastic deformation, and $\boldsymbol{F}^e$ represents the elastic response, $J^e \overset{\text{def}}{=} \det \boldsymbol{F}^e$. The corresponding velocity gradient is expressed as

$$\boldsymbol{L} = \boldsymbol{L}^e + \boldsymbol{F}^e (\boldsymbol{D}^p + \boldsymbol{D}^s) \boldsymbol{F}^{e-1}, \tag{5.5}$$

with

$$\boldsymbol{D}^s = \frac{1}{3} \frac{\dot{J}^s}{J^s} I \tag{5.6}$$

representing isotropic swelling stretching tensor through the swelling ratio J^s, and $\boldsymbol{D}^p$ the plastic stretching tensor. Plastic incompressibility ($J^p = \det \boldsymbol{F}^p = 1$) and irrotationality ($\boldsymbol{W}^p = 0$) are assumed. A plastic shear strain rate and flow direction are introduced

$$\nu^p = \sqrt{2} |\boldsymbol{D}^p|, \qquad \boldsymbol{N}^p = \frac{\boldsymbol{D}^p}{|\boldsymbol{D}^p|}, \tag{5.7}$$

leading to the kinematic relation

$$(\nabla\dot{\chi})\boldsymbol{F}^{-1} = \dot{\boldsymbol{F}}^e\boldsymbol{F}^{e-1} + \tfrac{1}{\sqrt{2}}\nu^p\boldsymbol{F}^e\boldsymbol{N}^p\boldsymbol{F}^{e-1} + \tfrac{1}{3}\frac{\dot{J}^s}{J^s}I. \tag{5.8}$$

Afshar et al. [89], on the other hand, split the deformation gradient into mechanical and chemical contributions:

$$\boldsymbol{F} = \boldsymbol{F}^m\boldsymbol{F}^c, \qquad \boldsymbol{F}^m = \boldsymbol{F}^e\boldsymbol{F}^p, \tag{5.9}$$

where $\boldsymbol{F}^m$ follows the classical elastic–plastic decomposition, while $\boldsymbol{F}^c$ represents chemically induced distortions. The associated Jacobians are defined as

$$J = J^mJ^c, \qquad J^m \overset{\text{def}}{=} \det\boldsymbol{F}^m > 0, \qquad J^c \overset{\text{def}}{=} \det\boldsymbol{F}^c > 0, \tag{5.10}$$

with J the total volume ratio.

The chemical velocity gradient is decomposed into diffusion- and reaction-driven parts, weighted by the normalized reaction extent $\bar{\xi} \in [0,1]$:

$$\boldsymbol{L}^c = (1-\bar{\xi})\boldsymbol{L}^{\alpha,D} + \bar{\xi}(\boldsymbol{L}^{\beta,D} + \boldsymbol{L}^{\beta,R}), \tag{5.11}$$

with $\boldsymbol{L}^{\alpha,D}$, $\boldsymbol{L}^{\beta,D}$, and $\boldsymbol{L}^{\beta,R}$ denoting distortions due to diffusion in the unreacted phase, diffusion in the reacted phase, and reaction-induced transformation, respectively. Assuming spin tensor $\boldsymbol{W}^c = 0$, the chemical stretching tensor becomes

$$\boldsymbol{D}^c = (1-\bar{\xi})\boldsymbol{D}^{\alpha,D} + \bar{\xi}(\boldsymbol{D}^{\beta,D} + \boldsymbol{D}^{\beta,R}), \tag{5.12}$$

with $\boldsymbol{D}^{\alpha,D} = \dot{c}\boldsymbol{N}^{\alpha,D}$, $\boldsymbol{D}^{\beta,D} = \dot{c}\boldsymbol{N}^{\beta,D}$, and $\boldsymbol{D}^{\beta,R} = \dot{\xi}\boldsymbol{N}^{\beta,R}$, where $\boldsymbol{N}^{\alpha,D}$ and $\boldsymbol{N}^{\beta,D}$ are the directions of diffusion-induced stretching in the unreacted and reacted material and $N^{\beta,R}$ is the direction of reaction induced deformation. Combining these yields

$$\begin{aligned}(\nabla\dot{\chi})\boldsymbol{F}^{-1} = {}& \dot{\boldsymbol{F}}^e\boldsymbol{F}^{e-1} + \tfrac{1}{\sqrt{2}}\nu^p\boldsymbol{F}^e\boldsymbol{N}^p\boldsymbol{F}^{e-1} \\ & + (1-\bar{\xi})\boldsymbol{F}^e\boldsymbol{F}^p(\dot{c}\boldsymbol{N}^{\alpha,D})\boldsymbol{F}^{p-1}\boldsymbol{F}^{e-1} \\ & + \bar{\xi}\boldsymbol{F}^e\boldsymbol{F}^p(\dot{c}\boldsymbol{N}^{\beta,D} + \dot{\xi}\boldsymbol{N}^{\beta,R})\boldsymbol{F}^{p-1}\boldsymbol{F}^{e-1}.\end{aligned} \tag{5.13}$$

Afshar et al. adopt classical J_2 plasticity with codirectionality, defining

$$\boldsymbol{D}^p = \tfrac{1}{\sqrt{2}}\nu^p\frac{\boldsymbol{M}_0^e}{|\boldsymbol{M}_0^e|}. \tag{5.14}$$

In addition, the direction of plastic flow and equivalent shear stress are as follows:

$$\boldsymbol{N}^p = \frac{\boldsymbol{M}_0^e}{|\boldsymbol{M}_0^e|}, \qquad \bar{\tau} = \tfrac{1}{\sqrt{2}}|\boldsymbol{M}_0^e|, \tag{5.15}$$

where $\boldsymbol{M}_0^e$ denotes the deviatoric part of Mandel stress $\boldsymbol{M}^e$ that will be derived in Section 5.4.3.

In summary, Anand isolates swelling as a distinct kinematic contribution through $\boldsymbol{F}^s$, whereas Afshar incorporates chemically induced distortions more broadly via $\boldsymbol{F}^c$, distinguishing diffusion- and reaction-driven strains. This reflects their respective emphases: diffusion-induced swelling versus reaction-driven transformations in conversion electrodes.

5.4.3 Principle of virtual power

The principle of virtual power provides a variational framework to derive balance laws at both macroscopic and microscopic levels. It requires that, for any part $\mathcal{P}$ of the body, the internal power expended by stresses equals the external power supplied by tractions and body forces, for all admissible virtual velocities. This systematically identifies the appropriate force systems conjugate to the rate-like kinematical descriptors.

Following Gurtin's formulation [111], Anand [86] postulates that each kinematical rate

$$\dot{\chi}, \quad \dot{\boldsymbol{F}}^e, \quad \nu^p, \quad \dot{c}_R, \quad \nabla \dot{c}_R$$

has an associated force system expending power over it. These rates are not independent but are constrained by the kinematic relation

$$(\nabla \dot{\chi})\boldsymbol{F}^{-1} = \dot{\boldsymbol{F}}^e \boldsymbol{F}^{e-1} + \tfrac{1}{\sqrt{2}} \nu^p \boldsymbol{F}^e \boldsymbol{N}^p \boldsymbol{F}^{e-1} + \tfrac{1}{3}\,\Theta(c_R)\dot{c}_R I, \tag{5.16}$$

derived earlier in Eq. (5.8). Here, the swelling distortions evolve according to

$$\dot{\boldsymbol{F}}^s = \boldsymbol{D}^s \boldsymbol{F}^s, \quad \boldsymbol{D}^s = \tfrac{1}{3}\Theta(c_R)\dot{c}_R I, \quad \Theta(c_R) = \frac{\Omega(c_R)}{J^s(c_R)}. \tag{5.17}$$

where $\Omega(c_R)$ is partial molar volume.

Accordingly, the external and internal powers over $\mathcal{P}$ are

$$\mathscr{W}_{\text{ext}} = \int_{\partial\mathcal{P}} t_R(n_R) \cdot \dot{\chi}\, da_R + \int_{\mathcal{P}} b_R \cdot \dot{\chi}\, dv_R + \int_{\partial\mathcal{P}} \zeta(n_R)\, \dot{c}_R\, da_R, \tag{5.18}$$

$$\mathscr{W}_{\text{int}} = \int_{\mathcal{P}} \left(\boldsymbol{S}^e : \dot{\boldsymbol{F}}^e + \pi \nu^p + \varpi \dot{c}_R + \boldsymbol{\xi} \cdot \nabla \dot{c}_R \right) dv_R. \tag{5.19}$$

With each evolution of the body we associate macroscopic and microscopic force systems. The macroscopic system is defined by a traction $t_R(n_R)$ (for each unit normal n_R) that expends power over the velocity $\dot{\chi}$, an external body force b_R that also expends power over $\dot{\chi}$, and a stress $\boldsymbol{S}^e$ that expends power over the elastic distortion rate $\dot{\boldsymbol{F}}^e$. In analogy, the microscopic system is described by a micro-traction $\zeta(n_R)$ acting on $\dot{c}_R$ at the boundary, a scalar

microstress ϖ conjugate to $\dot{c}_R$ in the bulk, a vectorial microstress $\boldsymbol{\xi}$ conjugate to $\nabla\dot{c}_R$, and an internal variable multiplier π conjugate to the inelastic rate ν^p. Since time scales associated with species diffusion are usually considerably longer than those of wave propagation, all inertial effects are neglected.

Applying standard variational arguments yields the equilibrium equations:

$$\text{Macroscopic:} \quad \operatorname{Div}\boldsymbol{T}_R + b_R = 0, \qquad t_R(n_R) = \boldsymbol{T}_R n_R, \tag{5.20}$$

$$\text{Microscopic:} \quad \pi = J^s \tfrac{1}{\sqrt{2}}\boldsymbol{M}_0^e : \boldsymbol{N}^p, \qquad \zeta(n_R) = \boldsymbol{\xi}\cdot n_R, \qquad \varpi = \Omega(c_R)\tfrac{1}{3}\operatorname{tr}\boldsymbol{M}^e + \operatorname{Div} \tag{5.21}$$

where T_R represents the classical Piola stress. Two important stress measures arise naturally: the elastic second Piola stress,

$$\boldsymbol{T}^e = J^e \boldsymbol{F}^{e-1}\boldsymbol{T}\boldsymbol{F}^{e-\top}, \tag{5.22}$$

where $\boldsymbol{T}$ represents Cauchy stress and the elastic Mandel stress,

$$\boldsymbol{M}^e = \boldsymbol{C}^e\boldsymbol{T}^e = J^e \boldsymbol{F}^{e\top}\boldsymbol{T}\boldsymbol{F}^{e-\top}. \tag{5.23}$$

Afshar et al. [89] extend the virtual power framework to systems with diffusion and reaction. Their generalized virtual velocities are

$$\mathscr{V} = (\delta\chi,\ \delta\boldsymbol{F}^e,\ \delta\nu^p,\ \delta c,\ \delta\xi,\ \nabla\delta\xi),$$

constrained by the chemo–mechanical kinematics in Eq. (5.13).

The external and internal virtual powers are

$$\delta\mathscr{W}_{\text{ext}} = \int_{\partial\mathcal{P}} t_R(n_R)\cdot\delta\chi\, da_R + \int_{\mathcal{P}} b_R\cdot\delta\chi\, dv_R + \int_{\partial\mathcal{P}} \eta\,\delta\xi\, da_R, \tag{5.24}$$

$$\delta\mathscr{W}_{\text{int}} = \int_{\mathcal{P}} \Big(\boldsymbol{S}^e : \delta\boldsymbol{F}^e + \pi\,\delta\nu^p + E\,\delta c + F\,\delta\xi + G\cdot\nabla\delta\xi\Big)\, dv_R, \tag{5.25}$$

where (π, E, F, G, η) are the microstresses conjugate to plastic flow, diffusion, reaction, and reaction-gradient processes.

The resulting balance laws are

$$\operatorname{Div}\boldsymbol{T}_R + b_R = 0, \quad t_R(n_R) = \boldsymbol{T}_R n_R, \tag{5.26}$$

$$\pi = J^c \tfrac{1}{\sqrt{2}}\boldsymbol{M}_0^e : \boldsymbol{N}^p, \tag{5.27}$$

$$E = J^c \boldsymbol{M}^m : \big((1-\bar{\xi})\boldsymbol{N}^{\alpha,D} + \bar{\xi}\boldsymbol{N}^{\beta,D}\big), \tag{5.28}$$

$$F - J^c\bar{\xi}\boldsymbol{M}^m : \boldsymbol{N}^{\beta,R} - \operatorname{Div} G = 0, \quad \eta = G\cdot n_R, \tag{5.29}$$

where $\boldsymbol{M}^m$ represents the mechanical Mandel stress.

5.4.4 Constitutive theory

Constitutive theory provides the relations between thermodynamic state variables, stresses, chemical potentials, and fluxes under the constraints of the free-energy imbalance. Both Anand [86] and Afshar et al. [89] formulate energetic and dissipative constitutive equations, though with different emphases: Anand focuses on diffusion–plasticity with swelling, whereas Afshar extends the framework to account explicitly for chemical reactions.

5.4.4.1 Energetic constitutive equations

Anand [86] proposes constitutive relations linking free energy ψ_R, elastic stress $\boldsymbol{T}^e$, net chemical potential μ_{net}, and microstress ξ:

$$\begin{aligned} &\psi_R = \hat{\psi}_R(\boldsymbol{C}^e, c_R, \nabla c_R), \quad \boldsymbol{T}^e = \hat{\boldsymbol{T}}^e(\boldsymbol{C}^e, c_R, \nabla c_R), \\ &\mu_{\text{net}} = \hat{\mu}_{\text{net}}(\boldsymbol{C}^e, c_R, \nabla c_R), \quad \xi = \hat{\xi}(\boldsymbol{C}^e, c_R, \nabla c_R), \end{aligned} \tag{5.30}$$

with $\boldsymbol{C}^e$ the elastic right Cauchy–Green tensor. Substituting these into the free-energy imbalance yields the reduced dissipation inequality

$$\Big[\frac{\partial \hat{\psi}_R}{\partial \boldsymbol{C}^e} - \tfrac{1}{2} J^s \boldsymbol{T}^e\Big] : \dot{\boldsymbol{C}}^e + \Big[\frac{\partial \hat{\psi}_R}{\partial c_R} - \mu_{\text{net}}\Big]\dot{c}_R + \Big[\frac{\partial \hat{\psi}_R}{\partial \nabla c_R} - \xi\Big] \cdot \nabla \dot{c}_R - \pi \nu^p - j_R \cdot \nabla \mu \le 0, \tag{5.31}$$

which leads to the thermodynamic restrictions

$$\boldsymbol{T}^e = 2 J^{s-1} \frac{\partial \hat{\psi}_R}{\partial \boldsymbol{C}^e}, \quad \mu_{\text{net}} = \frac{\partial \hat{\psi}_R}{\partial c_R}, \quad \xi = \frac{\partial \hat{\psi}_R}{\partial \nabla c_R}. \tag{5.32}$$

Afshar et al. [89] adopt a similar but more general setting, introducing an additional phase-field variable ξ for reaction progress:

$$\psi_R = \hat{\psi}_R(\boldsymbol{C}^e, c, \xi, \nabla \xi), \quad \boldsymbol{T}^e = \hat{\boldsymbol{T}}^e(\boldsymbol{C}^e, c, \xi, \nabla \xi), \quad \mu = \hat{\mu}(\boldsymbol{C}^e, c, \xi, \nabla \xi). \tag{5.33}$$

The corresponding dissipation inequality is

$$\begin{aligned} &\Big[\frac{\partial \hat{\psi}_R}{\partial \boldsymbol{C}^e} - \tfrac{1}{2} J^c T^e\Big] : \dot{\boldsymbol{C}}^e + \Big[\frac{\partial \hat{\psi}_R}{\partial c} - E - \mu\Big]\dot{c} + \Big[\frac{\partial \hat{\psi}_R}{\partial \xi} - F - \mu\Big]\dot{\xi} \\ &+ \Big[\frac{\partial \hat{\psi}_R}{\partial \nabla \xi} - G\Big] \cdot \nabla \dot{\xi} - \pi \nu^p - j_R \cdot \nabla \mu \le 0, \end{aligned} \tag{5.34}$$

leading to state relations

$$\boldsymbol{T}^e = 2 J^{c-1} \frac{\partial \hat{\psi}_R}{\partial C^e}, \quad \mu = \frac{\partial \hat{\psi}_R}{\partial c} - E, \quad G = \frac{\partial \hat{\psi}_R}{\partial \nabla \xi}. \tag{5.35}$$

5.4.4.2 Dissipative constitutive equations

Dissipative constitutive equations capture irreversible processes such as plasticity, diffusion, and chemical reactions. The dissipation inequality (Anand [86])

$$D = \pi\nu^p - j_R \cdot \nabla\mu \geq 0, \tag{5.36}$$

where diffusion flux follows

$$j_R = -\boldsymbol{M}(\boldsymbol{C}^e, c_R, \bar{\gamma}^p)\nabla\mu, \tag{5.37}$$

with $\bar{\gamma}^p$ the equivalent plastic shear strain and $\boldsymbol{M}$ a positive semi-definite mobility tensor.

Afshar et al. [89] extend this formulation by introducing a reaction driving force. The dissipation inequality reads

$$D = -\Big(\frac{\partial\hat{\psi}_R}{\partial\xi} - F - \mu\Big)\dot{\xi} + \pi\nu^p - j_R \cdot \nabla\mu \geq 0, \tag{5.38}$$

with the chemical potential of the reacted phase

$$\mu^\xi = \frac{\partial\hat{\psi}_R}{\partial\xi} - F, \tag{5.39}$$

and the thermodynamic driving force

$$\mathcal{F} = \mu^\xi - \mu. \tag{5.40}$$

Thus,

$$D = -\mathcal{F}\dot{\xi} + \pi\nu^p - j_R \cdot \nabla\mu \geq 0, \tag{5.41}$$

where the first term, $-\mathcal{F}\dot{\xi}$, captures reaction-induced dissipation, present even without plasticity or diffusion gradients and j_R is modeled as

$$j_R = -\boldsymbol{M}_{mob}(c, \xi)\nabla\mu, \tag{5.42}$$

where M_{mob} is the mobility tensor.

5.4.4.3 Material isotropy

Both Anand and Afshar assume isotropy, which simplifies the constitutive structure by restricting free-energy dependence to invariants of the strain measures.

In Anand's formulation [86], the free energy is expressed as

$$\hat{\psi}_R(\boldsymbol{C}^e, c_R, \nabla c_R) = \tilde{\psi}_R(I_{\boldsymbol{C}^e}, c_R, |\nabla c_R|), \tag{5.43}$$

where $I_{\boldsymbol{C}^e}$ are invariants of $\boldsymbol{C}^e$. This yields symmetric Mandel stress,

$$\boldsymbol{M}^e = \boldsymbol{T}^e \boldsymbol{C}^e. \tag{5.44}$$

Equivalent representations in terms of eigenvectors and principal stretches λ_i^e or the principal logarithmic strains E_i^e lead to

$$\boldsymbol{M}^e = J^{s-1} \sum_{i=1}^{3} \frac{\partial \breve{\psi}_R}{\partial E_i^e} r_i^e \otimes r_i^e, \tag{5.45}$$

and, for isotropic elastic free energies,

$$\psi_R = \breve{\psi}_R(I_{\boldsymbol{E}^e}, c_R, |\nabla c_R|), \quad \boldsymbol{T} = J^{e-1} \boldsymbol{R}^e \boldsymbol{M}^e \boldsymbol{R}^{e\top}, \tag{5.46}$$

where the right and left polar decompositions of $\boldsymbol{F}^e$ are given by

$$\boldsymbol{F}^e = \boldsymbol{R}^e \boldsymbol{U}^e = \boldsymbol{V}^e \boldsymbol{R}^e, \tag{5.47}$$

where $\boldsymbol{R}^e$ is the elastic rotation tensor. Afshar et al. [89] adopt an analogous isotropic form,

$$\psi_R = \tilde{\psi}_R(I_{\boldsymbol{C}^e}, c, \xi, |\nabla \xi|), \tag{5.48}$$

with invariants $I_{\boldsymbol{C}^e} = (I_1, I_2, I_3)$. Using the spectral decomposition of the elastic logarithmic strain with principal values

$$\boldsymbol{E}^e = \sum_{i=1}^{3} \ln \lambda_i^e \, r_i \otimes r_i, \tag{5.49}$$

the Mandel stress follows as

$$\boldsymbol{M}^e = J^{c-1} \sum_{i=1}^{3} \frac{\partial \breve{\psi}_R((I_{\boldsymbol{E}^e}, c, \xi, |\nabla \xi|))}{\partial E_i^e} r_i \otimes r_i. \tag{5.50}$$

In both frameworks, isotropy ensures that stress measures derive directly from invariants of the elastic strain, simplifying the constitutive structure while preserving thermodynamic consistency. Afshar's model, however, extends isotropy to include the additional phase-field variable ξ, reflecting the influence of reaction progress on material response.

5.4.5 Constitutive equations

Constitutive equations specify how stresses, chemical potentials, and internal variables depend on state variables and free energy, thus closing the system of balance laws. Anand [86] and Afshar et al. [89] provide complementary formulations: Anand emphasizes diffusion–plasticity with swelling, while

Afshar incorporates chemical reaction progress through an additional order parameter.

In Anand's framework, volumetric swelling due to species insertion is captured by the swelling ratio

$$J^s = \hat{J}^s(c_R), \tag{5.51}$$

linked to concentration c_R through the partial molar volume

$$\Omega(c_R) = \frac{d\hat{J}^s(c_R)}{dc_R} > 0. \tag{5.52}$$

From the free energy function $\breve{\psi}_R(I_{\boldsymbol{E}^e}, c_R, |\nabla c_R|)$, the following stress measures are derived:

$$\boldsymbol{M}^e = J^{s-1}\frac{\partial \breve{\psi}_R}{\partial \boldsymbol{E}^e}, \qquad \boldsymbol{T} = J^{-1}\boldsymbol{R}^e\frac{\partial \breve{\psi}_R}{\partial \boldsymbol{E}^e}\boldsymbol{R}^{eT}, \qquad \boldsymbol{T}_R = \big(\boldsymbol{R}^e\frac{\partial \breve{\psi}_R}{\partial \boldsymbol{E}^e}R^{eT}\big)\boldsymbol{F}^{-T}. \tag{5.53}$$

The chemical potential includes energetic, gradient, and stress contributions:

$$\mu = \frac{\partial \breve{\psi}_R}{\partial c_R} - \mathrm{Div}\Big(\frac{\partial \breve{\psi}_R}{\partial \nabla c_R}\Big) - \Omega(c_R)\tfrac{1}{3}\mathrm{tr}\,\boldsymbol{M}^e, \tag{5.54}$$

while the microstress is given by

$$\xi = \frac{\partial \breve{\psi}_R}{\partial \nabla c_R}. \tag{5.55}$$

Afshar et al. generalize the setting by introducing a reaction progress variable ξ. Stress measures derived from the free energy $\breve{\psi}_R(I_{\boldsymbol{E}^e}, c, \xi, |\nabla\xi|)$ include

$$\begin{aligned} &\boldsymbol{M}^e = J^{c-1}\frac{\partial \breve{\psi}_R}{\partial \boldsymbol{E}^e}, \qquad \boldsymbol{T} = J^{e-1}\boldsymbol{R}^e\boldsymbol{M}^e\boldsymbol{R}^{eT}, \\ &\boldsymbol{M}^m = \boldsymbol{F}^{pT}\boldsymbol{M}^e\boldsymbol{F}^{p-T}, \qquad \boldsymbol{T}_R = J^c\boldsymbol{F}^{e-T}\boldsymbol{M}^e\boldsymbol{F}^{p-T}. \end{aligned} \tag{5.56}$$

The chemical potential of the diffusing species is

$$\mu = \frac{\partial \psi_R}{\partial c} - J^c\boldsymbol{M}^m : \big((1-\bar{\xi})\boldsymbol{N}^{\alpha,D} + \bar{\xi}\boldsymbol{N}^{\beta,D}\big), \tag{5.57}$$

while the chemical potential of the reacted compound, from Eq. (5.39), is

$$\mu^\xi = \frac{\partial \psi_R}{\partial \xi} - J^c\bar{\xi}\boldsymbol{M}^m : \boldsymbol{N}^{\beta,R} - \mathrm{Div}\Big(\frac{\partial \psi_R}{\partial \nabla\xi}\Big). \tag{5.58}$$

Anand's model links swelling directly to concentration via $J^s(c_R)$, introducing stress contributions through the partial molar volume. Afshar,

in contrast, captures both diffusion- and reaction-induced deformations by decomposing the total deformation gradient $\boldsymbol{F} = \boldsymbol{F}^e \boldsymbol{F}^p \boldsymbol{F}^c$ into elastic, plastic, and chemical parts. In this framework, the chemical potential includes mechanical work terms through the mechanical Mandel stress $\boldsymbol{M}^m$, and distinguishes explicitly between unreacted and reacted phases.

Importantly, Afshar points out that while the elastic Mandel stress $\boldsymbol{M}^e$ is identical to Anand's definition, a pullback from the deformed body to the plastically distorted intermediate space, the decomposition introduces an additional mechanical Mandel stress $\boldsymbol{M}^m$, defined by a further pullback into the chemically distorted space. This distinction is absent in Anand's formulation, which assumes isotropic chemical expansion and therefore treats $\boldsymbol{M}^e$ and $\boldsymbol{M}^m$ as identical. In Afshar's theory, however, chemical expansion is kept general, separating the two stresses.

Thus, Anand's constitutive equations are tailored to diffusion–plasticity problems, while Afshar's framework broadens the scope to chemo–mechanical coupling with phase transformation, where it is specifically the mechanical Mandel stress $\boldsymbol{M}^m$ that is coupled to the chemical driving forces.

5.4.6 Specialization of the constitutive equations

This section compares how Anand [86] and Afshar et al. [89] specialize their constitutive frameworks to capture deformation, free energy, stress, chemical potential, flux, and plastic flow in electro-chemo-mechanical systems.

5.4.6.1 Deformations caused by diffusion and reaction

Anand assumes swelling to be linearly proportional to concentration through a simple constitutive relation:

$$J^s = 1 + \Omega c_R, \tag{5.59}$$

This emphasizes volumetric swelling due to insertion of species but does not explicitly model reaction-driven deformation.

In contrast, Afshar et al. explicitly couple volumetric deformation to both diffusion and reaction in FeS_2 electrodes. For isotropic swelling, the deformation gradient and stretching rate are

$$\boldsymbol{F}^c = J^{c^{1/3}} \mathbf{1}, \quad \frac{dJ^c}{dc} = \Omega = \text{constant}, \tag{5.60}$$

$$\boldsymbol{D}^c = \dot{\boldsymbol{F}}^c \boldsymbol{F}^{c^{-1}} = \frac{\Omega \dot{c}}{3(1+\Omega c)} \mathbf{1}, \tag{5.61}$$

capturing chemical- and diffusion-induced volume change.

5.4.6.2 Free energy

Anand introduces a separable free energy with contributions from chemical mixing, interfacial gradients, and elastic deformation:

$$\breve{\psi}_R(I_{\boldsymbol{E}^e}, c_R, |\nabla c_R|) = \psi_R^c(c_R) + \psi_R^s(|\nabla c_R|) + \psi_R^e(I_{\boldsymbol{E}^e}, c_R). \tag{5.62}$$

The explicit expression is

$$\begin{aligned}\psi_R = c_{\max}\Big[&\mu^0 \bar{c}_R + R\vartheta\big(\bar{c}_R \ln \bar{c}_R + (1-\bar{c}_R)\ln(1-\bar{c}_R) + \chi \bar{c}_R(1-\bar{c}_R)\big) \\ &+ \tfrac{1}{2}\lambda|\nabla \bar{c}_R|^2\Big] + J^s\Big[\tfrac{1}{2}\boldsymbol{E}^e : \boldsymbol{\mathcal{C}}(\bar{c}_R)\boldsymbol{E}^e\Big].\end{aligned} \tag{5.63}$$

where μ^0 is a reference value of the chemical potential of the diffusing species, R is the universal gas constant, ϑ is the absolute temperature (assumed to be constant), and $\bar{c}_R = c/c_{max}$ is a normalized species concentration, with $c_{\max}$ the concentration of the species in moles per unit reference volume when all the accommodating sites in the host material are filled. In addition, χ represents the interaction parameter, $\lambda \geq 0$ a gradient energy coefficient, and $\boldsymbol{\mathcal{C}}(\bar{c}_R)$ is the elasticity tensor.

Afshar et al. propose a separable free energy including mixing, reaction barriers, elastic energy, and interfacial terms:

$$\breve{\psi}_R(I_{\boldsymbol{E}^e}, c, \xi, |\nabla \xi|) = \psi_R^c(c,\xi) + \psi_R^\xi(\xi) + \psi_R^m(I_{\boldsymbol{E}^e}, c, \xi) + \psi_R^g(|\nabla \xi|). \tag{5.64}$$

Here ψ_R^c is the variation of the chemical free energy arising from mixing of the diffusing species

$$\begin{aligned}\psi_R^c(c,\xi) = (1-\xi)\, c_{\max}^D \left(\mu_0^\alpha \bar{c} + R\vartheta\big(\bar{c}\ln\bar{c} + (1-\bar{c})\ln(1-\bar{c})\big)\right) \\ + \xi\, c_{\max}^D \left(\mu_0^\beta \bar{c} + R\vartheta\big(\bar{c}\ln\bar{c} + (1-\bar{c})\ln(1-\bar{c})\big)\right),\end{aligned} \tag{5.65}$$

and

$$\psi_R^\xi(\xi) = E^a \bar{\xi}^2(1-\bar{\xi})^2 + \xi\mu_0^\xi, \tag{5.66}$$

where the first term introduces the reaction barrier E^a, and the second term sets the reference chemical potential to μ_0^ξ.

ψ_R^m is the contribution to changes in the free energy due to the elastic deformation of the host electrode material

$$\psi_R^m(\boldsymbol{E}^e, c, \xi) = J^c\Big[\tfrac{1}{2}\boldsymbol{E}^e : \boldsymbol{\mathcal{C}}(c,\xi)\boldsymbol{E}^e\Big], \tag{5.67}$$

where $\boldsymbol{\mathcal{C}}(c,\xi)$ is the elasticity tensor, with $\mathbb{I}$ and $\mathbf{1}$ the fourth- and second-order identity tensors.

$$\begin{aligned}&\boldsymbol{\mathcal{C}}(c,\xi) = 2G(c,\xi)\mathbb{I} + \Big(K(c,\xi) - \tfrac{2}{3}G(c,\xi)\Big)\mathbf{1}\otimes\mathbf{1}, \\ &G(c,\xi) = (1-\bar{\xi})G_\alpha(c) + \bar{\xi}G_\beta(c), \\ &K(c,\xi) = (1-\bar{\xi})K_\alpha(c) + \bar{\xi}K_\beta(c).\end{aligned} \tag{5.68}$$

The shear and bulk moduli are assumed to obey the following interpolation:

$$G(c) > 0, \qquad K(c) > 0,$$

where $G(c)$ and $K(c)$ are concentration-dependent shear and bulk moduli, and the subscripts α and β denote that these belong to either the unreacted or reacted phases of the solid. The interfacial term penalizes sharp gradients:

$$\psi_R^g(|\nabla\xi|) = \tfrac{1}{2}\lambda|\nabla\xi|^2. \tag{5.69}$$

The total free energy becomes

$$\begin{aligned}\psi_R = {} & (1-\bar{\xi})c^D_{\max}\big(\mu_0^\alpha\bar{c} + R\vartheta(\bar{c}\ln\bar{c} + (1-\bar{c})\ln(1-\bar{c}))\big) \\ & + \bar{\xi}c^D_{\max}\big(\mu_0^\beta\bar{c} + R\vartheta(\bar{c}\ln\bar{c} + (1-\bar{c})\ln(1-\bar{c}))\big) + \xi\mu_0^\xi \\ & + J^c\Big[\tfrac{1}{2}\boldsymbol{E}^e : \boldsymbol{\mathcal{C}}(c,\xi)\boldsymbol{E}^e\Big] + E^a\bar{\xi}^2(1-\bar{\xi})^2 + \tfrac{1}{2}\lambda|\nabla\xi|^2.\end{aligned} \tag{5.70}$$

Here, μ_0^α and μ_0^β represent the reference potentials of the diffusing species in the unreacted and reacted host phases, respectively. In addition, μ_0^ξ specifies the reference potential when the species is chemically reacted and incorporated into the new compound. The normalized concentration of diffusing species is introduced as

$$\bar{c} \overset{\text{def}}{=} \frac{c}{c^D_{\max}}. \tag{5.71}$$

5.4.6.3 Stress, and chemical potential

In Anand's setting, stress and chemical potential reflect swelling and concentration effects:

$$\boldsymbol{M}^e = 2G(\bar{c}_R)\boldsymbol{E}^e + \Big(K(\bar{c}_R) - \tfrac{2}{3}G(\bar{c}_R)\Big)(\mathrm{tr}\boldsymbol{E}^e)\mathbf{1}, \tag{5.72}$$

$$\begin{aligned}\mu = {} & \mu_0 + R\vartheta\Big[\ln\Big(\tfrac{\bar{c}_R}{1-\bar{c}_R}\Big) + \chi(1-2\bar{c}_R)\Big] - \lambda\Delta\bar{c}_R - \tfrac{\Omega}{3}\mathrm{tr}\boldsymbol{M}^e \\ & + J^s c_{\max}\Big(\tfrac{1}{2}\boldsymbol{E}^e : \tfrac{\partial\boldsymbol{\mathcal{C}}(\bar{c}_R)}{\partial\bar{c}_R}\boldsymbol{E}^e\Big) + \Omega\Big(\tfrac{1}{2}\boldsymbol{E}^e : \boldsymbol{\mathcal{C}}(\bar{c}_R)\boldsymbol{E}^e\Big),\end{aligned} \tag{5.73}$$

Afshar et al. extend these definitions to include reaction extent ξ:

$$\boldsymbol{M}^e = 2G(c,\xi)\boldsymbol{E}^e + \Big(K(c,\xi) - \tfrac{2}{3}G(c,\xi)\Big)(\mathrm{tr}\boldsymbol{E}^e)\mathbf{1}, \tag{5.74}$$

$$\mu = (1-\bar{\xi})\mu_0^\alpha + \bar{\xi}\mu_0^\beta + R\vartheta\ln\Big(\tfrac{\bar{c}}{1-\bar{c}}\Big) - J^c\boldsymbol{M}^m : ((1-\bar{\xi})\boldsymbol{N}^{\alpha,D} + \bar{\xi}\boldsymbol{N}^{\beta,D}). \tag{5.75}$$

5.4.7 Governing partial differential equations

Both studies begin with a local force balance equation, establishing a common foundation for ensuring mechanical equilibrium:

$$\operatorname{Div} \boldsymbol{T}_R + b_R = 0. \tag{5.76}$$

Mass and species balances are then formulated differently. In Anand's study [86]:

$$\dot{c}_R = -\operatorname{Div}(\boldsymbol{M}(c_R)\nabla\mu), \tag{5.77}$$

which captures purely diffusion-driven transport.

In contrast, Afshar et al. [89] add a reaction source term:

$$\dot{c} = -\operatorname{Div}(\boldsymbol{M}_{mob}(c,\xi)\nabla\mu) - \dot{\xi}, \tag{5.78}$$

where the reaction kinetics $\dot{\xi}$ are given by

$$\begin{aligned}
&\dot{\xi} = -R_0\mathcal{F},\\
&\mathcal{F} = \mu_\xi - \mu = \left(\tfrac{c^D_{\max}}{c^R_{\max}}\bar{c} + (1-\bar{\xi})\right)(\mu_0^\xi - \mu_0^\alpha)\\
&\qquad + \tfrac{E^a}{c^R_{\max}}(2\bar{\xi} - 6\bar{\xi}^2 + 4\bar{\xi}^3) - R\vartheta\ln\left(\tfrac{\bar{c}}{1-\bar{c}}\right)\\
&\qquad + J^c\boldsymbol{M}^m : \left((1-\bar{\xi})\boldsymbol{N}^{\alpha,D} + \bar{\xi}\boldsymbol{N}^{\beta,D} - \bar{\xi}\boldsymbol{N}^{\beta,R}\right) - \operatorname{Div}(\lambda\nabla\xi),
\end{aligned} \tag{5.79}$$

with $R_0 > 0$ a positive reaction rate constant. This highlights the interplay between energetic, entropic, and mechanical factors in chemical reaction kinetics. It also captures critical concentration effects for reaction initiation and the influence of stress on reaction rates, while remaining consistent with dissipative constraints.

5.4.8 Boundary conditions

Boundary and initial conditions define the physical constraints and starting states of the models within the context of coupled diffusion–reaction–deformation. The problem is studied over a finite time horizon $t \in [0,T]$, where T is the final observation time. The external boundary $\partial\mathcal{B}$ of the body is partitioned into complementary subsurfaces for displacement ($\mathcal{S}_1$) and traction($\mathcal{S}_2$).

In Anand's framework [86], the external boundary is also partitioned into complementary subsurfaces for concentration ($\mathcal{S}_{c_R}$), and flux ($\mathcal{S}_{j_R}$):

$$\begin{aligned}
&u = u^* \quad \text{on } \mathcal{S}_1 \times [0,T],\\
&\boldsymbol{T}_R n_R = t^* \quad \text{on } \mathcal{S}_2 \times [0,T],
\end{aligned} \tag{5.80}$$

$$\begin{aligned}
&c_R = c_R^* \quad \text{on } \mathcal{S}_{cR} \times [0,T],\\
&j_R \cdot n_R = j^* \quad \text{on } \mathcal{S}_{jR} \times [0,T].
\end{aligned} \tag{5.81}$$

Afshar et al. [89] follow a similar partition but introduce additional conditions for chemical potential ($\mathcal{S}_\mu$), the species flux ($\mathcal{S}_j$), reaction extent ($\mathcal{S}_\xi$), and wetting ($\mathcal{S}_\eta$):

$$\begin{aligned} &u = \hat{u} \quad \text{on } \mathcal{S}_1 \times (0,T), \\ &\boldsymbol{T}_R n_R = \hat{t}_R \quad \text{on } \mathcal{S}_2 \times (0,T), \end{aligned} \tag{5.82}$$

$$\begin{aligned} &\mu = \hat{\mu} \quad \text{on } \mathcal{S}_\mu \times (0,T), \\ &j_R \cdot n_R = \hat{j}_R \quad \text{on } \mathcal{S}_j \times (0,T), \end{aligned} \tag{5.83}$$

$$\begin{aligned} &\xi = \hat{\xi} \quad \text{on } \mathcal{S}_\xi \times (0,T), \\ &\lambda \nabla \xi \cdot n_R = \hat{\eta} \quad \text{on } \mathcal{S}_\eta \times (0,T). \end{aligned} \tag{5.84}$$

The initial conditions also reflect their respective emphases. For Anand:

$$u(X,0) = u_0(X), \qquad c_R(X,0) = c_{R0}(X), \tag{5.85}$$

while Afshar additionally prescribes the chemical potential and reaction extent:

$$u(X,0) = u_0(X), \quad \mu(X,0) = \mu_0(X), \quad \xi(X,0) = \xi_0(X). \tag{5.86}$$

Note: This comparative review is limited to the methodological frameworks. Numerical results and case studies presented in the original works are not included, since the focus here is on the derivation and structure of the models.

5.4.9 Conclusions

The comparative analysis of Anand [86] and Afshar et al. [89] highlights two complementary approaches for modeling chemo–mechanical processes in energy storage materials.

Anand's framework focuses on diffusion-induced stresses and swelling within a Cahn–Hilliard formulation, coupled to elastic–plastic deformations. This makes it well suited for studying mechanical integrity in electrodes undergoing large volume changes without significant chemical reactions.

Afshar's model extends the framework to include sharp-interface chemical reactions, capturing diffusion, reaction kinetics, and stress-driven interface morphology. This is particularly relevant for conversion-type electrodes where phase transformations strongly affect performance.

For Na–Sn electrodes, Anand's Cahn–Hilliard formulation provides a solid foundation to capture phase segregation and stress evolution. At the same time, Afshar's diffusion–reaction–deformation theory points toward future extensions that could better describe sharp reaction fronts in sodiation. Together, these studies outline the methodological landscape that informs the phase-field modeling strategy developed in this thesis.

Aspect	**Anand (2012)**	**Afshar et al. (2021)**
Mass balance	Cahn–Hilliard diffusion, conserved species concentration.	Diffusion + reaction term ($\dot{\xi}$), non-conserved concentration.
Kinematics	$\boldsymbol{F} = \boldsymbol{F}^e\boldsymbol{F}^p\boldsymbol{F}^s$ with elastic, plastic, and swelling parts.	$\boldsymbol{F} = \boldsymbol{F}^e\boldsymbol{F}^p\boldsymbol{F}^c$ with elastic, plastic, and chemical parts.
Constitutive laws	Free energy in terms of $\boldsymbol{C}^e$, c_R, ∇c_R; microstress ξ.	Free energy in terms of $\boldsymbol{C}^e$, c, ξ, $\nabla\xi$; chemical reaction energy barrier.
Dissipation	Plastic shear strain rate ν^p and mobility tensor M; diffusion-driven dissipation.	Reaction-driven dissipation via driving force $\mathcal{F}$ and $\dot{\xi}$; includes stress-coupling.
Focus	Diffusion-induced swelling and stress in intercalation electrodes.	Reaction fronts, morphology, and stress in conversion electrodes (e.g., FeS_2).
Relevance to Na–Sn	Baseline: phase segregation, swelling, chemo–mechanical stress.	Extension: reaction fronts and morphology changes during sodiation.

Table 5.1: Comparison of Anand (2012) and Afshar et al. (2021) frameworks.

Chapter 6

Phase-field modeling of phase segregation in Sn-based sodium-ion battery anodes (1D)

This chapter presents a continuum mechanics model for sodium-ion battery tin-based electrodes, with emphasis on phase segregation phenomena. The theoretical framework begins with an operator splitting approach (Section 6.1) and is extended to an operator splitting approach with penalty (Section 6.2). Subsequently, minimal 1D Frameworks for Mechanics and Chemo–Mechanical Coupling (Section 6.3). Finally, we introduce a comprehensive modeling strategy for multistep phase transformations in Na–Sn anodes (Section 6.4), which leverages reaction kinetics and a volume-fraction-based formulation to accurately capture the coexistence of multiple intermetallic phases, strong chemo–mechanical coupling, and large volumetric changes during sodiation and desodiation.

Our SIB model reuses LIB ingredients (mass conservation, gradient-energy regularization, chemo–mechanics) but adapts them to Na–Sn.

A detailed one-to-one comparison between these model trends and the experimental observations is presented in 7.

6.1 An operator splitting approach

6.1.1 Mass balance equation

The starting point is the mass balance for the concentration field $c(x,t)$, written in strong form as

$$\frac{\partial c}{\partial t} + \nabla \cdot \vec{h} = b, \tag{6.1}$$

where $\vec{h}$ denotes the mass flux and b is a source term representing volumetric reactions (e.g., interfacial alloying or side reactions).

The mass flux is assumed to follow a generalized Cahn–Hilliard law:

$$\vec{h} = -M(c)\,\nabla\mu = -\mathbb{D}\,\nabla c \;-\; M(c)\,\nabla\mu^{CH}, \tag{6.2}$$

where μ is the chemical potential, μ^{CH} is the contribution from the Cahn–Hilliard free energy, $\mathbb{D}$ is a reference diffusivity, and $M(c)$ is the mobility function. The mobility is taken as

$$M(c) = \frac{\mathbb{D}}{RT}\, c_{\max}\, \theta\,(1-\theta), \tag{6.3}$$

where R is the universal gas constant, T the absolute temperature, $c_{\max}$ the maximum concentration of sodium atoms, and

$$\theta = \frac{c}{c_{\max}}, \tag{6.4}$$

the dimensionless concentration.

Restricting to one spatial dimension ($x \in [0, L]$), the governing equation becomes

$$\frac{\partial c}{\partial t} - \frac{\partial}{\partial x}\left(\mathbb{D}\frac{\partial c}{\partial x}\right) - \frac{\partial}{\partial x}\left(M(c)\,\frac{\partial \mu^{CH}}{\partial x}\right) = b. \tag{6.5}$$

The associated 1D mass flux is

$$h_{1D} = -\mathbb{D}\,\frac{\partial c}{\partial x} - M(c)\,\frac{\partial \mu^{CH}}{\partial x}, \tag{6.6}$$

and, for convenience, the contribution stemming directly from the Cahn–Hilliard potential is denoted

$$h^{\mu}_{1D} = -M(c)\,\frac{\partial \mu^{CH}}{\partial x}. \tag{6.7}$$

6.1.1.1 1D weak form

Let $\varphi_i^{\theta}(x)$ be a suitable test function. Multiplying (6.5) by φ_i^{θ} and integrating over the domain $[0, L]$ yields

$$\int_0^L \varphi_i^{\theta}\frac{\partial c}{\partial t}\,\mathrm{d}x - \int_0^L \varphi_i^{\theta}\frac{\partial}{\partial x}\left(\mathbb{D}\frac{\partial c}{\partial x}\right)\,\mathrm{d}x - \int_0^L \varphi_i^{\theta}\frac{\partial}{\partial x}\left(M(c)\frac{\partial \mu^{CH}}{\partial x}\right)\,\mathrm{d}x \;=\; \int_0^L \varphi_i^{\theta}\, b\,\mathrm{d}x\,. \tag{6.8}$$

Integration by parts gives the weak form

$$\int_0^L \varphi_i^{\theta}\frac{\partial c}{\partial t}\,\mathrm{d}x + \int_0^L \mathbb{D}\frac{\partial c}{\partial x}\frac{\partial \varphi_i^{\theta}}{\partial x}\,\mathrm{d}x + \int_0^L M(c)\,\frac{\partial \mu^{CH}}{\partial x}\frac{\partial \varphi_i^{\theta}}{\partial x}\,\mathrm{d}x + \varphi_i^{\theta} h_{1D}\Big|_0^L = \int_0^L \varphi_i^{\theta} b\,\mathrm{d}x\,. \tag{6.9}$$

The boundary term $\varphi_i^{\theta} h_{1D}|_0^L$ vanishes on Dirichlet boundaries for θ and remains only on Neumann boundaries.

6.1.1.2 Separated variables discretization

To discretize, we expand the unknowns in basis functions:

$$c(x,t) = \sum_j c_j(t)\,\varphi_j^\theta(x), \qquad \mu^{CH}(x,t) = \sum_j \mu_j^{CH}(t)\,\varphi_j^\gamma(x). \tag{6.10}$$

Substituting these expansions into (6.9), the discrete weak form reads (Einstein summation implied):

$$\begin{aligned}\int_0^L \varphi_i^\theta \varphi_j^\theta \,\mathrm{d}x\ \frac{\partial c_j(t)}{\partial t} + \int_0^L \mathbb{D}\frac{\partial \varphi_i^\theta}{\partial x}\frac{\partial \varphi_j^\theta}{\partial x}\,\mathrm{d}x\ c_j(t) + \int_0^L M(c)\,\frac{\partial \varphi_i^\theta}{\partial x}\frac{\partial \varphi_j^\gamma}{\partial x}\,\mathrm{d}x\ \mu_j^{CH}(t) \\ = \int_0^L \varphi_i^\theta b\,\mathrm{d}x\ - \varphi_i^\theta h_{1D}\Big|_0^L.\end{aligned} \tag{6.11}$$

6.1.1.3 Euler integration schemes

For the time discretization, we approximate the derivative as

$$\frac{\partial c_j(t)}{\partial t} \approx \frac{c_j(t+\Delta t) - c_j(t)}{\Delta t}. \tag{6.12}$$

Using this, one obtains the Forward Euler scheme:

$$\begin{aligned}&\int_0^L \varphi_i^\theta \varphi_j^\theta \,\mathrm{d}x\ \frac{c_j(t+\Delta t)}{\Delta t} + \int_0^L \mathbb{D}\frac{\partial \varphi_i^\theta}{\partial x}\frac{\partial \varphi_j^\theta}{\partial x}\,\mathrm{d}x\ c_j(t+\Delta t) \\ &\quad + \int_0^L M(c(t))\,\frac{\partial \varphi_i^\theta}{\partial x}\frac{\partial \varphi_j^\gamma}{\partial x}\,\mathrm{d}x\ \mu_j^{CH}(t+\Delta t) \\ &= \int_0^L \varphi_i^\theta \varphi_j^\theta \,\mathrm{d}x\ \frac{c_j(t)}{\Delta t} + \int_0^L b\,\varphi_i^\theta\,\mathrm{d}x\ - \varphi_i^\theta h_{1D}\Big|_0^L.\end{aligned} \tag{6.13}$$

and the Backward Euler scheme:

$$\begin{aligned}&\int_0^L \varphi_i^\theta \varphi_j^\theta \,\mathrm{d}x\ \frac{c_j(t+\Delta t)}{\Delta t} + \int_0^L \mathbb{D}\frac{\partial \varphi_i^\theta}{\partial x}\frac{\partial \varphi_j^\theta}{\partial x}\,\mathrm{d}x\ c_j(t+\Delta t) \\ &\quad + \int_0^L M(c(t+\Delta t))\,\frac{\partial \varphi_i^\theta}{\partial x}\frac{\partial \varphi_j^\gamma}{\partial x}\,\mathrm{d}x\ \mu_j^{CH}(t+\Delta t) \\ &= \int_0^L \varphi_i^\theta \varphi_j^\theta \,\mathrm{d}x\ \frac{c_j(t)}{\Delta t} + \int_0^L b\,\varphi_i^\theta\,\mathrm{d}x\ - \varphi_i^\theta h_{1D}\Big|_0^L.\end{aligned} \tag{6.14}$$

Note that the Forward Euler scheme is linear, whereas the Backward Euler scheme is nonlinear due to the evaluation of $M(c)$ at the advanced time step.

6.1.1.4 Dimensionless form

To nondimensionalize, we define:

$$\gamma = \frac{\mu^{CH}}{\mu_{\text{ref}}}, \qquad \tilde{\mathbb{D}} = \mathbb{D}\,\frac{\Delta t}{\ell^2}, \tag{6.15}$$

where ℓ is a reference length scale and μ_{ref} is a reference chemical potential. In this form, the mobility becomes

$$\frac{\Delta t\,\mu_{\text{ref}}}{c_{\max}\ell^2}\,M(c(t)) = \tilde{\mathbb{D}}\,\frac{\mu_{\text{ref}}}{RT}\,\theta(t)\,(1-\theta(t)), \tag{6.16}$$

substituting into (6.13) and (6.14), we obtain the dimensionless Forward Euler scheme

$$\begin{aligned}
&\frac{1}{\ell}\int_0^L \varphi_i^\theta\varphi_j^\theta\,\mathrm{d}x\;\theta_j(t+\Delta t) + \tilde{\mathbb{D}}\;\ell\int_0^L \frac{\partial\varphi_i^\theta}{\partial x}\frac{\partial\varphi_j^\theta}{\partial x}\,\mathrm{d}x\;\theta_j(t+\Delta t) \\
&\quad+\tilde{\mathbb{D}}\,\frac{\mu_{\text{ref}}}{RT}\;\ell\int_0^L \varphi_k^\theta\,\frac{\partial\varphi_i^\theta}{\partial x}\frac{\partial\varphi_j^\gamma}{\partial x}\,\mathrm{d}x\;\theta_k(t)\;\gamma_j(t+\Delta t) \\
&\quad-\tilde{\mathbb{D}}\,\frac{\mu_{\text{ref}}}{RT}\;\ell\int_0^L \varphi_k^\theta\varphi_h^\theta\,\frac{\partial\varphi_i^\theta}{\partial x}\frac{\partial\varphi_j^\gamma}{\partial x}\,\mathrm{d}x\;\theta_h(t)\,\theta_k(t)\,\gamma_j(t+\Delta t) \\
&\quad=\frac{1}{\ell}\int_0^L \varphi_i^\theta\varphi_j^\theta\,\mathrm{d}x\;\frac{\theta_j(t)}{\Delta t} + \frac{1}{\ell}\int_0^L \varphi_i^\theta\,\frac{\Delta t\,b(x,t)}{c_{\max}}\,\mathrm{d}x - \varphi_i^\theta\,\frac{\Delta t\,h_{1D}(x,t)}{c_{\max}\,\ell}\Big|_0^L,
\end{aligned} \tag{6.17}$$

and the dimensionless Backward Euler scheme

$$\begin{aligned}
&\frac{1}{\ell}\int_0^L \varphi_i^\theta\varphi_j^\theta\,\mathrm{d}x\;\theta_j(t+\Delta t) + \tilde{\mathbb{D}}\;\ell\int_0^L \frac{\partial\varphi_i^\theta}{\partial x}\frac{\partial\varphi_j^\theta}{\partial x}\,\mathrm{d}x\;\theta_j(t+\Delta t) \\
&\quad+\tilde{\mathbb{D}}\,\frac{\mu_{\text{ref}}}{RT}\;\ell\int_0^L \varphi_k^\theta\,\frac{\partial\varphi_i^\theta}{\partial x}\frac{\partial\varphi_j^\gamma}{\partial x}\,\mathrm{d}x\;\theta_k(t+\Delta t)\;\gamma_j(t+\Delta t) \\
&\quad-\tilde{\mathbb{D}}\,\frac{\mu_{\text{ref}}}{RT}\;\ell\int_0^L \varphi_k^\theta\varphi_h^\theta\,\frac{\partial\varphi_i^\theta}{\partial x}\frac{\partial\varphi_j^\gamma}{\partial x}\,\mathrm{d}x\;\theta_h(t+\Delta t)\,\theta_k(t+\Delta t)\,\gamma_j(t+\Delta t) \\
&\quad=\frac{1}{\ell}\int_0^L \varphi_i^\theta\varphi_j^\theta\,\mathrm{d}x\;\frac{\theta_j(t)}{\Delta t} + \frac{1}{\ell}\int_0^L \frac{\Delta t\,b(x,t+\Delta t)}{c_{\max}}\,\varphi_i^\theta\,\mathrm{d}x - \varphi_i^\theta\,\frac{\Delta t\,h_{1D}(x,t+\Delta t)}{c_{\max}\,\ell}\Big|_0^L.
\end{aligned} \tag{6.18}$$

6.1.2 Chemical potential

6.1.2.1 Order-zero thermodynamics

We start from the Helmholtz free-energy density per reference volume, ψ_R, additively decomposed into transport and interfacial parts. Focusing here on pure transport contributions, we identify

$$\psi_R^{tr}(c) \;=\; c_{\max}\Big[\,\mu^0\,\theta \;-\; T\,\eta_R^{mix} \;-\; T\,\eta_R^{\chi}\,\Big], \tag{6.19}$$

where μ^0 is a reference chemical potential, and the entropic terms read

$$\eta_R^{mix} = -R\Big(\theta\,\ln\theta + (1-\theta)\,\ln(1-\theta)\Big), \tag{6.20}$$

$$\eta_R^{\chi} = -R\,\chi\,\theta(1-\theta). \tag{6.21}$$

Here R is the universal gas constant, T the absolute temperature, and χ is a (dimensionless) interaction parameter that promotes phase separation for $\chi > 0$.

Thermodynamics gives the chemical potential as the partial derivative of the free energy with respect to c:

$$\mu \;=\; \frac{\partial \psi_R}{\partial c} \;=\; \frac{1}{c_{\max}}\,\frac{\partial \psi_R}{\partial \theta}, \tag{6.22}$$

applying (6.22) to (6.19)–(6.21) yields the (order-zero) constitutive law

$$\mu^{tr} \;=\; \mu^0 + R\,T\,\ln\Big(\frac{\theta}{1-\theta}\Big) \;+\; R\,T\,\chi\,(1-2\theta). \tag{6.23}$$

6.1.2.2 Order-one thermodynamics

We enrich the free energy by including gradients of the composition (interfacial energy), leading to an "order-one" free energy

$$\psi_R^{en}(c, \nabla c) \;=\; \psi_R^{tr}(c) \;+\; \psi_R^{int}(\nabla c). \tag{6.24}$$

Using a Gateaux variation of the total free energy over a body $\mathcal{B}$ gives

$$\frac{\mathrm{d}}{\mathrm{d}\epsilon}\int_{\mathcal{B}} \psi_R(c+\epsilon\,\delta c, \nabla(c+\epsilon\,\delta c))\,\mathrm{d}V\Big|_{\epsilon=0} = \int_{\mathcal{B}}\Big[\,\frac{\partial \psi_R}{\partial c} - \nabla\cdot\Big(\frac{\partial \psi_R}{\partial \nabla c}\Big)\,\Big]\delta c\,\mathrm{d}V \tag{6.25}$$

$$+ \text{ boundary terms.}$$

Hence the localized constitutive relation becomes

$$\mu \;=\; \frac{\partial \psi_R^{tr}}{\partial c} \;-\; \nabla\cdot\Big(\frac{\partial \psi_R^{int}}{\partial \nabla c}\Big). \tag{6.26}$$

A standard choice for the interfacial contribution is [9, 86, 112]

$$\psi_R^{int}(\nabla c) \;=\; \frac{1}{2}\,c_{\max}\,\lambda\,\nabla\theta\cdot\nabla\theta, \tag{6.27}$$

where $\lambda > 0$ is a gradient-energy coefficient (assumed constant here), therefore

$$\mu^{int} = -\,\lambda\,\nabla\cdot(\nabla\theta) \;= -\,\lambda\,\Delta\theta, \tag{6.28}$$

combining with (6.23) gives the (order-one) chemical potential

$$\mu \;= \mu^0 \;+\; R\,T\,\ln\Big(\frac{\theta}{1-\theta}\Big) \;+\; R\,T\,\chi\,(1-2\theta) \;-\; \lambda\,\Delta\theta. \tag{6.29}$$

6.1.2.3 Cahn–Hilliard chemical potential

For later use in the mass balance, we split the chemical potential into an ideal/standard part and a Cahn–Hilliard part:

$$\mu \;=\; \mu^0 + R\,T\,\ln\!\Big(\frac{\theta}{1-\theta}\Big) \;+\; \mu^{CH}, \tag{6.30}$$

where the Cahn–Hilliard contribution collects the interaction and interfacial terms,

$$\mu^{CH} \;=\; R\,T\,\chi\,(1-2\theta) \;-\; \lambda\,\Delta\theta, \tag{6.31}$$

using the dimensionless CH potential γ yields

$$\gamma(x,t) \;=\; \frac{R\,T}{\mu_{\text{ref}}}\,\chi\,(1-2\theta) \;-\; \frac{\lambda}{\mu_{\text{ref}}}\,\Delta\theta. \tag{6.32}$$

6.1.2.4 1D Weak form

We adopt test functions φ_i^γ for the functional space of the dimensionless chemical potential $\gamma(x,t)$. Multiplying Eq. (6.32) by φ_i^γ and integrating over the volume V gives

$$\int_V \varphi_i^\gamma\,\gamma(x,t)\,\mathrm{d}V = \int_V \varphi_i^\gamma\,\frac{RT}{\mu_{\text{ref}}}\,\chi\,(1-2\theta)\,\mathrm{d}V - \int_V \varphi_i^\gamma\,\frac{\lambda}{\mu_{\text{ref}}}\,\nabla\cdot(\nabla\theta)\,\mathrm{d}V. \tag{6.33}$$

To restate $\nabla\theta$, we recall the definition of the flux $\vec{h}$ from Eq. (6.2), thus

$$-\nabla\theta = \frac{-\mathbb{D}\nabla c - M(c)\nabla\mu^{CH}}{\mathbb{D}c_{\max}} + \frac{M(c)\nabla\mu^{CH}}{\mathbb{D}c_{\max}} = \frac{\vec{h}}{\mathbb{D}c_{\max}} + \frac{M(c)\nabla\mu^{CH}}{\mathbb{D}c_{\max}}, \tag{6.34}$$

substituting this into (6.33) and integrating by parts, we obtain

$$\begin{aligned}\int_V \varphi_i^\gamma\,\gamma(x,t)\,\mathrm{d}V = \frac{RT}{\mu_{\text{ref}}}\,\chi\int_V \varphi_i^\gamma\,(1-2\theta)\,\mathrm{d}V + \frac{\lambda}{\mu_{\text{ref}}\,\mathbb{D}c_{\max}}\int_V \nabla\varphi_i^\gamma\cdot\mathbb{D}\nabla c\,\mathrm{d}V \\ + \frac{\lambda}{\mu_{\text{ref}}\,\mathbb{D}c_{\max}}\int_{\partial V} \varphi_i^\gamma\,M(c)\nabla\mu^{CH}\cdot\vec{n}\,\mathrm{d}S + \frac{\lambda}{\mu_{\text{ref}}\,\mathbb{D}c_{\max}}\int_{\partial^N V} \varphi_i^\gamma\,\vec{h}\cdot\vec{n}\,\mathrm{d}S.\end{aligned} \tag{6.35}$$

For a one-dimensional domain $(0,L)$, Eq. (6.35) specializes to

$$\begin{aligned}\int_0^L \varphi_i^\gamma\,\gamma(x,t)\;\mathrm{d}x \;=\; \frac{RT}{\mu_{\text{ref}}}\,\chi\int_0^L \varphi_i^\gamma\,(1-2\theta)\;\mathrm{d}x \;+\; \frac{\lambda}{\mu_{\text{ref}}\,\mathbb{D}c_{\max}}\int_0^L \frac{\partial\varphi_i^\gamma}{\partial x}\,\mathbb{D}\frac{\partial c}{\partial x}\;\mathrm{d}x \\ + \frac{\lambda}{\mu_{\text{ref}}\,\mathbb{D}c_{\max}}\Bigg[\varphi_i^\gamma\,M(c)\,\frac{\partial\mu^{CH}}{\partial x} + \varphi_i^\gamma\,h_{1D}\Bigg]_0^L.\end{aligned} \tag{6.36}$$

Since φ_i^γ represents the dimensionless chemical potential, the boundary contribution

$$\frac{\lambda}{\mu_{\text{ref}}\,\mathbb{D}c_{\max}}\left[\varphi_i^\gamma\, M(c)\frac{\partial \mu^{CH}}{\partial x}+\varphi_i^\gamma\, h_{1D}\right]_0^L, \tag{6.37}$$

vanishes on Dirichlet boundaries for γ.

Remark. Equation (6.32) is not a conservation law but a constitutive definition. Hence, no natural Dirichlet/Neumann boundary conditions are expected. The term involving $M(c)\,\partial_x\mu^{CH}$ in (6.37) must therefore be treated carefully. In manufactured solutions or many publications, this contribution is assumed given, and is treated analogously to a Neumann boundary condition. Using Eq. (6.7), this boundary contribution can be rewritten in terms of the CH flux as

$$-\frac{\lambda}{\mu_{\text{ref}}\,\mathbb{D}c_{\max}}\,\varphi_i^\gamma\, h_{1D}^\mu\,\Big|_0^L. \tag{6.38}$$

6.1.2.5 Dimensionless form

To nondimensionalize (6.36), we rescale by ℓ and $\tilde{\mathbb{D}}$. The result is

$$\begin{aligned}\frac{1}{\ell}\int_0^L \varphi_i^\gamma\gamma(x,t)\,\mathrm{d}x \;=\; &\frac{RT}{\mu_{\text{ref}}}\,\chi\left[\frac{1}{\ell}\int_0^L \varphi_i^\gamma\,\mathrm{d}x\;-2\,\frac{1}{\ell}\int_0^L \varphi_i^\gamma\,\theta\,\mathrm{d}x\right]\\ &+\frac{\lambda}{RT}\,\frac{RT}{\mu_{\text{ref}}}\frac{1}{\ell^2}\,\ell\int_0^L \frac{\partial\varphi_i^\gamma}{\partial x}\,\frac{\partial\theta}{\partial x}\,\mathrm{d}x\\ &+\frac{\lambda}{RT}\,\frac{RT}{\mu_{\text{ref}}}\frac{1}{\ell^2}\,\frac{1}{\tilde{\mathbb{D}}}\left[\varphi_i^\gamma\,\frac{\Delta t\, h_{1D}(x,t)}{c_{\max}\,\ell}\right]_0^L\\ &+\frac{\lambda}{RT}\,\frac{1}{\ell^2}\left[\varphi_i^\gamma\,\theta(1-\theta)\,\ell\,\frac{\partial\gamma}{\partial x}\right]_0^L.\end{aligned} \tag{6.39}$$

For the "Neumann kind" formulation, where h_{1D}^μ is prescribed, the boundary contribution is instead

$$\frac{1}{\ell}\int_0^L \varphi_i^\gamma\gamma(x,t)\,\mathrm{d}x \;=\cdots-\frac{\lambda}{RT}\,\frac{1}{\ell^2}\left[\varphi_i^\gamma\,\frac{\ell\, h_{1D}^\mu(x,t)}{c_{\max}\,\mu_{\text{ref}}\,M_0}\right]_0^L, \tag{6.40}$$

with h_{1D}^μ defined in Eq. (6.7), and where M_0 is a constant mobility scaling factor. Using (6.7), this boundary condition is equivalent to

$$-\,\theta(1-\theta)\,\ell\,\frac{\partial\gamma}{\partial x}.$$

6.1.2.6 Separated variables discretization

We approximate the fields by expansions in their respective bases,

$$\theta(x,t) \;\approx\; \sum_j \varphi_j^\theta(x)\,\theta_j(t), \qquad \gamma(x,t) \;\approx\; \sum_j \varphi_j^\gamma(x)\,\gamma_j(t). \tag{6.41}$$

Substituting these approximations into Eq. (6.39), and adopting Einstein's summation convention, the fully discrete system reads

$$\begin{aligned}
&\frac{1}{\ell}\int_0^L \varphi_i^\gamma\varphi_j^\gamma \,\mathrm{d}x\;\gamma_j(t+\Delta t) + 2\,\frac{RT}{\mu_{\mathrm{ref}}}\,\chi\,\frac{1}{\ell}\int_0^L \varphi_i^\gamma\varphi_j^\theta \,\mathrm{d}x\;\theta_j(t+\Delta t) \\
&-\frac{1}{\ell^2}\,\frac{\lambda}{RT}\,\frac{RT}{\mu_{\mathrm{ref}}}\,\ell\int_0^L \frac{\partial\varphi_i^\gamma}{\partial x}\frac{\partial\varphi_j^\theta}{\partial x}\,\mathrm{d}x\;\theta_j(t+\Delta t) \\
&-\frac{1}{\ell^2}\,\frac{\lambda}{RT}\left[\varphi_i^\gamma\,\varphi_h^\theta\theta_h(t+\Delta t)\left(1-\varphi_k^\theta\theta_k(t+\Delta t)\right)\ell\,\frac{\partial\varphi_j^\gamma}{\partial x}\,\gamma_j(t+\Delta t)\right]_0^L \\
&=\frac{RT}{\mu_{\mathrm{ref}}}\,\chi\,\frac{1}{\ell}\int_0^L \varphi_i^\gamma\,\mathrm{d}x + \frac{1}{\ell^2}\,\frac{\lambda}{RT}\,\frac{RT}{\mu_{\mathrm{ref}}}\,\frac{1}{\tilde{\mathbb{D}}}\left[\varphi_i^\gamma\,\frac{\Delta t}{c_{\max}\ell}\,h_{1D}(x,t+\Delta t)\right]_0^L.
\end{aligned} \tag{6.42}$$

If instead the Neumann-type treatment of the γ boundary contribution is adopted (cf. Remark 6.1.2.4), one obtains

$$\begin{aligned}
&\frac{1}{\ell}\int_0^L \varphi_i^\gamma\varphi_j^\gamma \,\mathrm{d}x\;\gamma_j(t+\Delta t) + 2\,\frac{RT}{\mu_{\mathrm{ref}}}\,\chi\,\frac{1}{\ell}\int_0^L \varphi_i^\gamma\varphi_j^\theta \,\mathrm{d}x\;\theta_j(t+\Delta t) \\
&-\frac{1}{\ell^2}\,\frac{\lambda}{RT}\,\frac{RT}{\mu_{\mathrm{ref}}}\,\ell\int_0^L \frac{\partial\varphi_i^\gamma}{\partial x}\frac{\partial\varphi_j^\theta}{\partial x}\,\mathrm{d}x\;\theta_j(t+\Delta t) \\
&=\frac{RT}{\mu_{\mathrm{ref}}}\,\chi\,\frac{1}{\ell}\int_0^L \varphi_i^\gamma\,\mathrm{d}x + \frac{1}{\ell^2}\,\frac{\lambda}{RT}\,\frac{RT}{\mu_{\mathrm{ref}}}\,\frac{1}{\tilde{\mathbb{D}}}\left[\varphi_i^\gamma\,\frac{\Delta t}{c_{\max}\ell}\,h_{1D}(x,t+\Delta t)\right]_0^L \\
&-\frac{1}{\ell^2}\,\frac{\lambda}{RT}\left[\varphi_i^\gamma\,\frac{\ell}{c_{\max}\,\mu_{\mathrm{ref}}\,M_0}\,h_{1D}^\mu(x,t+\Delta t)\right]_0^L.
\end{aligned} \tag{6.43}$$

Here h_{1D}^μ is the CH flux defined in Eq. (6.7), and $M_0 = \tilde{\mathbb{D}}/RT$ is a mobility scaling constant.

In both formulations, all unknown fields have been consistently evaluated at time $t+\Delta t$.

6.1.3 Manufactured solutions

We consider a 1D domain with spatial coordinate X_1 (identified with x in previous sections). Let the manufactured concentration be

$$\theta(X_1,t) \;=\; \frac{t}{\bar{t}}\Big(\alpha+\beta\,\frac{X_1}{L}\Big), \tag{6.44}$$

with $\bar{t}$ a reference time. Since θ is linear in X_1, one has $\nabla\theta=\partial_{X_1}\theta\,\mathbf{e}_1$ and $\nabla\cdot\nabla\theta=\partial_{X_1X_1}\theta=0$.

Using the Cahn–Hilliard chemical potential (6.31), the dimensionless chemical potential $\gamma=\mu^{CH}/\mu_{\mathrm{ref}}$ reads

$$\frac{\mu^{CH}}{\mu_{\mathrm{ref}}} \;=\; \frac{RT}{\mu_{\mathrm{ref}}}\,\chi\Big(1-2\theta\Big) \;=\; \frac{RT}{\mu_{\mathrm{ref}}}\,\chi\left[1-2\,\frac{t}{\bar{t}}\Big(\alpha+\beta\,\tfrac{X_1}{L}\Big)\right]. \tag{6.45}$$

The 1D mass flux (definition (6.6)) becomes

$$\begin{aligned} h_{1D} &= -\mathbb{D}\,c_{\max}\,\frac{\partial\theta}{\partial X_1} \;-\; M(c)\,\mu_{\mathrm{ref}}\,\frac{\partial}{\partial X_1}\left(\frac{\mu^{CH}}{\mu_{\mathrm{ref}}}\right) \\ &= -\mathbb{D}\,c_{\max}\,\frac{t}{\bar{t}}\,\frac{\beta}{L} \;-\; M(c)\,\mu_{\mathrm{ref}}\Big(-2\,\frac{RT}{\mu_{\mathrm{ref}}}\,\chi\,\frac{t}{\bar{t}}\,\frac{\beta}{L}\Big) \\ &= \frac{t}{\bar{t}}\,\frac{\beta}{L}\,\mathbb{D}\,c_{\max}\,[-1+2\,\theta(1-\theta)\,\chi]\,. \end{aligned} \tag{6.46}$$

Using the dimensionless diffusivity $\tilde{\mathbb{D}}$, we obtain

$$\frac{\Delta t\,h_{1D}(X_1,t)}{c_{\max}\,\ell} \;=\; \frac{t}{\bar{t}}\,\frac{\ell}{L}\,\tilde{\mathbb{D}}\,\beta\,\left[-1+2\,\frac{t}{\bar{t}}\Big(\alpha+\beta\,\tfrac{X_1}{L}\Big)\Big(1-\frac{t}{\bar{t}}\Big(\alpha+\beta\,\tfrac{X_1}{L}\Big)\Big)\,\chi\right]. \tag{6.47}$$

From the CH contribution (6.7),

$$h^{\mu}_{1D} \;=\; -M(c)\,\frac{\partial\mu^{CH}}{\partial X_1} \;=\; 2\,\frac{t}{\bar{t}}\,\frac{\beta}{L}\,\mathbb{D}\,c_{\max}\,\theta(1-\theta)\,\chi, \tag{6.48}$$

the boundary-scaled CH flux appearing in the Neumann-kind weak form reads

$$\frac{\ell\,h^{\mu}_{1D}(X_1,t)}{c_{\max}\,\mu_{\mathrm{ref}}\,M_0} \;=\; 2\,\frac{RT}{\mu_{\mathrm{ref}}}\,\frac{t}{\bar{t}}\,\frac{\ell}{L}\,\beta\,\theta(1-\theta)\,\chi. \tag{6.49}$$

Finally, the source term $b(X_1,t)$ is fixed by the mass balance,

$$\begin{aligned} b &= \frac{\partial c}{\partial t}+\frac{\partial h_{1D}}{\partial X_1} \;=\; c_{\max}\,\frac{\partial\theta}{\partial t}+2\,\chi\,\frac{t}{\bar{t}}\,\frac{\beta}{L}\,\mathbb{D}\,c_{\max}\,(1-2\theta)\,\frac{\partial\theta}{\partial X_1} \\ &= c_{\max}\,\frac{1}{\bar{t}}\Big(\alpha+\beta\,\tfrac{X_1}{L}\Big)+2\,\chi\,\mathbb{D}\,c_{\max}\,\left(\frac{t}{\bar{t}}\,\frac{\beta}{L}\right)^2\Big(1-2\,\theta\Big), \end{aligned} \tag{6.50}$$

hence the dimensionless form

$$\frac{\Delta t\, b(X_1,t)}{c_{\max}} \;=\; \frac{\Delta t}{\bar{t}}\Big(\alpha+\beta\,\tfrac{X_1}{L}\Big) \;+\; 2\,\chi\,\tilde{\mathrm{D}}\,\left(\beta\,\frac{t}{\bar{t}}\,\frac{\ell}{L}\right)^2\left[1-2\,\frac{t}{\bar{t}}\Big(\alpha+\beta\,\tfrac{X_1}{L}\Big)\right]. \tag{6.51}$$

6.1.4 Governing equations and numerical solution of the Neumann kind problem

6.1.4.1 Newton–Raphson scheme for θ

The discrete dimensionless weak form of "Neumann kind" for mass balance (6.18) yields

$$\begin{aligned}\mathcal{R}_\theta\big(\gamma_j(t{+}\Delta t),\theta_j(t{+}\Delta t)\big) &= \mathcal{A}_\theta\big(\theta_j(t{+}\Delta t)\big) \\ &+\; \tilde{\mathrm{D}}\,\frac{\mu_{\mathrm{ref}}}{RT}\,\ell\int_0^L \varphi_k^\theta\,\frac{\partial\varphi_i^\theta}{\partial x}\,\frac{\partial\varphi_j^\gamma}{\partial x}\,\mathrm{d}x\;\theta_k(t{+}\Delta t)\,\gamma_j(t{+}\Delta t) \\ &-\; \tilde{\mathrm{D}}\,\frac{\mu_{\mathrm{ref}}}{RT}\,\ell\int_0^L \varphi_k^\theta\varphi_h^\theta\,\frac{\partial\varphi_i^\theta}{\partial x}\,\frac{\partial\varphi_j^\gamma}{\partial x}\,\mathrm{d}x\;\theta_h(t{+}\Delta t)\theta_k(t{+}\Delta t)\,\gamma_j(t{+}\Delta t) \\ &+\; \mathcal{B}_\theta \;=\; 0,\end{aligned} \tag{6.52}$$

where the linear part

$$\mathcal{A}_\theta(\theta) = \frac{1}{\ell}\int_0^L \varphi_i^\theta\varphi_j^\theta\,\mathrm{d}x\;\theta_j \;+\; \tilde{\mathrm{D}}\,\ell\int_0^L \frac{\partial\varphi_i^\theta}{\partial x}\,\frac{\partial\varphi_j^\theta}{\partial x}\,\mathrm{d}x\;\theta_j, \tag{6.53}$$

and the known part

$$\mathcal{B}_\theta = -\frac{1}{\ell}\int_0^L \varphi_i^\theta\varphi_j^\theta\,\mathrm{d}x\;\frac{\theta_j(t)}{\Delta t} - \frac{1}{\ell}\int_0^L \varphi_i^\theta\,\frac{\Delta t\, b(x,t{+}\Delta t)}{c_{\max}}\,\mathrm{d}x + \left(\varphi_i^\theta\,\frac{\Delta t\, h_{1D}(x,t{+}\Delta t)}{c_{\max}\,\ell}\,\Big|_0^L\right). \tag{6.54}$$

The Newton–Raphson linearization reads

$$\begin{aligned}\frac{\partial}{\partial\epsilon}\,\mathcal{R}_\theta(\gamma_j{+}\epsilon\,\delta\gamma_j,\theta_j{+}\epsilon\,\delta\theta_j)\Big|_{\epsilon=0} &= \mathcal{A}_\theta(\delta\theta) \\ &+\; \tilde{\mathrm{D}}\,\frac{\mu_{\mathrm{ref}}}{RT}\,\ell\int_0^L \frac{\partial\varphi_h^\gamma}{\partial x}\,\gamma_h\,\frac{\partial\varphi_i^\theta}{\partial x}\,\varphi_j^\theta\,\mathrm{d}x\;\delta\theta_j \\ &-\; 2\,\tilde{\mathrm{D}}\,\frac{\mu_{\mathrm{ref}}}{RT}\,\ell\int_0^L \varphi_k^\theta\,\theta_k\,\frac{\partial\varphi_h^\gamma}{\partial x}\,\gamma_h\,\frac{\partial\varphi_i^\theta}{\partial x}\,\varphi_j^\theta\,\mathrm{d}x\;\delta\theta_j \\ &+\; \tilde{\mathrm{D}}\,\frac{\mu_{\mathrm{ref}}}{RT}\,\ell\int_0^L \varphi_k^\theta\,\theta_k\,\frac{\partial\varphi_i^\theta}{\partial x}\,\frac{\partial\varphi_j^\gamma}{\partial x}\,\mathrm{d}x\;\delta\gamma_j \\ &-\; \tilde{\mathrm{D}}\,\frac{\mu_{\mathrm{ref}}}{RT}\,\ell\int_0^L \varphi_h^\theta\,\theta_h\,\varphi_k^\theta\,\theta_k\,\frac{\partial\varphi_i^\theta}{\partial x}\,\frac{\partial\varphi_j^\gamma}{\partial x}\,\mathrm{d}x\;\delta\gamma_j \\ &=\; -\mathcal{R}_\theta(\gamma_j(t{+}\Delta t),\theta_j(t{+}\Delta t)).\end{aligned} \tag{6.55}$$

6.1.4.2 Newton–Raphson scheme for γ

Analogously, the dimensionless Backward Euler for γ in (6.43) can be written as the residual

$$\mathcal{R}_\gamma\big(\gamma_j(t{+}\Delta t),\theta_j(t{+}\Delta t)\big) = \mathcal{A}_\gamma\big(\gamma_j(t{+}\Delta t),\theta_j(t{+}\Delta t)\big) \;+\; \mathcal{B}_\gamma \;=\; 0, \quad (6.56)$$

with the (linear) left–hand operator

$$\begin{aligned}\mathcal{A}_\gamma(\gamma,\theta) = \frac{1}{\ell}\int_0^L \varphi_i^\gamma\varphi_j^\gamma \,\mathrm{d}x\;\gamma_j \;+\; 2\,\frac{RT}{\mu_{\mathrm{ref}}}\chi\,\frac{1}{\ell}\int_0^L \varphi_i^\gamma\varphi_j^\theta \,\mathrm{d}x\;\theta_j \\ -\;\frac{1}{\ell^2}\,\frac{\lambda}{RT}\,\frac{RT}{\mu_{\mathrm{ref}}}\,\ell\int_0^L \frac{\partial\varphi_i^\gamma}{\partial x}\frac{\partial\varphi_j^\theta}{\partial x}\,\mathrm{d}x\;\theta_j,\end{aligned} \quad (6.57)$$

and the known right–hand side grouped as

$$\mathcal{B}_\gamma = -\,\frac{RT}{\mu_{\mathrm{ref}}}\chi\,\frac{1}{\ell}\int_0^L \varphi_i^\gamma\,\mathrm{d}x \;-\; \frac{1}{\ell^2}\,\frac{\lambda}{RT}\,\frac{RT}{\mu_{\mathrm{ref}}}\,\frac{1}{\tilde{\mathfrak{D}}}\left(\varphi_i^\gamma\,\frac{\Delta t\,h_{1D}(x,t{+}\Delta t)}{c_{\max}\,\ell}\,\Big|_0^L\right) \quad (6.58)$$

$$+\;\frac{1}{\ell^2}\,\frac{\lambda}{RT}\,\left(\varphi_i^\gamma\,\frac{\ell\,h_{1D}^\mu(x,t{+}\Delta t)}{c_{\max}\,\mu_{\mathrm{ref}}\,M_0}\,\Big|_0^L\right).$$

The Newton–Raphson linearization is then

$$\frac{\partial}{\partial\epsilon}\,\mathcal{R}_\gamma(\gamma_j{+}\epsilon\,\delta\gamma_j,\theta_j{+}\epsilon\,\delta\theta_j)\Big|_{\epsilon=0} = \mathcal{A}_\gamma(\delta\gamma,\delta\theta) = -\mathcal{R}_\gamma(\gamma_j(t{+}\Delta t),\theta_j(t{+}\Delta t)). \quad (6.59)$$

The full set of governing equations, along with their discretization and the Newton–Raphson linearization for solving the nonlinear coupled system, are provided in Appendix A.1. This includes the detailed weak forms, residual definitions, and the step-by-step derivation of the tangent matrices required for implementation. Here, we focus on the physical modeling and interpretation, while the mathematical formulation of the numerical solution is deferred to the appendix for clarity.

6.1.5 Numerical results

We applied the computational framework to solve the coupled mass balance and Cahn–Hilliard chemical potential equations within a one-dimensional

domain of length 10^{-6} m, initially benchmarking the implementation against the manufactured solution introduced earlier.

The numerical experiments explored a broad range of physical and numerical parameters:

- the diffusivity $\mathbb{D}$, varied between 10^{-15} and 10^{-9} m^2/s;
- the dimensionless gradient energy coefficient, $\lambda/(RT\ell^2)$, varied between 4 and 0;
- the mesh resolution, ranging from 8 to 64 elements.

The Flory–Huggins interaction parameter was fixed at $\chi = 10$, quantifying the interaction strength between the diffusing sodium and the host tin-based material.

Our simulations showed that convergence of the numerical scheme was highly sensitive to the parameter set. For low diffusivity values and small $\lambda/(RT\ell^2)$, the model typically converged robustly. However, as the diffusivity increased and the interfacial term $\lambda/(RT\ell^2)$ became larger, convergence deteriorated, particularly when employing finer mesh discretizations. This behavior highlighted that the initial operator–splitting formulation was not sufficiently stable to handle the stiffness of the governing equations under demanding parameter regimes.

To address these limitations, in the following Section 6.2 we introduce a penalty–based operator splitting scheme. This modification improves numerical stability by penalizing inconsistencies between the split operators, thereby enabling convergence over a wider parameter space. The enhanced formulation is essential for accurately resolving the interplay between diffusion and interfacial energy contributions in sodium–tin electrodes.

6.2 A Penalty-enhanced operator splitting approach

We now revisit the mass balance Eq. (6.1), introducing a modified formulation of the constitutive law for the mass flux. Specifically, we replace (6.2) with

$$\vec{h}(c) = -\mathbb{\Phi}\, \nabla c - M(c)\, \nabla \mu^{int}(c)\ , \tag{6.60}$$

where the effective diffusivity is defined as

$$\mathbb{\Phi} = \Phi\ - 2\ \frac{M(c)}{c_{\max}}\, RT\chi\ . \tag{6.61}$$

Note that the diffusivity coefficient $\mathbb{\Phi}$, which multiplies ∇c, is no longer constant but depends explicitly on the concentration c.

Following the approach of [9, 113, 114], rather than treating μ^{int} as an additional unknown field depending directly on c, we introduce an auxiliary variable c^*. The interfacial chemical potential is then approximated as

$$\vec{h}(c, c^*) = -\mathbb{\Phi}\, \nabla c - M(c)\, \nabla \mu^{int}(c^*), \tag{6.62}$$

$$\mu^{int}(c^*) = -\frac{\lambda}{c_{\max}}\ \nabla \cdot \nabla c^*\ . \tag{6.63}$$

This approximation coincides with the original Cahn–Hilliard formulation (6.28) if $c^* = c$. To enforce this condition, we introduce the following constraint:

$$c - c^* = -l^2\ \nabla \cdot \nabla c^*, \tag{6.64}$$

where $l \to 0^+$ is a positive parameter with the physical interpretation of an internal length scale. Under this constraint, the interfacial chemical potential becomes

$$\mu^{int}(c^*) = \frac{\lambda}{l^2}\ \frac{1}{c_{\max}}\ (c - c^*)\ . \tag{6.65}$$

Defining the penalty parameter

$$\beta = \frac{\lambda}{l^2}, \tag{6.66}$$

which is positive and tends to $+\infty$, the flux approximation can finally be written as

$$\vec{h}(c, c^*) = -\mathbb{\Phi}\, \nabla c - \beta\ M(c)\, \nabla \frac{c - c^*}{c_{\max}}\ . \tag{6.67}$$

6.2.1 Mass Balance equation

The penalty formulation leads to the following mass balance law:

$$\frac{\partial c}{\partial t} - \nabla \cdot (\mathbb{D} \nabla c) - \nabla \cdot \left(\beta \, M(c) \, \nabla \frac{c - c^*}{c_{\max}} \right) = b, \tag{6.68}$$

where $\mathbb{D}$ is defined in Eq. (6.61).

Restricting to a one-dimensional domain $x \in [0, L]$ yields

$$\frac{\partial c}{\partial t} - \frac{\partial}{\partial x} \left(\mathbb{D} \frac{\partial c}{\partial x} \right) - \frac{\partial}{\partial x} \left(\beta \, M(c) \left(\frac{\partial \theta}{\partial x} - \frac{\partial \theta^*}{\partial x} \right) \right) = b, \tag{6.69}$$

where the normalized nonlocal species concentration is

$$\theta^* = \frac{c^*}{c_{\max}}. \tag{6.70}$$

It is convenient to introduce the following fluxes:

$$h_{1D} = -\mathbb{D} \frac{\partial c}{\partial x} - \beta \, M(c) \left(\frac{\partial \theta}{\partial x} - \frac{\partial \theta^*}{\partial x} \right), \tag{6.71}$$

$$h^*_{1D} = \frac{\partial \theta^*}{\partial x}. \tag{6.72}$$

6.2.1.1 1D Weak form

Let L denote the right end of the 1D domain, which starts at $x = 0$. The weak form of Eq. (6.69), with test functions φ_i^θ, reads

$$\int_0^L \varphi_i^\theta \frac{\partial c}{\partial t} \, \mathrm{d}x - \int_0^L \varphi_i^\theta \frac{\partial}{\partial x} \Big(\mathbb{D} \frac{\partial c}{\partial x} \Big) \, \mathrm{d}x - \int_0^L \varphi_i^\theta \frac{\partial}{\partial x} \Big(\beta \, M(c) \, \big(\tfrac{\partial \theta}{\partial x} - \tfrac{\partial \theta^*}{\partial x} \big) \Big) \, \mathrm{d}x \tag{6.73}$$

$$= \int_0^L \varphi_i^\theta \, b \, \mathrm{d}x \, .$$

Integration by parts gives

$$\int_0^L \varphi_i^\theta \frac{\partial c}{\partial t} \, \mathrm{d}x + \int_0^L \frac{\partial \varphi_i^\theta}{\partial x} \, \mathbb{D} \frac{\partial c}{\partial x} \, \mathrm{d}x + \int_0^L \frac{\partial \varphi_i^\theta}{\partial x} \, \beta \, M(c) \left(\frac{\partial \theta}{\partial x} - \frac{\partial \theta^*}{\partial x} \right) \mathrm{d}x + \varphi_i^\theta \, h_{1D} \Big|_0^L \tag{6.74}$$

$$= \int_0^L \varphi_i^\theta \, b \, \mathrm{d}x \, .$$

Since the test function φ_i^θ corresponds to the dimensionless concentration, the boundary term

$$\varphi_i^\theta \, h_{1D} \Big|_0^L \tag{6.75}$$

vanishes on Dirichlet boundaries for θ and is evaluated only on Neumann boundaries.

Finally, using Eq. (6.61), the weak form (6.74) can be restated as

$$\int_0^L \varphi_i^\theta \frac{\partial c}{\partial t}\,\mathrm{d}x + \int_0^L \frac{\partial \varphi_i^\theta}{\partial x}\,\mathbb{D}\,\frac{\partial c}{\partial x}\,\mathrm{d}x - 2\,\frac{RT\chi}{c_{\max}}\int_0^L \frac{\partial \varphi_i^\theta}{\partial x}\,M(c)\,\frac{\partial c}{\partial x}\,\mathrm{d}x \quad (6.76)$$
$$+ \int_0^L \frac{\partial \varphi_i^\theta}{\partial x}\,\beta\,M(c)\left(\frac{\partial \theta}{\partial x} - \frac{\partial \theta^*}{\partial x}\right)\mathrm{d}x + \varphi_i^\theta\,h_{1D}\Big|_0^L = \int_0^L \varphi_i^\theta\,b\,\mathrm{d}x\,.$$

6.2.1.2 Separated variables discretization

The concentration fields are expanded in terms of finite element basis functions, i.e.,

$$c(x,t) = \sum_j c_j(t)\,\varphi_j^\theta(x), \qquad c^*(x,t) = \sum_j c_j^*(t)\,\varphi_j^*(x)\,. \quad (6.77)$$

For simplicity, the same interpolation order is assumed for c and c^*, such that $\varphi_j^\theta \equiv \varphi_j^*$. Replacing these expressions into Eq. (6.76), one obtains the discrete weak form (Einstein summation convention implied):

$$\int_0^L \varphi_i^\theta\varphi_j^\theta\,\mathrm{d}x\;\frac{\partial c_j(t)}{\partial t} + \int_0^L \mathbb{D}\frac{\partial \varphi_i^\theta}{\partial x}\frac{\partial \varphi_j^\theta}{\partial x}\,\mathrm{d}x\;c_j(t) - 2\,\frac{RT\chi}{c_{\max}}\int_0^L \frac{\partial \varphi_i^\theta}{\partial x}\,M(c)\,\frac{\partial \varphi_j^\theta}{\partial x}\,\mathrm{d}x\;c_j(t) \quad (6.78)$$
$$+ \int_0^L \beta\,M(c)\,\frac{\partial \varphi_i^\theta}{\partial x}\frac{\partial \varphi_j^\theta}{\partial x}\,\mathrm{d}x\;\theta_j(t) - \int_0^L \beta\,M(c)\,\frac{\partial \varphi_i^\theta}{\partial x}\frac{\partial \varphi_j^\theta}{\partial x}\,\mathrm{d}x\;\theta_j^*(t)$$
$$= \int_0^L \varphi_i^\theta\,b\,\mathrm{d}x - \varphi_i^\theta\,h_{1D}\Big|_0^L\,.$$

6.2.1.3 Euler integration schemes

Using the forward finite difference approximation,

$$\frac{\partial c_j(t)}{\partial t} \approx \frac{c_j(t+\Delta t) - c_j(t)}{\Delta t}\,, \quad (6.79)$$

the discrete weak form leads to two alternative time integration schemes.

In the Forward Euler scheme (explicit), all terms are evaluated at the

known state $c(t)$:

$$\begin{aligned}
&\int_0^L \varphi_i^\theta \varphi_j^\theta \, \mathrm{d}x \; \frac{c_j(t+\Delta t)}{\Delta t} + \int_0^L \mathbb{D} \frac{\partial \varphi_i^\theta}{\partial x} \frac{\partial \varphi_j^\theta}{\partial x} \, \mathrm{d}x \; c_j(t+\Delta t) \\
&\quad - 2\,\frac{RT\chi}{c_{\max}} \int_0^L \frac{\partial \varphi_i^\theta}{\partial x} \, M(c(t)) \, \frac{\partial \varphi_j^\theta}{\partial x} \, \mathrm{d}x \; c_j(t+\Delta t) \\
&\quad + \int_0^L \beta \, M(c(t)) \, \frac{\partial \varphi_i^\theta}{\partial x} \frac{\partial \varphi_j^\theta}{\partial x} \, \mathrm{d}x \; \theta_j(t+\Delta t) \\
&\quad - \int_0^L \beta \, M(c(t)) \, \frac{\partial \varphi_i^\theta}{\partial x} \frac{\partial \varphi_j^\theta}{\partial x} \, \mathrm{d}x \; \theta_j^*(t+\Delta t) \\
&\quad = \int_0^L \varphi_i^\theta \varphi_j^\theta \, \mathrm{d}x \; \frac{c_j(t)}{\Delta t} + \int_0^L b \, \varphi_i^\theta \, \mathrm{d}x \; - \varphi_i^\theta \, h_{1D} \Big|_0^L .
\end{aligned} \tag{6.80}$$

In the Backward Euler scheme (implicit), all terms are evaluated at the unknown state $c(t+\Delta t)$, leading to a nonlinear problem:

$$\begin{aligned}
&\int_0^L \varphi_i^\theta \varphi_j^\theta \, \mathrm{d}x \; \frac{c_j(t+\Delta t)}{\Delta t} + \int_0^L \mathbb{D} \frac{\partial \varphi_i^\theta}{\partial x} \frac{\partial \varphi_j^\theta}{\partial x} \, \mathrm{d}x \; c_j(t+\Delta t) \\
&\quad - 2\,\frac{RT\chi}{c_{\max}} \int_0^L \frac{\partial \varphi_i^\theta}{\partial x} \, M(c(t+\Delta t)) \, \frac{\partial \varphi_j^\theta}{\partial x} \, \mathrm{d}x \; c_j(t+\Delta t) \\
&\quad + \int_0^L \beta \, M(c(t+\Delta t)) \, \frac{\partial \varphi_i^\theta}{\partial x} \frac{\partial \varphi_j^\theta}{\partial x} \, \mathrm{d}x \; \theta_j(t+\Delta t) \\
&\quad - \int_0^L \beta \, M(c(t+\Delta t)) \, \frac{\partial \varphi_i^\theta}{\partial x} \frac{\partial \varphi_j^\theta}{\partial x} \, \mathrm{d}x \; \theta_j^*(t+\Delta t) \\
&\quad = \int_0^L \varphi_i^\theta \varphi_j^\theta \, \mathrm{d}x \; \frac{c_j(t)}{\Delta t} + \int_0^L b \, \varphi_i^\theta \, \mathrm{d}x \; - \varphi_i^\theta \, h_{1D} \Big|_0^L .
\end{aligned} \tag{6.81}$$

6.2.1.4 Dimensionless form

To cast the Forward and Backward Euler formulations into dimensionless form, we use the normalized concentration θ, θ^* and the dimensionless diffusivity $\tilde{\mathbb{D}}$. Multiplying Eqs. (6.80) and (6.81) by the factor $\Delta t / c_{\max}\,\ell$, and recalling from Eq. (6.3) that

$$\frac{\Delta t}{c_{\max}\,\ell^2} \; \beta \, M(c(t)) = \tilde{\mathbb{D}} \, \frac{\beta}{RT} \; \theta(t) \; (1 - \theta(t)) \, , \tag{6.82}$$

we obtain the following discrete, dimensionless formulations.

When evaluated at the known state $\theta(t)$, the dimensionless Forward Euler

scheme reads:

$$\frac{1}{\ell}\int_0^L \varphi_i^\theta\varphi_j^\theta \,\mathrm{d}x\ \theta_j(t+\Delta t) + \tilde{\mathrm{D}}\,\ell\int_0^L \frac{\partial\varphi_i^\theta}{\partial x}\frac{\partial\varphi_j^\theta}{\partial x}\,\mathrm{d}x\ \theta_j(t+\Delta t) \tag{6.83}$$
$$+\tilde{\mathrm{D}}\left(\frac{\beta}{RT}-2\chi\right)\ell\int_0^L \varphi_k^\theta\theta_k(t)\left(1-\varphi_h^\theta\theta_h(t)\right)\frac{\partial\varphi_i^\theta}{\partial x}\frac{\partial\varphi_j^\theta}{\partial x}\,\mathrm{d}x\ \theta_j(t+\Delta t)$$
$$-\tilde{\mathrm{D}}\,\frac{\beta}{RT}\,\ell\int_0^L \varphi_k^\theta\theta_k(t)\left(1-\varphi_h^\theta\theta_h(t)\right)\frac{\partial\varphi_i^\theta}{\partial x}\frac{\partial\varphi_j^*}{\partial x}\,\mathrm{d}x\ \theta_j^*(t+\Delta t)$$
$$=\frac{1}{\ell}\int_0^L \varphi_i^\theta\varphi_j^\theta\,\mathrm{d}x\ \theta_j(t)+\frac{1}{\ell}\int_0^L\varphi_i^\theta\,\frac{\Delta t\,b(x,t)}{c_{\max}}\,\mathrm{d}x-\varphi_i^\theta\,\frac{\Delta t\,h_{1D}(x,t)}{c_{\max}\ell}\Big|_0^L.$$

When evaluated at the unknown state $\theta(t+\Delta t)$, the dimensionless Backward Euler scheme becomes nonlinear and is given by:

$$\frac{1}{\ell}\int_0^L \varphi_i^\theta\varphi_j^\theta \,\mathrm{d}x\ \theta_j(t+\Delta t) + \tilde{\mathrm{D}}\,\ell\int_0^L \frac{\partial\varphi_i^\theta}{\partial x}\frac{\partial\varphi_j^\theta}{\partial x}\,\mathrm{d}x\ \theta_j(t+\Delta t) \tag{6.84}$$
$$+\tilde{\mathrm{D}}\left(\frac{\beta}{RT}-2\chi\right)\ell\int_0^L \varphi_h^\theta\frac{\partial\varphi_i^\theta}{\partial x}\frac{\partial\varphi_j^\theta}{\partial x}\,\mathrm{d}x\ \theta_h(t+\Delta t)\,\theta_j(t+\Delta t)$$
$$-\tilde{\mathrm{D}}\left(\frac{\beta}{RT}-2\chi\right)\ell\int_0^L \varphi_h^\theta\varphi_k^\theta\frac{\partial\varphi_i^\theta}{\partial x}\frac{\partial\varphi_j^\theta}{\partial x}\,\mathrm{d}x\ \theta_h(t+\Delta t)\,\theta_k(t+\Delta t)\,\theta_j(t+\Delta t)$$
$$-\tilde{\mathrm{D}}\,\frac{\beta}{RT}\,\ell\int_0^L \varphi_h^\theta\frac{\partial\varphi_i^\theta}{\partial x}\frac{\partial\varphi_j^*}{\partial x}\,\mathrm{d}x\ \theta_h(t+\Delta t)\,\theta_j^*(t+\Delta t)$$
$$+\tilde{\mathrm{D}}\,\frac{\beta}{RT}\,\ell\int_0^L \varphi_h^\theta\varphi_k^\theta\frac{\partial\varphi_i^\theta}{\partial x}\frac{\partial\varphi_j^*}{\partial x}\,\mathrm{d}x\ \theta_h(t+\Delta t)\,\theta_k(t+\Delta t)\,\theta_j^*(t+\Delta t)$$
$$=\frac{1}{\ell}\int_0^L \varphi_i^\theta\varphi_j^\theta\,\mathrm{d}x\ \theta_j(t)+\frac{1}{\ell}\int_0^L\varphi_i^\theta\,\frac{\Delta t\,b(x,t)}{c_{\max}}\,\mathrm{d}x-\varphi_i^\theta\,\frac{\Delta t\,h_{1D}(x,t)}{c_{\max}\ell}\Big|_0^L.$$

6.2.2 Penalty constraint in dimensionless 1D weak form

The dimensionless 1D restriction of Eq. (6.64) reads

$$\theta-\theta^*+l^2\,\frac{\partial^2\theta^*}{\partial x^2}=0\,. \tag{6.85}$$

Denote by L the right end of the 1D domain, which starts at $x=0$. The weak form of Eq. (6.85) reads

$$\frac{1}{\ell}\int_0^L\varphi_i^*\,\theta\,\mathrm{d}x-\frac{1}{\ell}\int_0^L\varphi_i^*\,\theta^*\,\mathrm{d}x+\frac{1}{\ell}\int_0^L\varphi_i^*\,\frac{\partial}{\partial x}\left(l^2\frac{\partial\theta^*}{\partial x}\right)\mathrm{d}x=0\,. \tag{6.86}$$

Upon integration by parts, we obtain

$$\frac{1}{\ell}\int_0^L\varphi_i^*\,\theta\,\mathrm{d}x-\frac{1}{\ell}\int_0^L\varphi_i^*\,\theta^*\,\mathrm{d}x-\frac{l^2}{\ell^2}\,\ell\int_0^L\frac{\partial\varphi_i^*}{\partial x}\,\frac{\partial\theta^*}{\partial x}\,\mathrm{d}x+\frac{l^2}{\ell^2}\,\varphi_i^*\,\ell\,\frac{\partial\theta^*}{\partial x}\Big|_0^L=0\,. \tag{6.87}$$

Remark on boundary terms. Similarly to the discussion in Section 6.1.2.4, the penalty Eq. (6.87) does not represent a conservation law. Accordingly, no Dirichlet or Neumann boundary conditions are prescribed a priori. The boundary contribution

$$\frac{l^2}{\ell^2}\,\varphi_i^*\,\ell\,\frac{\partial\theta^*}{\partial x}\Big|_0^L \tag{6.88}$$

shall therefore be evaluated over the whole boundary.

In many publications, however, as well as in manufactured solutions, this term is given as data. We shall denote this approach as "Neumann kind." In view of Eq. (6.72), the prescribed contribution (6.88) may be equivalently expressed as

$$\varphi_i^*\,\frac{\lambda}{\beta\ell^2}\,\ell\,h_{1D}^*\Big|_0^L. \tag{6.89}$$

Remark on physical interpretation. It follows that

$$\frac{\lambda}{\beta\,\ell^2} = \frac{l^2}{\ell^2}\,. \tag{6.90}$$

Here, λ is the gradient energy coefficient, setting an intrinsic length scale associated with the diffuse interface thickness. The interfacial width at a given temperature is thus determined by the parameters λ and χ in the free energy. The constant β represents the penalty coefficient, while l is an inner length parameter introduced in Section 6.2. Physically, l controls the strength of the constraint linking c and c^*, with the penalty enforcing $c^* \to c$ as $l \to 0^+$ (equivalently, $\beta \to \infty$).

6.2.2.1 Separated variables discretization

$$\theta(x,t) = \sum_j \varphi_j^\theta(x)\,\theta_j(t), \qquad \theta^*(x,t) = \sum_j \varphi_j^*(x)\,\theta_j^*(t). \tag{6.91}$$

Replacing into Eq. (6.87) (the dimensionless weak form of the penalty constraint), and using Eq. (6.90), we obtain the following discrete statements (Einstein summation implied).

The 1D discrete dimensionless weak form with Neumann-kind boundary conditions is given by:

$$\begin{aligned}&\frac{1}{\ell}\int_0^L \varphi_i^*\varphi_j^\theta\,\mathrm{d}x\;\theta_j(t+\Delta t) - \frac{1}{\ell}\int_0^L \varphi_i^*\varphi_j^*\,\mathrm{d}x\;\theta_j^*(t+\Delta t)\\ &\quad - \frac{\lambda}{\beta\ell^2}\,\ell\int_0^L \frac{\partial\varphi_i^*}{\partial x}\,\frac{\partial\varphi_j^*}{\partial x}\,\mathrm{d}x\;\theta_j^*(t+\Delta t) \;+\; \frac{\lambda}{\beta\ell^2}\,\varphi_i^*\,\ell\,h_{1D}^*\Big|_0^L \;=\; 0\,,\end{aligned} \tag{6.92}$$

where $h^*_{1D} = \partial\theta^*/\partial x$ (see Eq. (6.72)) is prescribed on the boundary (Neumann-kind treatment).

The 1D discrete dimensionless weak form with natural boundary terms included is expressed as:

$$\frac{1}{\ell}\int_0^L \varphi_i^*\varphi_j^\theta \,\mathrm{d}x\; \theta_j(t+\Delta t) - \frac{1}{\ell}\int_0^L \varphi_i^*\varphi_j^* \,\mathrm{d}x\; \theta_j^*(t+\Delta t) \\ - \frac{\lambda}{\beta\ell^2}\,\ell\int_0^L \frac{\partial\varphi_i^*}{\partial x}\frac{\partial\varphi_j^*}{\partial x}\,\mathrm{d}x\; \theta_j^*(t+\Delta t) \;+\; \frac{\lambda}{\beta\ell^2}\,\varphi_i^*\,\ell\,\frac{\partial\varphi_j^*}{\partial x}\,\theta_j^*(t+\Delta t)\Big|_0^L \;=\; 0\,, \tag{6.93}$$

which retains the natural boundary term in terms of $\partial\theta^*/\partial x$.

6.2.3 Governing equations and numerical solution of the Neumann kind problem

6.2.3.1 Newton–Raphson scheme for θ

Equation (6.84) can be expressed in compact form as

$$\mathcal{R}_\theta({\theta^*}_j(t+\Delta t),\theta_j(t+\Delta t)) = \;\mathcal{A}_\theta({\theta^*}_j(t+\Delta t),\theta_j(t+\Delta t)) \\ + \tilde{\mathrm{D}}\left(\frac{\beta}{RT} - 2\,\chi\right)\,\ell\int_0^L \varphi_h^\theta\,\frac{\partial\varphi_i^\theta}{\partial x}\frac{\partial\varphi_j^\theta}{\partial x}\,\mathrm{d}x\;\theta_h(t+\Delta t)\,\theta_j(t+\Delta t) \\ - \tilde{\mathrm{D}}\left(\frac{\beta}{RT} - 2\,\chi\right)\,\ell\int_0^L \varphi_h^\theta\,\varphi_k^\theta\,\frac{\partial\varphi_i^\theta}{\partial x}\frac{\partial\varphi_j^\theta}{\partial x}\,\mathrm{d}x\;\;\theta_h(t+\Delta t)\,\theta_k(t+\Delta t)\,\theta_j(t+\Delta t) \\ - \tilde{\mathrm{D}}\,\frac{\beta}{RT}\,\ell\int_0^L \varphi_h^\theta\,\frac{\partial\varphi_i^\theta}{\partial x}\frac{\partial\varphi_j^*}{\partial x}\,\mathrm{d}x\;\;\theta_h(t+\Delta t)\,\theta_j^*(t+\Delta t) \\ + \tilde{\mathrm{D}}\,\frac{\beta}{RT}\,\ell\int_0^L \varphi_h^\theta\,\varphi_k^\theta\,\frac{\partial\varphi_i^\theta}{\partial x}\frac{\partial\varphi_j^*}{\partial x}\,\mathrm{d}x\;\theta_h(t+\Delta t)\,\theta_k(t+\Delta t)\,\theta_j^*(t+\Delta t) \\ +\;\mathcal{B}_\theta\;=0, \tag{6.94}$$

with

$$\mathcal{B}_\theta = -\frac{1}{\ell}\int_0^L \varphi_i^\theta\varphi_j^\theta\,\mathrm{d}x\;\frac{\theta_j(t)}{\Delta t} - \frac{1}{\ell}\int_0^L \varphi_i^\theta\,\frac{\Delta t\,b(x,t)}{c_{\max}}\,\mathrm{d}x + \varphi_i^\theta\,\frac{\Delta t\,h_{1D}(x,t)}{c_{\max}\ell}\Big|_0^L. \tag{6.95}$$

Linearization is performed by applying the Gateaux derivative, which yields the Jacobian contributions required for the Newton–Raphson iteration. For completeness, the full expansion of these Jacobian terms is reported in Appendix A.2.

6.2.3.2 Newton–Raphson scheme for θ^*

Analogously, Eq. (6.92) can be recast in compact residual form as

$$\mathcal{R}_{\theta^*}(\theta_j^*(t+\Delta t),\theta_j(t+\Delta t)) = \mathcal{A}_{\theta^*}(\theta_j^*(t+\Delta t),\theta_j(t+\Delta t)) + \mathcal{B}_{\theta^*} = 0\ , \tag{6.96}$$

with

$$\mathcal{B}_{\theta^*} = \frac{\lambda}{\beta\ell^2}\,\varphi_i^*\,\ell\,h_{1D}^*\Big|_0^L, \tag{6.97}$$

and $\mathcal{A}_{\theta^*}$ defined by comparison. The Newton–Raphson scheme follows from the Gateaux derivative:

$$\frac{\partial}{\partial\epsilon}\mathcal{R}_{\theta^*}(\theta_j^*+\epsilon\delta\theta_j^*,\theta_j+\epsilon\delta\theta_j)\Big|_{\epsilon=0} = \mathcal{A}_{\theta^*}(\delta\theta_j^*,\delta\theta_j) = -\mathcal{R}_{\theta^*}(\theta_j^*(t+\Delta t),\theta_j(t+\Delta t)). \tag{6.98}$$

For completeness, the derivation of the governing equations and Newton–Raphson scheme of the full problem (without the Neumann simplification) is reported in Appendix A.3.

6.2.4 Manufactured solutions

To validate the weak form and penalty formulation, a manufactured solution is adopted. We consider the concentration field

$$\theta(x,t) = \frac{t}{\overline{t}}\left(\overline{\alpha}+\overline{\beta}\frac{x}{L}\right)\ , \tag{6.99}$$

as already introduced in Eq. (6.44).

The corresponding flux reads

$$\frac{\Delta t\,h_{1D}(x,t)}{c_{\max}\,\ell} = \frac{t}{\overline{t}}\frac{\ell}{L}\,\tilde{\mathrm{D}}\,\overline{\beta}\,\left[-1+2\,\frac{t}{\overline{t}}\left(\overline{\alpha}+\overline{\beta}\frac{x}{L}\right)\left(1-\frac{t}{\overline{t}}\left(\overline{\alpha}+\overline{\beta}\frac{x}{L}\right)\right)\chi\right]. \tag{6.100}$$

Furthermore, from Eq. (6.72) we obtain the penalty flux

$$\ell\,h_{1D}^* = \ell\,\frac{\partial\theta^*}{\partial x} = \overline{\beta}\,\frac{t}{\overline{t}}\,\frac{\ell}{L}\ . \tag{6.101}$$

The mass supply $b(x,t)$ is derived from the mass balance equation and yields

$$\frac{\Delta t\;b(x,t)}{c_{\max}} = \frac{\Delta t}{\overline{t}}\left(\overline{\alpha}+\overline{\beta}\frac{x}{L}\right) + 2\chi\,\tilde{\mathrm{D}}\left(\overline{\beta}\,\frac{t}{\overline{t}}\,\frac{\ell}{L}\right)^2\left[1-2\,\frac{t}{\overline{t}}\left(\overline{\alpha}+\overline{\beta}\frac{x}{L}\right)\right]. \tag{6.102}$$

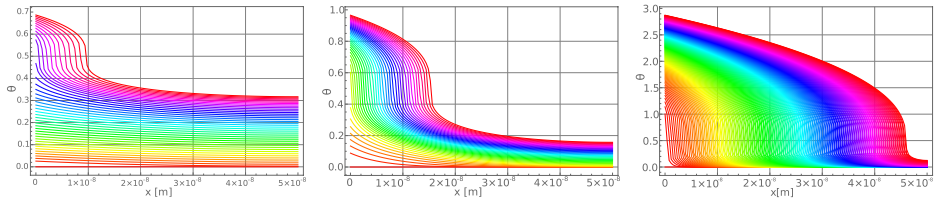

(a) $\mathbb{D} = 10^{-14}$. (b) $\mathbb{D} = 10^{-15}$. (c) $\mathbb{D} = 10^{-16}$.

Figure 6.1: Concentration evolution for three values of the diffusivity, with $\chi = 2$ and $\beta/RT = 1$.

6.2.5 Numerical results of the Neumann kind problem

Based on Eq. (6.84), the dimensionless parameters governing the numerical solution are the scaled diffusivity $\tilde{\mathbb{D}}$, the Flory–Huggins parameter χ, and the ratio β/RT. The latter vanishes when the interface energy λ is zero, since $\beta = \lambda l^{-2}$. With a uniform mesh of element size e_ℓ, all integrals scale

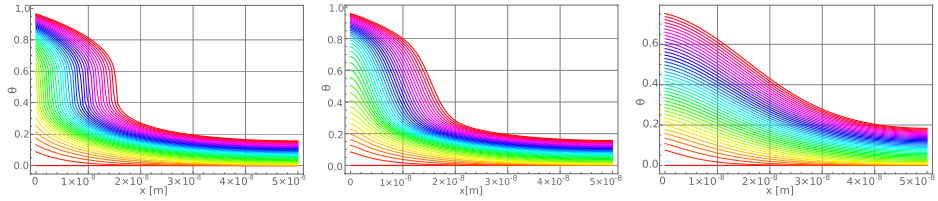

(a) $l = 0.001\ell$. (b) $l = 0.01\ell$. (c) $l = 0.1\ell$.

Figure 6.2: Influence of the internal length l on the diffuse–interface width at fixed $\mathbb{D} = 10^{-15}$, $\chi = 2$, $\beta = 8RT$, and varying l (hence $\lambda = \beta l^2$).

with e_ℓ or $1/e_\ell$, leading to the effective dimensionless diffusivity

$$\tilde{\mathbb{D}}^* = \tilde{\mathbb{D}}\,(\frac{\ell}{e_\ell})^2 = \frac{\mathbb{D}\,\Delta t}{e_\ell^2}. \tag{6.103}$$

Setup. Under this setting, we take $L = \ell = 5.0 \times 10^{-8}\,\mathrm{m} = 50\,\mathrm{nm}$ and study an alloying problem where a prescribed flux ($10^{-3}\,\mathrm{mol\ m^{-2}s^{-1}}$, arbitrarily chosen) enters the domain at $x = 0$, while no flow occurs at $x = L$. The mesh resolution is $e_\ell = \ell/128$, the final time $t_f = 2\,\mathrm{s}$, and the time step is chosen to satisfy $\mathbb{D}\,\Delta t\, e_\ell^{-2} < 1$.

Figure 6.1 shows higher diffusivity leads to rapid homogenization, whereas lower diffusivity preserves sharper concentration gradients, emphasizing the role of $\tilde{\mathbb{D}}$.

Figure 6.2 investigates the role of the internal length l. Since $\lambda = \beta l^2$,

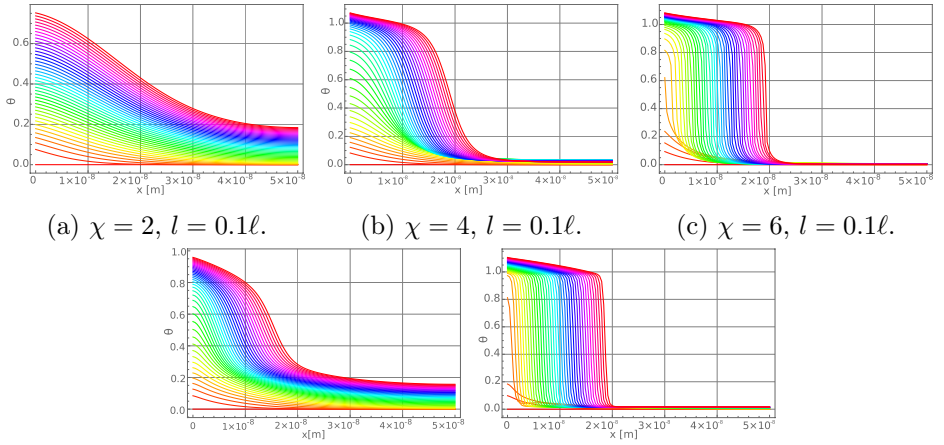

(a) $\chi = 2$, $l = 0.1\ell$. (b) $\chi = 4$, $l = 0.1\ell$. (c) $\chi = 6$, $l = 0.1\ell$.

(d) $\chi = 2$, $l = 0.01\ell$. (e) $\chi = 4$, $l = 0.01\ell$.

Figure 6.3: Combined effect of the Flory–Huggins interaction χ and the internal length l on concentration profiles at fixed $\mathbb{D} = 10^{-15}$, $\beta = 8RT$, and varying χ and l.

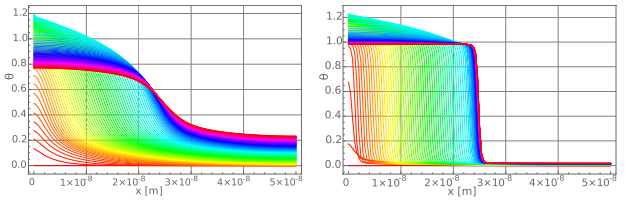

(a) $\chi = 2$. (b) $\chi = 4$.

Figure 6.4: Load–relaxation sequence at fixed $\mathbb{D} = 10^{-15}$, $\beta = 8RT$, $l = 0.01\ell$. A constant influx is applied at $x = 0$ for $0 \le t \le 1\,\mathrm{s}$, followed by open-circuit relaxation ($J = 0$) until $t_f = 2\,\mathrm{s}$; no-flux at $x = L$.

increasing l broadens the diffuse interface, while smaller l recovers sharper fronts.

Figure 6.3 compares cases with varying χ and l. Increasing χ strengthens phase segregation, producing more distinct concentration plateaus. The interface sharpness remains primarily governed by l.

We finally consider a load–relaxation experiment (Figures 6.4–6.5). During charging, species accumulate near the inflow boundary. When the inflow is suddenly stopped at $t = 0.5\,t_{sat}$, the system relaxes toward equilibrium by redistributing species and shifting the interface. Larger χ slows relaxation due to stronger phase separation.

Figure 6.5a confirms mass conservation: the inserted mass matches the integral of concentration over the domain. Figure 6.5b shows redistribution

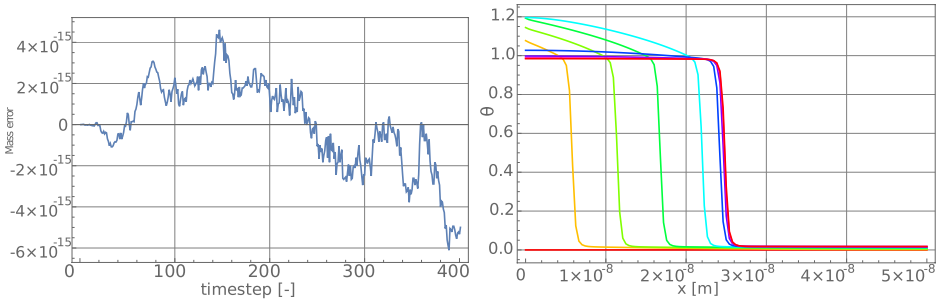

(a) Dimensionless mass error. (b) Mass accumulation.

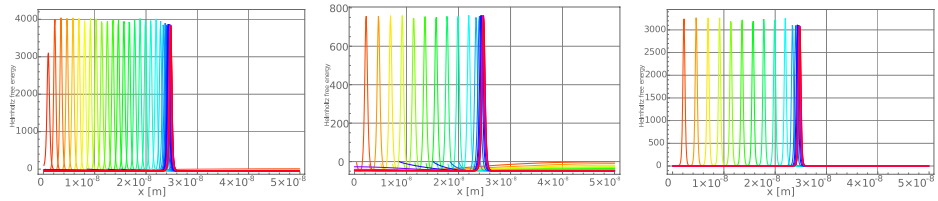

(c) $\psi_R/c_{\max}$. (d) $\psi_R^{tr}/c_{\max}$. (e) $\psi_R^{int}/c_{\max}$.

Figure 6.5: Load–relaxation experiment at $\mathrm{Pe} = 10^{-15}$, $\beta = 8RT$, $\chi = 4$, $l = 0.01\ell$. Helmholtz free energy decomposition during charging ($t = 1$ s) and relaxation ($t_f = 2$ s).

after inflow stops, with the interface moving toward the center as the system approaches a half-filled equilibrium. Figures 6.5c–6.5e decompose the Helmholtz free energy into reference, transport, and interfacial contributions, revealing how energetic terms evolve during relaxation.

6.3 Minimal 1D frameworks for mechanics and chemo–mechanical coupling

6.3.1 A minimal 1D mechanical problem description

This section establishes a baseline 1D mechanical model that isolates the elastic response to chemically induced swelling, excluding feedback from diffusion. We (i) define a slender-axis kinematics suitable for a cylindrical particle, (ii) prescribe isotropic chemical swelling via the multiplicative split, (iii) adopt a Saint–Venant elastic free energy to obtain stresses, and (iv) derive the dimensionless weak form of the 1D balance of momentum together with its Newton–Raphson linearization. This one-way setting (concentration $\rightarrow$ mechanics) serves as the reference against which the fully two-way coupled problem in Section 6.3.2 is built.

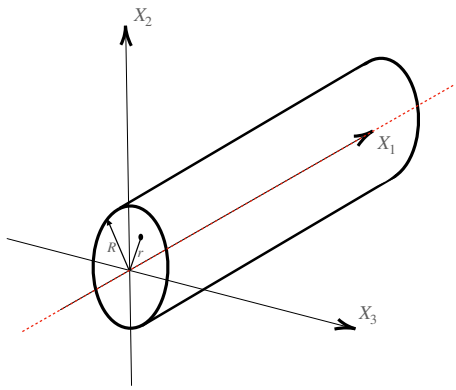

Figure 6.6: Schematic of the 1D cylindrical domain adopted for the mechanical problem.

6.3.1.1 Kinematics

Consider a cylindrical domain of radius R, as shown in Figure 6.6. We introduce a displacement field that captures both axial and radial deformations, namely

$$\vec{u} = u_1(X_1)\,\vec{e}_1 + g(X_1)\,f(r)\,\vec{e}_r, \tag{6.104}$$

with $r = \sqrt{X_2^2 + X_3^2}$ and $f(0) = 0$ to enforce axial symmetry with respect to the axis $X_2 = X_3 = 0$.

Focusing on a one-dimensional approximation of the cylinder, i.e. taking

$R \to 0^+$, we expand $f(r)$ in Taylor series:

$$f(r) = f(0) + \left.\frac{\partial f}{\partial r}\right|_0 r + o(r^2),$$

and write

$$\vec{u} = u_1(X_1)\,\vec{e}_1 + g(X_1)\,\left.\frac{\partial f}{\partial r}\right|_0 r\,\vec{e}_r. \tag{6.105}$$

Since $r\,\vec{e}_r = \sum_{k=2}^{3} X_k\,\vec{e}_k$, the displacement field becomes

$$\vec{u} = u_1(X_1)\,\vec{e}_1 + g(X_1)\,\left.\frac{\partial f}{\partial r}\right|_0 \sum_{k=2}^{3} X_k\,\vec{e}_k. \tag{6.106}$$

The deformation gradient along the axis $X_2 = X_3 = 0$ is then

$$\boldsymbol{F} = \mathbb{1} + \frac{\partial u_1}{\partial X_1}\vec{e}_1 \otimes \vec{e}_1 + g(X_1)\,\left.\frac{\partial f}{\partial r}\right|_0 \sum_{k=2}^{3} \vec{e}_k \otimes \vec{e}_k. \tag{6.107}$$

6.3.1.2 Chemical swelling and elastic response

The alloying of sodium with tin to form $\mathrm{Na}_x\mathrm{Sn}$ induces volumetric deformation. This is modeled through the multiplicative decomposition of the deformation gradient:

$$\boldsymbol{F} = \boldsymbol{F}^e\boldsymbol{F}^c, \tag{6.108}$$

where $\boldsymbol{F}^c$ represents the isotropic chemical swelling tensor,

$$\boldsymbol{F}^c = \mathbb{1}\,\sqrt[3]{J^c}, \qquad J^c = \det \boldsymbol{F}^c = 1 + c_R(\vec{X}, t)\,\Omega. \tag{6.109}$$

Here Ω is the partial molar volume and c_R the referential concentration. The elastic part $\boldsymbol{F}^e$ accounts for the mechanical response of the alloy[1]. Note that in this minimal formulation, plastic deformation is neglected, so the total deformation gradient is decomposed only into elastic and chemical swelling parts.

From Eqs. (6.107) and (6.109), one finds

$$\boldsymbol{F}^e = \boldsymbol{F}\boldsymbol{F}^{c-1} = \left[\left(1 + \frac{\partial u_1}{\partial X_1}\right)\vec{e}_1\otimes\vec{e}_1 + \left(1 + g(X_1)\,\left.\frac{\partial f}{\partial r}\right|_0\right)\sum_{k=2}^{3}\vec{e}_k\otimes\vec{e}_k\right] J^{c-1/3}. \tag{6.110}$$

Accordingly, the elastic right Cauchy–Green tensor is

$$\boldsymbol{C}^e = \boldsymbol{F}^{e\mathsf{T}}\boldsymbol{F}^e = \left[\left(1 + \frac{\partial u_1}{\partial X_1}\right)^2\vec{e}_1\otimes\vec{e}_1 + \left(1 + g(X_1)\,\left.\frac{\partial f}{\partial r}\right|_0\right)^2\sum_{k=2}^{3}\vec{e}_k\otimes\vec{e}_k\right] J^{c-2/3}. \tag{6.111}$$

[1] As remarked in [115], the intermediate configuration defined through $\boldsymbol{F}^c$ is a theoretical construct, as it does not satisfy geometrical compatibility.

6.3.1.3 Thermodynamics

Thermodynamic formulations have been developed following the traditional framework of [115], which combines the energy balance, entropy imbalance, Clausius–Duhem inequality, and Coleman–Noll procedure. Here we restrict attention to a minimal setting, where the referential Helmholtz free energy depends on the referential concentration and the Green–Lagrange strain tensor. By choosing the referential Helmholtz free energy density ψ_R as the thermodynamic potential, the second Piola–Kirchhoff stress $\boldsymbol{S}$ is obtained as

$$\boldsymbol{S} = \frac{\partial \psi_R}{\partial \boldsymbol{E}}\,, \tag{6.112}$$

with $\boldsymbol{E}$ the Green–Lagrange tensor and c_R the referential concentration.

The Helmholtz free energy is additively decomposed as

$$\psi_R(c_R, \boldsymbol{E}) = \psi_R^{en}(c_R) + \psi_R^{mech}(c_R, \boldsymbol{E}), \tag{6.113}$$

with ψ_R^{en} Eq. (6.24) and ψ_R^{mech} the mechanical contribution. The mechanical free energy density is derived from an elastic response, namely

$$\psi_R^{mech}(c_R, \boldsymbol{E}) = J^c\, \psi_R^{el}(\boldsymbol{E}^e), \tag{6.114}$$

where

$$\boldsymbol{E} = \tfrac{1}{2}(\boldsymbol{C} - \mathbb{1}), \tag{6.115}$$

is the Green–Lagrange tensor, and

$$\boldsymbol{C} = \boldsymbol{F}^{\mathsf{T}}\boldsymbol{F}, \tag{6.116}$$

is the right Cauchy–Green tensor, and

$$\boldsymbol{E}^e = J^{c^{-2/3}}\boldsymbol{E} + \tfrac{1}{2}(1 - J^{c^{-2/3}})\mathbb{1}, \tag{6.117}$$

is the elastic Green–Lagrange tensor. The elastic energy is assumed of Saint–Venant type:

$$\psi_R^{el}(\boldsymbol{E}^e) = \tfrac{1}{2}\left\{\lambda\ \mathrm{tr}\,\boldsymbol{E}^{e2} + 2\,G\,||\boldsymbol{E}^e||^2\right\}, \tag{6.118}$$

where λ and G are the Lamé parameters, related to the Young modulus E and Poisson ratio ν and

$$\mathrm{tr}\,\boldsymbol{E}^e = \tfrac{1}{2}\left(\mathrm{tr}\,\boldsymbol{C}^e - 3\right), \tag{6.119}$$

$$\mathrm{tr}\,\boldsymbol{C}^e = J^{c-2/3}\left[\left(1 + \frac{\partial u_1}{\partial X_1}\right)^2 + 2\left(1 + g(X_1)\,\left.\frac{\partial f}{\partial r}\right|_0\right)^2\right], \tag{6.120}$$

where $\boldsymbol{C}^e$ is the elastic right Cauchy–Green tensor. Specializing the stress components (see Appendix A.8) under the assumed kinematics leads to

$$\boldsymbol{S}^e_{11} = -\frac{3\lambda+2G}{2}+\frac{\lambda+2G}{2}J^{c^{-2/3}}\left(1+\frac{\partial u_1}{\partial X_1}\right)^2+\lambda J^{c^{-2/3}}\left(1+g(X_1)\left.\frac{\partial f}{\partial r}\right|_0\right)^2, \tag{6.121}$$

$$\boldsymbol{S}^e_{22} = \boldsymbol{S}^e_{33} = -\frac{3\lambda+2G}{2}+\frac{\lambda}{2}J^{c^{-2/3}}\left(1+\frac{\partial u_1}{\partial X_1}\right)^2+(\lambda+G)J^{c^{-2/3}}\left(1+g(X_1)\left.\frac{\partial f}{\partial r}\right|_0\right)^2 \tag{6.122}$$

The choice of the factor $g(X_1)\left.\frac{\partial f}{\partial r}\right|_0$ in Eq. (6.105) is influenced by the boundary conditions. One may impose incompressibility ($\det \boldsymbol{F} = 1$) or free lateral expansion ($\boldsymbol{S}^e_{22} = \boldsymbol{S}^e_{33} = 0$).

In the following we adopt the latter condition, consistent with unconstrained radial swelling of tin particles.

Defining

$$\aleph(\vec{X}, c) = J^{c-1/3}\left(1+\frac{\partial u_1}{\partial X_1}\right), \tag{6.123}$$

the stress component $\boldsymbol{S}^e_{11}$

$$\boldsymbol{S}^e_{11} = \frac{E}{2}\left[\aleph(\vec{X}, c)^2 - 1\right]. \tag{6.124}$$

Finally, the second Piola–Kirchhoff stress can be written as

$$\boldsymbol{S} = J^c \boldsymbol{F}^{c-1}\,\boldsymbol{S}^e\,\boldsymbol{F}^{c-\mathsf{T}} = J^{c1/3}\,\boldsymbol{S}^e_{11}\,\vec{e}_1\otimes\vec{e}_1, \tag{6.125}$$

from which the first Piola–Kirchhoff stress follows as

$$\boldsymbol{P} = \frac{E}{2}J^{c2/3}\,\aleph(\vec{X}, c)\left[\aleph(\vec{X}, c)^2 - 1\right]\vec{e}_1\otimes\vec{e}_1. \tag{6.126}$$

This expression highlights the coupling between chemical swelling (J^c) and elastic response in the axial stress state.

6.3.1.4 Momentum balance equation

The balance of linear momentum in referential form reads

$$\nabla\cdot\boldsymbol{P} + \vec{B} = \vec{0}\,. \tag{6.127}$$

Specializing Eq. (6.127) to the 1D minimal restriction, the weak form simplifies considerably. In dimensionless form, obtained by multiplying by G^{-1}

and introducing the scaled displacement $\upsilon_j = u_j/\ell$, it reads

$$\mathcal{R}_u(\theta_j, \upsilon_j) = \frac{1}{2}\,\frac{E}{G}\int_0^L \frac{\partial \varphi_i}{\partial X_1}\, J^{c2/3}\, \aleph(\theta_j, \upsilon_j)\left[\aleph(\theta_j, \upsilon_j)^2 - 1\right] \mathrm{d}X_1 \qquad (6.128)$$
$$- \frac{1}{\ell}\int_0^L \varphi_i\,\frac{B_1 \ell}{G}\,\mathrm{d}X_1 - \varphi_i\,\frac{\overline{p}}{G}\,\Big|_0^L = 0\,,$$

with $\overline{p}$ the boundary traction (evaluated only on the Neumann boundary). The coupling term is

$$\aleph(\theta_j, \upsilon_j) = \left(1 + \Omega\, c_{\max}\, \varphi_h^{\theta}\theta_h\right)^{-1/3}\left(1 + \ell\,\frac{\partial \varphi_j^u}{\partial X_1}\,\upsilon_j\right), \qquad (6.129)$$

which encodes the effect of chemical swelling (J^c) combined with the axial stretch.

The nonlinear residual (6.128) is solved iteratively using the Newton–Raphson method. The step-by-step linearization of $\mathcal{R}_u$ via the Gateaux derivative, together with the explicit expressions for the consistent tangent, is provided in Appendix A.4.

6.3.2 A minimal two-way coupled 1D problem

6.3.2.1 Chemo-mechanical potential equations

While the formulation captured in one-way coupling, namely the influence of concentration on mechanics via the swelling deformation, here we extend it to a fully two-way coupling by incorporating the mechanical contribution to the referential chemical potential.

We retain the kinematic setting of Section 6.3.1.1 and the multiplicative split of the deformation gradient, as introduced in Eqs. (6.108)–(6.109), where the second Piola–Kirchhoff stress and the total chemical potential are obtained from the Helmholtz free energy via Eqs. (6.112)–(6.22). Here, we focus specifically on the mechanical contribution to the chemical potential, μ^{mech},

$$\mu = \mu^{tr} + \mu^{int} + \mu^{mech} \,, \tag{6.130}$$

where the first two contributions, which are transport and interfacial terms, are derived in Section 6.1.2, and the additional contribution,

$$\mu^{mech} = \frac{\partial \psi_R^{mech}(c_R, \boldsymbol{E})}{\partial c_R} \,, \tag{6.131}$$

is the chemo–mechanical potential.

Using

$$\psi_R^{mech}(c_R, \boldsymbol{E}) = J^c(c_R)\, \psi_R^{el}(\boldsymbol{E}^e(c_R, \boldsymbol{E}))\,, \tag{6.132}$$

with Eq. 6.117 the chemo–mechanical potential becomes

$$\begin{aligned} \mu^{mech}(c_R, \boldsymbol{E}) &= \frac{\partial J^c}{\partial c_R}\, \psi_R^{el}(\boldsymbol{E}^e) + J^c\, \frac{\partial \psi_R^{el}(\boldsymbol{E}^e)}{\partial \boldsymbol{E}^e} : \frac{\partial \boldsymbol{E}^e}{\partial c_R} \\ &= \Omega\, \psi_R^{el}(\boldsymbol{E}^e) - \tfrac{1}{3}\, \Omega\, \boldsymbol{S}^e : \boldsymbol{C}^e \,, \end{aligned} \tag{6.133}$$

where $\boldsymbol{S}^e$ is the elastic second Piola–Kirchhoff stress, and a Saint–Venant type elastic free energy $\psi_R^{el}(\boldsymbol{E}^e)$ is introduced in Eq. (6.118). Thus,Eq. (6.133) specializes to

$$\mu^{mech} = \Omega \left\{ \tfrac{\lambda}{2}\ \mathrm{tr}\, \boldsymbol{E}^{e2} + G\, ||\boldsymbol{E}^e||^2 - \tfrac{1}{3}\, \boldsymbol{S}^e : \boldsymbol{C}^e \right\}. \tag{6.134}$$

Equation (6.134) shows explicitly how elastic energy storage and stress–strain coupling contribute directly to the driving force for diffusion, thereby completing the two-way chemo–mechanical interaction.

By defining the chemo-mechanical potential as in Eq. (6.134), we obtain in compact form

$$\gamma(X_1, t) = E\, \frac{\Omega}{\mu_{\mathrm{ref}}} \left\{ \alpha_4\, \aleph(c_R, u_1)^4 + \alpha_2\, \aleph(c_R, u_1)^2 + \frac{1}{8} \right\}, \tag{6.135}$$

with $\aleph(c_R, u_1)$ as defined in Eq. (6.123) and coefficients

$$\alpha_4 = -\frac{12\nu^2 + \nu + 1}{24(\nu+1)}\,, \qquad \alpha_2 = \frac{6\nu^2 + 5\nu - 1}{12(\nu+1)}\,.$$

Equation (6.135) follows from the full algebraic expansion of $\operatorname{tr} \boldsymbol{E}^e$, $\boldsymbol{E}^e \cdot \boldsymbol{E}^e$, and $\boldsymbol{S}^e \cdot \boldsymbol{C}^e$, which is reported in Appendix A.9 for completeness.

At the initial condition ($\aleph = 1$, i.e., vanishing displacements and concentrations), Eq. (6.135) consistently reduces to

$$\gamma(X_1, t)|_{\aleph=1} = \frac{\nu\, G\, \Omega}{\mu_{\text{ref}}}.$$

6.3.2.2 Mass balance equation

The mass balance equation reads as usual

$$\frac{\partial c_R}{\partial t} + \nabla \cdot \vec{h} = b\,, \tag{6.136}$$

with flux

$$\vec{h} = -M(c_R)\nabla\mu = -\mathbb{\Phi}\, \nabla c_R - M(c_R)\, \nabla \mu^{int}(c_R) - M(c_R)\, \nabla \mu^{mech}. \tag{6.137}$$

Here $M(c_R)$, $\mathbb{\Phi}$, and $\mu^{int}(c_R)$ are defined in Eq. (6.3), Eq. (6.61), and Eq. (6.28), respectively, while μ^{mech} is given by Eq. (6.133).

Using the penalty operator splitting approach of Section 6.2, an auxiliary variable c_R^* is introduced, so that the flux is approximated as

$$\vec{h}(c_R, c_R^*, \vec{u}) = -\mathbb{\Phi}\, \nabla c_R - \beta\, M(c_R)\, \nabla\left(\frac{c_R - c_R^*}{c_{\max}}\right) - M(c_R)\, \nabla \mu^{mech}(c_R, \vec{u}), \tag{6.138}$$

$$c_R - c_R^* = -l^2 \nabla^2 c_R^*, \tag{6.139}$$

$$\mu^{mech}(c_R, \vec{u}) = \Omega \left\{ \psi_R^{el}(\boldsymbol{E}^e) - \tfrac{1}{3}\, \boldsymbol{S}^e : \boldsymbol{C}^e \right\}. \tag{6.140}$$

The mass balance equation therefore becomes

$$\frac{\partial c_R}{\partial t} - \nabla\cdot(\mathbb{\Phi}\nabla c_R) - \nabla\cdot\Big(\beta\, M(c_R)\nabla\tfrac{c_R - c_R^*}{c_{\max}}\Big) - \nabla\cdot\Big(M(c_R)\nabla\mu^{mech}(c_R, \vec{u})\Big) = b. \tag{6.141}$$

In 1D form this reduces to

$$\begin{aligned} &\frac{\partial c_R}{\partial t} - \frac{\partial}{\partial X_1}\left(\mathbb{\Phi}\frac{\partial c_R}{\partial X_1}\right) - \frac{\partial}{\partial X_1}\Big(\beta\, M(c_R)\Big(\tfrac{\partial\theta}{\partial X_1} - \tfrac{\partial\theta^*}{\partial X_1}\Big)\Big) \\ &\quad - \frac{\partial}{\partial X_1}\left(M(c_R)\frac{\partial \mu^{mech}}{\partial X_1}\right) = b\,. \end{aligned} \tag{6.142}$$

For convenience we define

$$h_{1D}^{*} = \frac{\partial \theta^{*}}{\partial X_1} \,, \tag{6.143}$$

$$h_{1D}^{mech} = -M(c_R)\,\frac{\partial \mu^{mech}}{\partial X_1} \,, \tag{6.144}$$

so that the total flux reads

$$h_{1D} = -\mathbb{P}\,\frac{\partial c_R}{\partial X_1} - \beta\, M(c_R)\left(\frac{\partial \theta}{\partial X_1} - \frac{\partial \theta^{*}}{\partial X_1}\right) + h_{1D}^{mech}. \tag{6.145}$$

6.3.2.2.1 1D Weak form

Let L be the right end of the 1D reference configuration, with $X_1 \in [0, L]$. The weak form of Eq. (6.142) reads

$$\begin{aligned} &\int_0^L \varphi_i^{\theta}\,\frac{\partial c_R}{\partial t}\,\mathrm{d}X_1 - \int_0^L \varphi_i^{\theta}\,\frac{\partial}{\partial X_1}\left(\mathbb{P}\,\frac{\partial c_R}{\partial X_1}\right)\mathrm{d}X_1 \\ &\quad - \int_0^L \varphi_i^{\theta}\,\frac{\partial}{\partial X_1}\left(\beta\, M(c_R)\left(\tfrac{\partial \theta}{\partial X_1} - \tfrac{\partial \theta^{*}}{\partial X_1}\right)\right)\mathrm{d}X_1 \\ &\quad - \int_0^L \varphi_i^{\theta}\,\frac{\partial}{\partial X_1}\left(M(c_R)\,\frac{\partial \mu^{mech}}{\partial X_1}\right)\mathrm{d}X_1 = \int_0^L \varphi_i^{\theta}\, b\,\mathrm{d}X_1 \,. \end{aligned} \tag{6.146}$$

Integration by parts yields

$$\begin{aligned} &\int_0^L \varphi_i^{\theta}\,\frac{\partial c_R}{\partial t}\,\mathrm{d}X_1 + \int_0^L \frac{\partial \varphi_i^{\theta}}{\partial X_1}\,\mathbb{P}\,\frac{\partial c_R}{\partial X_1}\,\mathrm{d}X_1 + \int_0^L \frac{\partial \varphi_i^{\theta}}{\partial X_1}\,\beta\, M(c_R)\left(\tfrac{\partial \theta}{\partial X_1} - \tfrac{\partial \theta^{*}}{\partial X_1}\right)\mathrm{d}X_1 \\ &\quad + \int_0^L \frac{\partial \varphi_i^{\theta}}{\partial X_1}\, M(c_R)\,\frac{\partial \mu^{mech}}{\partial X_1}\,\mathrm{d}X_1 + \varphi_i^{\theta}\, h_{1D}\Big|_0^L = \int_0^L \varphi_i^{\theta}\, b\,\mathrm{d}X_1 \,. \end{aligned} \tag{6.147}$$

Since the test function φ_i^{θ} corresponds to the concentration field, the boundary contribution

$$\varphi_i^{\theta}\, h_{1D}\Big|_0^L \tag{6.148}$$

vanishes on Dirichlet boundaries for θ, and is evaluated only on Neumann boundaries of the mass balance problem.

Finally, using Eq. (6.61), the weak form (6.147) can be restated as

$$\int_0^L \varphi_i^\theta \,\frac{\partial c_R}{\partial t}\,\mathrm{d}X_1 + \int_0^L \frac{\partial \varphi_i^\theta}{\partial X_1}\,\mathbb{D}\,\frac{\partial c_R}{\partial X_1}\,\mathrm{d}X_1 - 2\,\frac{RT\chi}{c_{\max}}\int_0^L \frac{\partial \varphi_i^\theta}{\partial X_1}\,M(c_R)\,\frac{\partial c_R}{\partial X_1}\,\mathrm{d}X_1 \tag{6.149}$$
$$+ \int_0^L \frac{\partial \varphi_i^\theta}{\partial X_1}\,\beta\,M(c_R)\left(\tfrac{\partial\theta}{\partial X_1} - \tfrac{\partial\theta^*}{\partial X_1}\right)\mathrm{d}X_1 + \int_0^L \frac{\partial \varphi_i^\theta}{\partial X_1}\,M(c_R)\,\frac{\partial \mu^{mech}}{\partial X_1}\,\mathrm{d}X_1 + \varphi_i^\theta\,h_{1D}\Big|_0^L$$
$$= \int_0^L \varphi_i^\theta\,b\,\mathrm{d}X_1\,.$$

6.3.2.2.2 Separated variables discretization

We approximate the unknown fields using finite-dimensional expansions

$$c_R(X_1,t) = \sum_j c_j(t)\,\varphi_j^\theta(X_1), \qquad c_R^*(X_1,t) = \sum_j c_j^*(t)\,\varphi_j^*(X_1), \tag{6.150}$$
$$\mu^{mech}(X_1,t) = \sum_j \mu_j^{mech}(t)\,\varphi_j^\gamma(X_1)\,.$$

Substituting these expansions into Eq. (6.149) yields the discrete weak form (Einstein summation convention implied):

$$\int_0^L \varphi_i^\theta\,\varphi_j^\theta\,\mathrm{d}X_1\;\frac{\partial c_j(t)}{\partial t} + \int_0^L \mathbb{D}\,\frac{\partial \varphi_i^\theta}{\partial X_1}\,\frac{\partial \varphi_j^\theta}{\partial X_1}\,\mathrm{d}X_1\;c_j(t) \tag{6.151}$$
$$- 2\frac{RT\chi}{c_{\max}}\int_0^L \frac{\partial \varphi_i^\theta}{\partial X_1}\,M(c_R)\,\frac{\partial \varphi_j^\theta}{\partial X_1}\,\mathrm{d}X_1\;c_j(t)$$
$$+ \int_0^L \beta\,M(c_R)\,\frac{\partial \varphi_i^\theta}{\partial X_1}\,\frac{\partial \varphi_j^\theta}{\partial X_1}\,\mathrm{d}X_1\;\theta_j(t) - \int_0^L \beta\,M(c_R)\,\frac{\partial \varphi_i^\theta}{\partial X_1}\,\frac{\partial \varphi_j^*}{\partial X_1}\,\mathrm{d}X_1\;\theta_j^*(t)$$
$$+ \int_0^L M(c_R)\,\frac{\partial \varphi_i^\theta}{\partial X_1}\,\frac{\partial \varphi_j^\gamma}{\partial X_1}\,\mathrm{d}X_1\;\mu_j^{mech}(t) = \int_0^L \varphi_i^\theta\,b\,\mathrm{d}X_1 - \varphi_i^\theta\,h_{1D}\Big|_0^L\,.$$

The boundary term is nonzero only on Neumann boundaries, where the mass flux h_{1D} is prescribed.

6.3.2.2.3 Euler integration schemes

Using the forward finite difference

$$\frac{\partial c_j(t)}{\partial t} \approx \frac{c_j(t+\Delta t) - c_j(t)}{\Delta t}\,, \tag{6.152}$$

we obtain the following fully discrete formulations.

In the Forward Euler scheme (explicit), all terms are evaluated at the known state $c(t)$:

$$\begin{aligned}
&\int_0^L \varphi_i^\theta \varphi_j^\theta \,\mathrm{d}X_1 \, \frac{c_j(t+\Delta t)}{\Delta t} + \int_0^L \text{Đ} \frac{\partial \varphi_i^\theta}{\partial X_1} \frac{\partial \varphi_j^\theta}{\partial X_1} \,\mathrm{d}X_1 \, c_j(t+\Delta t) \\
&\quad - 2 \, \frac{RT\chi}{c_{\max}} \int_0^L \frac{\partial \varphi_i^\theta}{\partial X_1} \, M(c_R(t)) \, \frac{\partial \varphi_j^\theta}{\partial X_1} \,\mathrm{d}X_1 \, c_j(t+\Delta t) \\
&\quad + \int_0^L \beta \, M(c_R(t)) \, \frac{\partial \varphi_i^\theta}{\partial X_1} \frac{\partial \varphi_j^\theta}{\partial X_1} \,\mathrm{d}X_1 \, \theta_j(t+\Delta t) \\
&\quad - \int_0^L \beta \, M(c_R(t)) \, \frac{\partial \varphi_i^\theta}{\partial X_1} \frac{\partial \varphi_j^*}{\partial X_1} \,\mathrm{d}X_1 \, \theta_j^*(t+\Delta t) \\
&\quad + \int_0^L M(c_R(t)) \, \frac{\partial \varphi_i^\theta}{\partial X_1} \frac{\partial \varphi_j^\gamma}{\partial X_1} \,\mathrm{d}X_1 \, \mu_j^{mech}(t+\Delta t) \\
&\quad = \int_0^L \varphi_i^\theta \varphi_j^\theta \,\mathrm{d}X_1 \, \frac{c_j(t)}{\Delta t} + \int_0^L b \, \varphi_i^\theta \,\mathrm{d}X_1 - \varphi_i^\theta h_{1D} \Big|_0^L
\end{aligned} \tag{6.153}$$

In the Backward Euler scheme (implicit), all terms are evaluated at the unknown state $c(t+\Delta t)$, leading to a nonlinear problem:

$$\begin{aligned}
&\int_0^L \varphi_i^\theta \varphi_j^\theta \,\mathrm{d}X_1 \, \frac{c_j(t+\Delta t)}{\Delta t} + \int_0^L \text{Đ} \frac{\partial \varphi_i^\theta}{\partial X_1} \frac{\partial \varphi_j^\theta}{\partial X_1} \,\mathrm{d}X_1 \, c_j(t+\Delta t) \\
&\quad - 2 \, \frac{RT\chi}{c_{\max}} \int_0^L \frac{\partial \varphi_i^\theta}{\partial X_1} \, M(c_R(t+\Delta t)) \, \frac{\partial \varphi_j^\theta}{\partial X_1} \,\mathrm{d}X_1 \, c_j(t+\Delta t) \\
&\quad + \int_0^L \beta \, M(c_R(t+\Delta t)) \, \frac{\partial \varphi_i^\theta}{\partial X_1} \frac{\partial \varphi_j^\theta}{\partial X_1} \,\mathrm{d}X_1 \, \theta_j(t+\Delta t) \\
&\quad - \int_0^L \beta \, M(c_R(t+\Delta t)) \, \frac{\partial \varphi_i^\theta}{\partial X_1} \frac{\partial \varphi_j^*}{\partial X_1} \,\mathrm{d}X_1 \, \theta_j^*(t+\Delta t) \\
&\quad + \int_0^L M(c_R(t+\Delta t)) \frac{\partial \varphi_i^\theta}{\partial X_1} \frac{\partial \varphi_j^\gamma}{\partial X_1} \,\mathrm{d}X_1 \, \mu_j^{mech}(t+\Delta t) \\
&\quad = \int_0^L \varphi_i^\theta \varphi_j^\theta \,\mathrm{d}X_1 \, \frac{c_j(t)}{\Delta t} + \int_0^L b \, \varphi_i^\theta \,\mathrm{d}X_1 - \varphi_i^\theta h_{1D} \Big|_0^L
\end{aligned} \tag{6.154}$$

6.3.2.2.4 Dimensionless form

To render the Forward and Backward Euler formulations dimensionless, we set θ, $\tilde{\text{Đ}}$ as Eqs. (6.4), (6.15), and γ as

$$\gamma = \frac{\mu^{mech}}{\mu_{\text{ref}}}. \tag{6.155}$$

Multiplying Eqs. (6.153), (6.154) by $\Delta t/(c_{\max}\ell)$ and using the mobility definition (6.3),

$$\frac{\Delta t\,\beta}{c_{\max}\ell^2}\,M(c_R(t)) = \tilde{\mathfrak{D}}\,\frac{\beta}{RT}\,\theta(t)\big(1-\theta(t)\big), \tag{6.156}$$

$$\frac{\Delta t\,\mu_{\mathrm{ref}}}{c_{\max}\ell^2}\,M(c_R(t)) = \tilde{\mathfrak{D}}\,\frac{\mu_{\mathrm{ref}}}{RT}\,\theta(t)\big(1-\theta(t)\big), \tag{6.157}$$

one obtains the following dimensionless systems.

When evaluated at the known state $\theta(t)$, the dimensionless Forward Euler scheme reads:

$$\begin{aligned}
&\frac{1}{\ell}\int_0^L \varphi_i^\theta\varphi_j^\theta\,\mathrm{d}X_1\;\theta_j(t+\Delta t) + \tilde{\mathfrak{D}}\,\ell\int_0^L \frac{\partial\varphi_i^\theta}{\partial X_1}\frac{\partial\varphi_j^\theta}{\partial X_1}\,\mathrm{d}X_1\;\theta_j(t+\Delta t) \\
&\quad+\tilde{\mathfrak{D}}\left(\frac{\beta}{RT}-2\chi\right)\ell\int_0^L\big(\varphi_k^\theta\theta_k(t)\big)\Big(1-\varphi_h^\theta\theta_h(t)\Big)\frac{\partial\varphi_i^\theta}{\partial X_1}\frac{\partial\varphi_j^\theta}{\partial X_1}\,\mathrm{d}X_1\;\theta_j(t+\Delta t) \\
&\quad-\tilde{\mathfrak{D}}\,\frac{\beta}{RT}\,\ell\int_0^L\big(\varphi_k^\theta\theta_k(t)\big)\Big(1-\varphi_h^\theta\theta_h(t)\Big)\frac{\partial\varphi_i^\theta}{\partial X_1}\frac{\partial\varphi_j^*}{\partial X_1}\,\mathrm{d}X_1\;\theta_j^*(t+\Delta t) \\
&\quad+\tilde{\mathfrak{D}}\,\frac{\mu_{\mathrm{ref}}}{RT}\,\ell\int_0^L\big(\varphi_k^\theta\theta_k(t)\big)\Big(1-\varphi_h^\theta\theta_h(t)\Big)\frac{\partial\varphi_i^\theta}{\partial X_1}\frac{\partial\varphi_j^\gamma}{\partial X_1}\,\mathrm{d}X_1\;\gamma_j(t+\Delta t) \\
&\quad=\frac{1}{\ell}\int_0^L\varphi_i^\theta\varphi_j^\theta\,\mathrm{d}X_1\;\theta_j(t)+\frac{1}{\ell}\int_0^L\varphi_i^\theta\,\frac{\Delta t\,b(X_1,t)}{c_{\max}}\,\mathrm{d}X_1-\varphi_i^\theta\,\frac{\Delta t\,h_{1D}(X_1,t)}{c_{\max}\ell}\Big|_0^L.
\end{aligned} \tag{6.158}$$

When evaluated at the unknown state $\theta(t+\Delta t)$, the dimensionless Backward Euler scheme becomes nonlinear and is given by:

$$\begin{aligned}
&\frac{1}{\ell}\int_0^L \varphi_i^\theta\varphi_j^\theta\,\mathrm{d}X_1\;\theta_j(t+\Delta t) + \tilde{\mathfrak{D}}\,\ell\int_0^L \frac{\partial\varphi_i^\theta}{\partial X_1}\frac{\partial\varphi_j^\theta}{\partial X_1}\,\mathrm{d}X_1\;\theta_j(t+\Delta t) \\
&\quad+\tilde{\mathfrak{D}}\left(\frac{\beta}{RT}-2\chi\right)\ell\int_0^L\varphi_h^\theta\frac{\partial\varphi_i^\theta}{\partial X_1}\frac{\partial\varphi_j^\theta}{\partial X_1}\,\mathrm{d}X_1\;\theta_h(t+\Delta t)\,\theta_j(t+\Delta t) \\
&\quad-\tilde{\mathfrak{D}}\left(\frac{\beta}{RT}-2\chi\right)\ell\int_0^L\varphi_h^\theta\varphi_k^\theta\frac{\partial\varphi_i^\theta}{\partial X_1}\frac{\partial\varphi_j^\theta}{\partial X_1}\,\mathrm{d}X_1\;\theta_h(t+\Delta t)\,\theta_k(t+\Delta t)\,\theta_j(t+\Delta t) \\
&\quad-\tilde{\mathfrak{D}}\,\frac{\beta}{RT}\,\ell\int_0^L\varphi_h^\theta\frac{\partial\varphi_i^\theta}{\partial X_1}\frac{\partial\varphi_j^*}{\partial X_1}\,\mathrm{d}X_1\;\theta_h(t+\Delta t)\,\theta_j^*(t+\Delta t) \\
&\quad+\tilde{\mathfrak{D}}\,\frac{\beta}{RT}\,\ell\int_0^L\varphi_h^\theta\varphi_k^\theta\frac{\partial\varphi_i^\theta}{\partial X_1}\frac{\partial\varphi_j^*}{\partial X_1}\,\mathrm{d}X_1\;\theta_h(t+\Delta t)\,\theta_k(t+\Delta t)\,\theta_j^*(t+\Delta t) \\
&\quad-\tilde{\mathfrak{D}}\,\frac{\mu_{\mathrm{ref}}}{RT}\,\ell\int_0^L\varphi_h^\theta\frac{\partial\varphi_i^\theta}{\partial X_1}\frac{\partial\varphi_j^\gamma}{\partial X_1}\,\mathrm{d}X_1\;\theta_h(t+\Delta t)\,\gamma_j(t+\Delta t) \\
&\quad+\tilde{\mathfrak{D}}\,\frac{\mu_{\mathrm{ref}}}{RT}\,\ell\int_0^L\varphi_h^\theta\varphi_k^\theta\frac{\partial\varphi_i^\theta}{\partial X_1}\frac{\partial\varphi_j^\gamma}{\partial X_1}\,\mathrm{d}X_1\;\theta_h(t+\Delta t)\,\theta_k(t+\Delta t)\,\gamma_j(t+\Delta t) \\
&\quad=\frac{1}{\ell}\int_0^L\varphi_i^\theta\varphi_j^\theta\,\mathrm{d}X_1\;\theta_j(t)+\frac{1}{\ell}\int_0^L\varphi_i^\theta\,\frac{\Delta t\,b(X_1,t)}{c_{\max}}\,\mathrm{d}X_1-\varphi_i^\theta\,\frac{\Delta t\,h_{1D}(X_1,t)}{c_{\max}\ell}\Big|_0^L.
\end{aligned} \tag{6.159}$$

6.3.2.3 Governing equations and numerical solution of the Neumann kind problem

6.3.2.3.1 Newton–Raphson scheme for θ

Equation (6.159) can be recast compactly as a residual

$$\mathcal{R}_\theta(\theta_j(t+\Delta t), {\theta^*}_j(t+\Delta t),\ \gamma_j(t+\Delta t)) = \ \mathcal{A}_\theta({\theta^*}_j(t+\Delta t), \theta_j(t+\Delta t)) + \tag{6.160}$$

$$\begin{aligned}
&+ \tilde{\mathbb{D}}\ \left(\frac{\beta}{RT}\ - 2\,\chi\right)\ \ell\ \int_0^L \varphi_h^\theta\ \frac{\partial\varphi_i^\theta}{\partial x}\frac{\partial\varphi_j^\theta}{\partial x}\ \mathrm{d}x\ \ \theta_h(t+\Delta t)\ \theta_j(t+\Delta t)\\
&- \tilde{\mathbb{D}}\ \left(\frac{\beta}{RT}\ - 2\,\chi\right)\ \ell\ \int_0^L \varphi_h^\theta\ \varphi_k^\theta\ \frac{\partial\varphi_i^\theta}{\partial x}\frac{\partial\varphi_j^\theta}{\partial x}\ \mathrm{d}x\ \ \ \theta_h(t+\Delta t)\ \theta_k(t+\Delta t)\ \theta_j(t+\Delta t)\\
&- \tilde{\mathbb{D}}\ \frac{\beta}{RT}\ \ell\ \int_0^L \varphi_h^\theta\ \frac{\partial\varphi_i^\theta}{\partial x}\frac{\partial\varphi_j^*}{\partial x}\ \mathrm{d}x\ \ \ \theta_h(t+\Delta t)\ \theta_j^*(t+\Delta t)\\
&+ \tilde{\mathbb{D}}\ \frac{\beta}{RT}\ \ell\ \int_0^L \varphi_h^\theta\ \varphi_k^\theta\ \frac{\partial\varphi_i^\theta}{\partial x}\frac{\partial\varphi_j^*}{\partial x}\ \mathrm{d}x\ \ \theta_h(t+\Delta t)\ \theta_k(t+\Delta t)\ \theta_j^*(t+\Delta t)\\
&- \tilde{\mathbb{D}}\ \frac{\mu_{\mathrm{ref}}}{RT}\ \ell\ \int_0^L \varphi_h^\theta\ \frac{\partial\varphi_i^\theta}{\partial X_1}\frac{\partial\varphi_j^\gamma}{\partial X_1}\,\mathrm{d}X_1\ \theta_h(t+\Delta t)\ \gamma_j(t+\Delta t)\\
&+ \tilde{\mathbb{D}}\ \frac{\mu_{\mathrm{ref}}}{RT}\ \ell\ \int_0^L \varphi_h^\theta\ \varphi_k^\theta\ \frac{\partial\varphi_i^\theta}{\partial X_1}\frac{\partial\varphi_j^\gamma}{\partial X_1}\,\mathrm{d}X_1\ \theta_h(t+\Delta t)\ \theta_k(t+\Delta t)\ \gamma_j(t+\Delta t)\\
&+\ \mathcal{B}_\theta\ = 0
\end{aligned}$$

where $\mathcal{A}_\theta$ denotes the linear diffusion terms, and $\mathcal{B}_\theta$ the known right-hand side

$$\mathcal{B}_\theta = -\frac{1}{\ell}\int_0^L \varphi_i^\theta\varphi_j^\theta\,\mathrm{d}X_1\ \frac{\theta_j(t)}{\Delta t} - \frac{1}{\ell}\int_0^L \varphi_i^\theta\ \frac{\Delta t\, b(X_1,t)}{c_{\max}}\,\mathrm{d}X_1 + \varphi_i^\theta\frac{\Delta t\, h_{1D}(X_1,t)}{c_{\max}\ell}\Big|_0^L. \tag{6.161}$$

Linearization is performed by applying the Gateaux derivative, which yields the Jacobian contributions required for the Newton–Raphson iteration.

$$\frac{\partial}{\partial\epsilon}\mathcal{R}_\theta(\theta_j+\epsilon\delta\theta_j, \theta_j^*+\epsilon\delta\theta_j^*, \gamma_j+\epsilon\delta\gamma_j)\Big|_{\epsilon=0} = -\mathcal{R}_\theta(\theta_j,\theta_j^*,\gamma_j). \tag{6.162}$$

For completeness, the full expansion of these Jacobian terms is reported in Appendix A.5.

This yields a block-structured Jacobian involving contributions from: $\delta\theta_j$ terms (diffusion, Flory–Huggins, penalty, chemo–mechanical coupling), $\delta\theta_j^*$ terms (penalty constraint), $\delta\gamma_j$ terms (chemo–mechanical potential).

Explicit expressions are reported above. In practice, these blocks can be assembled into the global tangent matrix for the two-way coupled problem.

6.3.2.3.2 Newton–Raphson scheme for θ^*

The governing equations for the coupled chemo–mechanical case follow the same derivation as the purely diffusive case presented in Section 6.2.2, with the spatial coordinate now denoted by X_1 to emphasize the axial direction and mechanical coupling of the cylindrical particle. Since the mathematical steps are identical, this section reports only the final equations for clarity, while the complete step-by-step derivation is provided in Appendix A.6.

The discrete equation (A.19) can be written as

$$\begin{aligned}\mathcal{R}_{\theta^*}\big({\theta^*}_j(t+\Delta t),\,\theta_j(t+\Delta t)\big) &= \mathcal{A}_{\theta^*}\big({\theta^*}_j(t+\Delta t),\,\theta_j(t+\Delta t)\big) + \mathcal{B}_{\theta^*} \qquad (6.163)\\ &= \frac{1}{\ell}\int_0^L \varphi_i^*\,\varphi_j^\theta\,\mathrm{d}X_1\;\theta_j(t+\Delta t)\\ &\quad - \frac{1}{\ell}\int_0^L \varphi_i^*\,\varphi_j^*\,\mathrm{d}X_1\;\theta_j^*(t+\Delta t)\\ &\quad - \frac{\lambda}{\beta\ell^2}\,\ell\int_0^L \frac{\partial\varphi_i^*}{\partial X_1}\,\frac{\partial\varphi_j^*}{\partial X_1}\,\mathrm{d}X_1\;\theta_j^*(t+\Delta t)\\ &\quad + \frac{\lambda}{\beta\ell^2}\,\varphi_i^*\,\ell\,h_{1D}^*\Big|_0^L = 0\,,\end{aligned}$$

with Einstein summation over j, where the (known) boundary contribution is

$$\mathcal{B}_{\theta^*} = \frac{\lambda}{\beta\ell^2}\,\varphi_i^*\,\ell\,h_{1D}^*\Big|_0^L, \qquad (6.164)$$

and $\mathcal{A}_{\theta^*}$ is the linear form evaluated at time $t+\Delta t$.

6.3.2.3.3 Newton–Raphson scheme for γ

Adopting test functions φ_i^γ for the functional space of $\gamma(X_1,t)$, and denoting with $\upsilon_j = u_j/\ell$ the dimensionless displacement nodal values, the discrete weak form reads

$$\begin{aligned}\mathcal{R}_\gamma(\gamma_j,\theta_j,\upsilon_j) &= \frac{1}{\ell}\int_0^L \varphi_i^\gamma\varphi_j^\gamma\,\mathrm{d}X_1\;\gamma_j(t+\Delta t) \qquad (6.165)\\ &\quad - \frac{E\,\Omega}{\ell\,\mu_{\mathrm{ref}}}\int_0^L \varphi_i^\gamma\,\left\{\alpha_4\,\aleph(\theta_j,\upsilon_j)^4 + \alpha_2\,\aleph(\theta_j,\upsilon_j)^2\right\}\,\mathrm{d}X_1\\ &\quad - \frac{1}{8}\frac{E\,\Omega}{\ell\,\mu_{\mathrm{ref}}}\int_0^L \varphi_i^\gamma\,\mathrm{d}X_1 = \mathcal{A}_\gamma(\gamma_j(t+\Delta t))\\ &\quad - \frac{E\,\Omega}{\ell\,\mu_{\mathrm{ref}}}\int_0^L \varphi_i^\gamma\,\left\{\alpha_4\,\aleph(\theta_j,\upsilon_j)^4 + \alpha_2\,\aleph(\theta_j,\upsilon_j)^2\right\}\,\mathrm{d}X_1\\ &\quad + \mathcal{B}_\gamma = 0\,.\end{aligned}$$

with

$$\mathcal{A}_\gamma(\gamma_j(t+\Delta t)) = \frac{1}{\ell}\int_0^L \varphi_i^\gamma \varphi_j^\gamma \,\mathrm{d}X_1 \; \gamma_j(t+\Delta t) \;, \qquad \mathcal{B}_\gamma = -\frac{1}{8}\frac{E\,\Omega}{\ell\,\mu_{\mathrm{ref}}} \int_0^L \varphi_i^\gamma \,\mathrm{d}X_1 \;, \tag{6.166}$$

and

$$\aleph(\theta_j, \upsilon_j) = (1 + \Omega\, c_{\max}\, \varphi_h^\theta\, \theta_h)^{-1/3} \left(1 + \ell\, \frac{\partial \varphi_j^u}{\partial X_1}\, \upsilon_j\right) . \tag{6.167}$$

To solve Eq. (6.165), the Newton–Raphson linearization is carried out by means of the Gateaux derivative (see Appendix A.7.)

6.3.2.3.4 Newton–Raphson scheme for u

The balance of linear momentum for the two-way coupled problem follows the same mathematical derivation as the one-way case presented in Section 6.3.1.4. In both settings, the governing equations are obtained by restricting the general balance law to a one-dimensional geometry and expressing the axial stress in terms of the swelling deformation J^c and the displacement field u. The only difference lies in the physical interpretation: in the one-way case, the concentration field θ influences mechanics solely through swelling, whereas in the two-way case, the mechanical fields also feed back into the diffusion problem by contributing to the chemical potential.

Since the algebraic steps are identical to those already detailed in Section 6.3.1.4, they are not repeated here. For clarity, only the final expressions are reported below, while the full step-by-step derivation can be found in Section 6.3.1.4.

The dimensionless weak form reads

$$\begin{aligned}\mathcal{R}_u(\theta_j, \upsilon_j) = \frac{1}{2}\,\frac{E}{G}\int_0^L \frac{\partial \varphi_i}{\partial X_1} J^{c2/3} \aleph(\theta_j, \upsilon_j)\Big[\aleph(\theta_j, \upsilon_j)^2 - 1\Big]\,\mathrm{d}X_1 \\ - \frac{1}{\ell}\int_0^L \varphi_i\,\frac{B_1\,\ell}{G}\,\mathrm{d}X_1 - \varphi_i\,\frac{\overline{p}}{G}\,\Big|_0^L = 0 \;,\end{aligned} \tag{6.168}$$

where $\overline{p}$ is the traction applied on the Neumann boundary and

$$\aleph(\theta_j, \upsilon_j) = \big(1 + \Omega\, c_{\max}\, \varphi_h^\theta\, \theta_h\big)^{-1/3} \left(1 + \ell\, \frac{\partial \varphi_j^u}{\partial X_1}\, \upsilon_j\right). \tag{6.169}$$

The corresponding Newton–Raphson linearization is

$$\frac{\partial}{\partial \epsilon}\mathcal{R}_u\big(\theta_j + \epsilon\delta\theta_j,\; \upsilon_j + \epsilon\delta\upsilon_j\big)\Big|_{\epsilon=0} = -\mathcal{R}_u(\theta_j, \upsilon_j) \;, \tag{6.170}$$

with the fully expanded form given in Eq. (A.9).

This formulation is solved simultaneously with the diffusion equations, thus completing the two-way chemo–mechanical coupling in which concentration and mechanical fields evolve in a fully coupled manner.

6.3.2.4 Manufactured solutions

Consider the following manufactured solution for the concentration and displacement fields:

$$\theta(X_1,t) = \frac{t}{\bar{t}}\left(\alpha + \beta\frac{X_1}{L}\right), \tag{6.171}$$

$$\overline{v}(X_1,t) = \frac{t}{\bar{t}}\left(\gamma + \delta\frac{X_1}{L}\right), \tag{6.172}$$

with $\bar{t}$ a reference time.

The corresponding dimensionless chemical potential reads

$$\frac{\mu^{CH}+\mu^{mech}}{\mu_{\text{ref}}} = \frac{RT}{\mu_{\text{ref}}}\,\chi\,(1-2\,\theta) - \frac{\lambda}{\mu_{\text{ref}}}\nabla^2\theta + \frac{\mu^{mech}}{\mu_{\text{ref}}}, \tag{6.173}$$

where the chemo–mechanical contribution is given by

$$\frac{\mu^{mech}}{\mu_{\text{ref}}} = E\,\frac{\Omega}{\mu_{\text{ref}}}\left\{\alpha_4\,\aleph(\theta,\overline{v})^4 + \alpha_2\,\aleph(\theta,\overline{v})^2 + \frac{1}{8}\right\}, \tag{6.174}$$

with $\aleph$ defined as

$$\aleph(\theta,\overline{v}) = \left[1+\Omega\,c_{\max}\,\frac{t}{\bar{t}}\left(\alpha+\beta\frac{X_1}{L}\right)\right]^{-1/3}\left(1+\delta\,\frac{t}{\bar{t}}\,\frac{\ell}{L}\right). \tag{6.175}$$

The coefficients are

$$\alpha_4 = -\frac{12\nu^2+\nu+1}{24(\nu+1)}\,, \qquad \alpha_2 = \frac{6\nu^2+5\nu-1}{12(\nu+1)}\,.$$

The chemo–mechanical contribution couples the mass flux with the displacement field. Full analytical expressions for the resulting fluxes h_{1D}, h^{μ}_{1D} and the supply term $b(X_1,t)$ are reported in Appendix A.10.

6.3.2.5 Numerical results of the Neumann kind problem

Based on Eq. (6.159), the dimensionless numbers that govern the numerical solution of the mass balance equation are $\tilde{\mathbb{D}}$, χ, and the ratios $\frac{\beta}{RT}$ (which vanishes when the interface energy λ is zero, because $\beta = \lambda l^{-2}$) and $\frac{\mu_{\text{ref}}}{RT}$. Assuming a uniform discretization with element size e_ℓ, all integrals scale with

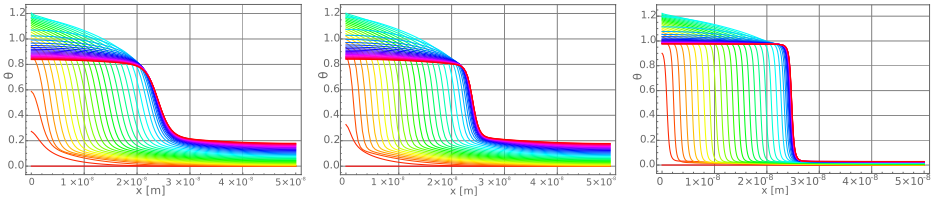

(a) $\chi = 2.5$, $l = 0.01\ell$. (b) $\chi = 2.5$, $l = 0.005\ell$. (c) $\chi = 4$, $l = 0.01\ell$.

Figure 6.7: Scenarios at $\mathbb{D} = 10^{-15}$, $\beta = 8RT$ upon charging until $t = 1s$ and self equilibrium until $t_f = 2s$.

e_ℓ or its inverse. Hence, the effective dimensionless diffusivity as introduced in (6.103).

The penalty constraint Eq. (A.20) is controlled by the ratio $\frac{l^2}{\ell^2}$ (see Eq. (A.17)). The chemo-mechanical potential evolution Eq. (6.165) is governed by a few additional dimensionless parameters: the Poisson ratio ν, the ratio $\frac{E\,\Omega}{\ell\,\mu_{\text{ref}}}$, and the product $\Omega\,c_{\max}$. Note that the setup is the same as that described in Section 6.2.5.

To explore the coupled chemo–mechanical effects, we prescribe a flux that charges the electrode until a saturation time t_{sat}, at which the electrode reaches full capacity $c_{\max}L$ starting from an initially empty state. The imposed flux reads

$$h_{1D}(0,t) = c_{\max}\frac{L}{t_{sat}}, \tag{6.176}$$

corresponding in dimensionless form to

$$\frac{\Delta t\; h_{1D}(0,t)}{c_{\max}\ell} = \frac{L}{\ell}\frac{\Delta t}{t_{sat}}. \tag{6.177}$$

At $t = 0.5\,t_{sat}$ the inflow is stopped, and the system relaxes to equilibrium. Fig. 6.7 illustrate this process for $\chi = 2.5$ and $\chi = 4$. The Flory-Huggins parameter χ establishes the loci of the two minima for the order-zero Helmholtz free energy (6.19), as seen in Fig. 6.8. Those two minima correspond to the concentrations at equilibrium in Fig. 6.7. On the other hand, higher values of χ steepen the concentration profile at the sodiated/prestine interface, together with the inner length parameter l. This event is made manifest in Fig. 6.7, in which the concentration profiles corresponding to two values of χ and of l are compared. During charging, the inserted mass $h_{1D}(0,t)\,\bar{t}$ matches closely the integrated concentration $\int c(x,\bar{t})\,dx$ (Fig. 6.9a), validating conservation. After inflow ceases, the species redistributes: the over-saturated region ($\theta > 1$) gradually shrinks, and the phase interface propagates toward the domain center (Fig. 6.9b). The Helmholtz free energy ψ_R from Eq. (6.24) is decomposed into entropic, interaction, interfacial, and mechanical parts.

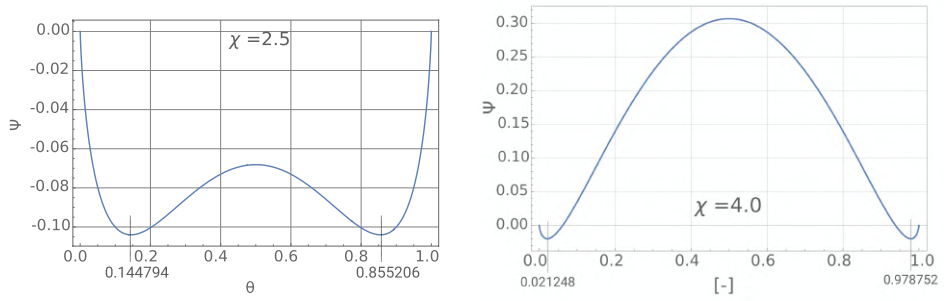

(a) $\chi = 2.5$. (b) $\chi = 4$.

Figure 6.8: Helmholtz free energy with respect to normalized concentration (6.19) for $\chi = 2.5$ and $\chi = 4$.

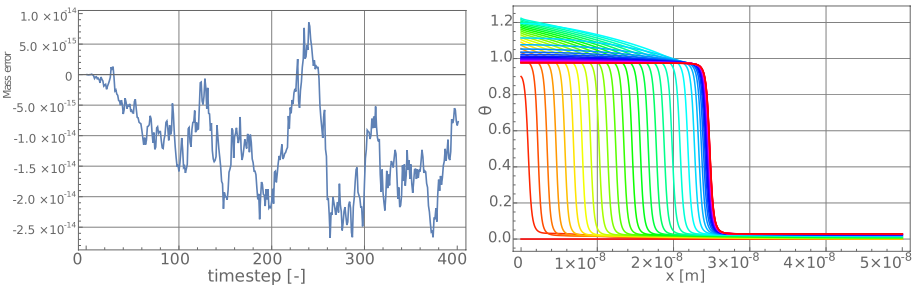

(a) Dimensionless mass error. (b) Mass accumulation.

Figure 6.9: Mass conservation and redistribution during charging and relaxation.

Figures 6.10a–6.10d display their evolution. The entropic and interaction contributions follow the concentration profile, capturing the thermodynamic drive for phase separation. The interfacial contribution peaks sharply at the sodiation front, penalizing steep concentration gradients. The mechanical part increases monotonically from right to left, saturating in the sodiated region. This illustrates how stress builds up in response to ion insertion.

Figs. 6.11–6.12 illustrate the evolution of the different contributions to the chemical potential during the charging and subsequent relaxation stages. Sodium inflow is applied until $t = 1\,\mathrm{s}$, after which the system evolves freely toward equilibrium until $t_f = 2\,\mathrm{s}$.

Entropic contribution, μ^{en} captures the effect of configurational entropy on diffusion, phase stability, and interface formation. Plotting the entropic potential reveals how entropy either resists or facilitates sodium transport, depending on the local concentration. At the inflow boundary ($x = 0$),

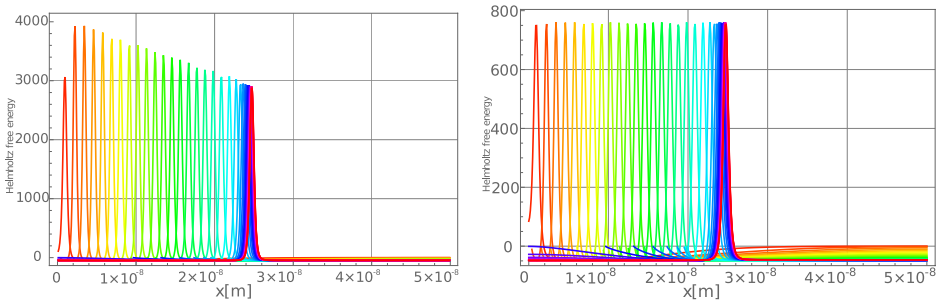

(a) $\psi_R/c_{\max}$. (b) $\psi_R^{tr}/c_{\max}$.

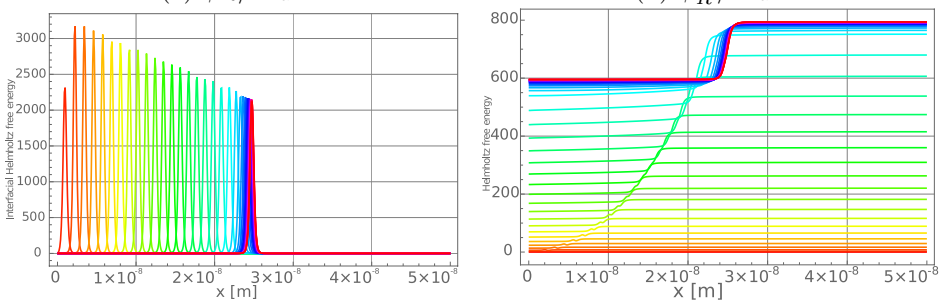

(c) $\psi_R^{int}/c_{\max}$. (d) $\psi_R^{mech}/c_{\max}$.

Figure 6.10: Helmholtz free energy components during charging and relaxation ($\mathbb{D} = 10^{-15}$, $\beta = 8RT$, $\chi = 4$, $l = 0.01\ell$).

sodium rapidly accumulates and the concentration θ approaches unity. Since

$$\mu^{en} \sim \ln\left(\frac{\theta}{1-\theta}\right),$$

the potential diverges for $\theta \to 0$ and $\theta \to 1$, producing steep curvature near fully desodiated or fully sodiated states. The resulting asymmetric curvature stems from the nonuniform spatial distribution of θ. During relaxation, the system evolves toward lower total energy as all driving forces dissipate, while at equilibrium the potentials (chemical and mechanical) become spatially uniform.

Interfacial contribution, μ^{int} penalizes sharp spatial concentration gradients and acts to smooth out abrupt changes in $\theta(x)$. It is proportional to the curvature of the concentration field:

$$\mu^{int} \sim -\frac{d^2\theta}{dx^2}.$$

Hence, $\mu^{int} > 0$ where the profile is concave down and $\mu^{int} < 0$ where it is concave up. Across the interface, μ^{int} changes sign, reflecting the restoring

force that tends to flatten steep gradients. Oscillations near the interface originate from local curvature changes during interface propagation and stabilization.

The interaction term

$$\mu^{\chi} = RT\chi(1 - 2\theta)$$

is positive for $\theta < 0.5$ and negative for $\theta > 0.5$. Thus, in Na-rich regions ($\theta \approx 1$), $\mu^{\chi} < 0$. When summed with μ^{int}, the total μ^{CH}(Eq. (6.31)) alternates between positive and negative near the interface, indicating the local driving force for Na redistribution, sodium tends to diffuse from regions of high potential toward low potential.

Chemo-mechanical contribution, μ^{mech}(Eq. (6.134)) originates from elastic stresses caused by volumetric expansion during Na insertion. Sodium accumulation in the left region generates compressive stress, increasing the local chemical potential and producing a stress-induced insertion barrier. The first two terms in the mechanical potential are quadratic in strain, representing stored elastic energy; these grow as the electrode swells nonuniformly. The third term accounts for anisotropic coupling via $S^e \cdot C^e$, linking stress to material stiffness. The scaling factor Ω highlights the effect of large molar volume changes (e.g., Sn $\rightarrow$ Na_xSn). Spatially, μ^{mech} increases where strain accumulates, showing how mechanical energy contributes directly to the total potential. Over time, it plateaus, indicating that mechanical equilibrium has been reached.

The main distinction between Fig. 6.11 and 6.12 lies in the simulation stage and time window. Fig. 6.11 covers the entire 2 s period, including both the charging phase ($0 < t < 1$ s) and subsequent relaxation ($1 < t < 2$ s), while Fig. 6.12 focuses exclusively on the relaxation phase beginning immediately after the inflow stops at $t = 1$ s.

- μ^{en} (Fig. 6.12a): At $t = 1$ s (red curve), the system already exhibits strong phase separation and steep gradients near the sodiation front. As relaxation proceeds, the profiles flatten within each phase, showing homogenization of the entropic contribution.

- μ^{int} (Fig. 6.12b): Initially sharp at the formed interface, μ^{int} becomes smoother as $\theta(x)$ relaxes and the curvature reduces. The interfacial tension thus diminishes once Na inflow ceases.

- μ^{mech} (Fig. 6.12c): The chemo-mechanical potential remains relatively stable. Most stress developed during charging ($t < 1$ s) and redistributes only slightly once inflow stops, consistent with primarily elastic accommodation.

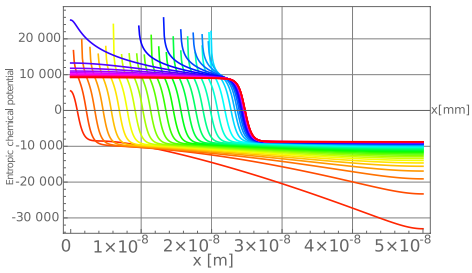

(a) μ^{en}.

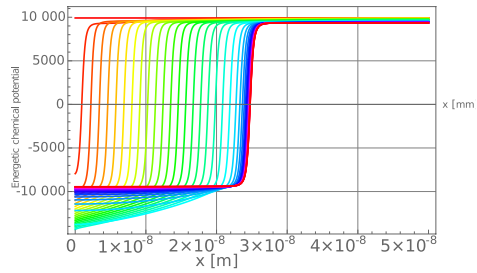

(b) μ^{int}.

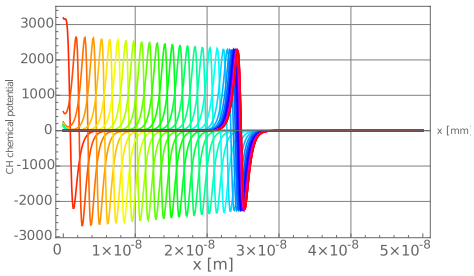

(c) μ^{CH}.

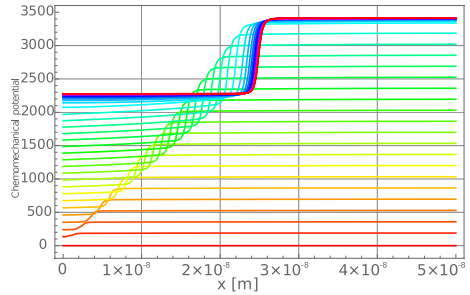

(d) μ^{mech}.

Figure 6.11: A numerical experiment with a given inflow for a limited amount of time. Scenarios at $\mathbb{D} = 10^{-15}$, $\beta = 8RT$, $\chi = 4$, $l = 0.01\ell$ upon charging until $t = 1s$ and self equilibrium until $t_f = 2s$.

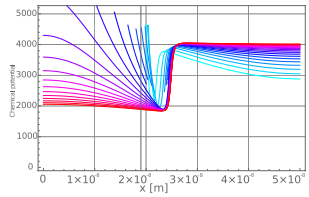

(a) μ^{en}.

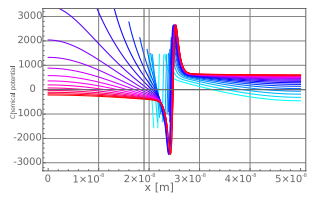

(b) μ^{int}.

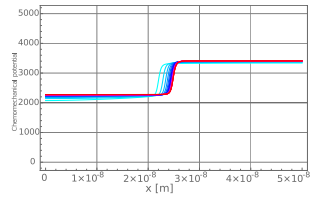

(c) μ^{mech}.

Figure 6.12: Chemical-potential decomposition during a load–relaxation run ($\mathbb{D} = 10^{-15}$, $\beta/RT = 8$, $\chi = 4$, $l = 0.01\ell$) upon charging until $t = 1s$ and self equilibrium until $t_f = 2s$.

The coupled chemo–mechanical analysis allows evaluation of stress measures (Fig. 6.13). As sodium enters, the sodiated half expands against the pristine half, generating compressive stress. At equilibrium, stresses saturate in the left half while remaining zero in the right. From the balance of momentum $\nabla \cdot \boldsymbol{P} = 0$, $\boldsymbol{P}_{11}(x)$ must be constant, apart from oscillations near the moving interface due to discretization. Mesh refinement reduces these

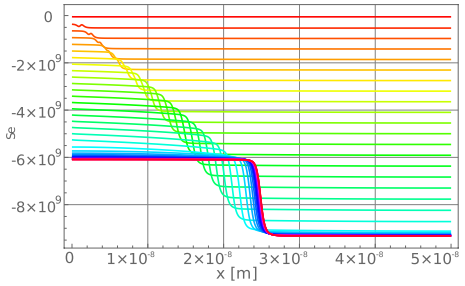

(a) Elastic S^e_{11}.

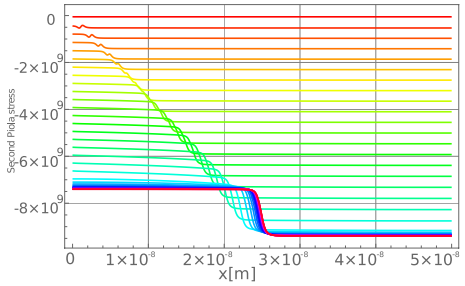

(b) Total S_{11}.

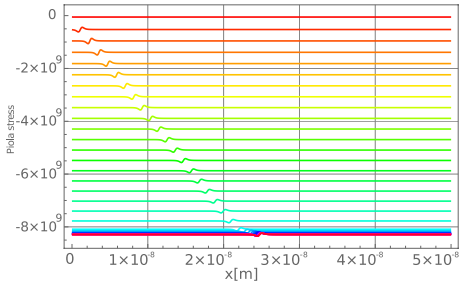

(c) Piola P_{11}.

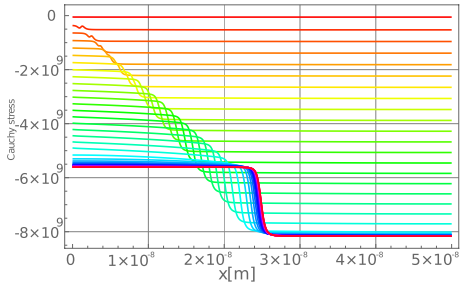

(d) momentum balance σ_{11}.

Figure 6.13: Stress measures during charging and relaxation ($\mathbb{D} = 10^{-15}$, $\beta = 8RT$, $\chi = 4$, $l = 0.01\ell$).

oscillations (Fig. 6.14).

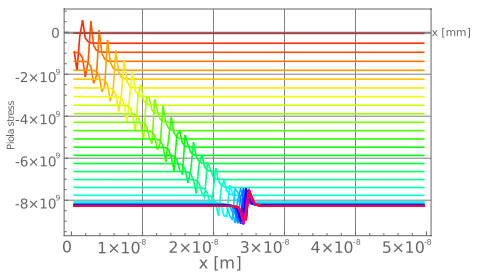

(a) $\boldsymbol{P}_{11}$ for a 128 panels uniform discretization.

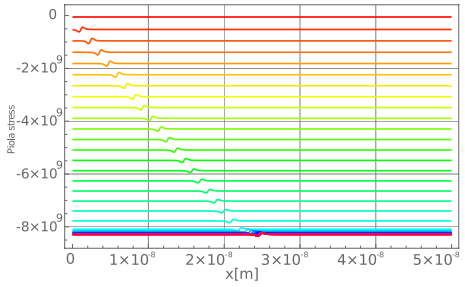

(b) $\boldsymbol{P}_{11}$ for a 512 panels uniform discretization.

Figure 6.14: A numerical experiment with a given inflow for a limited amount of time. Scenarios at $\mathbb{D} = 10^{-15}$, $\beta = 8RT$, $\chi = 4$, $l = 0.01\ell$ upon charging until $t = 1s$ and self equilibrium until $t_f = 2s$.

6.4 Modeling multistep phase transformations in Na–Sn anodes

6.4.1 From concentration-based models to volume-fraction formulation

Electrochemical systems such as sodium-ion batteries often undergo complex phase transformations during (de)intercalation, as shown in Figure 3.6. These involve the formation of multiple solid phases, large volumetric changes, and strong chemo–mechanical couplings. Traditionally, such systems have been modeled using concentration-based formulations, where the state of a chemical species is described by its molar concentration c^α (mol/m^3). While suitable for dilute systems, this framework faces limitations in solid-state electrodes with immobile host phases, sharp stoichiometric compounds, or large volume changes.

To overcome these issues, recent modeling approaches adopt volume fractions $\phi^\alpha \in [0, 1]$ as the primary state variables [11, 12]. The volume fraction ϕ^α represents the fraction of the local volume occupied by phase α, defined in either the reference or current configuration. Importantly, volume fractions naturally satisfy the volume-filling constraint

$$\sum_\alpha \phi^\alpha = 1, \tag{6.178}$$

which enforces local incompressibility of multiphase mixtures and avoids unphysical voids or overlaps. This is particularly important for solid–solid transformations in alloy anodes (e.g., Sn, $NaSn_3$, Na_9Sn_4, $Na_{15}Sn_4$), where multiple intermetallic phases coexist and transform without changing the total local volume. These benefits are reinforced in the literature. Tóth et al. [116] developed a Cahn–Hilliard framework for incompressible liquid mixtures using a Lagrange multiplier to enforce the summation constraint. Huang et al. [117] further proposed a conservative volume distribution algorithm that ensures mass conservation and interface consistency. Together, these contributions demonstrate the thermodynamic consistency and numerical robustness of the volume-fraction framework, making it well suited for modeling multiphase alloying reactions in Na–Sn anodes.

In Na-based alloy anodes, the relatively large ionic radius of sodium renders interstitial and substitutional diffusion energetically less favorable. Instead, vacancy diffusion emerges as the most likely mechanism for Na^+ transport within the solid host lattice. As highlighted in recent studies [118], the periodic arrangement of metal atoms in the anode crystal provides vacant lattice sites that enable Na^+ migration under the action of both chemical

potential and electric field gradients. At elevated temperatures, thermal activation increases the concentration of internal empty sites, thereby enhancing vacancy-assisted diffusion. This mechanistic understanding provides a sound justification for introducing a passive vacancy phase in our volume-fraction based formulation, ensuring consistency with the physical diffusion pathway of Na in Sn-based electrodes.

Our balance laws are formulated in the barycentric frame following classical non-equilibrium thermodynamics [119]: the mixture velocity $\boldsymbol{v}$ represents the center-of-mass motion and species transport is split into convection by $\boldsymbol{v}$ and relative (diffusive) fluxes. This split implies the standard mixture constraint that the sum of relative fluxes vanishes. The coupling between chemistry and mechanics is handled in the Larché–Cahn framework [120]. In practice, alloy anodes such as Na–Sn feature one dominant mobile species (Na), while host/intermetallic phases are effectively immobile; to satisfy local volume filling and the flux constraint when only one constituent is mobile, we introduce a passive vacancy/void phase V. The vacancy phase carries the compensating flux and absorbs any net reaction-induced volume change, thereby enforcing (6.178) pointwise in space and time. Closely related vacancy/void formulations are widely used to model Kirkendall porosity and electro-chemo-mechanical void growth in battery materials, ensuring thermodynamic consistency and numerical robustness in multiphase settings [121, 122].

6.4.2 Reaction mechanisms

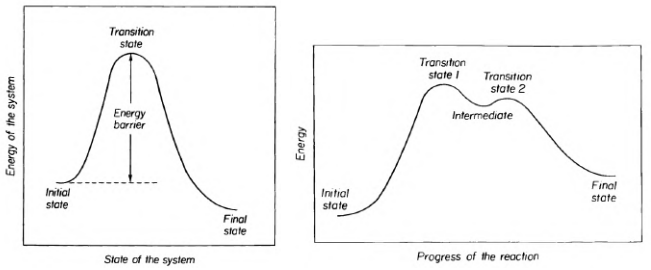

(a) One-step reaction. (b) Two-step reaction.

Figure 6.15: Schematic energy diagrams: (a) a one-step elementary reaction, (b) a two-step reaction with an intermediate [123].

Chemical reactions proceed along well-defined energy pathways comprising reactants, transition states, intermediates, and products. In a one-step elementary reaction (Fig. 6.15a), reactants must overcome an activation barrier to reach the transition state before forming products. More complex

reactions may involve multiple elementary steps (Fig. 6.15b), each with its own transition state and intermediate. In Na–Sn alloying, these steps correspond to sequential phase transformations between intermetallic compounds such as Sn, $NaSn_3$, Na_9Sn_4, and $Na_{15}Sn_4$.

6.4.3 Reaction kinetics

The proposed model is built upon the Larché–Cahn framework, which couples chemical and mechanical effects in solid electrodes, enabling the reaction kinetics to evolve consistently with stress and deformation [124, 125]. Sodium is assumed to flow into a hosting lattice, which can either be pristine Sn or its $NaSn_3$ alloy. The hosting material is the mere responsible for load-bearing capacity. Na-ions are extracted from the cathode (positive electrode) during charging and inserted back during discharging. The opposite holds for the anode (negative electrode). At the interface between electrolyte and the negative electrode, the following electrochemical charge transfer reaction

$$2\,\mathrm{Na}^+ + 2\,\mathrm{e}^- + 3\,\mathrm{Sn} \underset{k_b^{(1)}}{\overset{k_f^{(1)}}{\rightleftarrows}} \mathrm{NaSn_3} + \mathrm{Na} \tag{6.179}$$

occurs, provided that suitable values of the electric potentials are attained. We will model this reaction via a Butler-Volmer equation, as a boundary condition for the mass balance equation. It will be also assumed that sodium can flow in the hosting material, as the result of the chemical reaction

$$\mathrm{Na} + 3\,\mathrm{Sn} \underset{k_b^{(2)}}{\overset{k_f^{(2)}}{\rightleftarrows}} \mathrm{NaSn_3} \tag{6.180}$$

in the bulk. Sodium can then diffuse much faster than any $NaSn_3$ alloy, for its steric dimension. In fact, we may assume that transport of $NaSn_3$ via solid-state diffusion is a secondary effect. Further sodiation into several Na-rich amorphous phases and ultimately into the crystalline $Na_{15}Sn_4$ will be modeled via specific chemical reactions

$$8\,\mathrm{Na} + \mathrm{NaSn_3} + \mathrm{Sn} \underset{k_b^{(3)}}{\overset{k_f^{(3)}}{\rightleftarrows}} \mathrm{Na_9Sn_4} \tag{6.181}$$

$$6\,\mathrm{Na} + \mathrm{Na_9Sn_4} \underset{k_b^{(4)}}{\overset{k_f^{(4)}}{\rightleftarrows}} \mathrm{Na_{15}Sn_4} \tag{6.182}$$

6.4.3.1 Classical formulation

The law of mass action proposed by Guldberg–Waage over one hundred years ago is the most general empirical statement which synthesizes the dynamics of chemical reactions occurring in homogeneous gaseous or liquid phases. For any arbitrary reaction taking place at a given temperature T and pressure p which is of the form

$$\sum_{\text{reactants}} \nu_r A_r \rightleftharpoons \sum_{\text{products}} \nu_p B_p, \tag{6.183}$$

where A and B label the different species and the ν's are the stoichiometric coefficients, this law states that

$$\nu_i^{-1} \frac{\partial c_i}{\partial t} = k_f \prod_r c_r^{\nu_r} - k_b \prod_p c_p^{\nu_p}, \tag{6.184}$$

where c_i is the concentration of an arbitrary species at time t, c_r the concentration of reactant r at time t, c_p the concentration of product p at time t, and k_f, k_b are the so-called forward and backward rate constants which are functions of T and p only, [126].

6.4.3.2 Extension to solid-state electrodes

In battery electrodes, however, reaction kinetics are influenced not only by T and p, but also by species concentrations in the solid, elastic strains, large deformations, and trapping/detrapping phenomena. For this reason, the classical law of mass action is extended by adopting the chemo-mechanical formulation proposed in [88], where the reaction rate evolves with stress and deformation. In this framework, the referential rate factor $k_{\alpha R}$ is defined as

$$k_{\alpha_R} = J\, k, \tag{6.185}$$

where J is the Jacobian of deformation, so that rate constants evolve consistently with the strain of the body.

6.4.4 Definitions and relations

We consider the phases

$$\alpha \in \{\text{Na},\ \text{Sn},\ \text{NaSn}_3,\ \text{Na}_9\text{Sn}_4,\ \text{Na}_{15}\text{Sn}_4,\ \text{V}\},$$

where V denotes a passive vacancy/void phase [127].

The molar concentration c^α and volume fraction ϕ^α of phase α are linked by the partial molar volume Ω^α:

$$c^\alpha = \frac{\phi^\alpha}{\Omega^\alpha}.$$

For convenience, we introduce a normalized swelling factor

$$\omega^{\alpha} = \frac{\Omega^{\alpha}}{\bar{\Omega}_R},$$

which measures the current molar volume relative to a reference $\bar{\Omega}_R$. The referential volume fraction is then defined as

$$\phi_R^{\alpha} = \phi^{\alpha} \frac{J^c}{\omega^{\alpha}},$$

where J^c is the chemical contribution to the volume change.

6.4.5 Reaction rate associated with reaction (6.180)

As discussed in the previous subsection, electrochemical reactions in Na–Sn electrodes proceed through multiple sequential steps, with Na atoms diffusing and reacting with Sn to form intermetallic compounds. As discussed in the previous subsection, electrochemical reactions in Na–Sn electrodes proceed through multiple sequential steps, with Na atoms diffusing and reacting with Sn to form intermetallic compounds. Among these, the transformation 6.180 is of particular importance, since $NaSn_3$ represents the first stable alloy phase during sodiation and acts as a precursor for further transformations into Na_9Sn_4 and $Na_{15}Sn_4$. To capture the reaction (6.180) within a volume-fraction framework, the classical law of mass action is reformulated in terms of phase fractions and swelling factors.

Based on these definitions and following the generalized formulation in [88, 119, 128], the reaction rate for Eq. (6.180) reads

$$w_R^{(6.180)} = k_{f_R}^{(2)} \cdot \frac{\phi_R^{\mathrm{Na}}\, \omega^{\mathrm{Na}}}{J^c - \phi_R^{\mathrm{Na}}\, \omega^{\mathrm{Na}}} \cdot \left(\frac{\phi_R^{\mathrm{Sn}}\, \omega^{\mathrm{Sn}}}{J^c - \phi_R^{\mathrm{Sn}}\, \omega^{\mathrm{Sn}}} \right)^3 - k_{b_R}^{(2)} \cdot \frac{\phi_R^{\mathrm{NaSn_3}}\, \omega^{\mathrm{NaSn_3}}}{J^c - \phi_R^{\mathrm{NaSn_3}}\, \omega^{\mathrm{NaSn_3}}}. \tag{6.186}$$

where the forward and backward rate constants are related to the deformation through

$$k_{f_R}^{(2)} = k_{b_R}^{(2)} = J\, k^{(2)}.$$

and the total chemical Jacobian J^c is obtained by summing over all species:

$$\begin{aligned} J^c &= \sum_{\alpha} \phi_R^{\alpha}\, \omega^{\alpha} \qquad (6.187) \\ &= \phi_R^{\mathrm{Na}} \omega^{\mathrm{Na}} + \phi_R^{\mathrm{Sn}} \omega^{\mathrm{Sn}} + \phi_R^{\mathrm{NaSn_3}} \omega^{\mathrm{NaSn_3}} + \phi_R^{\mathrm{Na_9Sn_4}} \omega^{\mathrm{Na_9Sn_4}} + \\ &\phi_R^{\mathrm{Na_{15}Sn_4}} \omega^{\mathrm{Na_{15}Sn_4}} + \phi_R^{\mathrm{V}} \omega^{\mathrm{V}}. \end{aligned}$$

Using the volume-filling constraint

$$\sum_{\alpha} \phi_R^{\alpha} = \phi_R^{\mathrm{Na}} + \phi_R^{\mathrm{Sn}} + \phi_R^{\mathrm{NaSn_3}} + \phi_R^{\mathrm{Na_9Sn_4}} + \phi_R^{\mathrm{Na_{15}Sn_4}} + \phi_R^{\mathrm{V}} = 1, \tag{6.188}$$

and eliminating ϕ_R^{V}

$$\phi_R^{\mathrm{V}} = 1 - \left(\phi_R^{\mathrm{Na}} + \phi_R^{\mathrm{Sn}} + \phi_R^{\mathrm{NaSn_3}} + \phi_R^{\mathrm{Na_9Sn_4}} + \phi_R^{\mathrm{Na_{15}Sn_4}}\right). \tag{6.189}$$

yields a more compact form for J^c and, upon substitution, the reaction rate can be simplified as

$$w_R^{(6.180)} = k_{f_R}^{(2)} \cdot \frac{\phi_R^{\mathrm{Na}}\, \omega^{\mathrm{Na}}}{A_1} \cdot \left(\frac{\phi^{\mathrm{Sn}} \omega^{\mathrm{Sn}}}{A_2}\right)^3 - k_{b_R}^{(2)} \cdot \frac{\phi_R^{\mathrm{NaSn_3}}\, \omega^{\mathrm{NaSn_3}}}{A_3}, \tag{6.190}$$

Here, A_1, A_2, A_3 are the auxiliary quantities defined explicitly as

$$\begin{aligned}
A_1 &= \phi^{\mathrm{Sn}}\omega^{\mathrm{Sn}} + \phi_R^{\mathrm{NaSn_3}}\omega^{\mathrm{NaSn_3}} + \phi_R^{\mathrm{Na_9Sn_4}}\omega^{\mathrm{Na_9Sn_4}} + \phi_R^{\mathrm{Na_{15}Sn_4}}\omega^{\mathrm{Na_{15}Sn_4}} \\
&\quad + \left(1 - \phi_R^{\mathrm{Na}} - \phi_R^{\mathrm{Sn}} - \phi_R^{\mathrm{NaSn_3}} - \phi_R^{\mathrm{Na_9Sn_4}} - \phi_R^{\mathrm{Na_{15}Sn_4}}\right)\omega^{\mathrm{V}}, \\
A_2 &= \phi_R^{\mathrm{Na}}\omega^{\mathrm{Na}} + \phi_R^{\mathrm{NaSn_3}}\omega^{\mathrm{NaSn_3}} + \phi_R^{\mathrm{Na_9Sn_4}}\omega^{\mathrm{Na_9Sn_4}} + \phi_R^{\mathrm{Na_{15}Sn_4}}\omega^{\mathrm{Na_{15}Sn_4}} \\
&\quad + \left(1 - \phi_R^{\mathrm{Na}} - \phi_R^{\mathrm{Sn}} - \phi_R^{\mathrm{NaSn_3}} - \phi_R^{\mathrm{Na_9Sn_4}} - \phi_R^{\mathrm{Na_{15}Sn_4}}\right)\omega^{\mathrm{V}}, \\
A_3 &= \phi^{\mathrm{Sn}}\omega^{\mathrm{Sn}} + \phi_R^{\mathrm{Na}}\omega^{\mathrm{Na}} + \phi_R^{\mathrm{Na_9Sn_4}}\omega^{\mathrm{Na_9Sn_4}} + \phi_R^{\mathrm{Na_{15}Sn_4}}\omega^{\mathrm{Na_{15}Sn_4}} \\
&\quad + \left(1 - \phi_R^{\mathrm{Na}} - \phi_R^{\mathrm{Sn}} - \phi_R^{\mathrm{NaSn_3}} - \phi_R^{\mathrm{Na_9Sn_4}} - \phi_R^{\mathrm{Na_{15}Sn_4}}\right)\omega^{\mathrm{V}}.
\end{aligned} \tag{6.191}$$

This formulation highlights how the phase-field approach with volume fractions naturally embeds both stoichiometric constraints and volumetric effects. The reaction rate depends not only on local Na and Sn fractions, but also on the swelling factors ω^{α} and the chemical Jacobian J^c, thereby coupling reaction kinetics to volumetric changes during phase transformations. This framework provides a consistent basis for modeling subsequent transformations into Na_9Sn_4 and $Na_{15}Sn_4$.

To study the stability of the reaction rate expression derived, we compute the variation with respect to the volume fractions of the relevant species (see Appendix A.11). This provides the linearized sensitivity of the reaction kinetics to perturbations in ϕ_R^{α}, which is needed when formulating the weak form and implementing Newton–Raphson iterations for numerical simulations.

6.4.6 Reaction rate associated with reaction (6.181)

The second major phase transformation in the Na–Sn system corresponds to the reaction 6.181 which describes the growth of the Na-rich Na_9Sn_4

intermediate phase at the expense of sodium, pristine Sn, and $NaSn_3$. This reaction is crucial because it marks the progression from relatively Na-poor intermetallics to more Na-rich alloys, accompanied by significant volumetric expansion.

Following the general mass–action framework introduced earlier, the corresponding reaction rate $w_{\mathrm{R}}^{(6.181)}$ is expressed in terms of concentrations and volume fractions as [88, 119, 128]:

$$w_{\mathrm{R}}^{(6.181)} = k_{f_{\mathrm{R}}}^{(3)} \cdot \left(\frac{\phi_{\mathrm{R}}^{\mathrm{Na}} \omega^{\mathrm{Na}}}{J^c - \phi_{\mathrm{R}}^{\mathrm{Na}} \omega^{\mathrm{Na}}} \right)^8 \cdot \frac{\phi_{\mathrm{R}}^{\mathrm{NaSn_3}} \omega^{\mathrm{NaSn_3}}}{J^c - \phi_{\mathrm{R}}^{\mathrm{NaSn_3}} \omega^{\mathrm{NaSn_3}}} \cdot \frac{\phi_{\mathrm{R}}^{\mathrm{Sn}} \omega^{\mathrm{Sn}}}{J^c - \phi_{\mathrm{R}}^{\mathrm{Sn}} \omega^{\mathrm{Sn}}} \tag{6.192}$$

$$- k_{b_{\mathrm{R}}}^{(3)} \cdot \frac{\phi_{\mathrm{R}}^{\mathrm{Na_9Sn_4}} \omega^{\mathrm{Na_9Sn_4}}}{J^c - \phi_{\mathrm{R}}^{\mathrm{Na_9Sn_4}} \omega^{\mathrm{Na_9Sn_4}}}.$$

Here, as in the previous case,

$$k_{f_{\mathrm{R}}}^{(3)} = k_{b_{\mathrm{R}}}^{(3)} = J\, k^{(3)}, \tag{6.193}$$

so that the forward and backward rates evolve consistently with the local deformation.

Expanding the Jacobian J^c using the volume fraction constraint, the reaction rate becomes

After simplification, we obtain the compact form

$$w_{\mathrm{R}}^{(6.181)} = k_{f_R}^{(3)} \cdot \left(\frac{\phi_R^{\mathrm{Na}} \omega^{\mathrm{Na}}}{B_1} \right)^8 \cdot \frac{\phi_R^{\mathrm{NaSn_3}} \omega^{\mathrm{NaSn_3}}}{B_3} \cdot \frac{\phi^{\mathrm{Sn}} \omega^{\mathrm{Sn}}}{B_2} - k_{b_R}^{(3)} \cdot \frac{\phi_R^{\mathrm{Na_9Sn_4}} \omega^{\mathrm{Na_9Sn_4}}}{B_4}. \tag{6.194}$$

The auxiliary terms $B_1, \ldots, B_4$ collect combinations of volume fractions and swelling factors to simplify notation:

$$\begin{aligned}
B_1 &= \phi^{\mathrm{Sn}} \omega^{\mathrm{Sn}} + \phi_R^{\mathrm{NaSn_3}} \omega^{\mathrm{NaSn_3}} + \phi_R^{\mathrm{Na_9Sn_4}} \omega^{\mathrm{Na_9Sn_4}} + \phi_R^{\mathrm{Na_{15}Sn_4}} \omega^{\mathrm{Na_{15}Sn_4}} \\
&+ \left(1 - \phi_R^{\mathrm{Na}} - \phi_R^{\mathrm{Sn}} - \phi_R^{\mathrm{NaSn_3}} - \phi_R^{\mathrm{Na_9Sn_4}} - \phi_R^{\mathrm{Na_{15}Sn_4}}\right) \omega^{\mathrm{V}}, \\
B_2 &= \phi_R^{\mathrm{Na}} \omega^{\mathrm{Na}} + \phi_R^{\mathrm{NaSn_3}} \omega^{\mathrm{NaSn_3}} + \phi_R^{\mathrm{Na_9Sn_4}} \omega^{\mathrm{Na_9Sn_4}} + \phi_R^{\mathrm{Na_{15}Sn_4}} \omega^{\mathrm{Na_{15}Sn_4}} \\
&+ \left(1 - \phi_R^{\mathrm{Na}} - \phi_R^{\mathrm{Sn}} - \phi_R^{\mathrm{NaSn_3}} - \phi_R^{\mathrm{Na_9Sn_4}} - \phi_R^{\mathrm{Na_{15}Sn_4}}\right) \omega^{\mathrm{V}}, \\
B_3 &= \phi^{\mathrm{Sn}} \omega^{\mathrm{Sn}} + \phi_R^{\mathrm{Na}} \omega^{\mathrm{Na}} + \phi_R^{\mathrm{Na_9Sn_4}} \omega^{\mathrm{Na_9Sn_4}} + \phi_R^{\mathrm{Na_{15}Sn_4}} \omega^{\mathrm{Na_{15}Sn_4}} \\
&+ \left(1 - \phi_R^{\mathrm{Na}} - \phi_R^{\mathrm{Sn}} - \phi_R^{\mathrm{NaSn_3}} - \phi_R^{\mathrm{Na_9Sn_4}} - \phi_R^{\mathrm{Na_{15}Sn_4}}\right) \omega^{\mathrm{V}}, \\
B_4 &= \phi^{\mathrm{Sn}} \omega^{\mathrm{Sn}} + \phi_R^{\mathrm{Na}} \omega^{\mathrm{Na}} + \phi_R^{\mathrm{NaSn_3}} \omega^{\mathrm{NaSn_3}} + \phi_R^{\mathrm{Na_{15}Sn_4}} \omega^{\mathrm{Na_{15}Sn_4}} \\
&+ \left(1 - \phi_R^{\mathrm{Na}} - \phi_R^{\mathrm{Sn}} - \phi_R^{\mathrm{NaSn_3}} - \phi_R^{\mathrm{Na_9Sn_4}} - \phi_R^{\mathrm{Na_{15}Sn_4}}\right) \omega^{\mathrm{V}}.
\end{aligned} \tag{6.195}$$

This formulation emphasizes the highly nonlinear dependence of the $NaSn_3 \rightarrow Na_9Sn_4$ reaction rate on the sodium volume fraction and on the coexistence of multiple phases, highlighting the complex interplay of kinetics and mechanics during intermediate alloy formation.

The variation of the reaction rate required for computing the Gateaux derivative is provided in Appendix A.11.

6.4.7 Reaction rate associated with reaction (6.182)

We now consider the final sodiation step in the Na–Sn system, namely the bulk transformation of Na_9Sn_4 into $Na_{15}Sn_4$ mediated by mobile Na. Consistent with the volume-fraction formulation, the reaction rate is written in mass–action form using the referential phase fractions ϕ_R^α and the species swelling factors ω^α. As before, the finite-strain setting enters through the chemical Jacobian J^c in the activity-like ratios and through the referential rate factors $k_{\bullet R}^{(4)} = J\,k^{(4)}$.

The reaction rate $w_{\mathrm{R}}^{(6.182)}$ is related to the concentrations and volume fraction via the mass action law, as [88, 119, 128]

$$w_{\mathrm{R}}^{(6.182)} = k_{f_{\mathrm{R}}}^{(4)} \cdot \left(\frac{\phi_{\mathrm{R}}^{\mathrm{Na}} \omega^{\mathrm{Na}}}{J^c - \phi_{\mathrm{R}}^{\mathrm{Na}} \omega^{\mathrm{Na}}} \right)^6 \cdot \frac{\phi_{\mathrm{R}}^{\mathrm{Na_9Sn_4}} \omega^{\mathrm{Na_9Sn_4}}}{J^c - \phi_{\mathrm{R}}^{\mathrm{Na_9Sn_4}} \omega^{\mathrm{Na_9Sn_4}}} - k_{b_{\mathrm{R}}}^{(4)} \cdot \frac{\phi_{\mathrm{R}}^{\mathrm{Na_{15}Sn_4}} \omega^{\mathrm{Na_{15}Sn_4}}}{J^c - \phi_{\mathrm{R}}^{\mathrm{Na_{15}Sn_4}} \omega^{\mathrm{Na_{15}Sn_4}}}, \tag{6.196}$$

$$k_{f_{\mathrm{R}}}^{(4)} = k_{b_{\mathrm{R}}}^{(4)} = J\,k^{(4)} \tag{6.197}$$

After introducing compact denominators to streamline implementation, we obtain

$$w_R^{(6.182)} = k_{f_R}^{(4)} \cdot \left(\frac{\phi_R^{\mathrm{Na}}\,\omega^{\mathrm{Na}}}{C_1} \right)^6 \cdot \frac{\phi_{\mathrm{R}}^{\mathrm{Na_9Sn_4}} \omega^{\mathrm{Na_9Sn_4}}}{C_2} - k_{b_R}^{(4)} \cdot \frac{\phi_R^{\mathrm{Na_{15}Sn_4}}\,\omega^{\mathrm{Na_{15}Sn_4}}}{C_3} \tag{6.198}$$

where

$$\begin{aligned}
C_1 &= \phi^{\mathrm{Sn}}\omega^{\mathrm{Sn}} + \phi_R^{\mathrm{NaSn_3}}\omega^{\mathrm{NaSn_3}} + \phi_R^{\mathrm{Na_9Sn_4}}\omega^{\mathrm{Na_9Sn_4}} + \phi_R^{\mathrm{Na_{15}Sn_4}}\omega^{\mathrm{Na_{15}Sn_4}} \\
&+ \left(1 - \phi_R^{\mathrm{Na}} - \phi_R^{\mathrm{Sn}} - \phi_R^{\mathrm{NaSn_3}} - \phi_R^{\mathrm{Na_9Sn_4}} - \phi_R^{\mathrm{Na_{15}Sn_4}}\right)\omega^{\mathrm{V}}, \\
C_2 &= \phi^{\mathrm{Sn}}\omega^{\mathrm{Sn}} + \phi_R^{\mathrm{Na}}\omega^{\mathrm{Na}} + \phi_R^{\mathrm{NaSn_3}}\omega^{\mathrm{NaSn_3}} + \phi_R^{\mathrm{Na_{15}Sn_4}}\omega^{\mathrm{Na_{15}Sn_4}} \\
&+ \left(1 - \phi_R^{\mathrm{Na}} - \phi_R^{\mathrm{Sn}} - \phi_R^{\mathrm{NaSn_3}} - \phi_R^{\mathrm{Na_9Sn_4}} - \phi_R^{\mathrm{Na_{15}Sn_4}}\right)\omega^{\mathrm{V}}, \\
C_3 &= \phi^{\mathrm{Sn}}\omega^{\mathrm{Sn}} + \phi_R^{\mathrm{Na}}\omega^{\mathrm{Na}} + \phi_R^{\mathrm{NaSn_3}}\omega^{\mathrm{NaSn_3}} + \phi_R^{\mathrm{Na_9Sn_4}}\omega^{\mathrm{Na_9Sn_4}} \\
&+ \left(1 - \phi_R^{\mathrm{Na}} - \phi_R^{\mathrm{Sn}} - \phi_R^{\mathrm{NaSn_3}} - \phi_R^{\mathrm{Na_9Sn_4}} - \phi_R^{\mathrm{Na_{15}Sn_4}}\right)\omega^{\mathrm{V}}.
\end{aligned} \tag{6.199}$$

The denominators C_1, C_2, and C_3 collect the contributions of the coexisting phases and their swelling factors to the activity-like terms in the forward and backward rates. They are functions of the referential volume fractions ϕ_R^α and thus automatically satisfy the local volume-filling constraint through the definition of J^c used earlier. This compact form is convenient for assembling residuals and Jacobians in a Newton–Raphson scheme while preserving the exact mass–action structure and the finite-strain chemo–mechanical coupling.

Details of the reaction rate variation used in the Gateaux derivative computation are given in Appendix A.11.

6.4.8 Mass balance equations

The mass balance equations describe the spatial and temporal evolution of the referential volume fraction of each species α. These equations account for both diffusion and chemical reactions, ensuring conservation of mass throughout the sodiation process.

For computational convenience, the reference molar volume and saturation concentration are set to unity:

$$\bar{\Omega}_R = 1, \qquad c^\alpha_{\mathrm{sat,R}} = 1,$$

so that $c_R^\alpha = \phi_R^\alpha$. The mass balance equations simplify to:

$$\frac{\partial \phi_{\mathrm{R}}^{\mathrm{Na}}}{\partial t} + \nabla \cdot \vec{h}_{\mathrm{Na}} = -w_{\mathrm{R}}^{(6.180)} - 8\, w_{\mathrm{R}}^{(6.181)} - 6\, w_{\mathrm{R}}^{(6.182)}, \tag{6.200a}$$

$$\frac{\partial \phi_{\mathrm{R}}^{\mathrm{Sn}}}{\partial t} + \nabla \cdot \vec{h}_{\mathrm{Sn}} = -3\, w_{\mathrm{R}}^{(6.180)} - w_{\mathrm{R}}^{(6.181)}, \tag{6.200b}$$

$$\frac{\partial \phi_{\mathrm{R}}^{\mathrm{NaSn_3}}}{\partial t} + \nabla \cdot \vec{h}_{\mathrm{NaSn_3}} = w_{\mathrm{R}}^{(6.180)} - w_{\mathrm{R}}^{(6.181)}, \tag{6.200c}$$

$$\frac{\partial \phi_{\mathrm{R}}^{\mathrm{Na_9Sn_4}}}{\partial t} + \nabla \cdot \vec{h}_{\mathrm{Na_9Sn_4}} = w_{\mathrm{R}}^{(6.181)} - w_{\mathrm{R}}^{(6.182)}, \tag{6.200d}$$

$$\frac{\partial \phi_{\mathrm{R}}^{\mathrm{Na_{15}Sn_4}}}{\partial t} + \nabla \cdot \vec{h}_{\mathrm{Na_{15}Sn_4}} = w_{\mathrm{R}}^{(6.182)}, \tag{6.200e}$$

$$\frac{\partial \phi_{\mathrm{R}}^{\mathrm{V}}}{\partial t} + \nabla \cdot \vec{h}_{\mathrm{V}} = 0\,. \tag{6.200f}$$

The referential Na flux $\vec{h}_{\mathrm{Na}}$ comprises three terms: (i) a Fickian diffusion driven by gradients of $\phi_{\mathrm{R}}^{\mathrm{Na}}$, (ii) a penalty term that enforces the auxiliary field $\phi_R^{\mathrm{Na},*}$ (used for constraint regularization), and (iii) a chemo-mechanical drift driven by the mechanical contribution to the chemical potential using Eq. (6.138):

$$\vec{h}_{\mathrm{Na}}(\phi_R^{\mathrm{Na}}, \phi_R^{\mathrm{Na},*}, \vec{u}) = -\mathbb{D} \nabla \phi_R^{\mathrm{Na}} - \beta\, M(\phi_R^{\mathrm{Na}})\, \nabla(\phi_R^{\mathrm{Na}} - \phi_R^{\mathrm{Na},*}) - M(\phi_R^{\mathrm{Na}})\, \nabla \mu_{\mathrm{Na}}^{mech}(\phi_R^{\mathrm{Na}}, \vec{u}) \tag{6.201}$$

where the effective diffusivity $\mathbb{D}$ incorporates the Cahn–Hilliard interaction parameter χ through the mobility $M(\phi_R^{\mathrm{Na}})$:

$$\mathbb{D} = \mathbb{D} - 2\,M(\phi_R^{\mathrm{Na}})\,RT\,\chi, \tag{6.202}$$

$$M(\phi_R^{\mathrm{Na}}) = \frac{\mathbb{D}}{RT}\,\phi_R^{\mathrm{Na}}\,\left(1-\phi_R^{\mathrm{Na}}\right), \tag{6.203}$$

$\phi_R^{\mathrm{Na}} - \phi_R^{\mathrm{Na},*}$ represents the penalty term enforcing the constraint between the physical and auxiliary fields (Section 6.4.9), and μ_{Na}^{mech} couples ionic transport to the elastic fields (Section 6.4.10).

Among all species, sodium (Na) is the only mobile species. All other phases are considered immobile due to their large size and limited diffusivity:

$$\vec{h}_{\mathrm{Sn}} = \vec{h}_{\mathrm{NaSn_3}} = \vec{h}_{\mathrm{Na_9Sn_4}} = \vec{h}_{\mathrm{Na_{15}Sn_4}} = \vec{0}. \tag{6.204}$$

To satisfy the mixture constraint of Groot–Mazur [119], $\sum_\alpha \vec{h}_\alpha = \vec{0}$, we introduce a vacancy flux

$$\vec{h}_{\mathrm{V}} + \vec{h}_{\mathrm{Na}} = \vec{0}\,. \tag{6.205}$$

Vacancies keep the total sum of fluxes zero and ensure space is always fully filled.

6.4.8.1 Mass balance equation for ϕ^{Na}

We now specialize the mass balance equation (6.200a) to the only mobile species, sodium. In this case, the evolution of the referential volume fraction $\phi_{\mathrm{R}}^{\mathrm{Na}}$ is governed by diffusion and by the three bulk reactions consuming or producing sodium, with stoichiometric coefficients consistent with the mechanisms introduced earlier.

Substituting the flux (6.201) into the conservation law yields the PDE in strong form:

$$\begin{aligned}\frac{\partial \phi_{\mathrm{R}}^{\mathrm{Na}}}{\partial t} &- \nabla\cdot\mathbb{D}\,\nabla\phi_{\mathrm{R}}^{\mathrm{Na}} - \nabla\cdot\beta\,M(\phi_{\mathrm{R}}^{\mathrm{Na}})\,\nabla(\phi_{\mathrm{R}}^{\mathrm{Na}} - \phi_{\mathrm{R}}^{\mathrm{Na},*}) \\ &- \nabla\cdot M(\phi_R^{\mathrm{Na}})\,\nabla\mu_{\mathrm{Na}}^{mech}(\phi_R^{\mathrm{Na}},\vec{u}) \\ &= -w_{\mathrm{R}}^{(6.180)} - 6w_{\mathrm{R}}^{(6.181)} - 6w_{\mathrm{R}}^{(6.182)}.\end{aligned} \tag{6.206}$$

For 1D problems ($x \in [0, L]$), the equation becomes

$$\begin{aligned}&\frac{\partial \phi_{\mathrm{R}}^{\mathrm{Na}}}{\partial t} - \frac{\partial}{\partial x}\left(\mathbb{D}\frac{\partial \phi_{\mathrm{R}}^{\mathrm{Na}}}{\partial x}\right) - \frac{\partial}{\partial x}\left(\beta\,M(\phi_{\mathrm{R}}^{\mathrm{Na}})\,\left(\frac{\partial \phi_{\mathrm{R}}^{\mathrm{Na}}}{\partial x} - \frac{\partial \phi_R^{\mathrm{Na},*}}{\partial x}\right)\right) \\ &- \frac{\partial}{\partial x}\left(M(\phi_R^{\mathrm{Na}})\frac{\partial \mu_{\mathrm{Na}}^{mech}(\phi_R^{\mathrm{Na}},\vec{u})}{\partial x}\right) \\ &= -w_{\mathrm{R}}^{(6.180)} - 6w_{\mathrm{R}}^{(6.181)} - 6w_{\mathrm{R}}^{(6.182)}\ .\end{aligned} \tag{6.207}$$

For convenience, we denote the 1D mechanical flux contribution and the total 1D flux as

$$h_{1D}^{mech,\ \mathrm{Na}} = -M(\phi_R^{\mathrm{Na}})\,\frac{\partial \mu_{\mathrm{Na}}^{mech}(\phi_R^{\mathrm{Na}}, \vec{u})}{\partial x}, \tag{6.208}$$

$$h_{1D}^{\mathrm{Na}} = -\mathbb{P}\,\frac{\partial \phi_R^{\mathrm{Na}}}{\partial x} - \beta\, M(\phi_R^{\mathrm{Na}})\,\left(\frac{\partial \phi^{\mathrm{Na}}}{\partial x} - \frac{\partial \phi_R^{\mathrm{Na},*}}{\partial x}\right) + h_{1D}^{mech,\ \mathrm{Na}}. \tag{6.209}$$

6.4.8.1.1 1D Weak form

Multiplying (6.207) by a test function φ_i^{ϕ} and integrating over $[0, L]$, we obtain

$$\begin{aligned}
&\int_0^L \varphi_i^{\phi} \frac{\partial \phi_{\mathrm{R}}^{\mathrm{Na}}}{\partial t}\,\mathrm{d}x - \int_0^L \varphi_i^{\phi} \frac{\partial}{\partial x}\left(\mathbb{P}\frac{\partial \phi_{\mathrm{R}}^{\mathrm{Na}}}{\partial x}\right)\,\mathrm{d}x \\
&- \int_0^L \varphi_i^{\phi} \frac{\partial}{\partial x}\left(\beta\, M(\phi_{\mathrm{R}}^{\mathrm{Na}})\,\left(\frac{\partial \phi_{\mathrm{R}}^{\mathrm{Na}}}{\partial x} - \frac{\partial \phi_R^{\mathrm{Na},*}}{\partial x}\right)\right)\,\mathrm{d}x \\
&- \int_0^L \varphi_i^{\phi} \frac{\partial}{\partial x}\left(M(\phi_R^{\mathrm{Na}})\frac{\partial \mu_{\mathrm{Na}}^{mech}(\phi_R^{\mathrm{Na}}, \vec{u})}{\partial x}\right)\,\mathrm{d}x \\
&= \int_0^L (-w_{\mathrm{R}}^{(6.180)} - 6w_{\mathrm{R}}^{(6.181)} - 6w_{\mathrm{R}}^{(6.182)})\,\mathrm{d}x\,.
\end{aligned} \tag{6.210}$$

Integrating by parts gives

$$\begin{aligned}
&\int_0^L \varphi_i^{\phi} \frac{\partial \phi_{\mathrm{R}}^{\mathrm{Na}}}{\partial t}\,\mathrm{d}x + \int_0^L \frac{\partial \varphi_i^{\phi}}{\partial x}\,\mathbb{P}\frac{\partial \phi_{\mathrm{R}}^{\mathrm{Na}}}{\partial x}\,\mathrm{d}x + \int_0^L \frac{\partial \varphi_i^{\phi}}{\partial x}\,\beta\, M(\phi_{\mathrm{R}}^{\mathrm{Na}})\,\left(\frac{\partial \phi_{\mathrm{R}}^{\mathrm{Na}}}{\partial x} - \frac{\partial \phi_R^{\mathrm{Na},*}}{\partial x}\right)\,\mathrm{d}x \\
&+ \int_0^L \frac{\partial \varphi_i^{\phi}}{\partial x} M(\phi_R^{\mathrm{Na}}) \frac{\partial \mu_{\mathrm{Na}}^{mech}(\phi_R^{\mathrm{Na}}, \vec{u})}{\partial x}\,\mathrm{d}x \\
&- \varphi_i^{\phi}\,\left(\mathbb{P}\frac{\partial \phi_{\mathrm{R}}^{\mathrm{Na}}}{\partial x} + \beta\, M(\phi_{\mathrm{R}}^{\mathrm{Na}})\,\left(\frac{\partial \phi_{\mathrm{R}}^{\mathrm{Na}}}{\partial x} - \frac{\partial \phi_R^{\mathrm{Na},*}}{\partial x}\right) - h_{1D}^{mech,\ \mathrm{Na}}\right)\Big|_0^L \\
&= \int_0^L \varphi_i^{\phi}\,(-w_{\mathrm{R}}^{(6.180)} - 6w_{\mathrm{R}}^{(6.181)} - 6w_{\mathrm{R}}^{(6.182)})\,\mathrm{d}x\,.
\end{aligned} \tag{6.211}$$

Using Eq. (6.67) we obtain

$$\int_0^L \varphi_i^\phi \frac{\partial \phi_{\mathrm{R}}^{\mathrm{Na}}}{\partial t}\,\mathrm{d}x + \int_0^L \frac{\partial \varphi_i^\phi}{\partial x}\, \mathbb{D} \frac{\partial \phi_{\mathrm{R}}^{\mathrm{Na}}}{\partial x}\,\mathrm{d}x + \int_0^L \frac{\partial \varphi_i^\phi}{\partial x}\,\beta\, M(\phi_{\mathrm{R}}^{\mathrm{Na}}) \left(\frac{\partial \phi_{\mathrm{R}}^{\mathrm{Na}}}{\partial x} - \frac{\partial \phi_R^{\mathrm{Na},*}}{\partial x} \right) \mathrm{d}x \tag{6.212}$$
$$+ \int_0^L \frac{\partial \varphi_i^\phi}{\partial x} M(\phi_R^{\mathrm{Na}}) \frac{\partial \mu_{\mathrm{Na}}^{mech}(\phi_R^{\mathrm{Na}}, \vec{u})}{\partial x}\,\mathrm{d}x + \varphi_i^\phi\, \vec{h}_{1D}^{\mathrm{Na}}\Big|_0^L$$
$$= \int_0^L \varphi_i^\phi\, (-w_{\mathrm{R}}^{(6.180)} - 6w_{\mathrm{R}}^{(6.181)} - 6w_{\mathrm{R}}^{(6.182)})\,\mathrm{d}x\,.$$

Invoking Eq. (6.61) yields

$$\int_0^L \varphi_i^\phi \frac{\partial \phi_{\mathrm{R}}^{\mathrm{Na}}}{\partial t}\,\mathrm{d}x + \mathbb{D} \int_0^L \frac{\partial \varphi_i^\phi}{\partial x}\, \frac{\partial \phi_{\mathrm{R}}^{\mathrm{Na}}}{\partial x}\,\mathrm{d}x - 2\,RT\chi \int_0^L \frac{\partial \varphi_i^\phi}{\partial x}\, M(\phi_{\mathrm{R}}^{\mathrm{Na}})\, \frac{\partial \phi_{\mathrm{R}}^{\mathrm{Na}}}{\partial x}\,\mathrm{d}x \tag{6.213}$$
$$+ \int_0^L \frac{\partial \varphi_i^\phi}{\partial x}\,\beta\, M(\phi_{\mathrm{R}}^{\mathrm{Na}}) \left(\frac{\partial \phi_{\mathrm{R}}^{\mathrm{Na}}}{\partial x} - \frac{\partial \phi_R^{\mathrm{Na},*}}{\partial x} \right) \mathrm{d}x$$
$$+ \int_0^L \frac{\partial \varphi_i^\phi}{\partial x}\, M(\phi_R^{\mathrm{Na}})\, \frac{\partial \mu_{\mathrm{Na}}^{mech}(\phi_R^{\mathrm{Na}}, \vec{u})}{\partial x}\mathrm{d}x$$
$$+ \varphi_i^\phi\, \vec{h}_{1D}^{\mathrm{Na}}\Big|_0^L = \int_0^L \varphi_i^\phi\, (-w_{\mathrm{R}}^{(6.180)} - 6w_{\mathrm{R}}^{(6.181)} - 6w_{\mathrm{R}}^{(6.182)})\,\mathrm{d}x\,.$$

6.4.8.1.2 Separated variables discretization

Using separated variables,

$$\phi_{\mathrm{R}}^{\mathrm{Na}}(x,t) = \sum_j \phi_j^{\mathrm{Na}}(t)\varphi_j^\phi(x), \quad \phi_R^{\mathrm{Na},*}(x,t) = \sum_j \phi_j^{\mathrm{Na},*}(t)\varphi_j^{\phi,*}(x), \tag{6.214}$$
$$\mu^{mech,\ \mathrm{Na}}(x,t) = \sum_j \mu_j^{mech,\ \mathrm{Na}}(t)\varphi_j^\gamma(x),$$

we obtain the semi-discrete system

$$\int_0^L \varphi_i^\phi \varphi_j^\phi \, \mathrm{d}x \; \frac{\partial \phi_j^{\mathrm{Na}}(t)}{\partial t} + \mathbb{D} \int_0^L \frac{\partial \varphi_i^\phi}{\partial x} \frac{\partial \varphi_j^\phi}{\partial x} \, \mathrm{d}x \; \phi_j^{\mathrm{Na}}(t) \tag{6.215}$$

$$- 2 \, RT\chi \int_0^L \frac{\partial \varphi_i^\phi}{\partial x} \, M(\phi_R^{\mathrm{Na}}) \, \frac{\partial \varphi_j^\phi}{\partial x} \, \mathrm{d}x \; \phi_j^{\mathrm{Na}}(t)$$

$$+ \int_0^L \beta \, M(\phi_R^{\mathrm{Na}}) \, \frac{\partial \varphi_i^\phi}{\partial x} \frac{\partial \varphi_j^\phi}{\partial x} \, \mathrm{d}x \; \phi_j^{\mathrm{Na}}(t) - \int_0^L \beta \, M(\phi_R^{\mathrm{Na}}) \, \frac{\partial \varphi_i^\phi}{\partial x} \frac{\partial \varphi_j^{\phi,*}}{\partial x} \, \mathrm{d}x \; \phi_j^{\mathrm{Na},*}(t)$$

$$+ \int_0^L M(\phi_R^{\mathrm{Na}}) \frac{\partial \varphi_i^\phi}{\partial x} \frac{\partial \varphi_j^\gamma}{\partial x} \, \mathrm{d}x \, \mu_j^{mech,\ \mathrm{Na}}(t)$$

$$= \int_0^L \varphi_i^\phi \, (-w_{\mathrm{R}}^{(6.180)} - 6 w_{\mathrm{R}}^{(6.181)} - 6 w_{\mathrm{R}}^{(6.182)}) \, \mathrm{d}x \; - \varphi_i^\phi \vec{h}_{1D}^{\mathrm{Na}} \Big|_0^L .$$

6.4.8.1.3 Euler integration schemes

With the forward/backward Euler approximation

$$\frac{\partial \phi_j^{\mathrm{Na}}(t)}{\partial t} \approx \frac{\phi_j^{\mathrm{Na}}(t + \Delta t) - \phi_j^{\mathrm{Na}}(t)}{\Delta t},$$

we obtain the explicit (Forward Euler, linear in the state at t):

$$\int_0^L \varphi_i^\phi \varphi_j^\phi \, \mathrm{d}x \; \frac{\phi_j^{\mathrm{Na}}(t + \Delta t)}{\Delta t} + \mathbb{D} \int_0^L \frac{\partial \varphi_i^\phi}{\partial x} \frac{\partial \varphi_j^\phi}{\partial x} \, \mathrm{d}x \; \phi_j^{\mathrm{Na}}(t) \tag{6.216}$$

$$- 2 \, RT\chi \int_0^L \frac{\partial \varphi_i^\phi}{\partial x} \, M(\phi_R^{\mathrm{Na}}(t)) \, \frac{\partial \varphi_j^\phi}{\partial x} \, \mathrm{d}x \; \phi_j^{\mathrm{Na}}(t)$$

$$+ \int_0^L \beta \, M(\phi_R^{\mathrm{Na}}(t)) \, \frac{\partial \varphi_i^\phi}{\partial x} \frac{\partial \varphi_j^\phi}{\partial x} \, \mathrm{d}x \; \phi_j^{\mathrm{Na}}(t)$$

$$- \int_0^L \beta \, M(\phi_R^{\mathrm{Na}}(t)) \, \frac{\partial \varphi_i^\phi}{\partial x} \frac{\partial \varphi_j^{\phi,*}}{\partial x} \, \mathrm{d}x \; \phi_j^{\mathrm{Na},*}(t)$$

$$+ \int_0^L M(\phi_R^{\mathrm{Na}}(t)) \frac{\partial \varphi_i^\phi}{\partial x} \frac{\partial \varphi_j^\gamma}{\partial x} \, \mathrm{d}x \, \mu_j^{mech-\ Na}(t) = \int_0^L \varphi_i^\phi \varphi_j^\phi \, \mathrm{d}x \; \frac{\phi_j^{\mathrm{Na}}(t)}{\Delta t}$$

$$+ \int_0^L \varphi_i^\phi \, (-w_{\mathrm{R}}^{(6.180)} - 6 w_{\mathrm{R}}^{(6.181)} - 6 w_{\mathrm{R}}^{(6.182)}) \, \mathrm{d}x \; - \varphi_i^\phi \, \vec{h}_{1D}^{\mathrm{Na}} \Big|_0^L .$$

and the implicit (Backward Euler, nonlinear in the state at $t + \Delta t$):

$$\int_0^L \varphi_i^\phi \varphi_j^\phi \, \mathrm{d}x \; \frac{\phi_j^{\mathrm{Na}}(t+\Delta t)}{\Delta t} + \mathbb{D} \int_0^L \frac{\partial \varphi_i^\phi}{\partial x} \frac{\partial \varphi_j^\phi}{\partial x} \, \mathrm{d}x \; \phi_j^{\mathrm{Na}}(t+\Delta t) \tag{6.217}$$

$$- 2\, RT\chi \int_0^L \frac{\partial \varphi_i^\phi}{\partial x} \, M(\phi_R^{\mathrm{Na}}(t+\Delta t)) \, \frac{\partial \varphi_j^\phi}{\partial x} \, \mathrm{d}x \; \phi_j^{\mathrm{Na}}(t+\Delta t)$$

$$+ \int_0^L \beta \, M(\phi_R^{\mathrm{Na}}(t+\Delta t)) \, \frac{\partial \varphi_i^\phi}{\partial x} \frac{\partial \varphi_j^\phi}{\partial x} \, \mathrm{d}x \; \phi_j^{\mathrm{Na}}(t+\Delta t)$$

$$- \int_0^L \beta \, M(\phi_R^{\mathrm{Na}}(t+\Delta t)) \, \frac{\partial \varphi_i^\phi}{\partial x} \frac{\partial \varphi_j^{\phi,*}}{\partial x} \, \mathrm{d}x \; \phi_j^{\mathrm{Na},*}(t+\Delta t)$$

$$+ \int_0^L M(\phi_R^{\mathrm{Na}}(t+\Delta t)) \frac{\partial \varphi_i^\phi}{\partial x} \frac{\partial \varphi_j^\gamma}{\partial x} \, \mathrm{d}x \; \mu_j^{mech,\ \mathrm{Na}}(t+\Delta t) = \int_0^L \varphi_i^\phi \varphi_j^\phi \, \mathrm{d}x \; \frac{\phi_j^{\mathrm{Na}}(t)}{\Delta t}$$

$$+ \int_0^L \varphi_i^\phi \, (-w_{\mathrm{R}}^{(6.180)} - 6w_{\mathrm{R}}^{(6.181)} - 6w_{\mathrm{R}}^{(6.182)}) \, \mathrm{d}x \; - \varphi_i^\phi \, \vec{h}_{1D}^{\mathrm{Na}} \Big|_0^L .$$

6.4.8.1.4 Dimensionless form

To nondimensionalize the Forward/Backward Euler forms, define the dimensionless diffusivity $\tilde{\mathbb{D}} = \mathbb{D} \frac{\Delta t}{\ell^2}$ and the dimensionless chemo-mechanical potential $\gamma^{\mathrm{Na}} = \mu^{mech,\ \mathrm{Na}} / \mu_{\mathrm{ref}}$. Multiplying the discrete equations by $\Delta t / \ell$, one obtains

$$\frac{1}{\ell} \int_0^L \varphi_i^\phi \varphi_j^\phi \, \mathrm{d}x \; \phi_j^{\mathrm{Na}}(t+\Delta t) + \tilde{\mathbb{D}} \, \ell \int_0^L \frac{\partial \varphi_i^\phi}{\partial x} \frac{\partial \varphi_j^\phi}{\partial x} \, \mathrm{d}x \; \phi_j^{\mathrm{Na}}(t) \tag{6.218}$$

$$+ \tilde{\mathbb{D}} \left(\frac{\beta}{RT} - 2\,\chi \right) \ell \int_0^L \varphi_k^\phi \phi_k^{\mathrm{Na}}(t) \left(1 - \varphi_h^\phi \phi_h^{\mathrm{Na}}(t) \right) \frac{\partial \varphi_i^\phi}{\partial x} \frac{\partial \varphi_j^\phi}{\partial x} \, \mathrm{d}x \; \phi_j^{\mathrm{Na}}(t)$$

$$- \tilde{\mathbb{D}} \, \frac{\beta}{RT} \, \ell \int_0^L \varphi_k^\phi \phi_k^{\mathrm{Na}}(t) \left(1 - \varphi_h^\phi \phi_h^{\mathrm{Na}}(t) \right) \frac{\partial \varphi_i^\phi}{\partial x} \frac{\partial \varphi_j^{\phi,*}}{\partial x} \, \mathrm{d}x \; \phi_j^{\mathrm{Na},*}(t)$$

$$+ \tilde{\mathbb{D}} \, \frac{\mu_{\mathrm{ref}}}{RT} \, \ell \int_0^L \varphi_k^\phi \phi_k^{\mathrm{Na}}(t) \left(1 - \varphi_h^\phi \phi_h^{\mathrm{Na}}(t) \right) \frac{\partial \varphi_i^\phi}{\partial x} \frac{\partial \varphi_j^\gamma}{\partial x} \, \mathrm{d}x \, \gamma_j^{\mathrm{Na}}(t)$$

$$= \frac{1}{\ell} \int_0^L \varphi_i^\phi \varphi_j^\phi \, \mathrm{d}x \; \phi_j^{\mathrm{Na}}(t)$$

$$+ \frac{1}{\ell} \int_0^L \varphi_i^\phi \, \Delta t \, (-w_{\mathrm{R}}^{(6.180)} - 6w_{\mathrm{R}}^{(6.181)} - 6w_{\mathrm{R}}^{(6.182)}) \, \mathrm{d}x$$

$$- \varphi_i^\phi \frac{\Delta t \, \vec{h}_{1D}^{\mathrm{Na}}(x,t)}{\ell} \Big|_0^L ,$$

and

$$\frac{1}{\ell}\int_0^L \varphi_i^\phi\varphi_j^\phi \,\mathrm{d}x\ \phi_j^{\mathrm{Na}}(t+\Delta t) + \tilde{\mathrm{D}}\,\ell\int_0^L \frac{\partial\varphi_i^\phi}{\partial x}\frac{\partial\varphi_j^\phi}{\partial x}\,\mathrm{d}x\ \phi_j^{\mathrm{Na}}(t+\Delta t) \tag{6.219}$$
$$+\tilde{\mathrm{D}}\left(\frac{\beta}{RT}-2\,\chi\right)\ell\int_0^L \varphi_h^\phi\frac{\partial\varphi_i^\phi}{\partial x}\frac{\partial\varphi_j^\phi}{\partial x}\,\mathrm{d}x\ \phi_h^{\mathrm{Na}}(t+\Delta t)\,\phi_j^{\mathrm{Na}}(t+\Delta t)$$
$$-\tilde{\mathrm{D}}\left(\frac{\beta}{RT}-2\,\chi\right)\ell\int_0^L \varphi_h^\phi\,\varphi_k^\phi\frac{\partial\varphi_i^\phi}{\partial x}\frac{\partial\varphi_j^\phi}{\partial x}\,\mathrm{d}x\ \ \phi_h^{\mathrm{Na}}(t+\Delta t)\,\phi_k^{\mathrm{Na}}(t+\Delta t)\,\phi_j^{\mathrm{Na}}(t+\Delta t)$$
$$-\tilde{\mathrm{D}}\,\frac{\beta}{RT}\,\ell\int_0^L \varphi_h^\phi\frac{\partial\varphi_i^\phi}{\partial x}\frac{\partial\varphi_j^{\phi,*}}{\partial x}\,\mathrm{d}x\ \ \phi_h^{\mathrm{Na}}(t+\Delta t)\,\phi_j^{\mathrm{Na},*}(t+\Delta t)$$
$$+\tilde{\mathrm{D}}\,\frac{\beta}{RT}\,\ell\int_0^L \varphi_h^\phi\,\varphi_k^\phi\frac{\partial\varphi_i^\phi}{\partial x}\frac{\partial\varphi_j^{\phi,*}}{\partial x}\,\mathrm{d}x\ \phi_h^{\mathrm{Na}}(t+\Delta t)\,\phi_k^{\mathrm{Na}}(t+\Delta t)\,\phi_j^{\mathrm{Na},*}(t+\Delta t)$$
$$-\tilde{\mathrm{D}}\,\frac{\mu_{\mathrm{ref}}}{RT}\,\ell\int_0^L \varphi_h^\phi\frac{\partial\varphi_i^\phi}{\partial x}\frac{\partial\varphi_j^\gamma}{\partial x}\,\mathrm{d}x\ \phi_h^{\mathrm{Na}}(t+\Delta t)\,\gamma_j^{\mathrm{Na}}(t+\Delta t)$$
$$+\tilde{\mathrm{D}}\,\frac{\mu_{\mathrm{ref}}}{RT}\,\ell\int_0^L \varphi_h^\phi\,\varphi_k^\phi\frac{\partial\varphi_i^\phi}{\partial x}\frac{\partial\varphi_j^\gamma}{\partial x}\,\mathrm{d}x\ \phi_h^{\mathrm{Na}}(t+\Delta t)\,\phi_k^{\mathrm{Na}}(t+\Delta t)\,\gamma_j^{\mathrm{Na}}(t+\Delta t)$$
$$=\frac{1}{\ell}\int_0^L \varphi_i^\phi\varphi_j^\phi\,\mathrm{d}x\ \phi_j^{\mathrm{Na}}(t)$$
$$+\frac{1}{\ell}\int_0^L \varphi_i^\phi\,\Delta t\,(-w_{\mathrm{R}}^{(6.180)}-6w_{\mathrm{R}}^{(6.181)}-6w_{\mathrm{R}}^{(6.182)})\,\mathrm{d}x$$
$$-\varphi_i^\phi\frac{\Delta t\ \vec{h}_{1D}^{\mathrm{Na}}(x,t)}{\ell}\Big|_0^L.$$

6.4.8.2 Mass balance equation for ϕ^{Sn}

Considering (6.200b) we write weak form and then dimensionless form.

6.4.8.2.1 1D Weak form

Multiplying the strong form by a test function φ_i^ϕ and integrating over the domain $[0, L]$, we obtain:

$$\int_0^L \varphi_i^\phi\frac{\partial\phi_{\mathrm{R}}^{\mathrm{Sn}}}{\partial t}\,\mathrm{d}x = \int_0^L \varphi_i^\phi\left(-3w_{\mathrm{R}}^{(6.180)}-w_{\mathrm{R}}^{(6.181)}\right)\mathrm{d}x \tag{6.220}$$

6.4.8.2.2 Separated variable discretization

The phase field $\phi_{\mathrm{R}}^{\mathrm{Sn}}$ is approximated using a finite element basis:

$$\phi_{\mathrm{R}}^{\mathrm{Sn}}(x,t) = \sum_j \phi_j^{\mathrm{Sn}}(t)\,\varphi_j^{\phi}(x), \tag{6.221}$$

leading to the semi-discrete form:

$$\int_0^L \varphi_i^{\phi}\varphi_j^{\phi}\,\mathrm{d}x\,\frac{\partial \phi_j^{\mathrm{Sn}}(t)}{\partial t} = \int_0^L \varphi_i^{\phi}\left(-3w_{\mathrm{R}}^{(6.180)} - w_{\mathrm{R}}^{(6.181)}\right)\mathrm{d}x. \tag{6.222}$$

6.4.8.2.3 Euler integration schemes

Time discretization is performed using an Euler scheme. The time derivative is approximated as:

$$\frac{\partial \phi_j^{\mathrm{Sn}}(t)}{\partial t} \approx \frac{\phi_j^{\mathrm{Sn}}(t+\Delta t) - \phi_j^{\mathrm{Sn}}(t)}{\Delta t}. \tag{6.223}$$

Time-discretizing the weak form using the Forward Euler scheme yields:

$$\begin{aligned}\int_0^L \varphi_i^{\phi}\varphi_j^{\phi}\,\mathrm{d}x\,\frac{\phi_j^{\mathrm{Sn}}(t+\Delta t)}{\Delta t} &= \int_0^L \varphi_i^{\phi}\varphi_j^{\phi}\,\mathrm{d}x\,\frac{\phi_j^{\mathrm{Sn}}(t)}{\Delta t} \\ &\quad + \int_0^L \varphi_i^{\phi}\left(-3w_{\mathrm{R}}^{(6.180)}(t) - w_{\mathrm{R}}^{(6.181)}(t)\right)\mathrm{d}x.\end{aligned} \tag{6.224}$$

For the implicit Backward Euler scheme, the update equation becomes:

$$\begin{aligned}\int_0^L \varphi_i^{\phi}\varphi_j^{\phi}\,\mathrm{d}x\,\frac{\phi_j^{\mathrm{Sn}}(t+\Delta t)}{\Delta t} &= \int_0^L \varphi_i^{\phi}\varphi_j^{\phi}\,\mathrm{d}x\,\frac{\phi_j^{\mathrm{Sn}}(t)}{\Delta t} \\ &\quad + \int_0^L \varphi_i^{\phi}\left(-3w_{\mathrm{R}}^{(6.180)}(t+\Delta t) - w_{\mathrm{R}}^{(6.181)}(t+\Delta t)\right)\mathrm{d}x.\end{aligned} \tag{6.225}$$

6.4.8.2.4 Dimensionless form

To improve numerical conditioning, the system is written in dimensionless form by dividing through by the characteristic length ℓ:

$$\begin{aligned}\frac{1}{\ell}\int_0^L \varphi_i^{\phi}\varphi_j^{\phi}\,\mathrm{d}x\,\phi_j^{\mathrm{Sn}}(t+\Delta t) &= \frac{1}{\ell}\int_0^L \varphi_i^{\phi}\varphi_j^{\phi}\,\mathrm{d}x\,\phi_j^{\mathrm{Sn}}(t) \\ &\quad + \frac{1}{\ell}\int_0^L \varphi_i^{\phi}\,\Delta t\,\left(-3w_{\mathrm{R}}^{(6.180)}(t) - w_{\mathrm{R}}^{(6.181)}(t)\right)\mathrm{d}x.\end{aligned} \tag{6.226}$$

Similarly, the Backward Euler scheme in dimensionless form is:

$$\begin{aligned}\frac{1}{\ell}\int_0^L \varphi_i^{\phi}\varphi_j^{\phi}\,\mathrm{d}x\,\phi_j^{\mathrm{Sn}}(t+\Delta t) &= \frac{1}{\ell}\int_0^L \varphi_i^{\phi}\varphi_j^{\phi}\,\mathrm{d}x\,\phi_j^{\mathrm{Sn}}(t) \\ &\quad + \frac{1}{\ell}\int_0^L \varphi_i^{\phi}\,\Delta t\,\left(-3w_{\mathrm{R}}^{(6.180)}(t+\Delta t) - w_{\mathrm{R}}^{(6.181)}(t+\Delta t)\right)\mathrm{d}x.\end{aligned} \tag{6.227}$$

6.4.8.3 Mass balance equation for $\phi^{\mathrm{NaSn_3}}$

The evolution of the volume fraction of the intermediate phase $NaSn_3$ follows the mass balance equation (6.200c). Its formation occurs through the forward reaction (6.180), while its consumption arises from its transformation into the next intermetallic phase, Na_9Sn_4, via reaction (6.181). Since $NaSn_3$ is a bulky, immobile intermetallic phase, its flux term vanishes ($\vec{h}_{\mathrm{NaSn_3}} = 0$), leaving only the source and sink terms on the right-hand side.

6.4.8.3.1 1D Weak form

Multiplying the strong form by a test function φ_i^{ϕ} and integrating over the domain $[0, L]$, we obtain:

$$\int_0^L \varphi_i^{\phi} \frac{\partial \phi_{\mathrm{R}}^{\mathrm{NaSn_3}}}{\partial t} \,\mathrm{d}x = \int_0^L \varphi_i^{\phi} \left(w_{\mathrm{R}}^{(6.180)} - w_{\mathrm{R}}^{(6.181)} \right) \mathrm{d}x \tag{6.228}$$

6.4.8.3.2 Separated variable discretization

The phase field $\phi_{\mathrm{R}}^{\mathrm{NaSn_3}}$ is approximated using a finite element basis:

$$\phi_{\mathrm{R}}^{\mathrm{NaSn_3}}(x,t) = \sum_j \phi_j^{\mathrm{NaSn_3}}(t)\, \varphi_j^{\phi}(x), \tag{6.229}$$

leading to the semi-discrete form:

$$\int_0^L \varphi_i^{\phi} \varphi_j^{\phi} \,\mathrm{d}x \, \frac{\partial \phi_j^{\mathrm{NaSn_3}}(t)}{\partial t} = \int_0^L \varphi_i^{\phi} \left(w_{\mathrm{R}}^{(6.180)} - w_{\mathrm{R}}^{(6.181)} \right) \mathrm{d}x. \tag{6.230}$$

6.4.8.3.3 Euler integration schemes

Time discretization is performed using an Euler scheme. The time derivative is approximated as:

$$\frac{\partial \phi_j^{\mathrm{NaSn_3}}(t)}{\partial t} \approx \frac{\phi_j^{\mathrm{NaSn_3}}(t + \Delta t) - \phi_j^{\mathrm{NaSn_3}}(t)}{\Delta t}. \tag{6.231}$$

Time-discretizing the weak form using the Forward Euler scheme yields:

$$\begin{aligned} \int_0^L \varphi_i^{\phi} \varphi_j^{\phi} \,\mathrm{d}x \, \frac{\phi_j^{\mathrm{NaSn_3}}(t + \Delta t)}{\Delta t} &= \int_0^L \varphi_i^{\phi} \varphi_j^{\phi} \,\mathrm{d}x \, \frac{\phi_j^{\mathrm{NaSn_3}}(t)}{\Delta t} \\ &\quad + \int_0^L \varphi_i^{\phi} \left(w_{\mathrm{R}}^{(6.180)}(t) - w_{\mathrm{R}}^{(6.181)}(t) \right) \mathrm{d}x. \end{aligned} \tag{6.232}$$

For the implicit Backward Euler scheme, the update equation becomes:

$$\int_0^L \varphi_i^\phi \varphi_j^\phi \,\mathrm{d}x \,\frac{\phi_j^{\mathrm{NaSn_3}}(t+\Delta t)}{\Delta t} = \int_0^L \varphi_i^\phi \varphi_j^\phi \,\mathrm{d}x \,\frac{\phi_j^{\mathrm{NaSn_3}}(t)}{\Delta t} + \int_0^L \varphi_i^\phi \left(w_{\mathrm{R}}^{(6.180)}(t+\Delta t) - w_{\mathrm{R}}^{(6.181)}(t+\Delta t) \right) \mathrm{d}x. \tag{6.233}$$

6.4.8.3.4 Dimensionless form

To improve numerical conditioning, the system is written in dimensionless form by dividing through by the characteristic length ℓ:

$$\frac{1}{\ell}\int_0^L \varphi_i^\phi \varphi_j^\phi \,\mathrm{d}x \,\phi_j^{\mathrm{NaSn_3}}(t+\Delta t) = \frac{1}{\ell}\int_0^L \varphi_i^\phi \varphi_j^\phi \,\mathrm{d}x \,\phi_j^{\mathrm{NaSn_3}}(t) + \frac{1}{\ell}\int_0^L \varphi_i^\phi \,\Delta t \,\left(w_{\mathrm{R}}^{(6.180)}(t) - w_{\mathrm{R}}^{(6.181)}(t) \right) \mathrm{d}x. \tag{6.234}$$

Similarly, the Backward Euler scheme in dimensionless form is:

$$\frac{1}{\ell}\int_0^L \varphi_i^\phi \varphi_j^\phi \,\mathrm{d}x \,\phi_j^{\mathrm{NaSn_3}}(t+\Delta t) = \frac{1}{\ell}\int_0^L \varphi_i^\phi \varphi_j^\phi \,\mathrm{d}x \,\phi_j^{\mathrm{NaSn_3}}(t) + \frac{1}{\ell}\int_0^L \varphi_i^\phi \,\Delta t \,\left(w_{\mathrm{R}}^{(6.180)}(t+\Delta t) - w_{\mathrm{R}}^{(6.181)}(t+\Delta t) \right) \mathrm{d}x. \tag{6.235}$$

6.4.8.4 Mass balance equation for $\phi^{\mathrm{Na_9Sn_4}}$

The intermediate phase $\mathrm{Na_9Sn_4}$ is produced through the $\mathrm{NaSn_3}$ to $\mathrm{Na_9Sn_4}$ reaction (6.181) and consumed via the subsequent $\mathrm{Na_9Sn_4}$ to $\mathrm{Na_{15}Sn_4}$ reaction (6.182). Its evolution follows the mass balance form (6.200d), where, being a bulky and immobile intermetallic, the flux term vanishes ($\vec{h}_{\mathrm{Na_9Sn_4}} = 0$). As a result, the governing equation reduces to a purely reaction-driven balance between its production and consumption terms.

6.4.8.4.1 1D weak form. Multiplying the strong form by a test function φ_i^ϕ and integrating over $[0, L]$:

$$\int_0^L \varphi_i^\phi \frac{\partial \phi_{\mathrm{R}}^{\mathrm{Na_9Sn_4}}}{\partial t} \,\mathrm{d}x = \int_0^L \varphi_i^\phi \,\left(w_{\mathrm{R}}^{(6.181)} - w_{\mathrm{R}}^{(6.182)} \right) \,\mathrm{d}x \tag{6.236}$$

6.4.8.4.2 Separated variable discretization

We approximate the field with a finite-element expansion,

$$\phi_{\mathrm{R}}^{\mathrm{Na_9Sn_4}}(x,t) = \sum_j \phi_j^{\mathrm{Na_9Sn_4}}(t)\varphi_j^{\phi}(x) \tag{6.237}$$

which yields the semi-discrete system

$$\int_0^L \varphi_i^{\phi}\varphi_j^{\phi}\ \mathrm{d}x\ \frac{\partial \phi_j^{\mathrm{Na_9Sn_4}}(t)}{\partial t} = \int_0^L \varphi_i^{\phi}\ \left(w_{\mathrm{R}}^{(6.181)} - w_{\mathrm{R}}^{(6.182)}\right)\ \mathrm{d}x \tag{6.238}$$

6.4.8.4.3 Euler integration scheme

The time derivative is approximated as

$$\frac{\partial \phi_j^{\mathrm{Na_9Sn_4}}(t)}{\partial t} \approx \frac{\phi_j^{\mathrm{Na_9Sn_4}}(t+\Delta t) - \phi_j^{\mathrm{Na_9Sn_4}}(t)}{\Delta t} \tag{6.239}$$

leading to the following update formulas.

Time-discretizing the weak form using the Forward Euler scheme yields:

$$\begin{aligned}\int_0^L \varphi_i^{\phi}\varphi_j^{\phi}\ \mathrm{d}x\ \frac{\phi_j^{\mathrm{Na_9Sn_4}}(t+\Delta t)}{\Delta t} &= \int_0^L \varphi_i^{\phi}\varphi_j^{\phi}\ \mathrm{d}x\ \frac{\phi_j^{\mathrm{Na_9Sn_4}}(t)}{\Delta t} \\ &+ \int_0^L \varphi_i^{\phi}\ \left(w_{\mathrm{R}}^{(6.181)}(t) - w_{\mathrm{R}}^{(6.182)}(t)\right)\ \mathrm{d}x\end{aligned} \tag{6.240}$$

For the implicit Backward Euler scheme, the update equation becomes:

$$\begin{aligned}\int_0^L \varphi_i^{\phi}\varphi_j^{\phi}\ \mathrm{d}x\ \frac{\phi_j^{\mathrm{Na_9Sn_4}}(t+\Delta t)}{\Delta t} &= \int_0^L \varphi_i^{\phi}\varphi_j^{\phi}\ \mathrm{d}x\ \frac{\phi_j^{\mathrm{Na_9Sn_4}}(t)}{\Delta t} \\ &+ \int_0^L \varphi_i^{\phi}\ \left(w_{\mathrm{R}}^{(6.181)}(t+\Delta t) - w_{\mathrm{R}}^{(6.182)}(t+\Delta t)\right)\ \mathrm{d}x\end{aligned} \tag{6.241}$$

6.4.8.4.4 Dimensionless form

For better numerical conditioning, we rewrite the updates dividing by a characteristic length ℓ:

$$\begin{aligned}\frac{1}{\ell}\ \int_0^L \varphi_i^{\phi}\varphi_j^{\phi}\ \mathrm{d}x\ \phi_j^{\mathrm{Na_9Sn_4}}(t+\Delta t) &= \frac{1}{\ell}\ \int_0^L \varphi_i^{\phi}\varphi_j^{\phi}\ \mathrm{d}x\ \phi_j^{\mathrm{Na_9Sn_4}}(t) \\ &+ \frac{1}{\ell}\ \int_0^L \varphi_i^{\phi}\,\Delta t\ \left(w_{\mathrm{R}}^{(6.181)}(t) - w_{\mathrm{R}}^{(6.182)}(t)\right)\ \mathrm{d}x\end{aligned} \tag{6.242}$$

and

$$\frac{1}{\ell}\int_0^L \varphi_i^\phi \varphi_j^\phi \,\mathrm{d}x\;\phi_j^{\mathrm{Na_9Sn_4}}(t+\Delta t) = \frac{1}{\ell}\int_0^L \varphi_i^\phi \varphi_j^\phi \,\mathrm{d}x\;\phi_j^{\mathrm{Na_9Sn_4}}(t) + \frac{1}{\ell}\int_0^L \varphi_i^\phi\,\Delta t\,\left(w_{\mathrm{R}}^{(6.181)}(t+\Delta t) - w_{\mathrm{R}}^{(6.182)}(t+\Delta t)\right)\,\mathrm{d}x \tag{6.243}$$

6.4.8.5 Mass balance equation for $\phi^{\mathrm{Na_{15}Sn_4}}$

The terminal sodiation product $Na_{15}Sn_4$ is formed exclusively through the Na_9Sn_4 to $Na_{15}Sn_4$ reaction (6.182). Its evolution follows the mass balance form (6.200e). Since $Na_{15}Sn_4$ is a dense, immobile solid phase, the flux term is zero ($\vec{h}_{\mathrm{Na_{15}Sn_4}} = 0$), reducing the governing equation to a purely reaction-controlled evolution driven solely by its formation rate.

6.4.8.5.1 1D weak form

Multiplying by a test function φ_i^ϕ and integrating over the 1D domain $[0, L]$ yields

$$\int_0^L \varphi_i^\phi \frac{\partial \phi_{\mathrm{R}}^{\mathrm{Na_{15}Sn_4}}}{\partial t}\,\mathrm{d}x = \int_0^L \varphi_i^\phi\, w_{\mathrm{R}}^{(6.182)}\,\mathrm{d}x \tag{6.244}$$

6.4.8.5.2 Separated variable discretization

We approximate the field as

$$\phi_{\mathrm{R}}^{\mathrm{Na_{15}Sn_4}}(x,t) = \sum_j \phi_j^{\mathrm{Na_{15}Sn_4}}(t)\varphi_j^\phi(x) \tag{6.245}$$

which gives the semi-discrete system

$$\int_0^L \varphi_i^\phi \varphi_j^\phi \,\mathrm{d}x\;\frac{\partial \phi_j^{\mathrm{Na_{15}Sn_4}}(t)}{\partial t} = \int_0^L \varphi_i^\phi\, w_{\mathrm{R}}^{(6.182)}\,\mathrm{d}x \tag{6.246}$$

6.4.8.5.3 Euler integration schemes

With

$$\frac{\partial \phi_j^{\mathrm{Na_{15}Sn_4}}(t)}{\partial t} \approx \frac{\phi_j^{\mathrm{Na_{15}Sn_4}}(t+\Delta t) - \phi_j^{\mathrm{Na_{15}Sn_4}}(t)}{\Delta t} \tag{6.247}$$

we obtain the following updates.

Time-discretizing the weak form using the Forward Euler scheme yields:

$$\int_0^L \varphi_i^\phi \varphi_j^\phi \, \mathrm{d}x \; \frac{\phi_j^{\mathrm{Na_{15}Sn_4}}(t+\Delta t)}{\Delta t} = \int_0^L \varphi_i^\phi \varphi_j^\phi \, \mathrm{d}x \; \frac{\phi_j^{\mathrm{Na_{15}Sn_4}}(t)}{\Delta t} + \int_0^L \varphi_i^\phi \, w_{\mathrm{R}}^{(6.182)}(t) \, \mathrm{d}x \tag{6.248}$$

For the implicit Backward Euler scheme, the update equation becomes:

$$\int_0^L \varphi_i^\phi \varphi_j^\phi \, \mathrm{d}x \; \frac{\phi_j^{\mathrm{Na_{15}Sn_4}}(t+\Delta t)}{\Delta t} = \int_0^L \varphi_i^\phi \varphi_j^\phi \, \mathrm{d}x \; \frac{\phi_j^{\mathrm{Na_{15}Sn_4}}(t)}{\Delta t} + \int_0^L \varphi_i^\phi \, w_{\mathrm{R}}^{(6.182)}(t+\Delta t) \, \mathrm{d}x \tag{6.249}$$

6.4.8.5.4 Dimensionless form

Dividing by a characteristic length ℓ for conditioning gives

$$\frac{1}{\ell} \int_0^L \varphi_i^\phi \varphi_j^\phi \, \mathrm{d}x \; \phi_j^{\mathrm{Na_{15}Sn_4}}(t+\Delta t) = \frac{1}{\ell} \int_0^L \varphi_i^\phi \varphi_j^\phi \, \mathrm{d}x \; \phi_j^{\mathrm{Na_{15}Sn_4}}(t) + \frac{1}{\ell} \int_0^L \varphi_i^\phi \, \Delta t \, w_{\mathrm{R}}^{(6.182)}(t) \, \mathrm{d}x \tag{6.250}$$

and

$$\frac{1}{\ell} \int_0^L \varphi_i^\phi \varphi_j^\phi \, \mathrm{d}x \; \phi_j^{\mathrm{Na_{15}Sn_4}}(t+\Delta t) = \frac{1}{\ell} \int_0^L \varphi_i^\phi \varphi_j^\phi \, \mathrm{d}x \; \phi_j^{\mathrm{Na_{15}Sn_4}}(t) + \frac{1}{\ell} \int_0^L \varphi_i^\phi \, \Delta t \, w_{\mathrm{R}}^{(6.182)}(t+\Delta t) \, \mathrm{d}x \tag{6.251}$$

6.4.9 Penalty constraint in dimensionless 1D weak form for Na

This section enforces the auxiliary penalty constraint that ties the physical volume fraction ϕ^{Na} to the smoothed (penalty) field $\phi^{\mathrm{Na},*}$. The constraint supplies interface regularization with internal length l and does not represent a conservation law; rather, it is solved alongside the mass balances in an operator-splitting fashion.

The dimensionless 1D restriction of Eq. (6.64) reads:

$$\phi^{\mathrm{Na}} - \phi^{\mathrm{Na},*} + l^2 \, \frac{\partial}{\partial X_1} \frac{\partial \phi^{\mathrm{Na},*}}{\partial X_1} = 0 \, . \tag{6.252}$$

Denote with L the right end of the 1D domain, which starts in $x = 0$. The weak form of (6.252) is:

$$\frac{1}{\ell}\int_0^L \varphi_i^*\phi^{\mathrm{Na}}\,\mathrm{d}X_1 - \frac{1}{\ell}\int_0^L \varphi_i^*\phi^{\mathrm{Na},*}\,\mathrm{d}X_1 + \frac{1}{\ell}\int_0^L \varphi_i^*\frac{\partial}{\partial X_1}\left(l^2\frac{\partial\phi^{\mathrm{Na},*}}{\partial X_1}\right)\mathrm{d}X_1 = 0\,. \tag{6.253}$$

Upon integration by parts we obtain

$$\begin{aligned}&\frac{1}{\ell}\int_0^L \varphi_i^*\phi^{\mathrm{Na}}\,\mathrm{d}X_1 - \frac{1}{\ell}\int_0^L \varphi_i^*\phi^{\mathrm{Na},*}\,\mathrm{d}X_1 - \frac{l^2}{\ell^2}\,\ell\int_0^L \frac{\partial\varphi_i^*}{\partial X_1}\,\frac{\partial\phi^{\mathrm{Na},*}}{\partial X_1}\mathrm{d}X_1 \\ &+ \frac{l^2}{\ell^2}\,\varphi_i^*\,\ell\frac{\partial\phi^{\mathrm{Na},*}}{\partial X_1}\bigg|_0^L = 0\end{aligned} \tag{6.254}$$

Remark As discussed in Section 6.1.2.4, the penalty Eq. (6.254) is not a balance law; thus, Dirichlet/Neumann boundary data are not a priori required. The boundary contribution

$$\frac{l^2}{\ell^2}\,\varphi_i^*\,\ell\frac{\partial\phi^{\mathrm{Na},*}}{\partial X_1}\bigg|_0^L \tag{6.255}$$

is therefore evaluated over the entire boundary. Nevertheless, in many studies (and in manufactured solutions) this term is prescribed, which we refer to as the "Neumann kind" (see Section 6.2.2 for its physical interpretation). Using definition (6.143), the given boundary contribution (6.255) is written as

$$\varphi_i^*\,\frac{\lambda}{\beta\ell^2}\,\ell\,h_{1D}^*\bigg|_0^L\,. \tag{6.256}$$

6.4.9.1 Separated variables discretization

We expand the unknowns as

$$\phi^{\mathrm{Na}}(X_1,t) = \sum_j\,\varphi_j^\phi(X_1)\,\phi_j^{\mathrm{Na}}(t)\,,\qquad \phi^{\mathrm{Na},*}(X_1,t) = \sum_j\,\varphi_j^*(X_1)\,\phi_j^{\mathrm{Na},*}(t)\,. \tag{6.257}$$

Replacing into (6.147), we obtain the discrete weak form of "Neumann kind":

$$\begin{aligned}&\frac{1}{\ell}\int_0^L \varphi_i^*\,\varphi_j^\phi\,\mathrm{d}X_1\,\phi_j^{\mathrm{Na}}(t+\Delta t) - \frac{1}{\ell}\int_0^L \varphi_i^*\,\varphi_j^*\,\mathrm{d}X_1\,\phi_j^{\mathrm{Na},*}(t+\Delta t) \\ &\quad - \frac{\lambda}{\beta\ell^2}\,\ell\int_0^L \frac{\partial\varphi_i^*}{\partial X_1}\,\frac{\partial\varphi_j^*}{\partial X_1}\mathrm{d}X_1\,\phi_j^{\mathrm{Na},*}(t+\Delta t) + \frac{\lambda}{\beta\ell^2}\,\varphi_i^*\,\ell\,h_{1D}^*\bigg|_0^L = 0\,.\end{aligned} \tag{6.258}$$

1D discrete dimensionless weak form with natural boundary terms is expressed as:

$$\frac{1}{\ell}\int_0^L \varphi_i^*\,\varphi_j^{\phi}\,\mathrm{d}X_1\,\phi_j^{\mathrm{Na}}(t+\Delta t) - \frac{1}{\ell}\int_0^L \varphi_i^*\,\varphi_j^*\,\mathrm{d}X_1\,\phi_j^{\mathrm{Na},*}(t+\Delta t) \tag{6.259}$$
$$-\frac{\lambda}{\beta\ell^2}\,\ell\int_0^L \frac{\partial\varphi_i^*}{\partial X_1}\frac{\partial\varphi_j^*}{\partial X_1}\mathrm{d}X_1\,\phi_j^{\mathrm{Na},*}(t+\Delta t) + \frac{\lambda}{\beta\ell^2}\,\varphi_i^*\,\ell\,\frac{\partial\varphi_j^*}{\partial X_1}\,\phi_j^{\mathrm{Na},*}(t+\Delta t)\Big|_0^L = 0$$

All fields are treated implicitly at $t+\Delta t$.

6.4.10 Chemo–mechanical potential equations

As introduced in Section 6.3.1.3, the mechanical contribution to the free energy density is based on a finite–strain elastic formulation. The constitutive law is given by Eq. (6.114), with the Saint–Venant elastic energy in Eq. (6.118). The stress components follow from the standard derivation (Eqs. (6.121)–(6.122)). We denote by $\boldsymbol{\phi}_R = \{\phi_R^\alpha\}_\alpha$ the vector of reference volume fractions.

To streamline the one–dimensional presentation and make the coupling to composition explicit, define

$$\aleph(\vec{X},\boldsymbol{\phi}_R) = (J^c)^{-1/3}\left(1+\frac{\partial u_1}{\partial X_1}\right), \tag{6.260}$$

which encodes chemical swelling (via $J^c(\boldsymbol{\phi}_R)$) and axial deformation (via $\partial u_1/\partial X_1$). With this definition, the axial component of the elastic second Piola–Kirchhoff stress and the trace–like quantity J^e read

$$\boldsymbol{S}^e_{11} = \frac{E}{2}\Big(\aleph(\vec{X},\boldsymbol{\phi}_R)^2-1\Big), \tag{6.261}$$

$$J^e = \frac{1}{2}\,\aleph(\vec{X},\boldsymbol{\phi}_R)\Big(2(1+\nu)-2\nu\,\aleph(\vec{X},\boldsymbol{\phi}_R)^2\Big). \tag{6.262}$$

The total second Piola–Kirchhoff stress follows from Eq. (6.112) or, equivalently, by a pullback through the chemical deformation,

$$\boldsymbol{S} = J^c\boldsymbol{F}^{c-1}\boldsymbol{S}^e\boldsymbol{F}^{c-\mathsf{T}} = (J^c)^{1/3}\,\boldsymbol{S}^e_{11}\,\vec{e}_1\otimes\vec{e}_1,$$

leading to the first Piola–Kirchhoff stress

$$\boldsymbol{P} = \frac{E}{2}\,(J^c)^{2/3}\,\aleph(\vec{X},\boldsymbol{\phi}_R)\,\Big(\aleph(\vec{X},\boldsymbol{\phi}_R)^2-1\Big)\,\vec{e}_1\otimes\vec{e}_1. \tag{6.263}$$

Since Na is the only mobile species, the driving potential for diffusion is the sodium chemical potential. Its mechanical part is

$$\mu^{mech}_{\mathrm{Na}}(\phi^{\mathrm{Na}}_R,\vec{u}) = \Omega^{\mathrm{Na}}\left\{\frac{\lambda}{2}\,\mathrm{tr}\,\boldsymbol{E}^{e2} + G\,\boldsymbol{E}^e\!:\!\boldsymbol{E}^e - \frac{1}{3}\,\boldsymbol{S}^e\!:\!\boldsymbol{C}^e\right\}, \tag{6.264}$$

where $\boldsymbol{E}^e$, $\boldsymbol{S}^e$ and $\boldsymbol{C}^e$ depend on $\aleph(\boldsymbol{\phi}_R, u_1)$ as below:

$$\boldsymbol{E}^e : \boldsymbol{E}^e = \frac{1-2\nu^2}{4}\,\aleph^4 - \frac{1-2\nu}{2}\,\aleph^2 + \frac{2(1+\nu)^2 - 4(1+\nu) + 3}{4}, \tag{6.265}$$

$$\operatorname{tr} \boldsymbol{E}^e = \frac{1-2\nu}{2}\,\aleph^2 + \frac{2(1+\nu) - 3}{2}, \tag{6.266}$$

$$\boldsymbol{S}^e = \frac{E}{2}\big(\aleph^2 - 1\big)\,\vec{e}_1 \otimes \vec{e}_1, \tag{6.267}$$

$$\boldsymbol{C}^e = \Big(\vec{e}_1 \otimes \vec{e}_1 - \nu \sum_{k=2}^{3} \vec{e}_k \otimes \vec{e}_k\Big)\aleph^2 + (1+\nu) \sum_{k=2}^{3} \vec{e}_k \otimes \vec{e}_k, \tag{6.268}$$

with $\aleph \equiv \aleph(\boldsymbol{\phi}_R, u_1)$ for brevity.

Introducing the dimensionless sodium chemo–mechanical potential $\gamma^{\mathrm{Na}} = \mu^{mech}_{\mathrm{Na}} / \mu^{\mathrm{Na}}_{\mathrm{ref}}$, we obtain

$$\gamma^{\mathrm{Na}}(X_1, t) = E\,\frac{\Omega^{\mathrm{Na}}}{\mu^{\mathrm{Na}}_{\mathrm{ref}}} \left\{ \alpha_4\, \aleph(\boldsymbol{\phi}_R, u_1)^4 + \alpha_2\, \aleph(\boldsymbol{\phi}_R, u_1)^2 + \frac{1}{8} \right\}, \tag{6.269}$$

with

$$\alpha_4 = -\frac{12\nu^2 + \nu + 1}{24(\nu+1)}\,, \qquad \alpha_2 = \frac{6\nu^2 + 5\nu - 1}{12(\nu+1)}.$$

As a check, for $\aleph = 1$ (vanishing displacement and reference composition),

$$\gamma^{\mathrm{Na}}\big|_{\aleph=1} = \frac{\nu\, G\, \Omega^{\mathrm{Na}}}{\mu^{\mathrm{Na}}_{\mathrm{ref}}}.$$

6.4.11 Interfacial reaction–diffusion–mechanics model

We model the charge–transfer reaction (6.179) at the electrolyte–solid interface, by an interfacial molar rate $\widehat{w}$ ($\mathrm{mol\,m^{-2}\,s^{-1}}$).

6.4.11.1 Flux boundary condition for mobile Na

At $x = 0$ the interfacial reaction (6.179) injects/consumes neutral Na in the solid. With the outward unit normal $\vec{n}$ (pointing out of the solid), we impose

$$-\,\vec{h}_{\mathrm{Na}} \cdot \vec{n} = \widehat{w}^{(6.179)}, \qquad \text{at } x = 0, \tag{6.270}$$

which is consistent with the sign convention already used in the Na flux definition (Section 6.4.8).

6.4.11.2 Interfacial electrochemical affinity and potentials

The thermodynamic driving force (affinity) of reaction (6.179) is

$$A^{(6.179)} = \tilde{\mu}^{s}_{\mathrm{NaSn_3}} + \tilde{\mu}^{s}_{\mathrm{Na}} - 3\,\tilde{\mu}^{s}_{\mathrm{Sn}} - 2\,\tilde{\mu}^{e}_{\mathrm{Na^+}} - 2\,\tilde{\mu}^{s}_{\mathrm{e^-}}, \tag{6.271}$$

where "s" denotes solid (cathode or anode) and "e" electrolyte. Each $\tilde{\mu}$ is an electrochemical potential, including entropic, electrical, and in the solid (in our case only for the cathode), mechanical:

$$\tilde{\mu}_i^{\,s} = \mu_i^{en} + z_i F\,\phi_s + \mu_i^{mech}, \qquad \tilde{\mu}^{e}_{\mathrm{Na^+}} = \mu^{en}_{\mathrm{Na^+}} + F\,\phi_e, \qquad \tilde{\mu}^{s}_{\mathrm{e^-}} = \mu^{en}_{\mathrm{e^-}} - F\,\phi_s. \tag{6.272}$$

From Eq. (6.130), at the surface (solid), the resulting chemical potentials are

$$\begin{aligned}
\mu^{\mathrm{s}}_{\mathrm{Na}} &= \mu^{0}_{\mathrm{Na}} + RT\ln\frac{\phi^{\mathrm{Na}}_{\mathrm{R}}}{1-\phi^{\mathrm{Na}}_{\mathrm{R}}} + RT\,\chi(1-2\phi^{\mathrm{Na}}_{\mathrm{R}}) - \lambda\nabla^2\phi^{\mathrm{Na}}_{\mathrm{R}} \\
&\quad + \Omega^{\mathrm{Na}}\Big[\tfrac{\lambda}{2}\,\mathrm{tr}(\boldsymbol{E}^e)^2 + G\,\|\boldsymbol{E}^e\|^2 - \tfrac{1}{3}\,\boldsymbol{S}^e : \boldsymbol{C}^e\Big], \\
\mu^{\mathrm{s}}_{\mathrm{Sn}} &= \mu^{0}_{\mathrm{Sn}} + RT\ln\frac{\phi^{\mathrm{Sn}}_{\mathrm{R}}}{1-\phi^{\mathrm{Sn}}_{\mathrm{R}}} + RT\,\chi(1-2\phi^{\mathrm{Sn}}_{\mathrm{R}}) - \lambda\,\nabla^2\phi^{\mathrm{Sn}}_{\mathrm{R}}, \\
\mu^{\mathrm{s}}_{\mathrm{NaSn_3}} &= \mu^{0}_{\mathrm{NaSn_3}} + RT\ln\frac{\phi^{\mathrm{NaSn_3}}_{\mathrm{R}}}{1-\phi^{\mathrm{NaSn_3}}_{\mathrm{R}}} + RT\,\chi(1-2\phi^{\mathrm{NaSn_3}}_{\mathrm{R}}) - \lambda\,\nabla^2\phi^{\mathrm{NaSn_3}}_{\mathrm{R}}.
\end{aligned} \tag{6.273}$$

Natural boundary conditions for gradient terms (no surface energy) are $\vec{n}\cdot(\lambda\,\nabla\phi^{\alpha}) = 0$.

6.4.11.3 Interface electrochemistry

The equilibrium potential follows from $A = 0$:

$$E_{\mathrm{eq}} = \frac{\mu^{\mathrm{s}}_{\mathrm{NaSn_3}} + \mu^{\mathrm{s}}_{\mathrm{Na}} - 3\,\mu^{\mathrm{s}}_{\mathrm{Sn}} - 2\,\mu^{\mathrm{e}}_{\mathrm{Na^+}}}{2F} = E^0 + \frac{\mu^{\mathrm{s}}_{\mathrm{NaSn_3}} + \mu^{\mathrm{s}}_{\mathrm{Na}} - 3\,\mu^{\mathrm{s}}_{\mathrm{Sn}}}{2F}, \tag{6.274}$$

$$\eta = (\phi_s - \phi_e) - E_{\mathrm{eq}}, \tag{6.275}$$

where E^0 is constant (electrolyte concentration fixed), η is overpotential, ϕ_s the solid potential, and ϕ_e the electrolyte potential. Butler–Volmer kinetics (see Section 2.5.4) give

$$j = j_0\Big[e^{\frac{\alpha F\eta}{RT}} - e^{\frac{-(1-\alpha)F\eta}{RT}}\Big], \qquad \widehat{w}^{(6.179)} = \frac{j}{2F}, \tag{6.276}$$

with $n = 2$ electrons per event (matching the reaction stoichiometry).

We treat j_0 as a constant parameter and determine it by fitting the small-overpotential BV slope (or Electrochemical Impedance Spectroscopy R_{ct} from Electrochemical Impedance Spectroscopy (EIS)), following standard practice [129].

6.4.11.3.1 Overpotential and linearized Butler–Volmer.

We take $j_0 = 1.3\ \mathrm{A\,m^{-2}}$ [21, 130], $T = 298\ \mathrm{K}$, $F = 96485\ \mathrm{C\,mol^{-1}}$ and $F/RT \approx 38.92\ \mathrm{V^{-1}}$. Using the experimental choices V_{app}: purple curve (second sodiation, loaded) and U_{OCV} (Fig. 3.11b [58]): black squares (120 °C, near-equilibrium proxy), the overpotential is

$$\eta = V_{\mathrm{app}} - U_{\mathrm{OCV}} = -0.230\ \mathrm{V}.$$

With the linearized Butler–Volmer law [90] and assumed $\alpha = \frac{1}{2}$,

$$j \approx j_0 \frac{F}{RT}\,\eta = (1.3\ \mathrm{A\,m^{-2}})\,(38.92\ \mathrm{V^{-1}})\,(-0.230\ \mathrm{V}) = -11.63\ \mathrm{A\,m^{-2}}.$$

For the reaction 6.179, the interfacial molar rate is

$$\widehat{\omega} = \frac{j}{2F} = \frac{-11.63\ \mathrm{A\,m^{-2}}}{2 \times 96485\ \mathrm{C\,mol^{-1}}} = -6.03 \times 10^{-5}\ \mathrm{mol\,m^{-2}\,s^{-1}}.$$

6.4.12 Governing equations

6.4.12.1 Newton–Raphson scheme for ϕ^{Na}

For the backward (nonlinear) scheme, we assemble the residual $\mathcal{R}_\phi = 0$ and its Gateaux derivative for Newton iterations:

$$\begin{aligned}
\mathcal{R}_\phi({\phi^{\mathrm{Na},*}}_j(t+\Delta t), \phi_j^{\mathrm{Na}}(t+\Delta t)) = {}& \mathcal{A}_\phi({\phi^{\mathrm{Na},*}}_j(t+\Delta t), \phi_j^{\mathrm{Na}}(t+\Delta t)) \\
& + \tilde{\mathrm{D}}\ \left(\frac{\beta}{RT}\ - 2\,\chi\right)\ \ell\ \int_0^L \varphi_h^\phi\ \frac{\partial \varphi_i^\phi}{\partial x}\frac{\partial \varphi_j^\phi}{\partial x}\ \mathrm{d}x\ \ \phi_h^{\mathrm{Na}}(t+\Delta t)\ \phi_j^{\mathrm{Na}}(t+\Delta t) \\
& - \tilde{\mathrm{D}}\ \left(\frac{\beta}{RT}\ - 2\,\chi\right)\ \ell\ \int_0^L \varphi_h^\phi\ \varphi_k^\phi\ \frac{\partial \varphi_i^\phi}{\partial x}\frac{\partial \varphi_j^\phi}{\partial x}\ \mathrm{d}x\ \ \phi_h^{\mathrm{Na}}(t+\Delta t)\ \phi_k^{\mathrm{Na}}(t+\Delta t)\ \phi_j^{\mathrm{Na}}(t+\Delta t) \\
& - \tilde{\mathrm{D}}\ \frac{\beta}{RT}\ \ell\ \int_0^L \varphi_h^\phi\ \frac{\partial \varphi_i^\phi}{\partial x}\frac{\partial \varphi_j^{\phi,*}}{\partial x}\ \mathrm{d}x\ \ \phi_h^{\mathrm{Na}}(t+\Delta t)\ \phi_j^{\mathrm{Na},*}(t+\Delta t) \\
& + \tilde{\mathrm{D}}\ \frac{\beta}{RT}\ \ell\ \int_0^L \varphi_h^\phi\ \varphi_k^\phi\ \frac{\partial \varphi_i^\phi}{\partial x}\frac{\partial \varphi_j^{\phi,*}}{\partial x}\ \mathrm{d}x\ \ \phi_h^{\mathrm{Na}}(t+\Delta t)\ \phi_k^{\mathrm{Na}}(t+\Delta t)\ \phi_j^{\mathrm{Na},*}(t+\Delta t) \\
& - \tilde{\mathrm{D}}\ \frac{\mu_{\mathrm{ref}}}{RT}\ \ell\ \int_0^L \varphi_h^\phi\ \frac{\partial \varphi_i^\phi}{\partial x}\frac{\partial \varphi_j^\gamma}{\partial x}\ \mathrm{d}x\ \phi_h^{\mathrm{Na}}(t+\Delta t)\ \gamma_j^{\mathrm{Na}}(t+\Delta t) \\
& + \tilde{\mathrm{D}}\ \frac{\mu_{\mathrm{ref}}}{RT}\ \ell\ \int_0^L \varphi_h^\phi\ \varphi_k^\phi\ \frac{\partial \varphi_i^\phi}{\partial x}\frac{\partial \varphi_j^\gamma}{\partial x}\ \mathrm{d}x\ \phi_h^{\mathrm{Na}}(t+\Delta t)\ \phi_k^{\mathrm{Na}}(t+\Delta t)\ \gamma_j^{\mathrm{Na}}(t+\Delta t) \\
& - \frac{1}{\ell}\ \int_0^L \varphi_i^\phi\ \Delta t\,(-w_{\mathrm{R}}^{(6.180)} - 6w_{\mathrm{R}}^{(6.181)} - 6w_{\mathrm{R}}^{(6.182)})\ \mathrm{d}x \\
& + \ \mathcal{B}_\phi\ = 0,
\end{aligned} \tag{6.277}$$

with

$$\mathcal{B}_\phi = -\frac{1}{\ell}\int_0^L \varphi_i^\phi \varphi_j^\phi \,\mathrm{d}x\;\phi_j^{\mathrm{Na}}(t) + \varphi_i^\phi \frac{\Delta t\,\vec{h}_{1D}^{\mathrm{Na}}(x,t)}{\ell}\Bigg|_0^L, \tag{6.278}$$

and $\mathcal{A}_\phi(\phi_j^{\mathrm{Na},*}(t+\Delta t), \phi_j^{\mathrm{Na}}(t+\Delta t))$ linear (defined by comparison (6.219)). The Newton–Raphson step is built from the Gateaux derivative:

$$\begin{aligned}
&\frac{\partial}{\partial\epsilon}\mathcal{R}_\phi({\phi^{\mathrm{Na},*}}_j + \epsilon\delta{\phi^{\mathrm{Na},*}}_j, \phi_j^{\mathrm{Na}} + \epsilon\delta\phi_j^{\mathrm{Na}})\Big|_{\epsilon=0} = \qquad (6.279)\\
&\quad \mathcal{A}_\phi(\delta\phi_j^{\mathrm{Na},*}, \delta\phi_j^{\mathrm{Na}}) + \cdots\\
&\quad -\frac{1}{\ell}\int_0^L \varphi_i^\phi\,\Delta t\,(-\delta w_{\mathrm{R}}^{(6.180)} - 6\delta w_{\mathrm{R}}^{(6.181)} - 6\delta w_{\mathrm{R}}^{(6.182)})\,\mathrm{d}x\\
&= -\mathcal{R}_\phi({\phi^{\mathrm{Na},*}}_j(t+\Delta t), \phi_j^{\mathrm{Na}}(t+\Delta t))\,. \qquad (6.280)
\end{aligned}$$

6.4.12.2 Newton–Raphson scheme for ϕ^{Sn}

The fully implicit form requires solving a nonlinear system using Newton-Raphson iterations. The residual is defined as:

$$\mathcal{R}_\phi(\phi_j^{\mathrm{Sn}}(t+\Delta t)) = \mathcal{A}_\phi(\phi_j^{\mathrm{Sn}}(t+\Delta t)) - \frac{1}{\ell}\int_0^L \varphi_i^\phi\,\Delta t\,\left(-3w_{\mathrm{R}}^{(6.180)} - w_{\mathrm{R}}^{(6.181)}\right)\mathrm{d}x \tag{6.281}$$

$$+\,\mathcal{B}_\phi = 0,$$

where $\mathcal{A}_\phi$ is the linear part of Eq. (6.227)

$$\mathcal{B}_\phi = -\frac{1}{\ell}\int_0^L \varphi_i^\phi \varphi_j^\phi\,\mathrm{d}x\,\phi_j^{\mathrm{Sn}}(t). \tag{6.282}$$

The linearization using the Gateaux derivative is:

$$\frac{\partial}{\partial\epsilon}\mathcal{R}_\phi(\phi_j^{\mathrm{Sn}} + \epsilon\delta\phi_j^{\mathrm{NaSn_3}})\Big|_{\epsilon=0} = \mathcal{A}_\phi(\delta\phi_j^{\mathrm{Sn}}) - \frac{1}{\ell}\int_0^L \varphi_i^\phi\,\Delta t\,\left(-3\delta w_{\mathrm{R}}^{(6.180)} - \delta w_{\mathrm{R}}^{(6.181)}\right)\mathrm{d}x \tag{6.283}$$

$$= -\mathcal{R}_\phi(\phi_j^{\mathrm{Sn}}(t+\Delta t)).$$

6.4.12.3 Newton-Raphson scheme for $\phi^{\mathrm{NaSn_3}}$

The fully implicit form requires solving a nonlinear system using Newton-Raphson iterations. The residual is defined as:

$$\mathcal{R}_\phi(\phi_j^{\mathrm{NaSn_3}}(t+\Delta t)) = \mathcal{A}_\phi(\phi_j^{\mathrm{NaSn_3}}(t+\Delta t)) - \frac{1}{\ell}\int_0^L \varphi_i^\phi\,\Delta t\,\left(w_{\mathrm{R}}^{(6.180)} - w_{\mathrm{R}}^{(6.181)}\right)\mathrm{d}x \tag{6.284}$$

$$+\,\mathcal{B}_\phi = 0,$$

where $\mathcal{A}_\phi$ is the linear part of Eq. (6.235)

$$\mathcal{B}_\phi = -\frac{1}{\ell}\int_0^L \varphi_i^\phi \varphi_j^\phi \,\mathrm{d}x\, \phi_j^{\mathrm{NaSn_3}}(t). \tag{6.285}$$

The linearization using the Gateaux derivative is:

$$\frac{\partial}{\partial\epsilon}\mathcal{R}_\phi(\phi_j^{\mathrm{NaSn_3}} + \epsilon\delta\phi_j^{\mathrm{NaSn_3}})\Big|_{\epsilon=0} = \mathcal{A}_\phi(\delta\phi_j^{\mathrm{NaSn_3}}) - \frac{1}{\ell}\int_0^L \varphi_i^\phi\, \Delta t\, \left(\delta w_{\mathrm{R}}^{(6.180)} - \delta w_{\mathrm{R}}^{(6.181)}\right)\mathrm{d}x \tag{6.286}$$

$$= -\mathcal{R}_\phi(\phi_j^{\mathrm{NaSn_3}}(t+\Delta t)).$$

6.4.12.4 Newton–Raphson scheme for $\phi^{\mathrm{Na_9Sn_4}}$

For the Backward Euler step, we solve a nonlinear system by Newton iterations. We define the residual:

$$\begin{aligned}\mathcal{R}_\phi(\phi_j^{\mathrm{Na_9Sn_4}}(t+\Delta t)) = {}& \mathcal{A}_\phi(\phi_j^{\mathrm{Na_9Sn_4}}(t+\Delta t)) \\ & - \frac{1}{\ell}\int_0^L \varphi_i^\phi\, \Delta t\, (w_{\mathrm{R}}^{(6.181)} - w_{\mathrm{R}}^{(6.182)})\,\mathrm{d}x \\ & + \mathcal{B}_\phi = 0\end{aligned} \tag{6.287}$$

with the known term

$$\mathcal{B}_\phi = -\frac{1}{\ell}\int_0^L \varphi_i^\phi \varphi_j^\phi \,\mathrm{d}x\; \phi_j^{\mathrm{Na_9Sn_4}}(t) \tag{6.288}$$

and where $\mathcal{A}_\phi(\phi_j^{\mathrm{Na_9Sn_4}}(t+\Delta t))$ is linear and defined by comparison with Eq. (6.242) with the dimensionless BE form above. The Newton linearization via the Gateaux derivative reads:

$$\frac{\partial}{\partial\epsilon}\mathcal{R}_\phi(\phi_j^{\mathrm{Na_9Sn_4}} + \epsilon\delta\phi_j^{\mathrm{Na_9Sn_4}})\Big|_{\epsilon=0} = \tag{6.289}$$

$$\mathcal{A}_\phi(\delta\phi_j^{\mathrm{Na_9Sn_4}}) - \frac{1}{\ell}\int_0^L \varphi_i^\phi\, \Delta t\, (\delta w_{\mathrm{R}}^{(6.181)} - \delta w_{\mathrm{R}}^{(6.182)})\,\mathrm{d}x$$

$$= -\mathcal{R}_\phi(\phi_j^{\mathrm{Na_9Sn_4}}(t+\Delta t))\,. \tag{6.290}$$

6.4.12.5 Newton–Raphson scheme for $\phi^{\mathrm{Na_{15}Sn_4}}$

For the Backward Euler step, we solve the nonlinear system by Newton iterations. Define the residual

$$\begin{aligned}\mathcal{R}_\phi(\phi_j^{\mathrm{Na_{15}Sn_4}}(t+\Delta t)) = {}& \mathcal{A}_\phi(\phi_j^{\mathrm{Na_{15}Sn_4}}(t+\Delta t)) \\ & - \frac{1}{\ell}\int_0^L \varphi_i^\phi\, \Delta t\, w_{\mathrm{R}}^{(6.182)}\,\mathrm{d}x \\ & + \mathcal{B}_\phi = 0\end{aligned} \tag{6.291}$$

with the known term

$$\mathcal{B}_\phi = -\frac{1}{\ell}\int_0^L \varphi_i^\phi \varphi_j^\phi \,\mathrm{d}x \;\; \phi_j^{\mathrm{Na_{15}Sn_4}}(t) \tag{6.292}$$

and where $\mathcal{A}_\phi(\cdot)$ is linear and defined by comparison (6.243) with the dimensionless BE form. The Newton linearization (Gateaux derivative) reads

$$\frac{\partial}{\partial\epsilon}\mathcal{R}_\phi(\phi_j^{\mathrm{Na_{15}Sn_4}} + \epsilon\delta\phi_j^{\mathrm{Na_{15}Sn_4}})\Big|_{\epsilon=0} = \tag{6.293}$$

$$\mathcal{A}_\phi(\delta\phi_j^{\mathrm{Na_{15}Sn_4}}) - \frac{1}{\ell}\int_0^L \varphi_i^\phi \,\Delta t\; \delta w_{\mathrm{R}}^{(6.182)}\,\mathrm{d}x$$

$$= -\mathcal{R}_\phi(\phi_j^{\mathrm{Na_{15}Sn_4}}(t+\Delta t))\,. \tag{6.294}$$

6.4.12.6 Newton–Raphson scheme for $\phi^{\mathrm{Na},*}$

Equation (6.258) can be written compactly as

$$\mathcal{R}_{\phi^{\mathrm{Na},*}}({\phi^{\mathrm{Na},*}}_j(t+\Delta t), \phi_j^{\mathrm{Na}}(t+\Delta t)) = \mathcal{A}_{\phi^{\mathrm{Na},*}}({\phi^{\mathrm{Na},*}}_j(t+\Delta t), \phi_j^{\mathrm{Na}}(t+\Delta t)) \tag{6.295}$$

$$+\ \mathcal{B}_{\phi^{\mathrm{Na},*}} = 0$$

with

$$\mathcal{B}_{\phi^{\mathrm{Na},*}} = \frac{\lambda}{\beta\ell^2}\,\varphi_i^*\,\ell\,h_{1D}^*\Big|_0^L\,, \tag{6.296}$$

and where $\mathcal{A}_{\phi^{\mathrm{Na},*}}(\cdot)$ is linear and defined by comparison. The Newton step is given by the Gateaux derivative

$$\frac{\partial}{\partial\epsilon}\mathcal{R}_{\phi^{\mathrm{Na},*}}({\phi^*}_j + \epsilon\delta{\phi^{\mathrm{Na},*}}_j, \phi_j^{\mathrm{Na}} + \epsilon\delta\phi_j^{\mathrm{Na}})\Big|_{\epsilon=0} = \mathcal{A}_{\phi^{\mathrm{Na},*}}(\delta{\phi^{\mathrm{Na},*}}_j, \delta\phi_j^{\mathrm{Na}}) \tag{6.297}$$

$$= -\mathcal{R}_{\phi^{\mathrm{Na},*}}({\phi^{\mathrm{Na},*}}_j(t+\Delta t), \phi_j^{\mathrm{Na}}(t+\Delta t))\,.$$

6.4.12.7 Newton–Raphson scheme for γ^{Na}

Using test functions φ_i^γ and the dimensionless nodal displacement unknowns $\upsilon_j = u_j/\ell$, the nonlinear residual reads

$$\mathcal{R}_{\gamma_{\mathrm{Na}}}(\gamma_j^{\mathrm{Na}}, \boldsymbol{\phi}_j, \upsilon_j) = \frac{1}{\ell}\int_0^L \varphi_i^\gamma\varphi_j^\gamma\,\mathrm{d}X_1\;\gamma_{\mathrm{Na},j}(t+\Delta t)$$

$$-\frac{E\,\Omega^{\mathrm{Na}}}{\ell\,\mu_{\mathrm{ref}}^{\mathrm{Na}}}\int_0^L \varphi_i^\gamma\Big\{\alpha_4\,\aleph(\boldsymbol{\phi}_j,\upsilon_j)^4 + \alpha_2\,\aleph(\boldsymbol{\phi}_j,\upsilon_j)^2\Big\}\,\mathrm{d}X_1$$

$$-\frac{1}{8}\frac{E\,\Omega^{\mathrm{Na}}}{\ell\,\mu_{\mathrm{ref}}^{\mathrm{Na}}}\int_0^L \varphi_i^\gamma\,\mathrm{d}X_1 \;=\; 0.$$

Let

$$\mathcal{A}_{\gamma^{\mathrm{Na}}}(\gamma_j^{\mathrm{Na}}(t+\Delta t)) = \frac{1}{\ell}\int_0^L \varphi_i^\gamma \varphi_j^\gamma \,\mathrm{d}X_1 \,\gamma_j^{\mathrm{Na}}(t+\Delta t), \quad \mathcal{B}_{\gamma^{\mathrm{Na}}} = -\frac{1}{8}\,\frac{E\,\Omega^{\mathrm{Na}}}{\ell\,\mu_{\mathrm{ref}}^{\mathrm{Na}}}\int_0^L \varphi_i^\gamma \,\mathrm{d}X_1.$$

The consistent tangent (Gateaux derivative) used in Newton–Raphson is reported in Appendix A.12.

6.4.12.8 Newton–Raphson scheme for u

The balance of momentum for the volume-fraction model follows the same steps as the concentration-based derivation presented in Section 6.3.1.4. The key difference lies in the definition of the coupling term $\aleph$, which now accounts for multiple phases through the weighted volume fractions $\boldsymbol{\phi}^\alpha$.

The final weak form in dimensionless variables is

$$\begin{aligned}\mathcal{R}_u(\boldsymbol{\phi}_j, \upsilon_j) = \frac{1}{2}\frac{E}{G}\int_0^L \frac{\partial \varphi_i}{\partial X_1} J^{c2/3}\,\aleph(\boldsymbol{\phi}_j,\upsilon_j)\left[\aleph(\boldsymbol{\phi}_j,\upsilon_j)^2 - 1\right]\,\mathrm{d}X_1 \\ - \frac{1}{\ell}\int_0^L \varphi_i\,\frac{B_1\ell}{G}\,\mathrm{d}X_1 - \varphi_i\,\frac{\overline{p}}{G}\Big|_0^L = 0,\end{aligned} \tag{6.298}$$

where

$$\aleph(\boldsymbol{\phi}_j,\upsilon_j) = \left(\varphi_h^\phi \sum_\alpha \phi_h^\alpha \omega^\alpha\right)^{-1/3}\left(1 + \ell\frac{\partial \varphi_j^u}{\partial X_1}\upsilon_j\right). \tag{6.299}$$

The detailed derivation of the consistent tangent operator via the Gateaux derivative is provided in Appendix A.12.

6.4.13 Discussion

The proposed volume-fraction and reaction-rate framework addresses several challenges associated with modeling multiphase transformations in sodium–tin alloy anodes. By replacing traditional concentration-based variables with volume fractions, the model ensures boundedness and local conservation, naturally representing phase coexistence and transitions between intermetallic compounds such as Sn, $NaSn_3$, Na_9Sn_4, and $Na_{15}Sn_4$. This improvement is particularly important for systems exhibiting sharp interfaces and large volumetric changes, where concentration-based models may violate physical constraints or require ad hoc corrections.

The incorporation of thermodynamically consistent reaction kinetics is another key advancement. Bulk reaction rates are derived directly from the mass-action law, expressed in terms of volume fractions to maintain correct stoichiometric balance and phase-fraction transfer. Moreover, the coupling with mechanics through the chemo-mechanical contribution μ^{mech} allows the

model to capture how stress and deformation influence both bulk diffusion and interfacial electrochemical reactions. This is crucial for Na–Sn electrodes, where significant swelling and stress generation are observed experimentally during cycling.

From a computational perspective, the framework supports both explicit (Forward Euler) and implicit (Backward Euler) time integration schemes. The Newton–Raphson linearization improves convergence for strongly coupled fields, such as volume fractions, chemo-mechanical potential, and displacement. Dimensionless groups such as the scaled diffusivity $\tilde{\mathbb{D}}$ and the penalty parameter $\lambda/(\beta\ell^2)$ emerge naturally, providing physical insight into numerical stability and interface regularization.

While the framework provides a unified and physically grounded description, certain limitations remain. The calibration of reaction rate constants and interfacial parameters requires careful comparison with experimental data, such as plateau voltages and galvanostatic/potentiostatic profiles. Future extensions may include temperature dependence, plastic deformation, and three-dimensional simulations to capture the full complexity of realistic electrode architectures.

Overall, this framework bridges the gap between thermodynamic rigor and numerical practicality, enabling the simulation of multiphase transport, interfacial reactions, and mechanics in Na–Sn alloy electrodes under realistic operating conditions.

6.5 Conclusions

This chapter presented a comprehensive continuum mechanics model tailored for the simulation of sodium-ion batteries with tin-based electrodes. The model integrates the effects of phase segregation and is capable of describing the interplay between mechanical and chemical phenomena within the battery's electrode materials.

We began by employing an operator splitting approach to handle the coupling of mechanical and chemical behaviors, which was further refined with a penalty approach to better manage the interface energy's influence on phase segregation. Furthermore, the decomposition of the fourth-order differential equation into two second-order equations simplified the computations significantly, aligning well with the numerical methods used and enhancing the model's computational efficiency. This adjustment helps to handle the boundary conditions and stress–strain behaviors observed during the simulations.

Through a series of detailed numerical simulations, we investigated the effects of diffusivity ($\mathbb{D}$), interaction parameter (χ), and the gradient energy coefficient (λ) on the behavior of the electrodes. The model demonstrated how varying χ impacts the energetic interactions between diffusing species and the host material, leading to varying tendencies towards phase separation. Higher χ values produced sharper interfaces and more distinct phase segregations, underscoring the parameter's role in modulating material behavior under electrochemical stress. Similarly, adjustments in λ influenced the stability of the system by penalizing sharp concentration gradients, thereby stabilizing the interfaces between phases. These findings highlight the model's capability to capture the thermodynamic and kinetic mechanisms that govern phase evolution.

Beyond concentration evolution, the decomposition of the Helmholtz free energy into entropic, interfacial, interaction, and mechanical contributions provided deeper insights into the thermodynamic processes driving phase segregation and stress generation. The mechanical energy component was observed to increase monotonically in the sodiated regions, illustrating how stress builds up during sodium insertion. The coupled chemo–mechanical analysis also enabled direct evaluation of stress fields: as sodium entered the electrode, compressive stresses developed in the sodiated regions while the pristine regions remained nearly stress-free. During the subsequent relaxation phase, these stresses redistributed and reached equilibrium, confirming that mechanical effects play a central role in long-term electrode performance. Mesh-refined simulations further verified that the Piola stress remained constant away from the moving interface, validating the accuracy of the momentum balance implementation.

A key outcome of this study is the demonstrated importance of accounting for both chemical and mechanical factors when designing and optimizing tin-based electrodes for sodium-ion batteries. The observed stress relaxation suggests that over time, the electrode material adapts to internal stresses induced by ion intercalation, which in turn impacts its electrochemical performance and durability.

Future work should focus on extending the model to three-dimensional simulations and exploring the effects of more complex boundary conditions and realistic operating conditions. Additionally, experimental validation of the model's predictions will be crucial to improve the reliability and practical applicability of tin-based electrodes in sodium-ion battery technologies.

Finally, this chapter introduced a thermodynamically consistent framework that leverages volume fractions as primary state variables, enabling a natural and bounded representation of multiphase evolution. The proposed formulation unifies bulk diffusion, interfacial reactions, and mechanical effects by coupling reaction kinetics with the chemo–mechanical contribution to the chemical potential. This integrated approach provides a robust foundation for future modeling of multiphase electrode materials and offers insights for the design and optimization of sodium-ion batteries with Sn-based anodes.

Chapter 7

Conclusion

This thesis set out to understand, model, and experimentally validate tin-based alloy anodes for sodium-ion batteries (SIBs), focusing on how multistep phase transformations and large (de)sodiation-induced volume changes govern stability, rate capability, and lifetime. By combining multimodal characterization with thermodynamically consistent phase-field modeling, we identified the materials, architectural, and numerical factors that most strongly influence performance, and we translated those insights into concrete design guidance.

On the materials side, commercial Sn powders with a broad grain-size distribution hindered homogeneous electrode formation and limited Na diffusion into particles, yielding poor electrochemical behavior. Among the electrolytes tested, $NaPF_6$ in EC:DEC delivered marginally superior results and was adopted in subsequent trials. Work on Sn+CNF composites clarified that binder–collector compatibility is pivotal: CMC binder together with an Al+C current collector produced the most consistent performance, whereas PVDF electrodes improved only when mechanically pressed, underscoring the role of polymer mechanics, adhesion, and electronic pathways.

Two synthesis routes were then contrasted. The chelation route (Sn+SA) produced highly carbon-coated, weakly crystalline Sn; despite a modest Sn fraction, these electrodes achieved higher specific capacities than commercial powders, especially under controlled compression (Hohsen cells). Cycling stability and morphology indicate partial formation of Na–Sn intermetallics within a porous carbon matrix, with overall volume change mitigated by confinement in the carbon–binder network. The aqueous infiltration route, which grows Sn directly on conductive carbon sponges, reached $\sim$500–600 $\mathrm{mAh\,g^{-1}}$ at C/10 with average working potentials $< 0.5\,\mathrm{V}$ vs. Na/Na^+. However, thick sponge electrodes exhibited unstable behavior at higher currents due to poor Na-ion transport, revealing a clear thickness/transport limitation

that constrains rate capability.

Microstructural evidence across techniques converged on a common picture. SEM of pristine electrodes showed Sn grains embedded and partially encapsulated by carbon, sometimes as tin veins (Fig. 4.25d). After cycling, structures became more porous and less compact, with fewer distinct grains but more extended veins (Fig. 4.26b). Synchrotron tomography corroborated these trends: voxel-intensity profiles (Dragonfly) indicated density loss (red arrows, Fig. 4.33), cracks (white arrows), and fractures (black arrows), with some intact Sn particles persisting (yellow arrows). In both chelation-derived and sponge-infiltrated electrodes, tomography/SEM revealed fragmentation, void formation, and partial densification; yet macroscopic expansion was more limited for Sn+SA due to carbon confinement, while transport limitations in sponges led to capacity losses at higher rates (Figs. 4.28, 4.30, 4.34, 4.31). BSE contrast reductions were consistent with Na incorporation; EDX confirmed residual Na and $NaPF_6$, with an average Na:Sn of ∼13.4:3.8 compatible with $Na_{15}Sn_4$. Electrochemistry (Table 4.3) captured the expected sequence, SEI formation (∼0.75 V), SnO_2 reduction (∼0.41 V), and alloying through $NaSn_3$ (0.36 V), NaSn (0.19 V), Na_9Sn_4 (0.08–0.06 V), and $Na_{15}Sn_4$ (0.035 V), with progressive current decay reflecting rising resistance from evolving microstructural damage.

On the modeling side, we developed and verified a 1D continuum phase-field framework that couples Cahn–Hilliard transport, interfacial energetics, and elasticity to capture segregation fronts, interface motion, and stress generation during (de)sodiation. Parameter sweeps spanned $\mathbb{D} \in [10^{-15}, 10^{-9}]\,\mathrm{m}^2/\mathrm{s}$, $\lambda/(RT\ell^2) \in [0, 4]$, and mesh sizes from 8 to 64 elements (with $\chi = 10$ in the baseline), and they exposed a key numerical insight: the baseline operator-splitting becomes fragile as diffusivity and gradient penalties increase, especially on fine meshes, due to problem stiffness. A penalty-based operator-splitting scheme that enforces consistency between split subproblems restored convergence across a much broader regime while preserving physical modularity. Targeted experiments (e.g., prescribed-flux charge followed by relaxation) confirmed mass conservation (inserted mass vs. $\int c\,dx$), clarified the role of χ (stronger segregation slows relaxation), and decomposed the Helmholtz free energy into entropic, interaction, interfacial, and mechanical components, showing interfacial maxima at moving fronts and monotonic mechanical-energy accumulation in sodiated regions. The mechanical contribution to the chemical potential, μ^{mech}, rose with swelling and dominated near equilibrium; stress fields were consistent with the 1D balance $\nabla \cdot \boldsymbol{P} = 0$ (nearly constant P_{11} apart from mesh-scale oscillations near the front).

To better represent multistep intermetallic formation and large volumetric changes, we advanced a volume-fraction formulation that tracks phases

$\phi^\alpha \in [0,1]$ (e.g., Sn, $NaSn_3$, Na_9Sn_4, $Na_{15}Sn_4$), guaranteeing boundedness, local filling, and coexistence. Bulk reaction rates follow mass action written directly in ϕ^α, ensuring stoichiometric phase transfer; interfacial electrochemical reactions are mapped to thin volumetric layers to keep boundary fluxes consistent with volumetric sources/sinks. Coupling to mechanics through μ^{mech} closes the chemo-mechanical loop. The framework supports explicit/implicit time integration with Newton–Raphson linearization; key dimensionless groups (scaled diffusivity, interfacial length, penalty ratios) rationalize stability windows.

Taken together, experiment and simulation tell a consistent story. Confinement of Sn within compliant, conductive carbon networks curbs macroscopic expansion and better sustains capacity at C/10 than transport-limited sponges; imaging-derived signatures (fragmentation, voiding, partial densification) align with simulated segregation fronts and compressive-stress build-up. The observed Na:Sn ratio ∼13.4:3.8 and low-voltage plateaus are consistent with $Na_{15}Sn_4$ formation; in the model, stronger interaction (χ) and smaller interfacial length scales sharpen phase separation while elevating stresses.

Model–experiment correspondence.

Model prediction	**Experimental observation**
Segregation fronts sharpen with higher χ and smaller l (Fig. 6.7); interfacial energy localizes gradients.	SEM/BSE shows fragmentation and partial densification; tomography reveals morphology changes consistent with front motion (Fig. 4.33–4.34).
Peak compressive σ_{11} and elastic second Piola stress coincide with the front during charge and relax after t_f (Fig. 6.13).	Post-cycling micrographs show vein-like Sn and porosity patterns consistent with stress-driven reorganization (Fig. 4.25–4.26).
Model scaling predicts larger concentration polarization as the effective path length increases.	Sponge electrodes show unstable behavior at higher currents (C-rates), indicating Na-transport limits (Sec. 4.4).

Table 7.1: Correspondence between model predictions and experimental observations.

Design guidelines. Favor carbon-confined Sn architectures over sponge layouts to limit expansion and retain capacity at rate; minimize transport

pathlengths (reduce thickness, engineer porosity/tortuosity) to avoid high-current fade; pair CMC binder with Al+C current collectors for robust performance; apply controlled compression/pressing where compatible with the architecture; prefer $NaPF_6$ EC:DEC among the tested electrolytes; and, for modeling, employ penalty-stabilized operator splitting (or fully implicit coupling) in stiff regimes and use volume-fraction variables with thin-layer reaction mapping to enforce physical constraints.

In closing, this work delivers an experimental and mechanical basis for designing durable Sn-based SIB anodes. The synthesis of microstructural evidence with a physically constrained, numerically robust modeling framework yields specific, guidance on materials and computation, and sets a path toward calibrated, 3D, and fracture-aware predictions that can accelerate the deployment of sodium-ion technology in renewable-integrated storage.

Limitations & outlook. The present study deliberately adopts a one-dimensional formulation to isolate the essential couplings among transport, interfacial thermodynamics, and mechanics; this choice, while enabling broad parametric exploration, limits geometric realism and microstructure-specific predictions. In future work, we will extend the framework to three-dimensional, voxelized microstructures derived from imaging, allowing spatially resolved fields and morphology-sensitive responses to be captured. Model parameters governing interfacial kinetics and segregation, notably χ, and the gradient length scale l, will be calibrated against plateau voltages and galvanostatic charge–discharge curves, aiming for quantitative agreement over relevant C-rates. To better represent irreversible deformation and failure, the constitutive description will be augmented with plasticity, enabling the prediction of densification under large (de)sodiation strains. Finally, we will pursue systematic validation against SEM and X-ray tomography, comparing phase-sequence evolution, interface widths, and areal-capacity/rate trends to close the loop between theory and experiment and to establish the predictive scope of the proposed framework.

Appendix A

Appendix

A.1 Governing equations of the full problem

A.1.1 Newton–Raphson scheme for γ

The discrete dimensionless weak form (6.42) (with the nonlinear boundary contribution) becomes

$$\mathcal{R}_\gamma(\gamma_j,\theta_j) = \mathcal{A}_\gamma(\gamma_j,\theta_j) \;-\; \frac{1}{\ell^2}\,\frac{\lambda}{RT}\,\Big(\,\varphi_i^\gamma\;\varphi_h^\theta\,\theta_h\,\big(1-\varphi_k^\theta\,\theta_k\big)\;\ell\,\frac{\partial\varphi_j^\gamma}{\partial x}\,\gamma_j\,\Big|_0^L\Big) \;+\; \mathcal{B}_\gamma \;=\; 0, \tag{A.1}$$

with $\mathcal{A}_\gamma$ linear and defined by comparison and

$$\mathcal{B}_\gamma = -\,\frac{RT}{\mu_{\text{ref}}}\chi\,\frac{1}{\ell}\int_0^L \varphi_i^\gamma\,\mathrm{d}x \;-\; \frac{1}{\ell^2}\,\frac{\lambda}{RT}\,\frac{RT}{\mu_{\text{ref}}}\,\frac{1}{\tilde{\mathrm{D}}}\,\Big(\,\varphi_i^\gamma\,\frac{\Delta t\,h_{1D}(x,t{+}\Delta t)}{c_{\max}\,\ell}\,\Big|_0^L\Big). \tag{A.2}$$

The Newton–Raphson scheme can be written by means of the Gateaux derivative

$$\begin{aligned}\frac{\partial}{\partial\epsilon}\,\mathcal{R}_\gamma(\gamma_j{+}\epsilon\,\delta\gamma_j,\theta_j{+}\epsilon\,\delta\theta_j)\Big|_{\epsilon=0} &= \mathcal{A}_\gamma(\delta\gamma,\delta\theta) \\ &\quad -\;\frac{1}{\ell^2}\,\frac{\lambda}{RT}\,\Big(\,\ell\;\varphi_i^\gamma\;\big(1-2\,\varphi_k^\theta\,\theta_k\big)\;\frac{\partial\varphi_h^\gamma}{\partial x}\,\gamma_h\;\varphi_j^\theta\,\delta\theta_j\;\Big|_0^L\Big) \\ &\quad -\;\frac{1}{\ell^2}\,\frac{\lambda}{RT}\,\Big(\,\ell\;\varphi_i^\gamma\;\varphi_h^\theta\,\theta_h\,\big(1-\varphi_k^\theta\,\theta_k\big)\;\frac{\partial\varphi_j^\gamma}{\partial x}\,\delta\gamma_j\;\Big|_0^L\Big) \\ &=\; -\mathcal{R}_\gamma(\gamma_j(t{+}\Delta t),\theta_j(t{+}\Delta t)).\end{aligned} \tag{A.3}$$

The governing equations for the mass balance in the full problem are the same as those detailed in Section 6.1.4, namely (6.52), (6.54), and (6.55).

A.2 Gateaux derivative for the penalty formulation of Eq. (6.84)

We report the detailed expressions of the weak forms, the full Gateaux derivative expansions used in the Newton–Raphson schemes, associated with Eq. (6.84), and the corresponding Jacobian contributions. The Gateaux derivative of the residual $\mathcal{R}_\theta$ with respect to the perturbations $\delta\theta_j$ and $\delta\theta_j^*$ reads:

$$
\begin{aligned}
&\frac{\partial}{\partial\epsilon}\mathcal{R}_\theta(\theta_j^* + \epsilon\delta\theta_j^*, \theta_j + \epsilon\delta\theta_j)\bigg|_{\epsilon=0} = \mathcal{A}_\theta(\delta\theta_j^*, \delta\theta_j) \qquad \text{(A.4)}\\
&\quad + \tilde{\mathbb{D}}\left(\frac{\beta}{RT} - 2\chi\right)\ell\int_0^L \frac{\partial\varphi_h^\theta}{\partial x}\,\theta_h(t+\Delta t)\,\frac{\partial\varphi_i^\theta}{\partial x}\,\varphi_j^\theta\;\mathrm{d}x\;\;\delta\theta_j(t+\Delta t)\\
&\quad + \tilde{\mathbb{D}}\left(\frac{\beta}{RT} - 2\chi\right)\ell\int_0^L \varphi_h^\theta\,\theta_h(t+\Delta t)\,\frac{\partial\varphi_i^\theta}{\partial x}\frac{\partial\varphi_j^\theta}{\partial x}\;\mathrm{d}x\;\;\delta\theta_j(t+\Delta t)\\
&\quad - 2\tilde{\mathbb{D}}\left(\frac{\beta}{RT} - 2\chi\right)\ell\int_0^L \varphi_k^\theta\,\theta_k(t+\Delta t)\,\frac{\partial\varphi_h^\theta}{\partial x}\,\theta_h(t+\Delta t)\,\frac{\partial\varphi_i^\theta}{\partial x}\,\varphi_j^\theta\;\mathrm{d}x\;\;\delta\theta_j(t+\Delta t)\\
&\quad - \tilde{\mathbb{D}}\left(\frac{\beta}{RT} - 2\chi\right)\ell\int_0^L \varphi_h^\theta\,\theta_h(t+\Delta t)\,\varphi_k^\theta\,\theta_k(t+\Delta t)\,\frac{\partial\varphi_i^\theta}{\partial x}\frac{\partial\varphi_j^\theta}{\partial x}\;\mathrm{d}x\;\;\delta\theta_j(t+\Delta t)\\
&\quad - \tilde{\mathbb{D}}\frac{\beta}{RT}\,\ell\int_0^L \frac{\partial\varphi_h^*}{\partial x}\,\theta_h^*(t+\Delta t)\,\frac{\partial\varphi_i^\theta}{\partial x}\,\varphi_j^\theta\;\mathrm{d}x\;\;\delta\theta_j(t+\Delta t)\\
&\quad - \tilde{\mathbb{D}}\frac{\beta}{RT}\,\ell\int_0^L \varphi_h^\theta\,\theta_h(t+\Delta t)\,\frac{\partial\varphi_i^\theta}{\partial x}\frac{\partial\varphi_j^*}{\partial x}\;\mathrm{d}x\;\;\delta\theta_j^*(t+\Delta t)\\
&\quad + 2\tilde{\mathbb{D}}\frac{\beta}{RT}\,\ell\int_0^L \varphi_k^\theta\,\theta_k(t+\Delta t)\,\frac{\partial\varphi_h^*}{\partial x}\,\theta_h^*(t+\Delta t)\,\frac{\partial\varphi_i^\theta}{\partial x}\,\varphi_j^\theta\;\mathrm{d}x\;\;\delta\theta_j(t+\Delta t)\\
&\quad + \tilde{\mathbb{D}}\frac{\beta}{RT}\,\ell\int_0^L \varphi_h^\theta\,\theta_h(t+\Delta t)\,\varphi_k^\theta\,\theta_k(t+\Delta t)\,\frac{\partial\varphi_i^\theta}{\partial x}\frac{\partial\varphi_j^*}{\partial x}\;\mathrm{d}x\;\;\delta\theta_j^*(t+\Delta t)\\
&\quad = -\mathcal{R}_\theta(\theta_j^*(t+\Delta t), \theta_j(t+\Delta t))\;.
\end{aligned}
$$

A.3 Governing equations of the full penalty problem

For completeness, we report here the governing equations and Newton–Raphson scheme for the full penalty problem. The formulation only differs from the "Neumann kind" discussed in Section 6.2.3 by the treatment of the penalty constraint.

A.3.1 Newton–Raphson scheme

The discrete governing equation for the penalty constraint in 1D reads

$$\frac{1}{\ell}\int_0^L \varphi_i^*\,\varphi_j^\theta\;\mathrm{d}x\;\theta_j(t+\Delta t) - \frac{1}{\ell}\int_0^L \varphi_i^*\,\varphi_j^*\;\mathrm{d}x\;\theta_j^*(t+\Delta t) \tag{A.5}$$
$$-\frac{\lambda}{\beta\ell^2}\,\ell\int_0^L \frac{\partial\varphi_i^*}{\partial x}\frac{\partial\varphi_j^*}{\partial x}\;\mathrm{d}x\;\theta_j^*(t+\Delta t) + \frac{\lambda}{\beta\ell^2}\,\varphi_i^*\,\ell\,\frac{\partial\varphi_j^*}{\partial x}\,\theta_j^*(t+\Delta t)\Big|_0^L = 0\,.$$

This equation is linear and homogeneous, and can be compactly written as

$$\mathcal{R}_{\theta^*}(\theta_j^*(t+\Delta t),\theta_j(t+\Delta t)) = \mathcal{A}_{\theta^*}(\theta_j^*(t+\Delta t),\theta_j(t+\Delta t)) = 0\,. \tag{A.6}$$

The Newton–Raphson linearization is obtained via the Gateaux derivative:

$$\frac{\partial}{\partial\epsilon}\mathcal{R}_{\theta^*}(\theta_j^*+\epsilon\delta\theta_j^*,\theta_j+\epsilon\delta\theta_j)\Big|_{\epsilon=0} = \mathcal{A}_{\theta^*}(\delta\theta_j^*,\delta\theta_j) = -\mathcal{R}_{\theta^*}(\theta_j^*(t+\Delta t),\theta_j(t+\Delta t))\,. \tag{A.7}$$

A.4 Gateaux derivative for u of Eq. (6.128)

The nonlinear residual (6.128) is linearized by means of the Gateaux derivative, yielding,

$$\frac{\partial}{\partial\epsilon}\mathcal{R}_u(\theta_j+\epsilon\delta\theta_j,\upsilon_j+\epsilon\delta\upsilon_j)\Big|_{\epsilon=0} = -\mathcal{R}_u(\theta_j,\upsilon_j)\,. \tag{A.8}$$

Explicitly,

$$\frac{\partial}{\partial\epsilon}\mathcal{R}_u(\theta_j+\epsilon\delta\theta_j,\upsilon_j+\epsilon\delta\upsilon_j)\Big|_{\epsilon=0} = (1+\nu)\int_0^L \frac{\partial\varphi_i}{\partial X_1}J^{c2/3}\left[3\aleph(\theta_j,\upsilon_j)^2-1\right] \tag{A.9}$$
$$\frac{\partial}{\partial\epsilon}\aleph(\theta_j+\epsilon\delta\theta_j,\upsilon_j+\epsilon\delta\upsilon_j)\Big|_{\epsilon=0}\,\mathrm{d}X_1$$
$$+\frac{2}{3}(1+\nu)\int_0^L \frac{\partial\varphi_i}{\partial X_1}\,\aleph(\theta_j,\upsilon_j)$$
$$\left[\aleph(\theta_j,\upsilon_j)^2-1\right]\frac{\Omega\,c_{\max}}{J^{c1/3}}\varphi_j^\theta\,\delta\theta_j\,\mathrm{d}X_1.$$

The sensitivity of $\aleph$ to perturbations in θ_j and υ_j is

$$\frac{\partial}{\partial\epsilon}\aleph(\theta_j+\epsilon\delta\theta_j,\upsilon_j+\epsilon\delta\upsilon_j)\Big|_{\epsilon=0} = \left(1+\Omega\,c_{\max}\,\varphi_h^\theta\theta_h\right)^{-4/3} \tag{A.10}$$
$$\times\left[-\frac{\Omega\,c_{\max}}{3}\left(1+\ell\,\frac{\partial\varphi_k^u}{\partial X_1}\,\upsilon_k\right)\varphi_j^\theta\,\delta\theta_j\right.$$
$$\left.+\left(1+\Omega\,c_{\max}\,\varphi_h^\theta\theta_h\right)\ell\,\frac{\partial\varphi_j^\upsilon}{\partial X_1}\,\delta\upsilon_j\right].$$

A.5 Gateaux derivative for θ of Eq. (6.160)

The Newton-Raphson scheme (6.160) can be written by means of the Gateaux derivative

$$
\begin{aligned}
&\frac{\partial}{\partial\epsilon}\mathcal{R}_\theta({\theta^*}_j+\epsilon\delta{\theta^*}_j,\theta_j+\epsilon\delta\theta_j,\gamma_j+\epsilon\delta\gamma_j)\Big|_{\epsilon=0} = \mathcal{A}_\theta(\delta{\theta^*}_j,\delta\theta_j) \qquad \text{(A.11)}\\
&+\tilde{\mathrm{D}}\left(\frac{\beta}{RT}-2\,\chi\right)\ell\int_0^L\frac{\partial\varphi_h^\theta}{\partial x}\,\theta_h(t+\Delta t)\,\frac{\partial\varphi_i^\theta}{\partial x}\,\varphi_j^\theta\,\mathrm{d}x\;\delta\theta_j(t+\Delta t)\\
&+\tilde{\mathrm{D}}\left(\frac{\beta}{RT}-2\,\chi\right)\ell\int_0^L\varphi_h^\theta\,\theta_h(t+\Delta t)\,\frac{\partial\varphi_i^\theta}{\partial x}\frac{\partial\varphi_j^\theta}{\partial x}\,\mathrm{d}x\;\delta\theta_j(t+\Delta t)\\
&-2\,\tilde{\mathrm{D}}\left(\frac{\beta}{RT}-2\,\chi\right)\ell\int_0^L\varphi_k^\theta\,\theta_k(t+\Delta t)\,\frac{\partial\varphi_h^\theta}{\partial x}\,\theta_h(t+\Delta t)\,\frac{\partial\varphi_i^\theta}{\partial x}\,\varphi_j^\theta\,\mathrm{d}x\;\delta\theta_j(t+\Delta t)\\
&-\tilde{\mathrm{D}}\left(\frac{\beta}{RT}-2\,\chi\right)\ell\int_0^L\varphi_h^\theta\,\theta_h(t+\Delta t)\,\varphi_k^\theta\,\theta_k(t+\Delta t)\,\frac{\partial\varphi_i^\theta}{\partial x}\,\frac{\partial\varphi_j^\theta}{\partial x}\,\mathrm{d}x\;\delta\theta_j(t+\Delta t)\\
&-\tilde{\mathrm{D}}\,\frac{\beta}{RT}\,\ell\int_0^L\frac{\partial\varphi_h^*}{\partial x}\,\theta_h^*(t+\Delta t)\,\frac{\partial\varphi_i^\theta}{\partial x}\,\varphi_j^\theta\,\mathrm{d}x\;\delta\theta_j(t+\Delta t)\\
&-\tilde{\mathrm{D}}\,\frac{\beta}{RT}\,\ell\int_0^L\varphi_h^\theta\,\theta_h(t+\Delta t)\,\frac{\partial\varphi_i^\theta}{\partial x}\frac{\partial\varphi_j^*}{\partial x}\,\mathrm{d}x\;\delta\theta_j^*(t+\Delta t)\\
&+2\,\tilde{\mathrm{D}}\,\frac{\beta}{RT}\,\ell\int_0^L\varphi_k^\theta\,\theta_k(t+\Delta t)\,\frac{\partial\varphi_h^*}{\partial x}\,\theta_h^*(t+\Delta t)\;\frac{\partial\varphi_i^\theta}{\partial x}\,\varphi_j^\theta\,\mathrm{d}x\;\delta\theta_j(t+\Delta t)\\
&+\tilde{\mathrm{D}}\,\frac{\beta}{RT}\,\ell\int_0^L\varphi_h^\theta\,\theta_h(t+\Delta t)\,\varphi_k^\theta\,\theta_k(t+\Delta t)\,\frac{\partial\varphi_i^\theta}{\partial x}\frac{\partial\varphi_j^*}{\partial x}\,\mathrm{d}x\;\delta\theta_j^*(t+\Delta t)\\
&-\tilde{\mathrm{D}}\,\frac{\mu_{\mathrm{ref}}}{RT}\,\ell\int_0^L\frac{\partial\varphi_h^\gamma}{\partial x}\,\gamma_h(t+\Delta t)\,\frac{\partial\varphi_i^\theta}{\partial x}\,\varphi_j^\theta\,\mathrm{d}x\;\delta\theta_j(t+\Delta t)\\
&-\tilde{\mathrm{D}}\,\frac{\mu_{\mathrm{ref}}}{RT}\,\ell\int_0^L\varphi_h^\theta\,\theta_h(t+\Delta t)\,\frac{\partial\varphi_i^\theta}{\partial x}\frac{\partial\varphi_j^\gamma}{\partial x}\,\mathrm{d}x\;\delta\gamma_j(t+\Delta t)\\
&+2\,\tilde{\mathrm{D}}\,\frac{\mu_{\mathrm{ref}}}{RT}\,\ell\int_0^L\varphi_k^\theta\,\theta_k(t+\Delta t)\,\frac{\partial\varphi_h^\gamma}{\partial x}\,\gamma_h(t+\Delta t)\;\frac{\partial\varphi_i^\theta}{\partial x}\,\varphi_j^\theta\,\mathrm{d}x\;\delta\theta_j(t+\Delta t)\\
&+\tilde{\mathrm{D}}\,\frac{\mu_{\mathrm{ref}}}{RT}\,\ell\int_0^L\varphi_h^\theta\,\theta_h(t+\Delta t)\,\varphi_k^\theta\,\theta_k(t+\Delta t)\,\frac{\partial\varphi_i^\theta}{\partial x}\frac{\partial\varphi_j^\gamma}{\partial x}\,\mathrm{d}x\;\delta\gamma_j(t+\Delta t)\\
&=-\mathcal{R}_\theta({\theta^*}_j(t+\Delta t),\theta_j(t+\Delta t),\gamma_j(t+\Delta t))\,.
\end{aligned}
$$

A.6 Penalty operator splitting constraint equation

The dimensionless 1D restriction of eq. (6.64) reads:

$$\theta - \theta^* + l^2 \, \frac{\partial}{\partial X_1} \frac{\partial \theta^*}{\partial X_1} = 0 \, . \tag{A.12}$$

Denote with L the right end of the 1D domain, which starts in $x = 0$. The weak form of (A.12) reads:

$$\frac{1}{\ell} \int_0^L \varphi_i^* \theta \, \mathrm{d}X_1 - \frac{1}{\ell} \int_0^L \varphi_i^* \theta^* \, \mathrm{d}X_1 + \frac{1}{\ell} \int_0^L \varphi_i^* \frac{\partial}{\partial X_1} \left(l^2 \frac{\partial \theta^*}{\partial X_1} \right) \mathrm{d}X_1 = 0 \, . \tag{A.13}$$

Upon integration by parts we obtain

$$\frac{1}{\ell} \int_0^L \varphi_i^* \theta \, \mathrm{d}X_1 - \frac{1}{\ell} \int_0^L \varphi_i^* \theta^* \, \mathrm{d}X_1 - \frac{l^2}{\ell^2} \, \ell \int_0^L \frac{\partial \varphi_i^*}{\partial X_1} \frac{\partial \theta^*}{\partial X_1} \mathrm{d}X_1 + \frac{l^2}{\ell^2} \, \varphi_i^* \, \ell \frac{\partial \theta^*}{\partial X_1} \Big|_0^L = 0 \tag{A.14}$$

Remark. Similarly to what discussed in section 6.1.2.4, the penalty equation (6.254) does not convey any meaning of a conservation law. For this reason, neither Dirichlet nor Neumann boundaries are expected for the equation (6.254) . The contribution

$$\frac{l^2}{\ell^2} \, \varphi_i^* \, \ell \frac{\partial \theta^*}{\partial X_1} \Big|_0^L \tag{A.15}$$

in equation (6.254) shall therefore be evaluated on the whole boundary. In most publications, though, as well as in manufactured solutions, the contribution defined by equation (A.15) is given. The latter approach will be called "of Neumann kind" in what follows. In view of definition (6.143), the given contribution (A.15) will be expressed as

$$\varphi_i^* \, \frac{\lambda}{\beta \ell^2} \, \ell \, h_{1D}^* \Big|_0^L \, . \tag{A.16}$$

Remark. Note that

$$\frac{\lambda}{\beta \ell^2} = \frac{l^2}{\ell^2} \, . \tag{A.17}$$

It has been remarked in section 6.2 that l has the physical meaning of an inner length.

λ is a gradient energy coefficient, that introduces an internal length scale for the width of interfaces between distinct phases. The width of the interface between faces at a given temperature depends only on the two physical parameters λ and χ in the free energy. β is a penalty energy coefficient.

A.6.1 Separated variables discretization

$$\theta(X_1,t)=\sum_j\ \varphi_j^{\theta}(X_1)\ \theta_j(t)\ ,\qquad \theta^*(X_1,t)=\sum_j\ \varphi_j^*(X_1)\ \theta_j^*(t)\ . \tag{A.18}$$

Replacing into (6.147), we get the discrete weak form as (with Einstein summation convention):

A.6.2 1D Discrete Dimensionless Weak form (Neumann kind)

With Einstein summation over j and h_{1D}^* defined in (6.143),

$$\begin{aligned}&\frac{1}{\ell}\int_0^L \varphi_i^*\,\varphi_j^{\theta}\,\mathrm{d}X_1\ \theta_j(t+\Delta t)-\frac{1}{\ell}\int_0^L \varphi_i^*\,\varphi_j^*\,\mathrm{d}X_1\ \theta_j^*(t+\Delta t)\\ &\quad-\frac{\lambda}{\beta\ell^2}\,\ell\int_0^L\frac{\partial\varphi_i^*}{\partial X_1}\,\frac{\partial\varphi_j^*}{\partial X_1}\,\mathrm{d}X_1\ \theta_j^*(t+\Delta t)+\frac{\lambda}{\beta\ell^2}\ \varphi_i^*\,\ell\,h_{1D}^*\Big|_0^L=0\ .\end{aligned} \tag{A.19}$$

A.6.3 1D Discrete Dimensionless Weak form (natural boundary term)

$$\begin{aligned}&\frac{1}{\ell}\int_0^L \varphi_i^*\,\varphi_j^{\theta}\,\mathrm{d}X_1\ \theta_j(t+\Delta t)-\frac{1}{\ell}\int_0^L \varphi_i^*\,\varphi_j^*\,\mathrm{d}X_1\ \theta_j^*(t+\Delta t)\\ &\quad-\frac{\lambda}{\beta\ell^2}\,\ell\int_0^L\frac{\partial\varphi_i^*}{\partial X_1}\,\frac{\partial\varphi_j^*}{\partial X_1}\,\mathrm{d}X_1\ \theta_j^*(t+\Delta t)+\frac{\lambda}{\beta\ell^2}\ \varphi_i^*\,\ell\,\frac{\partial\varphi_j^*}{\partial X_1}\,\theta_j^*(t+\Delta t)\Big|_0^L=0\ .\end{aligned} \tag{A.20}$$

In both cases all fields are taken at time $t+\Delta t$. The first form prescribes the boundary contribution of $\ell\,\partial\theta^*/\partial X_1$ ("Neumann kind" via h_{1D}^*), whereas the second retains the natural boundary term arising from integration by parts.

A.6.4 Newton–Raphson scheme for θ^*

The discrete equation (A.19) can be written compactly as

$$\mathcal{R}_{\theta^*}\big({\theta^*}_j(t{+}\Delta t),\,\theta_j(t{+}\Delta t)\big)=\mathcal{A}_{\theta^*}\big({\theta^*}_j(t{+}\Delta t),\,\theta_j(t{+}\Delta t)\big)+\mathcal{B}_{\theta^*}=0\,, \tag{A.21}$$

with Einstein summation over j, where the (known) boundary contribution is

$$\mathcal{B}_{\theta^*}=\frac{\lambda}{\beta\ell^2}\ \varphi_i^*\,\ell\,h_{1D}^*\Big|_0^L, \tag{A.22}$$

and $\mathcal{A}_{\theta^*}(\cdot,\cdot)$ is the linear form obtained by comparison with (A.19) and evaluated at time $t+\Delta t$.

The Newton–Raphson linearization follows from the Gateaux derivative:

$$\begin{aligned}\frac{\partial}{\partial\epsilon}\mathcal{R}_{\theta^*}\big({\theta^*}_j+\epsilon\,\delta{\theta^*}_j,\,\theta_j+\epsilon\,\delta\theta_j\big)\Big|_{\epsilon=0} &= \mathcal{A}_{\theta^*}\big(\delta{\theta^*}_j,\,\delta\theta_j\big) \\ &= -\,\mathcal{R}_{\theta^*}\big({\theta^*}_j(t{+}\Delta t),\,\theta_j(t{+}\Delta t)\big).\end{aligned} \tag{A.23}$$

Here $\mathcal{A}_{\theta^*}$ is the Jacobian (bilinear form) of the residual with respect to $({\theta^*}_j,\theta_j)$; $\mathcal{B}_{\theta^*}$ collects the prescribed Neumann-kind boundary term via h^*_{1D}.

A.7 Gateaux derivative for γ of Eq. (6.165)

The Gateaux derivative of Eq. (6.165) is

$$\frac{\partial}{\partial\epsilon}\mathcal{R}_\gamma(\gamma_j+\epsilon\delta\gamma_j,\theta_j+\epsilon\delta\theta_j,\upsilon_j+\epsilon\delta\upsilon_j)\Big|_{\epsilon=0} = -\mathcal{R}_\gamma(\gamma_j,\theta_j,\upsilon_j)\;, \tag{A.24}$$

thus

$$\begin{aligned}&\frac{1}{\ell}\int_0^L \varphi_i^\gamma\varphi_j^\gamma\,\mathrm{d}X_1\;\delta\gamma_j(t) \\ &\quad-4\alpha_4\,\frac{E\,\Omega}{\ell\,\mu_{\mathrm{ref}}}\int_0^L \varphi_i^\gamma\,\aleph(\theta_j,\upsilon_j)^3\,\frac{\partial}{\partial\epsilon}\aleph(\theta_j+\epsilon\delta\theta_j,\upsilon_j+\epsilon\delta\upsilon_j)\Big|_{\epsilon=0}\mathrm{d}X_1 \\ &\quad-2\alpha_2\frac{E\,\Omega}{\ell\,\mu_{\mathrm{ref}}}\int_0^L \varphi_i^\gamma\,\aleph(\theta_j,\upsilon_j)\,\frac{\partial}{\partial\epsilon}\aleph(\theta_j+\epsilon\delta\theta_j,\upsilon_j+\epsilon\delta\upsilon_j)\Big|_{\epsilon=0}\mathrm{d}X_1=0\;,\end{aligned}$$

where $\aleph(\theta_j,\upsilon_j)$ is defined in Eq. (6.167) and the corresponding derivative

$$\begin{aligned}&\frac{\partial}{\partial\epsilon}\aleph(\theta_j+\epsilon\delta\theta_j,\upsilon_j+\epsilon\delta\upsilon_j)\Big|_{\epsilon=0} \\ &\quad=(1+\Omega\,c_{\max}\,\varphi_h^\theta\theta_h)^{-4/3}\left\{-\frac{\Omega\,c_{\max}}{3}\left(1+\ell\,\frac{\partial\varphi_k^u}{\partial X_1}\,\upsilon_k\right)\varphi_j^\theta\delta\theta_j\right. \\ &\quad\left.+(1+\Omega\,c_{\max}\,\varphi_h^\theta\theta_h)\ell\,\frac{\partial\varphi_j^\upsilon}{\partial X_1}\delta\upsilon_j\right\}\;.\end{aligned} \tag{A.25}$$

A.8 Proof of $\boldsymbol{S}^e$ (6.122)

Recall the Eq. (6.107), (6.110), and (6.111) the trace of $\boldsymbol{E}^e$ is derived

$$\operatorname{tr}\boldsymbol{E}^e=\frac{1}{2}(\operatorname{tr}\boldsymbol{C}^e{-}3)=\frac{1}{2}\left(J^{c-2/3}\left[\left(1+\frac{\partial u_1}{\partial X_1}\right)^2+2\left(1+g(X_1)\;\frac{\partial f}{\partial r}\Big|_0\right)^2\right]-3\right). \tag{A.26}$$

Thus, the elastic second Piola-Kirchhoff stress tensor can be expressed as follows:

$$\begin{aligned}\boldsymbol{S}^e &= 2G\boldsymbol{E}^e + \lambda\,\mathrm{tr}(\boldsymbol{E}^e)\mathbb{1} \qquad (A.27)\\ &= G\left(\left[\left(1+\frac{\partial u_1}{\partial X_1}\right)^2 \vec{e}_1\otimes\vec{e}_1 + \left(1+g(X_1)\left.\frac{\partial f}{\partial r}\right|_0\right)^2 \sum_{k=2}^{3}\vec{e}_k\otimes\vec{e}_k\right] J^{c-2/3} - \mathbb{1}\right)\\ &+ \lambda\frac{1}{2}\left(J^{c-2/3}\left[\left(1+\frac{\partial u_1}{\partial X_1}\right)^2 + 2\left(1+g(X_1)\left.\frac{\partial f}{\partial r}\right|_0\right)^2\right] - 3\right)\mathbb{1}.\end{aligned}$$

A.9 Detailed derivations for the chemo-mechanical potential

For completeness, we report here the full derivation of Eq. (6.135). Starting from

$$\mu^{mech} = \Omega\left\{\frac{\lambda}{2}\,\mathrm{tr}\,\boldsymbol{E}^{e2} + G\,\boldsymbol{E}^e\cdot\boldsymbol{E}^e - \tfrac{1}{3}\,\boldsymbol{S}^e\cdot\boldsymbol{C}^e\right\},$$

we need explicit expressions for the elastic strain invariants.

A.9.1 Elastic strain measures

From the kinematics and isotropic swelling decomposition, one obtains:

$$\mathrm{tr}\,\boldsymbol{E}^e = \frac{1-2\nu}{2}\,\aleph(c_R,u_1)^2 + \frac{2(1+\nu)-3}{2}, \qquad (A.28)$$

$$\boldsymbol{E}^e\cdot\boldsymbol{E}^e = \frac{1-2\nu^2}{4}\,\aleph(c_R,u_1)^4 - \frac{1-2\nu}{2}\,\aleph(c_R,u_1)^2 + \frac{2(1+\nu)^2-4(1+\nu)+3}{4}, \qquad (A.29)$$

$$\boldsymbol{S}^e = \frac{E}{2}\Big(\aleph(c_R,u_1)^2 - 1\Big)\,\vec{e}_1\otimes\vec{e}_1, \qquad (A.30)$$

$$\boldsymbol{C}^e = \left[\vec{e}_1\otimes\vec{e}_1 - \nu\sum_{k=2}^{3}\vec{e}_k\otimes\vec{e}_k\right]\aleph(c_R,u_1)^2 + (1+\nu)\sum_{k=2}^{3}\vec{e}_k\otimes\vec{e}_k. \qquad (A.31)$$

A.9.2 Chemo-mechanical potential

Plugging these expressions into μ^{mech} and introducing the dimensionless chemical potential $\gamma = \mu^{mech}/\mu_{\mathrm{ref}}$, one arrives at:

$$\gamma(X_1,t) = E\,\frac{\Omega}{\mu_{\mathrm{ref}}}\left\{\alpha_4\,\aleph^4 + \alpha_2\,\aleph^2 + \tfrac{1}{8}\right\},$$

with coefficients

$$\alpha_4 = -\frac{12\nu^2+\nu+1}{24(\nu+1)}, \qquad \alpha_2 = \frac{6\nu^2+5\nu-1}{12(\nu+1)}.$$

This coincides with Eq. (6.135) in the main text.

A.10 Detailed derivations for the manufactured solution

For the manufactured fields defined in Eq. (6.172), the total dimensionless chemical potential is

$$\begin{aligned}\frac{\mu^{CH}+\mu^{mech}}{\mu_{\text{ref}}} &= \frac{RT}{\mu_{\text{ref}}}\,\chi\,(1-2\,\theta) - \frac{\lambda}{\mu_{\text{ref}}}\nabla^2\theta \\ &\quad + E\,\frac{\Omega}{\mu_{\text{ref}}}\left\{\alpha_4\,\aleph(\theta,\overline{v})^4 + \alpha_2\,\aleph(\theta,\overline{v})^2 + \frac{1}{8}\right\}.\end{aligned} \tag{A.32}$$

A.10.1 Fluxes

By definition (6.6), the mass flux is

$$h_{1D} = -\mathbb{D}\,c_{\max}\,\frac{\partial\theta}{\partial X_1} - M(c)\,\mu_{\text{ref}}\,\frac{\partial}{\partial X_1}\left(\frac{\mu^{CH}+\mu^{mech}}{\mu_{\text{ref}}}\right). \tag{A.33}$$

Expanding this expression leads to

$$\begin{aligned}h_{1D} &= \frac{t}{\bar{t}}\,\frac{\beta}{L}\,\mathbb{D}\,c_{\max}\,[-1+2\,\theta\,(1-\theta)\,\chi] \\ &\quad - M(c)\,\frac{E\,\Omega}{\ell}\;\left[4\,\alpha_4\,\aleph(\theta,\overline{v})^2 + 2\,\alpha_2\right]\aleph(\theta,\overline{v})\;\ell\,\frac{\partial\aleph(\theta,\overline{v})}{\partial X_1}.\end{aligned} \tag{A.34}$$

The auxiliary flux associated with μ^{CH} is

$$h^{\mu}_{1D} = -M(c)\,\frac{\partial\mu^{CH}}{\partial X_1} = 2\,\frac{t}{\bar{t}}\,\frac{\beta}{L}\,\mathbb{D}\,c_{\max}\,\theta\,(1-\theta)\,\chi. \tag{A.35}$$

A.10.2 Mass supply

The mass supply is obtained from the balance law

$$b = \frac{\partial c}{\partial t} + \frac{\partial h_{1D}}{\partial x}. \tag{A.36}$$

Substituting the manufactured solutions and fluxes, one finds after algebraic manipulation

$$\frac{\Delta t\; b(X_1,t)}{c_{\max}} = \frac{\Delta t}{\bar{t}}\left(\alpha+\beta\frac{X_1}{L}\right) + 2\chi\;\tilde{\mathfrak{D}}\left(\beta\,\frac{t}{\bar{t}}\,\frac{\ell}{L}\right)^2\left[1-2\,\frac{t}{\bar{t}}\left(\alpha+\beta\frac{X_1}{L}\right)\right] \tag{A.37}$$

$$\begin{aligned}
&- \frac{E\,\Omega}{RT}\,\tilde{\mathfrak{D}}\left\{ (1-2\,\theta)\,\frac{t}{\bar{t}}\,\frac{\ell}{L}\,\beta\left[4\,\alpha_4\,\aleph(\theta,\overline{v})^3+2\,\alpha_2\,\aleph(\theta,\overline{v})\right]\ell\,\frac{\partial\aleph(\theta,\overline{v})}{\partial X_1}\right.\\
&\quad + \theta\,(1-\theta)\,\left[12\,\alpha_4\,\aleph(\theta,\overline{v})^2+2\,\alpha_2\right]\left(\ell\,\frac{\partial\aleph(\theta,\overline{v})}{\partial X_1}\right)^2\\
&\left.\quad + \theta\,(1-\theta)\,\left[4\,\alpha_4\,\aleph(\theta,\overline{v})^3+2\,\alpha_2\,\aleph(\theta,\overline{v})\right]\ell^2\,\frac{\partial^2\aleph(\theta,\overline{v})}{\partial X_1^2}\right\}.
\end{aligned}$$

A.11 Variation of reaction rates

A.11.1 Variation of $w_{\mathrm{R}}^{(6.180)}$

The total variation of $w_{\mathrm{R}}^{(6.180)}$ can be decomposed as the sum of contributions associated with each phase variable:

$$\delta w_{\mathrm{R}}^{(6.180)} = \delta w\big|_{\delta\phi_R^{\mathrm{Na}}} + \delta w\big|_{\delta\phi_R^{\mathrm{Sn}}} + \delta w\big|_{\delta\phi_R^{\mathrm{NaSn_3}}} + \delta w\big|_{\delta\phi_R^{\mathrm{Na_9Sn_4}}} + \delta w\big|_{\delta\phi_R^{\mathrm{Na_{15}Sn_4}}}.$$

The first contribution, associated with the variation of sodium, is

$$\begin{aligned}
\delta w\big|_{\delta\phi_R^{\mathrm{Na}}} = k_{f_R}^{(2)}\Bigg[&\left(\frac{\omega^{\mathrm{Na}}A_1+\phi_R^{\mathrm{Na}}\omega^{\mathrm{Na}}\omega^{\mathrm{V}}}{A_1^2}\right)\left(\frac{\phi^{\mathrm{Sn}}\omega^{\mathrm{Sn}}}{A_2}\right)^3\\
&+\frac{\phi_R^{\mathrm{Na}}\omega^{\mathrm{Na}}}{A_1}\,3\left(\frac{\phi^{\mathrm{Sn}}\omega^{\mathrm{Sn}}}{A_2}\right)^2\left(-\frac{\phi^{\mathrm{Sn}}\omega^{\mathrm{Sn}}}{A_2^2}\right)(\omega^{\mathrm{Na}}-\omega^{\mathrm{V}})\Bigg]\delta\phi_R^{\mathrm{Na}}\\
&+\;k_{b_R}^{(2)}\,\frac{\phi_R^{\mathrm{NaSn_3}}\omega^{\mathrm{NaSn_3}}}{A_3^2}\,(\omega^{\mathrm{Na}}-\omega^{\mathrm{V}})\,\delta\phi_R^{\mathrm{Na}}.
\end{aligned} \tag{A.38}$$

The second contribution, associated with the variation of Tin

$$\begin{aligned}
\delta w\big|_{\delta\phi_R^{\mathrm{Sn}}} = k_{f_R}^{(2)}\Bigg[&\frac{\phi_R^{\mathrm{Na}}\,\omega^{\mathrm{Na}}}{A_1}\,3\left(\frac{\phi^{\mathrm{Sn}}\,\omega^{\mathrm{Sn}}}{A_2}\right)^2\left(\frac{\omega^{\mathrm{Sn}}}{A_2}+\frac{\phi^{\mathrm{Sn}}\,\omega^{\mathrm{Sn}}\,\omega^{\mathrm{V}}}{A_2^2}\right)\\
&-\frac{\phi_R^{\mathrm{Na}}\,\omega^{\mathrm{Na}}}{A_1^2}\,(\omega^{\mathrm{Sn}}-\omega^{\mathrm{V}})\left(\frac{\phi^{\mathrm{Sn}}\,\omega^{\mathrm{Sn}}}{A_2}\right)^3\Bigg]\delta\phi_R^{\mathrm{Sn}}\\
&+\;k_{b_R}^{(2)}\,\frac{\phi_R^{\mathrm{NaSn_3}}\,\omega^{\mathrm{NaSn_3}}}{A_3^2}\,(\omega^{\mathrm{Sn}}-\omega^{\mathrm{V}})\,\delta\phi_R^{\mathrm{Sn}}.
\end{aligned} \tag{A.39}$$

For $NaSn_3$, the variation reads

$$\delta w\big|_{\delta\phi_R^{\mathrm{NaSn_3}}} = k_{f_R}^{(2)}\Bigg[\left(-\frac{\phi_R^{\mathrm{Na}}\omega^{\mathrm{Na}}}{A_1^2}\right)(\omega^{\mathrm{NaSn_3}}-\omega^{\mathrm{V}})\left(\frac{\phi^{\mathrm{Sn}}\omega^{\mathrm{Sn}}}{A_2}\right)^3 + \frac{\phi_R^{\mathrm{Na}}\omega^{\mathrm{Na}}}{A_1}\,3\left(\frac{\phi^{\mathrm{Sn}}\omega^{\mathrm{Sn}}}{A_2}\right)^2\left(-\frac{\phi^{\mathrm{Sn}}\omega^{\mathrm{Sn}}}{A_2^2}\right)(\omega^{\mathrm{NaSn_3}}-\omega^{\mathrm{V}})\Bigg]\delta\phi_R^{\mathrm{NaSn_3}} - k_{b_R}^{(2)}\left[\frac{\omega^{\mathrm{NaSn_3}}}{A_3} - \frac{\phi_R^{\mathrm{NaSn_3}}\omega^{\mathrm{NaSn_3}}}{A_3^2}(\omega^{\mathrm{NaSn_3}}-\omega^{\mathrm{V}})\right]\delta\phi_R^{\mathrm{NaSn_3}}\,. \tag{A.40}$$

The contribution from

$$\delta w\big|_{\delta\phi_R^{\mathrm{Na_9Sn_4}}} = k_{f_R}^{(2)}\Bigg[\left(-\frac{\phi_R^{\mathrm{Na}}\omega^{\mathrm{Na}}}{A_1^2}\right)(\omega^{\mathrm{Na_9Sn_4}}-\omega^{\mathrm{V}})\left(\frac{\phi^{\mathrm{Sn}}\omega^{\mathrm{Sn}}}{A_2}\right)^3 + \frac{\phi_R^{\mathrm{Na}}\omega^{\mathrm{Na}}}{A_1}\,3\left(\frac{\phi^{\mathrm{Sn}}\omega^{\mathrm{Sn}}}{A_2}\right)^2\left(-\frac{\phi^{\mathrm{Sn}}\omega^{\mathrm{Sn}}}{A_2^2}\right)(\omega^{\mathrm{Na_9Sn_4}}-\omega^{\mathrm{V}})\Bigg]\delta\phi_R^{\mathrm{Na_9Sn_4}} + k_{b_R}^{(2)}\,\frac{\phi_R^{\mathrm{NaSn_3}}\omega^{\mathrm{NaSn_3}}}{A_3^2}\,(\omega^{\mathrm{Na_9Sn_4}}-\omega^{\mathrm{V}})\,\delta\phi_R^{\mathrm{Na_9Sn_4}}\,. \tag{A.41}$$

Finally, for $Na_{15}Sn_4$ one obtains

$$\delta w\big|_{\delta\phi_R^{\mathrm{Na_{15}Sn_4}}} = k_{f_R}^{(2)}\Bigg[\left(-\frac{\phi_R^{\mathrm{Na}}\omega^{\mathrm{Na}}}{A_1^2}\right)(\omega^{\mathrm{Na_{15}Sn_4}}-\omega^{\mathrm{V}})\left(\frac{\phi^{\mathrm{Sn}}\omega^{\mathrm{Sn}}}{A_2}\right)^3 + \frac{\phi_R^{\mathrm{Na}}\omega^{\mathrm{Na}}}{A_1}\,3\left(\frac{\phi^{\mathrm{Sn}}\omega^{\mathrm{Sn}}}{A_2}\right)^2\left(-\frac{\phi^{\mathrm{Sn}}\omega^{\mathrm{Sn}}}{A_2^2}\right)(\omega^{\mathrm{Na_{15}Sn_4}}-\omega^{\mathrm{V}})\Bigg]\delta\phi_R^{\mathrm{Na_{15}Sn_4}} + k_{b_R}^{(2)}\,\frac{\phi_R^{\mathrm{NaSn_3}}\omega^{\mathrm{NaSn_3}}}{A_3^2}\,(\omega^{\mathrm{Na_{15}Sn_4}}-\omega^{\mathrm{V}})\,\delta\phi_R^{\mathrm{Na_{15}Sn_4}}\,. \tag{A.42}$$

Here, the auxiliary quantities A_1, A_2, A_3 are the same as those introduced in Eq. (6.192). They compactly encode the dependence of the reaction rate on the combined contributions of all phases and their swelling factors.

A.11.2 Variation of $w_{\mathrm{R}}^{(6.181)}$

To linearize the reaction rate with respect to the phase volume fractions, we decompose the firstew variation of $w_{\mathrm{R}}^{(6.181)}$ against the independent perturbations $\delta\phi_R^{\alpha}$, with $\alpha \in \{\mathrm{Na}, \mathrm{Sn}, \mathrm{NaSn_3}, \mathrm{Na_9Sn_4}, \mathrm{Na_{15}Sn_4}\}$:

$$\delta w_{\mathrm{R}}^{(6.181)} = \delta w\big|_{\delta\phi_R^{\mathrm{Na}}} + \delta w\big|_{\delta\phi_R^{\mathrm{Sn}}} + \delta w\big|_{\delta\phi_R^{\mathrm{NaSn_3}}} + \delta w\big|_{\delta\phi_R^{\mathrm{Na_9Sn_4}}} + \delta w\big|_{\delta\phi_R^{\mathrm{Na_{15}Sn_4}}}.$$

Each contribution below comes from applying the product, power, and quotient rules to the compact form of $w_{\mathrm{R}}^{(6.181)}$ in terms of $B_1, \ldots, B_4$. Recall that $B_i = B_i(\phi_R^{\mathrm{Na}}, \phi_R^{\mathrm{Sn}}, \phi_R^{\mathrm{NaSn_3}}, \phi_R^{\mathrm{Na_9Sn_4}}, \phi_R^{\mathrm{Na_{15}Sn_4}})$ so their variations also enter via the chain rule.

Variation with respect to

$$
\begin{aligned}
\delta w\big|_{\delta\phi_R^{\mathrm{Na}}} = k_{f_R}^{(3)} \Bigg[& 6 \left(\frac{\phi_R^{\mathrm{Na}} \omega^{\mathrm{Na}}}{B_1} \right)^5 \left(\frac{\omega^{\mathrm{Na}}}{B_1} + \frac{\phi_R^{\mathrm{Na}} \omega^{\mathrm{Na}} \omega^{\mathrm{V}}}{B_1^2} \right) \frac{\phi_R^{\mathrm{NaSn_3}} \omega^{\mathrm{NaSn_3}}}{B_3} \frac{\phi^{\mathrm{Sn}} \omega^{\mathrm{Sn}}}{B_2} \\
& - \left(\frac{\phi_R^{\mathrm{Na}} \omega^{\mathrm{Na}}}{B_1} \right)^6 \left(\frac{\phi_R^{\mathrm{NaSn_3}} \omega^{\mathrm{NaSn_3}}}{B_3^2} \right) (\omega^{\mathrm{Na}} - \omega^{\mathrm{V}}) \frac{\phi^{\mathrm{Sn}} \omega^{\mathrm{Sn}}}{B_2} \\
& - \left(\frac{\phi_R^{\mathrm{Na}} \omega^{\mathrm{Na}}}{B_1} \right)^6 \frac{\phi_R^{\mathrm{NaSn_3}} \omega^{\mathrm{NaSn_3}}}{B_3} \frac{\phi^{\mathrm{Sn}} \omega^{\mathrm{Sn}}}{B_2^2} (\omega^{\mathrm{Na}} - \omega^{\mathrm{V}}) \Bigg] \delta\phi_R^{\mathrm{Na}} \\
& + k_{b_R}^{(3)} \left(\frac{\phi_R^{\mathrm{Na_9Sn_4}} \omega^{\mathrm{Na_9Sn_4}}}{B_4^2} \right) (\omega^{\mathrm{Na}} - \omega^{\mathrm{V}}) \, \delta\phi_R^{\mathrm{Na}}.
\end{aligned}
\tag{A.43}
$$

Variation with respect to $\delta\phi_R^{\mathrm{Sn}}$

$$
\begin{aligned}
\delta w\Big|_{\delta\phi_R^{\mathrm{Sn}}} = k_{f_R}^{(3)} \Bigg[& 6 \left(\frac{\phi_R^{\mathrm{Na}} \, \omega^{\mathrm{Na}}}{B_1} \right)^5 \left(- \frac{\phi_R^{\mathrm{Na}} \, \omega^{\mathrm{Na}}}{B_1^2} \right) (\omega^{\mathrm{Sn}} - \omega^{\mathrm{V}}) \, \frac{\phi_R^{\mathrm{NaSn_3}} \, \omega^{\mathrm{NaSn_3}}}{B_3} \, \frac{\phi^{\mathrm{Sn}} \, \omega^{\mathrm{Sn}}}{B_2} \\
& + \left(\frac{\phi_R^{\mathrm{Na}} \, \omega^{\mathrm{Na}}}{B_1} \right)^6 \left(- \frac{\phi_R^{\mathrm{NaSn_3}} \, \omega^{\mathrm{NaSn_3}}}{B_3^2} \right) (\omega^{\mathrm{Sn}} - \omega^{\mathrm{V}}) \, \frac{\phi^{\mathrm{Sn}} \, \omega^{\mathrm{Sn}}}{B_2} \\
& + \left(\frac{\phi_R^{\mathrm{Na}} \, \omega^{\mathrm{Na}}}{B_1} \right)^6 \frac{\phi_R^{\mathrm{NaSn_3}} \, \omega^{\mathrm{NaSn_3}}}{B_3} \, 3 \left(\frac{\phi^{\mathrm{Sn}} \, \omega^{\mathrm{Sn}}}{B_2} \right)^2 \left(\frac{\omega^{\mathrm{Sn}}}{B_2} + \frac{\phi^{\mathrm{Sn}} \, \omega^{\mathrm{Sn}} \, \omega^{\mathrm{V}}}{B_2^2} \right) \Bigg] \delta\phi_R^{\mathrm{Sn}} \\
& + k_{b_R}^{(3)} \, \frac{\phi_R^{\mathrm{Na9Sn_4}} \, \omega^{\mathrm{Na9Sn_4}}}{B_4^2} \, (\omega^{\mathrm{Sn}} - \omega^{\mathrm{V}}) \, \delta\phi_R^{\mathrm{Sn}}.
\end{aligned}
\tag{A.44}
$$

Variation with respect to

$$\delta w\big|_{\delta\phi_R^{\mathrm{NaSn_3}}} = \tag{A.45}$$
$$k_{f_R}^{(3)}\Bigg[6\left(\frac{\phi_R^{\mathrm{Na}}\,\omega^{\mathrm{Na}}}{B_1}\right)^5\left(-\frac{\phi_R^{\mathrm{Na}}\omega^{\mathrm{Na}}}{B_1^2}\right)(\omega^{\mathrm{NaSn_3}}-\omega^{\mathrm{V}})\,\frac{\phi_R^{\mathrm{NaSn_3}}\,\omega^{\mathrm{NaSn_3}}}{B_3}\,\frac{\phi^{\mathrm{Sn}}\omega^{\mathrm{Sn}}}{B_2}$$
$$+\left(\frac{\phi_R^{\mathrm{Na}}\,\omega^{\mathrm{Na}}}{B_1}\right)^6\left(\frac{\omega^{\mathrm{NaSn_3}}}{B_3}+\frac{\phi_R^{\mathrm{NaSn_3}}\omega^{\mathrm{NaSn_3}}\,\omega^{\mathrm{V}}}{B_3^2}\right)\frac{\phi^{\mathrm{Sn}}\omega^{\mathrm{Sn}}}{B_2}$$
$$-\left(\frac{\phi_R^{\mathrm{Na}}\,\omega^{\mathrm{Na}}}{B_1}\right)^6\frac{\phi_R^{\mathrm{NaSn_3}}\,\omega^{\mathrm{NaSn_3}}}{B_3}\,\frac{\phi^{\mathrm{Sn}}\omega^{\mathrm{Sn}}}{B_2^2}\,(\omega^{\mathrm{NaSn_3}}-\omega^{\mathrm{V}})\Bigg]\delta\phi_R^{\mathrm{NaSn_3}}$$
$$+\;k_{b_R}^{(3)}\left(\frac{\phi_R^{\mathrm{Na_9Sn_4}}\omega^{\mathrm{Na_9Sn_4}}}{B_4^2}\right)(\omega^{\mathrm{NaSn_3}}-\omega^{\mathrm{V}})\,\delta\phi_R^{\mathrm{NaSn_3}}.$$

Variation with respect to

$$\delta w\big|_{\delta\phi_R^{\mathrm{Na_9Sn_4}}} = \tag{A.46}$$
$$k_{f_R}^{(3)}\Bigg[6\left(\frac{\phi_R^{\mathrm{Na}}\omega^{\mathrm{Na}}}{B_1}\right)^5\left(-\frac{\phi_R^{\mathrm{Na}}\omega^{\mathrm{Na}}}{B_1^2}\right)(\omega^{\mathrm{Na_9Sn_4}}-\omega^{\mathrm{V}})\,\frac{\phi_R^{\mathrm{NaSn_3}}\omega^{\mathrm{NaSn_3}}}{B_3}\,\frac{\phi^{\mathrm{Sn}}\omega^{\mathrm{Sn}}}{B_2}$$
$$-\left(\frac{\phi_R^{\mathrm{Na}}\omega^{\mathrm{Na}}}{B_1}\right)^6\left(\frac{\phi_R^{\mathrm{NaSn_3}}\omega^{\mathrm{NaSn_3}}}{B_3^2}\right)(\omega^{\mathrm{Na_9Sn_4}}-\omega^{\mathrm{V}})\,\frac{\phi^{\mathrm{Sn}}\omega^{\mathrm{Sn}}}{B_2}$$
$$-\left(\frac{\phi_R^{\mathrm{Na}}\omega^{\mathrm{Na}}}{B_1}\right)^6\frac{\phi_R^{\mathrm{NaSn_3}}\omega^{\mathrm{NaSn_3}}}{B_3}\,\frac{\phi^{\mathrm{Sn}}\omega^{\mathrm{Sn}}}{B_2^2}\,(\omega^{\mathrm{Na_9Sn_4}}-\omega^{\mathrm{V}})\Bigg]\delta\phi_R^{\mathrm{Na_9Sn_4}}$$
$$-\;k_{b_R}^{(3)}\left[\frac{\omega^{\mathrm{Na_9Sn_4}}}{B_4}+\frac{\phi_R^{\mathrm{Na_9Sn_4}}\omega^{\mathrm{Na_9Sn_4}}\omega^{\mathrm{V}}}{B_4^2}\right]\delta\phi_R^{\mathrm{Na_9Sn_4}}.$$

Variation with respect to

$$\delta w\big|_{\delta\phi_R^{\mathrm{Na_{15}Sn_4}}} = \tag{A.47}$$
$$k_{f_R}^{(3)}\Bigg[-\,6\left(\frac{\phi_R^{\mathrm{Na}}\omega^{\mathrm{Na}}}{B_1}\right)^5\left(\frac{\phi_R^{\mathrm{Na}}\omega^{\mathrm{Na}}}{B_1^2}\right)(\omega^{\mathrm{Na_{15}Sn_4}}-\omega^{\mathrm{V}})\,\frac{\phi_R^{\mathrm{NaSn_3}}\omega^{\mathrm{NaSn_3}}}{B_3}\,\frac{\phi^{\mathrm{Sn}}\omega^{\mathrm{S}}}{B_2}$$
$$-\left(\frac{\phi_R^{\mathrm{Na}}\omega^{\mathrm{Na}}}{B_1}\right)^6\left(\frac{\phi_R^{\mathrm{NaSn_3}}\omega^{\mathrm{NaSn_3}}}{B_3^2}\right)(\omega^{\mathrm{Na_{15}Sn_4}}-\omega^{\mathrm{V}})\,\frac{\phi^{\mathrm{Sn}}\omega^{\mathrm{Sn}}}{B_2}$$
$$-\left(\frac{\phi_R^{\mathrm{Na}}\omega^{\mathrm{Na}}}{B_1}\right)^6\frac{\phi_R^{\mathrm{NaSn_3}}\omega^{\mathrm{NaSn_3}}}{B_3}\,\frac{\phi^{\mathrm{Sn}}\omega^{\mathrm{Sn}}}{B_2^2}\,(\omega^{\mathrm{Na_{15}Sn_4}}-\omega^{\mathrm{V}})\Bigg]\delta\phi_R^{\mathrm{Na_{15}Sn_4}}$$
$$-\;k_{b_R}^{(3)}\left(\frac{\phi_R^{\mathrm{Na_9Sn_4}}\omega^{\mathrm{Na_9Sn_4}}}{B_4^2}\right)(\omega^{\mathrm{Na_{15}Sn_4}}-\omega^{\mathrm{V}})\,\delta\phi_R^{\mathrm{Na_{15}Sn_4}}.$$

These expressions are directly suitable for Jacobian assembly in a Newton–Raphson scheme. They make explicit how the variation of each phase fraction affects the forward and backward contributions through the implicit dependence of $B_1, \ldots, B_4$ on the ϕ_R^α's and their distinct swelling factors ω^α.

A.11.3 Variation of $w_{\mathrm{R}}^{(6.182)}$

The final stage of the Na–Sn sodiation pathway, namely the transformation from Na_9Sn_4 to $Na_{15}Sn_4$, requires the linearization of the reaction rate with respect to the volume fractions of all coexisting phases. The Gateaux derivative of $w_{\mathrm{R}}^{(6.182)}$ with respect to the referential phase fractions is expressed as

$$\delta w_{\mathrm{R}}^{(6.182)} = \delta w\big|_{\delta\phi_R^{\mathrm{Na}}} + \delta w\big|_{\delta\phi_R^{\mathrm{Sn}}} + \delta w\big|_{\delta\phi_R^{\mathrm{NaSn_3}}} + \delta w\big|_{\delta\phi_R^{\mathrm{Na_9Sn_4}}} + \delta w\big|_{\delta\phi_R^{\mathrm{Na_{15}Sn_4}}}.$$

Each term corresponds to the variation with respect to a specific phase. We report them explicitly below for completeness.

The sodium fraction affects both the forward and the backward terms:

$$\begin{aligned}
\delta w\big|_{\delta\phi_R^{\mathrm{Na}}} = k_{f_R}^{(4)} \Bigg[& 6 \left(\frac{\phi_R^{\mathrm{Na}} \omega^{\mathrm{Na}}}{C_1} \right)^5 \left(\frac{\omega^{\mathrm{Na}}}{C_1} + \frac{\phi_R^{\mathrm{Na}} \omega^{\mathrm{Na}} \omega^{\mathrm{V}}}{C_1^2} \right) \frac{\phi_R^{\mathrm{Na_9Sn_4}} \omega^{\mathrm{Na_9Sn_4}}}{C_2} \frac{\phi_R^{\mathrm{Na_{15}Sn_4}} \omega^{\mathrm{Na_{15}Sn_4}}}{C_3} \\
& - \left(\frac{\phi_R^{\mathrm{Na}} \omega^{\mathrm{Na}}}{C_1} \right)^6 \left(\frac{\phi_R^{\mathrm{Na_9Sn_4}} \omega^{\mathrm{Na_9Sn_4}}}{C_2^2} \right) (\omega^{\mathrm{Na}} - \omega^{\mathrm{V}}) \frac{\phi_R^{\mathrm{Na_{15}Sn_4}} \omega^{\mathrm{Na_{15}Sn_4}}}{C_3} \\
& - \left(\frac{\phi_R^{\mathrm{Na}} \omega^{\mathrm{Na}}}{C_1} \right)^6 \frac{\phi_R^{\mathrm{Na_9Sn_4}} \omega^{\mathrm{Na_9Sn_4}}}{C_2} \left(\frac{\phi_R^{\mathrm{Na_{15}Sn_4}} \omega^{\mathrm{Na_{15}Sn_4}}}{C_3^2} \right) (\omega^{\mathrm{Na}} - \omega^{\mathrm{V}}) \Bigg] \delta\phi_R^{\mathrm{Na}} \\
& + k_{b_R}^{(4)} \left(\frac{\phi_R^{\mathrm{Na_{15}Sn_4}} \omega^{\mathrm{Na_{15}Sn_4}}}{C_3^2} \right) (\omega^{\mathrm{Na}} - \omega^{\mathrm{V}}) \, \delta\phi_R^{\mathrm{Na}} .
\end{aligned} \tag{A.48}$$

The tin fraction affects the forward and the backward terms:

$$\begin{aligned}
\delta w\Big|_{\delta\phi_R^{\mathrm{Sn}}} = k_{f_R}^{(4)} \Bigg[& - 6 \left(\frac{\phi_R^{\mathrm{Na}} \, \omega^{\mathrm{Na}}}{C_1} \right)^6 \frac{(\omega^{\mathrm{Sn}} - \omega^{\mathrm{V}})}{C_1} \frac{\phi_R^{\mathrm{Na9Sn_4}} \, \omega^{\mathrm{Na9Sn_4}}}{C_2} \frac{\phi_R^{\mathrm{Na15Sn_4}} \, \omega^{\mathrm{Na15Sn_4}}}{C_3} \\
& - \left(\frac{\phi_R^{\mathrm{Na}} \, \omega^{\mathrm{Na}}}{C_1} \right)^6 \frac{\phi_R^{\mathrm{Na9Sn_4}} \, \omega^{\mathrm{Na9Sn_4}}}{C_2^2} (\omega^{\mathrm{Sn}} - \omega^{\mathrm{V}}) \frac{\phi_R^{\mathrm{Na15Sn_4}} \, \omega^{\mathrm{Na15Sn_4}}}{C_3} \\
& - \left(\frac{\phi_R^{\mathrm{Na}} \, \omega^{\mathrm{Na}}}{C_1} \right)^6 \frac{\phi_R^{\mathrm{Na9Sn_4}} \, \omega^{\mathrm{Na9Sn_4}}}{C_2} \frac{\phi_R^{\mathrm{Na15Sn_4}} \, \omega^{\mathrm{Na15Sn_4}}}{C_3^2} (\omega^{\mathrm{Sn}} - \omega^{\mathrm{V}}) \Bigg] \delta\phi_R^{\mathrm{Sn}} \\
& + k_{b_R}^{(4)} \frac{\phi_R^{\mathrm{Na15Sn_4}} \, \omega^{\mathrm{Na15Sn_4}}}{C_3^2} (\omega^{\mathrm{Sn}} - \omega^{\mathrm{V}}) \, \delta\phi_R^{\mathrm{Sn}}.
\end{aligned} \tag{A.49}$$

Even though $NaSn_3$ does not explicitly appear in the main reaction, its fraction enters through C_1, C_2, C_3:

$$\delta w\big|_{\delta\phi_R^{\mathrm{NaSn_3}}} = k_{f_R}^{(4)}\Bigg[-\,6\left(\frac{\phi_R^{\mathrm{Na}}\omega^{\mathrm{Na}}}{C_1}\right)^5\left(\frac{\phi_R^{\mathrm{Na}}\omega^{\mathrm{Na}}}{C_1^2}\right)(\omega^{\mathrm{NaSn_3}}-\omega^{\mathrm{V}})\,\frac{\phi_R^{\mathrm{Na_9Sn_4}}\omega^{\mathrm{Na_9Sn_4}}}{C_2} \tag{A.50}$$

$$\frac{\phi_R^{\mathrm{Na_{15}Sn_4}}\omega^{\mathrm{Na_{15}Sn_4}}}{C_3}$$

$$-\left(\frac{\phi_R^{\mathrm{Na}}\omega^{\mathrm{Na}}}{C_1}\right)^6\left(\frac{\phi_R^{\mathrm{Na_9Sn_4}}\omega^{\mathrm{Na_9Sn_4}}}{C_2^2}\right)(\omega^{\mathrm{NaSn_3}}-\omega^{\mathrm{V}})$$

$$\frac{\phi_R^{\mathrm{Na_{15}Sn_4}}\omega^{\mathrm{Na_{15}Sn_4}}}{C_3}$$

$$-\left(\frac{\phi_R^{\mathrm{Na}}\omega^{\mathrm{Na}}}{C_1}\right)^6\frac{\phi_R^{\mathrm{Na_9Sn_4}}\omega^{\mathrm{Na_9Sn_4}}}{C_2}\left(\frac{\phi_R^{\mathrm{Na_{15}Sn_4}}\omega^{\mathrm{Na_{15}Sn_4}}}{C_3^2}\right)(\omega^{\mathrm{NaSn_3}}-\omega^{\mathrm{V}})\Bigg]$$

$$\delta\phi_R^{\mathrm{NaSn_3}}$$

$$+\;k_{b_R}^{(4)}\left(\frac{\phi_R^{\mathrm{Na_{15}Sn_4}}\omega^{\mathrm{Na_{15}Sn_4}}}{C_3^2}\right)(\omega^{\mathrm{NaSn_3}}-\omega^{\mathrm{V}})\,\delta\phi_R^{\mathrm{NaSn_3}}\;.$$

As a direct reactant, Na_9Sn_4 contributes strongly both in numerator and denominator terms:

$$\delta w\big|_{\delta\phi_R^{\mathrm{Na_9Sn_4}}} = k_{f_R}^{(4)}\Bigg[-\,6\left(\frac{\phi_R^{\mathrm{Na}}\omega^{\mathrm{Na}}}{C_1}\right)^5\left(\frac{\phi_R^{\mathrm{Na}}\omega^{\mathrm{Na}}}{C_1^2}\right)(\omega^{\mathrm{Na_9Sn_4}}-\omega^{\mathrm{V}})\,\frac{\phi_R^{\mathrm{Na_9Sn_4}}\omega^{\mathrm{Na_9Sn_4}}}{C_2} \tag{A.51}$$

$$\frac{\phi_R^{\mathrm{Na_{15}Sn_4}}\omega^{\mathrm{Na_{15}Sn_4}}}{C_3}$$

$$+\left(\frac{\phi_R^{\mathrm{Na}}\omega^{\mathrm{Na}}}{C_1}\right)^6\left(\frac{\omega^{\mathrm{Na_9Sn_4}}}{C_2}-\frac{\phi_R^{\mathrm{Na_9Sn_4}}\omega^{\mathrm{Na_9Sn_4}}}{C_2^2}(\omega^{\mathrm{Na_9Sn_4}}-\omega^{\mathrm{V}})\right)$$

$$\frac{\phi_R^{\mathrm{Na_{15}Sn_4}}\omega^{\mathrm{Na_{15}Sn_4}}}{C_3}$$

$$-\left(\frac{\phi_R^{\mathrm{Na}}\omega^{\mathrm{Na}}}{C_1}\right)^6\frac{\phi_R^{\mathrm{Na_9Sn_4}}\omega^{\mathrm{Na_9Sn_4}}}{C_2}\left(\frac{\phi_R^{\mathrm{Na_{15}Sn_4}}\omega^{\mathrm{Na_{15}Sn_4}}}{C_3^2}\right)(\omega^{\mathrm{Na_9Sn_4}}-\omega^{\mathrm{V}})\Bigg]$$

$$\delta\phi_R^{\mathrm{Na_9Sn_4}}$$

$$+\;k_{b_R}^{(4)}\left(\frac{\phi_R^{\mathrm{Na_{15}Sn_4}}\omega^{\mathrm{Na_{15}Sn_4}}}{C_3^2}\right)(\omega^{\mathrm{Na_9Sn_4}}-\omega^{\mathrm{V}})\,\delta\phi_R^{\mathrm{Na_9Sn_4}}\;.$$

Finally, as the reaction product, $Na_{15}Sn_4$ enters predominantly in the backward term:

$$\delta w\big|_{\delta\phi_R^{\mathrm{Na_{15}Sn_4}}} = k_{f_R}^{(4)}\Bigg[-6\left(\frac{\phi_R^{\mathrm{Na}}\omega^{\mathrm{Na}}}{C_1}\right)^5\left(\frac{\phi_R^{\mathrm{Na}}\omega^{\mathrm{Na}}}{C_1^2}\right)(\omega^{\mathrm{Na_{15}Sn_4}}-\omega^{\mathrm{V}})\,\frac{\phi_R^{\mathrm{Na_9Sn_4}}\omega^{\mathrm{Na_9Sn_4}}}{C_2} \tag{A.52}$$

$$\frac{\phi_R^{\mathrm{Na_{15}Sn_4}}\omega^{\mathrm{Na_{15}Sn_4}}}{C_3}$$

$$-\left(\frac{\phi_R^{\mathrm{Na}}\omega^{\mathrm{Na}}}{C_1}\right)^6\left(\frac{\phi_R^{\mathrm{Na_9Sn_4}}\omega^{\mathrm{Na_9Sn_4}}}{C_2^2}\right)(\omega^{\mathrm{Na_{15}Sn_4}}-\omega^{\mathrm{V}})\,\frac{\phi_R^{\mathrm{Na_{15}Sn_4}}\omega^{\mathrm{Na_{15}Sn_4}}}{C_3}$$

$$+\left(\frac{\phi_R^{\mathrm{Na}}\omega^{\mathrm{Na}}}{C_1}\right)^6\frac{\phi_R^{\mathrm{Na_9Sn_4}}\omega^{\mathrm{Na_9Sn_4}}}{C_2}$$

$$\left[\frac{\omega^{\mathrm{Na_{15}Sn_4}}}{C_3}-\frac{\phi_R^{\mathrm{Na_{15}Sn_4}}\omega^{\mathrm{Na_{15}Sn_4}}}{C_3^2}(\omega^{\mathrm{Na_{15}Sn_4}}-\omega^{\mathrm{V}})\right]\Bigg]\delta\phi_R^{\mathrm{Na_{15}Sn_4}}$$

$$-\,k_{b_R}^{(4)}\left(\frac{\omega^{\mathrm{Na_{15}Sn_4}}}{C_3}+\frac{\phi_R^{\mathrm{Na_{15}Sn_4}}\omega^{\mathrm{Na_{15}Sn_4}}}{C_3^2}(\omega^{\mathrm{Na_{15}Sn_4}}-\omega^{\mathrm{V}})\right)\delta\phi_R^{\mathrm{Na_{15}Sn_4}}.$$

In summary, the expressions above provide the explicit linearization of the reaction rate with respect to each phase fraction, ensuring that the Jacobian assembly in a Newton–Raphson solver fully accounts for forward and backward contributions, as well as the finite-strain coupling contained in the denominators C_1, C_2, C_3.

A.12 Detailed Gateaux derivatives for Newton–Raphson scheme

A.12.1 Gateaux derivative for γ^{Na}

The nonlinear residual (6.165) is solved via Newton–Raphson. The Gateaux derivative gives

$$\frac{\partial}{\partial\epsilon}\mathcal{R}_\gamma(\gamma_j^{\mathrm{Na}}+\epsilon\delta\gamma_j^{\mathrm{Na}},\phi_j^{\mathrm{Na}}+\epsilon\delta\phi_j^{\mathrm{Na}},\upsilon_j+\epsilon\delta\upsilon_j)\Big|_{\epsilon=0} = -\mathcal{R}_\gamma(\gamma_j^{\mathrm{Na}},\phi_j^{\mathrm{Na}},\upsilon_j)\,. \tag{A.53}$$

With $\mathcal{R}_\gamma$ as in Eq. (6.165), the linearization reads

$$
\begin{aligned}
&\frac{\partial}{\partial\epsilon}\mathcal{R}_\gamma(\gamma_j^{\mathrm{Na}}+\epsilon\delta\gamma_j^{\mathrm{Na}},\phi_j^{\mathrm{Na}}+\epsilon\delta\phi_j^{\mathrm{Na}},\upsilon_j+\epsilon\delta\upsilon_j)\Big|_{\epsilon=0} = \\
&\quad \frac{1}{\ell}\int_0^L \varphi_i^\gamma\varphi_j^\gamma \,\mathrm{d}X_1 \;\delta\gamma_j^{\mathrm{Na}}(t) \\
&\quad -\frac{E\,\Omega^{\mathrm{Na}}}{\ell\,\mu_{\mathrm{ref}}}\alpha_4\int_0^L \varphi_i^\gamma\frac{\partial}{\partial\epsilon}\aleph(\boldsymbol{\phi}_j+\epsilon\delta\boldsymbol{\phi}_j,\upsilon_j+\epsilon\delta\upsilon_j)^4\Big|_{\epsilon=0}\mathrm{d}X_1 \\
&\quad -\frac{E\,\Omega^{\mathrm{Na}}}{\ell\,\mu_{\mathrm{ref}}}\alpha_2\int_0^L \varphi_i^\gamma\frac{\partial}{\partial\epsilon}\aleph(\boldsymbol{\phi}_j+\epsilon\delta\boldsymbol{\phi}_j,\upsilon_j+\epsilon\delta\upsilon_j)^2\Big|_{\epsilon=0}\mathrm{d}X_1 = \\
&\quad = \frac{1}{\ell}\int_0^L \varphi_i^\gamma\varphi_j^\gamma \,\mathrm{d}X_1 \;\delta\gamma_j^{\mathrm{Na}}(t) \\
&\quad -4\,\alpha_4\frac{E\,\Omega^{\mathrm{Na}}}{\ell\,\mu_{\mathrm{ref}}}\int_0^L \varphi_i^\gamma\aleph(\boldsymbol{\phi}_j,\upsilon_j)^3\frac{\partial}{\partial\epsilon}\aleph(\boldsymbol{\phi}_j+\epsilon\delta\boldsymbol{\phi}_j,\upsilon_j+\epsilon\delta\upsilon_j)\Big|_{\epsilon=0}\mathrm{d}X_1 \\
&\quad -2\,\alpha_2\frac{E\,\Omega^{\mathrm{Na}}}{\ell\,\mu_{\mathrm{ref}}}\int_0^L \varphi_i^\gamma\aleph(\boldsymbol{\phi}_j,\upsilon_j)\frac{\partial}{\partial\epsilon}\aleph(\boldsymbol{\phi}_j+\epsilon\delta\boldsymbol{\phi}_j,\upsilon_j+\epsilon\delta\upsilon_j)\Big|_{\epsilon=0}\mathrm{d}X_1 = 0
\end{aligned}
$$

with $\aleph(\boldsymbol{\phi}_j,\upsilon_j)$ as in Eq. (6.260) and

$$
\begin{aligned}
\frac{\partial}{\partial\epsilon}\,\aleph(\phi_j+\epsilon\,\delta\phi_j,\;u_j+\epsilon\,\delta\upsilon_j)\Big|_{\epsilon=0} &= (J_j^c)^{-1/3}\,\frac{\partial(\delta\upsilon_1)}{\partial X_1} \\
&\quad -\frac{1}{3}\,(J_j^c)^{-4/3}\left(1+\frac{\partial u_{1,j}}{\partial X_1}\right)\big[(\omega^{\mathrm{Na}}-\omega^{\mathrm{V}})\,\delta\phi_{R,j}^{\mathrm{Na}} \\
&\quad +(\omega^{\mathrm{Sn}}-\omega^{\mathrm{V}})\,\delta\phi_{R,j}^{\mathrm{Sn}}+(\omega^{\mathrm{NaSn_3}}-\omega^{\mathrm{V}})\,\delta\phi_{R,j}^{\mathrm{NaSn_3}} \\
&\quad +(\omega^{\mathrm{Na_9Sn_4}}-\omega^{\mathrm{V}})\,\delta\phi_{R,j}^{\mathrm{Na_9Sn_4}} \\
&\quad +(\omega^{\mathrm{Na_{15}Sn_4}}-\omega^{\mathrm{V}})\,\delta\phi_{R,j}^{\mathrm{Na_{15}Sn_4}}\big].
\end{aligned}
\tag{A.54}
$$

A.12.2 Gateaux derivative for u

The nonlinear residual (6.168) is solved via Newton–Raphson. Using the Gateaux derivative, we linearize about the current iterate:

$$
\frac{\partial}{\partial\epsilon}\mathcal{R}_u(\boldsymbol{\phi}_j+\epsilon\delta\boldsymbol{\phi}_j,\upsilon_j+\epsilon\delta\upsilon_j)\Big|_{\epsilon=0} = -\mathcal{R}_u(\boldsymbol{\phi}_j,\upsilon_j)\,. \tag{A.55}
$$

With $\mathcal{R}_u$ as in Eq. (6.168), the consistent tangent reads

$$\begin{aligned}
&\frac{\partial}{\partial\epsilon}\mathcal{R}_u(\boldsymbol{\phi}_j+\epsilon\delta\boldsymbol{\phi}_j,\upsilon_j+\epsilon\delta\upsilon_j)\Big|_{\epsilon=0} = \\
&\quad \frac{1}{2}\,\frac{E}{G}\,\int_0^L \frac{\partial\varphi_i}{\partial X_1}\,\frac{\partial}{\partial\epsilon}\,J^{c2/3}\,\aleph(\boldsymbol{\phi}_j+\epsilon\delta\boldsymbol{\phi}_j,\upsilon_j+\epsilon\delta\upsilon_j) \\
&\quad \big[\,\aleph(\boldsymbol{\phi}_j+\epsilon\delta\boldsymbol{\phi}_j,\upsilon_j+\epsilon\delta\upsilon_j)^2-1\big]\,\Big|_{\epsilon=0}\,\mathrm{d}X_1 \\
&\quad = (1+\nu)\;\int_0^L \frac{\partial\varphi_i}{\partial X_1}\,J^{c2/3}\;\big[3\aleph(\boldsymbol{\phi}_j,\upsilon_j)^2-1\,\big] \\
&\quad \frac{\partial}{\partial\epsilon}\,\aleph(\boldsymbol{\phi}_j+\epsilon\delta\boldsymbol{\phi}_j,\upsilon_j+\epsilon\delta\upsilon_j)\,\Big|_{\epsilon=0}\,\mathrm{d}X_1 \\
&\quad + \frac{2}{3}\,(1+\nu)\;\int_0^L \frac{\partial\varphi_i}{\partial X_1}\,\aleph(\boldsymbol{\phi}_j,\upsilon_j)\;\big[\,\aleph(\boldsymbol{\phi}_j,\upsilon_j)^2-1\big]\;\frac{\sum_\alpha \delta\phi_j^\alpha\,\omega^\alpha}{J^{c1/3}}\;\varphi_j^\phi\;\mathrm{d}X_1\,.
\end{aligned} \tag{A.56}$$

Bibliography

[1] Sung-Wook Kim et al. "Electrode Materials for Rechargeable Sodium-Ion Batteries: Potential Alternatives to Current Lithium-Ion Batteries". In: *Advanced Energy Materials* 2.7 (2012), pp. 710–721. DOI: https://doi.org/10.1002/aenm.201200026. eprint: https://onlinelibrary.wiley.com/doi/pdf/10.1002/aenm.201200026. URL: https://onlinelibrary.wiley.com/doi/abs/10.1002/aenm.201200026.

[2] Wanyu Lu, Zijie Wang, and Shuhang Zhong. "Sodium-ion battery technology: Advanced anodes, cathodes and electrolytes". In: *Journal of Physics: Conference Series* 2109.1 (2021), p. 012004. DOI: 10.1088/1742-6596/2109/1/012004. URL: https://dx.doi.org/10.1088/1742-6596/2109/1/012004.

[3] Tahira Perveen et al. "Prospects in anode materials for sodium ion batteries - A review". In: *Renewable and Sustainable Energy Reviews* 119 (Dec. 2019), p. 109549. DOI: 10.1016/j.rser.2019.109549.

[4] Yue Chu et al. "Reconfiguring Hard Carbons with Emerging Sodium-Ion Batteries: A Perspective". In: *Advanced Materials* 35.31 (2023), p. 2212186. DOI: https://doi.org/10.1002/adma.202212186. eprint: https://onlinelibrary.wiley.com/doi/pdf/10.1002/adma.202212186. URL: https://onlinelibrary.wiley.com/doi/abs/10.1002/adma.202212186.

[5] Suzhe Liang et al. "A Chronicle Review of Nonsilicon (Sn, Sb, Ge)-Based Lithium/Sodium-Ion Battery Alloying Anodes". In: *Small Methods* 4.8 (2020), p. 2000218. DOI: https://doi.org/10.1002/smtd.202000218. eprint: https://onlinelibrary.wiley.com/doi/pdf/10.1002/smtd.202000218. URL: https://onlinelibrary.wiley.com/doi/abs/10.1002/smtd.202000218.

[6] Lichuan Wang et al. "Promises and challenges of alloy-type and conversion-type anode materials for sodium–ion batteries". In: *Materi-*

als today energy 11 (Mar. 2019), pp. 46–60. DOI: 10.1016/j.mtener.2018.10.017. URL: https://hal.science/hal-02350959.

[7] Qiao Wang et al. "Application of phase-field method in rechargeable batteries". In: *npj Computational Materials* 6.1 (2020), p. 176. ISSN: 2057-3960. DOI: 10.1038/s41524-020-00445-w. URL: https://doi.org/10.1038/s41524-020-00445-w.

[8] Erika O. Avila-Davila, Victor M. Lopez-Hirata, and Maribel L. Saucedo-Muñoz. "Application of Phase-Field Method to the Analysis of Phase Decomposition of Alloys". In: *Modeling and Simulation in Engineering Sciences*. Ed. by Noreen Sher Akbar and O. Anwar Beg. Rijeka: IntechOpen, 2016. Chap. 10. DOI: 10.5772/64153. URL: https://doi.org/10.5772/64153.

[9] Claudio V. Di Leo, Elisha Rejovitzky, and Lallit Anand. "A Cahn–Hilliard-type phase-field theory for species diffusion coupled with large elastic deformations: Application to phase-separating Li-ion electrode materials". In: *Journal of the Mechanics and Physics of Solids* 70 (2014), pp. 1–29. ISSN: 0022-5096. DOI: https://doi.org/10.1016/j.jmps.2014.05.001. URL: https://www.sciencedirect.com/science/article/pii/S0022509614000842.

[10] P. Areias, E. Samaniego, and T. Rabczuk. "A staggered approach for the coupling of Cahn—Hilliard type diffusion and finite strain elasticity". In: *Comput. Mech.* 57.2 (Feb. 2016), pp. 339–351. ISSN: 0178-7675. DOI: 10.1007/s00466-015-1235-1. URL: https://doi.org/10.1007/s00466-015-1235-1.

[11] Britta Nestler et al. "Phase-field model for multiphase systems with preserved volume fractions". In: *Phys. Rev. E* 78 (1 2008), p. 011604. DOI: 10.1103/PhysRevE.78.011604. URL: https://link.aps.org/doi/10.1103/PhysRevE.78.011604.

[12] Simon Daubner et al. "Combined study of phase transitions in the P2-type NaXNi1/3Mn2/3O2 cathode material: experimental, ab-initio and multiphase-field results". In: *npj Computational Materials* 10.1 (2024), p. 75. ISSN: 2057-3960. DOI: 10.1038/s41524-024-01258-x. URL: https://doi.org/10.1038/s41524-024-01258-x.

[13] Hongliang Li. "Research on Calculating the Internal Resistance of Battery Cell". In: *The Frontiers of Society, Science and Technology* 6.6 (2024), pp. 81–85. DOI: 10.25236/FSST.2024.060613. URL: https://doi.org/10.25236/FSST.2024.060613.

[14] Mathias Petzl and Michael A. Danzer. "Advancements in OCV Measurement and Analysis for Lithium-Ion Batteries". In: *IEEE Transactions on Energy Conversion* 28.3 (2013), pp. 675–681. DOI: 10.1109/TEC.2013.2259490.

[15] C. R. Birkl et al. "A Parametric Open Circuit Voltage Model for Lithium Ion Batteries". In: *Journal of The Electrochemical Society* 162.12 (2015), A2271. DOI: 10.1149/2.0331512jes. URL: https://dx.doi.org/10.1149/2.0331512jes.

[16] Hrvoje Bašić, Vedran Bobanac, and Hrvoje Pandžić. "Determination of Lithium-Ion Battery Capacity for Practical Applications". In: *Batteries* 9.9 (2023). ISSN: 2313-0105. DOI: 10.3390/batteries9090459. URL: https://www.mdpi.com/2313-0105/9/9/459.

[17] R. Huggins. *Energy Storage: Fundamentals, Materials and Applications*. Springer International Publishing, 2016. ISBN: 9783319331089. URL: https://books.google.it/books?id=GXnUtAEACAAJ.

[18] Jinhui Wang et al. "Study on the impact of cutoff voltage on structural and electrochemical stability of sodium-ion layered cathodes". In: *Chemical Engineering Journal* 500 (2024), p. 157032. ISSN: 1385-8947. DOI: https://doi.org/10.1016/j.cej.2024.157032. URL: https://www.sciencedirect.com/science/article/pii/S1385894724085231.

[19] C. Postigo et al. "Groundwater Pollution: Sources, Mechanisms, and Prevention". In: *Encyclopedia of the Anthropocene*. Ed. by Dominick A. Dellasala and Michael I. Goldstein. Oxford: Elsevier, 2018, pp. 87–96. ISBN: 978-0-12-813576-1. DOI: https://doi.org/10.1016/B978-0-12-809665-9.09880-3. URL: https://www.sciencedirect.com/science/article/pii/B9780128096659098803.

[20] Gregory Plett. 2015.

[21] Susmita Sarkar, Ankit Verma, and Partha P. Mukherjee. "Quantifying Sodiation Kinetics in Alloying Tin Electrodes for Sodium-Ion Batteries". In: *Journal of The Electrochemical Society* 168.9 (2021), p. 090550. DOI: 10.1149/1945-7111/ac2708. URL: https://dx.doi.org/10.1149/1945-7111/ac2708.

[22] Priyavi Singh. "Trends in the Gravimetric and Volumetric Energy Densities of Lithium-Ion Batteries over the Past Decade". In: *International Journal of Science and Research (IJSR)* 12.12 (2023), pp. 2037–2041. DOI: 10.21275/SR231227103409. URL: https://www.ijsr.net/getabstract.php?paperid=SR231227103409.

[23] Hang Zhang et al. "Long-Cycle-Life Cathode Materials for Sodium-Ion Batteries toward Large-Scale Energy Storage Systems". In: *Advanced Energy Materials* 13.23 (2023), p. 2300149. DOI: https://doi.org/10.1002/aenm.202300149. eprint: https://onlinelibrary.wiley.com/doi/pdf/10.1002/aenm.202300149. URL: https://onlinelibrary.wiley.com/doi/abs/10.1002/aenm.202300149.

[24] Jie Xiao et al. "Understanding and Applying Coulombic Efficiency in Lithium Metal Batteries". In: *Nature Energy* 5.8 (2020), pp. 561–568. DOI: 10.1038/s41560-020-0648-z. URL: https://doi.org/10.1038/s41560-020-0648-z.

[25] Nicholas Weadock et al. "Determination of mechanical properties of the SEI in sodium ion batteries via colloidal probe microscopy". In: *Nano Energy* 2.5 (2013), pp. 713–719. ISSN: 2211-2855. DOI: https://doi.org/10.1016/j.nanoen.2013.08.005. URL: https://www.sciencedirect.com/science/article/pii/S2211285513001456.

[26] Deepika Velumani and Ankit Bansal. "Thermal Behavior of Lithium- and Sodium-Ion Batteries: A Review on Heat Generation, Battery Degradation, Thermal Runway – Perspective and Future Directions". In: *Energy & Fuels* 36.23 (2022), pp. 14000–14029. DOI: 10.1021/acs.energyfuels.2c02889. eprint: https://doi.org/10.1021/acs.energyfuels.2c02889. URL: https://doi.org/10.1021/acs.energyfuels.2c02889.

[27] Yongbing Yue et al. "Thermal runaway hazards comparison between sodium-ion and lithium-ion batteries using accelerating rate calorimetry". In: *Process Safety and Environmental Protection* 189 (2024), pp. 61–70. ISSN: 0957-5820. DOI: https://doi.org/10.1016/j.psep.2024.06.032. URL: https://www.sciencedirect.com/science/article/pii/S095758202400716X.

[28] F. Licht, M.A. Davis, and H.A. Andreas. "Charge redistribution and electrode history impact galvanostatic charging/discharging and associated figures of merit". In: *Journal of Power Sources* 446 (2020), p. 227354. ISSN: 0378-7753. DOI: https://doi.org/10.1016/j.jpowsour.2019.227354. URL: https://www.sciencedirect.com/science/article/pii/S0378775319313473.

[29] Shahbaz Ahmad and Mehmet Egilmez. "Battery Testing Methods in Fuel Cell Research". In: (Sept. 2022). DOI: 10.48550/arXiv.2209.14541.

[30] Changsuk Yun and Seongpil Hwang. "Analysis of the Charging Current in Cyclic Voltammetry and Supercapacitor's Galvanostatic Charging Profile Based on a Constant-Phase Element". In: *ACS Omega* 6.1 (2021). PMID: 33458488, pp. 367–373. DOI: 10.1021/acsomega.0c04702. eprint: https://doi.org/10.1021/acsomega.0c04702. URL: https://doi.org/10.1021/acsomega.0c04702.

[31] Ahmed Barhoum and M. Luisa García-Betancourt. "Chapter 10 - Physicochemical characterization of nanomaterials: size, morphology, optical, magnetic, and electrical properties". In: *Emerging Applications of Nanoparticles and Architecture Nanostructures*. Ed. by Ahmed Barhoum and Abdel Salam Hamdy Makhlouf. Micro and Nano Technologies. Elsevier, 2018, pp. 279–304. ISBN: 978-0-323-51254-1. DOI: https://doi.org/10.1016/B978-0-323-51254-1.00010-5. URL: https://www.sciencedirect.com/science/article/pii/B9780323512541000105.

[32] Dean J. Miller et al. "Observation of Microstructural Evolution in Li Battery Cathode Oxide Particles by In Situ Electron Microscopy". In: *Advanced Energy Materials* 3.8 (2013), pp. 1098–1103. DOI: https://doi.org/10.1002/aenm.201300015. eprint: https://onlinelibrary.wiley.com/doi/pdf/10.1002/aenm.201300015. URL: https://onlinelibrary.wiley.com/doi/abs/10.1002/aenm.201300015.

[33] Jesse D. Benck et al. "Apparatus for operando x-ray diffraction of fuel electrodes in high temperature solid oxide electrochemical cells". In: *Review of Scientific Instruments* 90.2 (Feb. 2019), p. 023910. ISSN: 0034-6748. DOI: 10.1063/1.5050999. eprint: https://pubs.aip.org/aip/rsi/article-pdf/doi/10.1063/1.5050999/15649126/023910_1_online.pdf. URL: https://doi.org/10.1063/1.5050999.

[34] Pandian Bothi Raja et al. "5 - Characterization of nanomaterial used in nanobioremediation". In: *Nano-Bioremediation : Fundamentals and Applications*. Ed. by Hafiz M.N. Iqbal, Muhammad Bilal, and Tuan Anh Nguyen. Micro and Nano Technologies. Elsevier, 2022, pp. 57–83. ISBN: 978-0-12-823962-9. DOI: https://doi.org/10.1016/B978-0-12-823962-9.00037-4. URL: https://www.sciencedirect.com/science/article/pii/B9780128239629000374.

[35] Xiujuan Wei et al. "Operando X-ray Diffraction Characterization for Understanding the Intrinsic Electrochemical Mechanism in Rechargeable Battery Materials". In: *Small Methods* 1.5 (2017), p. 1700083. DOI: https://doi.org/10.1002/smtd.201700083. eprint: https://onlinelibrary.wiley.com/doi/pdf/10.1002/smtd.201700083.

URL: https://onlinelibrary.wiley.com/doi/abs/10.1002/smtd.201700083.

[36] Rajiv Kohli. "Chapter 3 - Methods for Monitoring and Measuring Cleanliness of Surfaces". In: *Developments in Surface Contamination and Cleaning*. Ed. by Rajiv Kohli and K.L. Mittal. Oxford: William Andrew Publishing, 2012, pp. 107–178. ISBN: 978-1-4377-7883-0. DOI: https://doi.org/10.1016/B978-1-4377-7883-0.00003-1. URL: https://www.sciencedirect.com/science/article/pii/B9781437778830000031.

[37] Valerie Randle. "Electron backscatter diffraction: Strategies for reliable data acquisition and processing". In: *Materials Characterization* 60.9 (2009), pp. 913–922. ISSN: 1044-5803. DOI: https://doi.org/10.1016/j.matchar.2009.05.011. URL: https://www.sciencedirect.com/science/article/pii/S1044580309001879.

[38] Taha Roodbar Shojaei, Soroush Soltani, and Mohammad Derakhshani. "Chapter 6 - Synthesis, properties, and biomedical applications of inorganic bionanomaterials". In: *Fundamentals of Bionanomaterials*. Ed. by Ahmed Barhoum, Jaison Jeevanandam, and Michael K. Danquah. Micro and Nano Technologies. Elsevier, 2022, pp. 139–174. ISBN: 978-0-12-824147-9. DOI: https://doi.org/10.1016/B978-0-12-824147-9.00006-6. URL: https://www.sciencedirect.com/science/article/pii/B9780128241479000066.

[39] Fengcheng Tang et al. "Synchrotron X-Ray Tomography for Rechargeable Battery Research: Fundamentals, Setups and Applications". In: *Small Methods* 5.9 (2021), p. 2100557. DOI: https://doi.org/10.1002/smtd.202100557.

[40] Long Gu et al. "Synchrotron X-ray Characterization Techniques for the Development of Aqueous Zinc Ion Batteries". In: *ChemElectroChem* 11.7 (2024), e202300602. DOI: https://doi.org/10.1002/celc.202300602. eprint: https://chemistry-europe.onlinelibrary.wiley.com/doi/pdf/10.1002/celc.202300602. URL: https://chemistry-europe.onlinelibrary.wiley.com/doi/abs/10.1002/celc.202300602.

[41] Jitendra Pal Singh et al. "Synchrotron radiation based X-ray techniques for analysis of cathodes in Li rechargeable batteries". In: *RSC Adv.* 12 (31 2022), pp. 20360–20378. DOI: 10.1039/D2RA01250B. URL: http://dx.doi.org/10.1039/D2RA01250B.

[42] Xi Wu et al. "Density functional theory calculations: A powerful tool to simulate and design high-performance energy storage and conversion materials". In: *Progress in Natural Science: Materials International* 29.3 (2019). Special Issue of Computational Materials, pp. 247–255. ISSN: 1002-0071. DOI: https://doi.org/10.1016/j.pnsc.2019.04.003. URL: https://www.sciencedirect.com/science/article/pii/S1002007119302400.

[43] Qiu He et al. "Density Functional Theory for Battery Materials". In: *ENERGY & ENVIRONMENTAL MATERIALS* 2.4 (2019), pp. 264–279. DOI: https://doi.org/10.1002/eem2.12056. eprint: https://onlinelibrary.wiley.com/doi/pdf/10.1002/eem2.12056. URL: https://onlinelibrary.wiley.com/doi/abs/10.1002/eem2.12056.

[44] Vamsi Krishna Garapati et al. "Physics-Based Reduced Order Model for Sodium-Ion Batteries". In: *Journal of The Electrochemical Society* 170.1 (2023), p. 010517. DOI: 10.1149/1945-7111/acb01b. URL: https://dx.doi.org/10.1149/1945-7111/acb01b.

[45] Sanaa El Aggadi et al. "Progress towards efficient phosphate-based materials for sodium-ion batteries in electrochemical energy storage". In: *Ionics* 29.6 (2023), pp. 2099–2113. ISSN: 1862-0760. DOI: 10.1007/s11581-023-04936-w. URL: https://doi.org/10.1007/s11581-023-04936-w.

[46] Jianmin Ma et al. "Sodium-based Batteries: From Critical Materials to Battery Systems". In: *Journal of Materials Chemistry A* 7 (Mar. 2019). DOI: 10.1039/C8TA11999F.

[47] Jens F. Peters, Alexandra Peña Cruz, and Marcel Weil. "Exploring the Economic Potential of Sodium-Ion Batteries". In: *Batteries* 5.1 (2019). ISSN: 2313-0105. DOI: 10.3390/batteries5010010. URL: https://www.mdpi.com/2313-0105/5/1/10.

[48] Lina Zhao et al. "Engineering of sodium-ion batteries: Opportunities and challenges". In: *Engineering* (2022). ISSN: 2095-8099. DOI: https://doi.org/10.1016/j.eng.2021.08.032. URL: https://www.sciencedirect.com/science/article/pii/S2095809922003630.

[49] Hangjun Ying and Wei-Qiang Han. "Metallic Sn-Based Anode Materials: Application in High-Performance Lithium-Ion and Sodium-Ion Batteries". In: *Advanced Science* 4.11 (2017), p. 1700298. DOI: https://doi.org/10.1002/advs.201700298. eprint: https://onlinelibrary.wiley.com/doi/pdf/10.1002/advs.201700298. URL: https://onlinelibrary.wiley.com/doi/abs/10.1002/advs.201700298.

[50] Jia Zhang and Tianye Zheng. "Group IVA Alloy Anodes for Sodium-Ion Rechargeable Batteries: Electrochemistry, Mechanics, and Kinetics". In: *Batteries & Supercaps* n/a.n/a (), e202400823. DOI: https://doi.org/10.1002/batt.202400823. eprint: https://chemistry-europe.onlinelibrary.wiley.com/doi/pdf/10.1002/batt.202400823. URL: https://chemistry-europe.onlinelibrary.wiley.com/doi/abs/10.1002/batt.202400823.

[51] Amalie Skurtveit et al. "Benefits and Development Challenges for Conversion-Alloying Anode Materials in Na-Ion Batteries". In: *Frontiers in Energy Research* 10 (2022). ISSN: 2296-598X. DOI: 10.3389/fenrg.2022.897755. URL: https://www.frontiersin.org/articles/10.3389/fenrg.2022.897755.

[52] Hongyan Kang et al. "Update on anode materials for Na-ion batteries". In: *J. Mater. Chem. A* 3 (35 2015), pp. 17899–17913. DOI: 10.1039/C5TA03181H. URL: http://dx.doi.org/10.1039/C5TA03181H.

[53] Mengmeng Lao et al. "Alloy-Based Anode Materials toward Advanced Sodium-Ion Batteries". In: *Advanced Materials* 29.48 (2017), p. 1700622. DOI: https://doi.org/10.1002/adma.201700622. eprint: https://onlinelibrary.wiley.com/doi/pdf/10.1002/adma.201700622. URL: https://onlinelibrary.wiley.com/doi/abs/10.1002/adma.201700622.

[54] Jiang Wei Wang et al. "Microstructural Evolution of Tin Nanoparticles during In Situ Sodium Insertion and Extraction". In: *Nano Letters* 12.11 (2012). PMID: 23092238, pp. 5897–5902. DOI: 10.1021/nl303305c. eprint: https://doi.org/10.1021/nl303305c. URL: https://doi.org/10.1021/nl303305c.

[55] Sang Yun Han et al. "Stress evolution during cycling of alloy-anode solid-state batteries". In: *Joule* 5.9 (2021), pp. 2450–2465. ISSN: 2542-4351. DOI: https://doi.org/10.1016/j.joule.2021.07.002. URL: https://www.sciencedirect.com/science/article/pii/S2542435121003147.

[56] Lichuan Wang et al. "Promises and challenges of alloy-type and conversion-type anode materials for sodium–ion batteries". In: *Materials Today Energy* 11 (2019), pp. 46–60. ISSN: 2468-6069. DOI: https://doi.org/10.1016/j.mtener.2018.10.017. URL: https://www.sciencedirect.com/science/article/pii/S2468606918302491.

[57] Behdokht Farbod et al. "Anodes for Sodium Ion Batteries Based on Tin–Germanium–Antimony Alloys". In: *ACS Nano* 8.5 (2014). PMID: 24735277, pp. 4415–4429. DOI: 10.1021/nn4063598. eprint:

https://doi.org/10.1021/nn4063598. URL: https://doi.org/10.1021/nn4063598.

[58] L. D. Ellis, T. D. Hatchard, and M. N. Obrovac. "Reversible Insertion of Sodium in Tin". In: *Journal of The Electrochemical Society* 159.11 (2012), A1801. DOI: 10.1149/2.037211jes. URL: https://dx.doi.org/10.1149/2.037211jes.

[59] Dewen Hou et al. "Spatial and Temporal Analysis of Sodium-Ion Batteries". In: *ACS Energy Letters* 6.11 (2021), pp. 4023–4054. DOI: 10.1021/acsenergylett.1c01868. eprint: https://doi.org/10.1021/acsenergylett.1c01868. URL: https://doi.org/10.1021/acsenergylett.1c01868.

[60] Tao Li et al. "Insight on the Failure Mechanism of Sn Electrodes for Sodium-Ion Batteries: Evidence of Pore Formation during Sodiation and Crack Formation during Desodiation". In: *ACS Applied Energy Materials* 2.1 (2019), pp. 860–866. DOI: 10.1021/acsaem.8b01934. eprint: https://doi.org/10.1021/acsaem.8b01934. URL: https://doi.org/10.1021/acsaem.8b01934.

[61] Joshua M. Stratford et al. "Investigating Sodium Storage Mechanisms in Tin Anodes: A Combined Pair Distribution Function Analysis, Density Functional Theory, and Solid-State NMR Approach". In: *Journal of the American Chemical Society* 139.21 (2017). PMID: 28471174, pp. 7273–7286. DOI: 10.1021/jacs.7b01398. eprint: https://doi.org/10.1021/jacs.7b01398. URL: https://doi.org/10.1021/jacs.7b01398.

[62] Wen Tao Jing, Chun Cheng Yang, and Qing Jiang. "Recent progress on metallic Sn- and Sb-based anodes for sodium-ion batteries". In: *J. Mater. Chem. A* 8 (6 2020), pp. 2913–2933. DOI: 10.1039/C9TA11782B. URL: http://dx.doi.org/10.1039/C9TA11782B.

[63] Keming Song et al. "Recent Progress on the Alloy-Based Anode for Sodium-Ion Batteries and Potassium-Ion Batteries". In: *Small* 17.9 (2021), p. 1903194. DOI: https://doi.org/10.1002/smll.201903194. eprint: https://onlinelibrary.wiley.com/doi/pdf/10.1002/smll.201903194. URL: https://onlinelibrary.wiley.com/doi/abs/10.1002/smll.201903194.

[64] Zhi Li, Jia Ding, and David Mitlin. "Tin and Tin Compounds for Sodium Ion Battery Anodes: Phase Transformations and Performance". In: *Accounts of Chemical Research* 48.6 (2015). PMID: 26046961, pp. 1657–1665. DOI: 10.1021/acs.accounts.5b00114. eprint: https://doi.org/10.1021/acs.accounts.5b00114. URL: https://doi.org/10.1021/acs.accounts.5b00114.

[65] Do-Hwan Nam et al. “Electrochemical Properties of Electrodeposited Sn Anodes for Na-Ion Batteries”. In: *The Journal of Physical Chemistry C* 118.35 (2014), pp. 20086–20093. DOI: 10.1021/jp504055j. eprint: https://doi.org/10.1021/jp504055j. URL: https://doi.org/10.1021/jp504055j.

[66] Loïc Baggetto et al. “Characterization of sodium ion electrochemical reaction with tin anodes: Experiment and theory”. In: *Journal of Power Sources* 234 (2013), pp. 48–59. ISSN: 0378-7753. DOI: https://doi.org/10.1016/j.jpowsour.2013.01.083. URL: https://www.sciencedirect.com/science/article/pii/S0378775313001328.

[67] Daniele Spada et al. “Inside the failure mechanism of tin oxide as anode for sodium ion batteries”. In: *Journal of Solid State Electrochemistry* 25.4 (2021), pp. 1401–1410. ISSN: 1433-0768. DOI: 10.1007/s10008-021-04919-9. URL: https://doi.org/10.1007/s10008-021-04919-9.

[68] Sayed Youssef Sayed et al. “Stabilizing Tin Anodes in Sodium-Ion Batteries by Alloying with Silicon”. In: *ACS Applied Energy Materials* 3.10 (2020), pp. 9950–9962. DOI: 10.1021/acsaem.0c01641. eprint: https://doi.org/10.1021/acsaem.0c01641. URL: https://doi.org/10.1021/acsaem.0c01641.

[69] Changhyeon Kim et al. “A self-healing Sn anode with an ultra-long cycle life for sodium-ion batteries”. In: *J. Mater. Chem. A* 6 (45 2018), pp. 22809–22818. DOI: 10.1039/C8TA09544B. URL: http://dx.doi.org/10.1039/C8TA09544B.

[70] Matthew T. McDowell, Shuman Xia, and Ting Zhu. “The mechanics of large-volume-change transformations in high-capacity battery materials”. In: *Extreme Mechanics Letters* 9 (2016). Mechanics of Energy Materials, pp. 480–494. ISSN: 2352-4316. DOI: https://doi.org/10.1016/j.eml.2016.03.004. URL: https://www.sciencedirect.com/science/article/pii/S2352431616300037.

[71] Seong-Min Bak et al. “In situ/operando synchrotron-based X-ray techniques for lithium-ion battery research”. In: *NPG Asia Materials* 10.7 (2018), pp. 563–580. ISSN: 1884-4057. DOI: 10.1038/s41427-018-0056-z. URL: https://doi.org/10.1038/s41427-018-0056-z.

[72] Jianfeng Mao et al. “Two-dimensional nanostructures for sodium-ion battery anodes”. In: *Journal of Materials Chemistry A* 6 (2018), pp. 3284–3303. DOI: 10.1039/C7TA10500B. URL: https://doi.org/10.1039/C7TA10500B.

[73] Zhiqiang Zhu et al. "Ultrasmall Sn Nanoparticles Embedded in Nitrogen-Doped Porous Carbon As High-Performance Anode for Lithium-Ion Batteries". In: *Nano Letters* 14.1 (2014). PMID: 24328829, pp. 153–157. DOI: https://doi.org/10.1021/nl403631h.

[74] Tao Li et al. "Damage Formation in Sn Film Anodes of Na-Ion Batteries". In: *The Journal of Physical Chemistry C* 123.24 (2019), pp. 15244–15250. DOI: 10.1021/acs.jpcc.9b02004. eprint: https://doi.org/10.1021/acs.jpcc.9b02004. URL: https://doi.org/10.1021/acs.jpcc.9b02004.

[75] Jacob S. Gutiérrez-Kolar et al. "Interpreting Electrochemical and Chemical Sodiation Mechanisms and Kinetics in Tin Antimony Battery Anodes Using in Situ Transmission Electron Microscopy and Computational Methods". In: *ACS Applied Energy Materials* 2.5 (2019), pp. 3578–3586. DOI: 10.1021/acsaem.9b00310. eprint: https://doi.org/10.1021/acsaem.9b00310. URL: https://doi.org/10.1021/acsaem.9b00310.

[76] Jing Xu et al. "Achieving high-performance sodium metal anodes: From structural design to reaction kinetic improvement". In: *Nano Research* 17.3 (2024), pp. 1288–1312. ISSN: 1998-0000. DOI: 10.1007/s12274-023-5889-2. URL: https://doi.org/10.1007/s12274-023-5889-2.

[77] Mark N. Obrovac and Vincent L. Chevrier. "Alloy Negative Electrodes for Li-Ion Batteries". In: *Chemical Reviews* 114.23 (2014). Epub 2014-11-17. Erratum: *Chem. Rev.* 2015, 115(4), 2043. doi:10.1021/acs.chemrev.5b0006 pp. 11444–11502. DOI: 10.1021/cr500207g.

[78] H. Mou et al. "Tin and Tin Compound Materials as Anodes in Lithium-Ion and Sodium-Ion Batteries: A Review". In: *Frontiers in Chemistry* 8 (2020), p. 141. DOI: 10.3389/fchem.2020.00141.

[79] Davide Grazioli, Marco Magri, and Alberto Salvadori. "Computational modeling of Li-ion batteries". In: *Computational Mechanics* 58 (Dec. 2016). DOI: 10.1007/s00466-016-1325-8.

[80] Zhenzhu Wang et al. "Theoretical Simulation and Modeling of Three-Dimensional Batteries". In: *Cell Reports Physical Science* 1.6 (2020), p. 100078. ISSN: 2666-3864. DOI: https://doi.org/10.1016/j.xcrp.2020.100078. URL: https://www.sciencedirect.com/science/article/pii/S2666386420300734.

[81] A. Salvadori et al. “A multiscale-compatible approach in modeling ionic transport in the electrolyte of (Lithium ion) batteries”. In: *Journal of Power Sources* 293 (2015), pp. 892–911. ISSN: 0378-7753. DOI: https://doi.org/10.1016/j.jpowsour.2015.05.114. URL: https://www.sciencedirect.com/science/article/pii/S0378775315010241.

[82] Binghe Liu et al. “A Simultaneous Multiscale and Multiphysics Model and Numerical Implementation of a Core-Shell Model for Lithium-Ion Full-Cell Batteries”. In: *Journal of Applied Mechanics* 86.4 (Jan. 2019). DOI: 10.1115/1.4042432. URL: https://doi.org/10.1115/1.4042432.

[83] Kudakwashe Chayambuka et al. “Physics-based modeling of sodium-ion batteries part I: Experimental parameter determination”. In: *Electrochimica Acta* 404 (2022), p. 139726. ISSN: 0013-4686. DOI: https://doi.org/10.1016/j.electacta.2021.139726. URL: https://www.sciencedirect.com/science/article/pii/S0013468621020107.

[84] Vittorio Marangon et al. “Cell design and chemistry of commercial sodium-ion battery cells”. In: *Journal of Power Sources* 634 (2025). Open Access under CC BY license, p. 236496. DOI: 10.1016/j.jpowsour.2025.236496. URL: https://doi.org/10.1016/j.jpowsour.2025.236496.

[85] Kudakwashe Chayambuka et al. “Physics-based modeling of sodium-ion batteries part II. Model and validation”. In: *Electrochimica Acta* 404 (2022), p. 139764. ISSN: 0013-4686. DOI: https://doi.org/10.1016/j.electacta.2021.139764. URL: https://www.sciencedirect.com/science/article/pii/S0013468621020478.

[86] Lallit Anand. “A Cahn–Hilliard-type theory for species diffusion coupled with large elastic–plastic deformations”. In: *Journal of the Mechanics and Physics of Solids* 60.12 (2012), pp. 1983–2002. ISSN: 0022-5096. DOI: https://doi.org/10.1016/j.jmps.2012.08.001. URL: https://www.sciencedirect.com/science/article/pii/S002250961200155X.

[87] A. Salvadori et al. “A coupled model of transport-reaction-mechanics with trapping. Part I – Small strain analysis”. In: *Journal of the Mechanics and Physics of Solids* 114 (2018), pp. 1–30. ISSN: 0022-5096. DOI: https://doi.org/10.1016/j.jmps.2018.02.006. URL: https://www.sciencedirect.com/science/article/pii/S0022509617311067.

[88] Matteo Arricca et al. “A coupled model of transport-reaction-mechanics with trapping, Part II: Large strain analysis”. In: *J MECH PHYS SOLIDS* 181 (2023), p. 105425.

[89] Arman Afshar and Claudio V. Di Leo. "A thermodynamically consistent gradient theory for diffusion–reaction–deformation in solids: Application to conversion-type electrodes". In: *Journal of the Mechanics and Physics of Solids* 151 (2021), p. 104368. ISSN: 0022-5096. DOI: https://doi.org/10.1016/j.jmps.2021.104368. URL: https://www.sciencedirect.com/science/article/pii/S0022509621000594.

[90] Allan F. Bower, Pradeep R. Guduru, and Eric Chason. "Analytical solutions for composition and stress in spherical elastic–plastic lithium-ion electrode particles containing a propagating phase boundary". In: *International Journal of Solids and Structures* 69-70 (2015), pp. 328–342. ISSN: 0020-7683. DOI: https://doi.org/10.1016/j.ijsolstr.2015.05.018. URL: https://www.sciencedirect.com/science/article/pii/S0020768315002280.

[91] Aarne Pohjonen. "Full Field Model Describing Phase Front Propagation, Transformation Strains, Chemical Partitioning, and Diffusion in Solid–Solid Phase Transformations". In: *Advanced Theory and Simulations* 6.3 (2023), p. 2200771. DOI: https://doi.org/10.1002/adts.202200771. eprint: https://onlinelibrary.wiley.com/doi/pdf/10.1002/adts.202200771. URL: https://onlinelibrary.wiley.com/doi/abs/10.1002/adts.202200771.

[92] Hector Gomez, Miguel Bures, and Adrian Moure. "A review on computational modelling of phase-transition problems". In: *Philos. Trans. R. Soc. A* 377.2143 (2019), p. 20180203. DOI: 10.1098/rsta.2018.0203. eprint: https://royalsocietypublishing.org/doi/pdf/10.1098/rsta.2018.0203. URL: https://royalsocietypublishing.org/doi/abs/10.1098/rsta.2018.0203.

[93] Tao Zhang and Marc Kamlah. "Sodium Ion Batteries Particles: Phase-Field Modeling with Coupling of Cahn-Hilliard Equation and Finite Deformation Elasticity". In: *Journal of The Electrochemical Society* 165.10 (2018), A1997. DOI: 10.1149/2.0141810jes. URL: https://dx.doi.org/10.1149/2.0141810jes.

[94] Tao Zhang and Marc Kamlah. "Microstructure evolution and intermediate phase-induced varying solubility limits and stress reduction behavior in sodium ion batteries particles of NaxFePO4 (0<x<1)". In: *J. Power Sources* 483 (2021), p. 229187. ISSN: 0378-7753. DOI: https://doi.org/10.1016/j.jpowsour.2020.229187. URL: https://www.sciencedirect.com/science/article/pii/S0378775320314762.

[95] Tao Zhang et al. “3D microstructure evolution in NaxFePO4 storage particles for sodium-ion batteries”. In: *J. Power Sources* 565 (2023), p. 232902. ISSN: 0378-7753. DOI: https://doi.org/10.1016/j.jpowsour.2023.232902. URL: https://www.sciencedirect.com/science/article/pii/S037877532300277X.

[96] Tobias Hofmann et al. “Numerical simulation of phase separation in cathode materials of lithium ion batteries”. In: *International Journal of Solids and Structures* 100-101 (2016), pp. 456–469. ISSN: 0020-7683. DOI: https://doi.org/10.1016/j.ijsolstr.2016.09.018. URL: https://www.sciencedirect.com/science/article/pii/S0020768316302670.

[97] Ying Zhao, Peter Stein, and Bai-Xiang Xu. “Isogeometric analysis of mechanically coupled Cahn–Hilliard phase segregation in hyperelastic electrodes of Li-ion batteries”. In: *Computer Methods in Applied Mechanics and Engineering* 297 (2015), pp. 325–347. ISSN: 0045-7825. DOI: https://doi.org/10.1016/j.cma.2015.09.008. URL: https://www.sciencedirect.com/science/article/pii/S0045782515003023.

[98] Srivatsan Hulikal et al. “Experimental Calibration of a Cahn-Hilliard Phase-Field Model for Phase Transformations in Li-Sn Electrodes”. In: *Journal of The Electrochemical Society* 163.13 (2016), A2647. DOI: 10.1149/2.0701613jes. URL: https://dx.doi.org/10.1149/2.0701613jes.

[99] Martin Z. Bazant. “Theory of Chemical Kinetics and Charge Transfer based on Nonequilibrium Thermodynamics”. In: *Accounts of Chemical Research* 46.5 (2013). PMID: 23520980, pp. 1144–1160. DOI: 10.1021/ar300145c. eprint: https://doi.org/10.1021/ar300145c. URL: https://doi.org/10.1021/ar300145c.

[100] W. Beck Andrews and Katsuyo Thornton. “Elucidating the complex interplay between thermodynamics, kinetics, and electrochemistry in battery electrodes through phase-field modeling”. In: *MRS Bulletin* 49.6 (2024), pp. 644–654. ISSN: 1938-1425. DOI: 10.1557/s43577-024-00732-7. URL: https://doi.org/10.1557/s43577-024-00732-7.

[101] Simon Daubner et al. “Modeling intercalation in cathode materials with phase-field methods: Assumptions and implications using the example of LiFePO4”. In: *Electrochimica Acta* 421 (2022), p. 140516. ISSN: 0013-4686. DOI: https://doi.org/10.1016/j.electacta.2022.140516. URL: https://www.sciencedirect.com/science/article/pii/S0013468622006752.

[102] I. Steinbach and F. Pezzolla. "A generalized field method for multiphase transformations using interface fields". In: *Physica D: Nonlinear Phenomena* 134.4 (1999), pp. 385–393. ISSN: 0167-2789. DOI: https://doi.org/10.1016/S0167-2789(99)00129-3. URL: https://www.sciencedirect.com/science/article/pii/S0167278999001293.

[103] Britta Nestler, Harald Garcke, and Björn Stinner. "Multicomponent alloy solidification: Phase-field modeling and simulations". In: *Phys. Rev. E* 71 (4 2005), p. 041609. DOI: 10.1103/PhysRevE.71.041609. URL: https://link.aps.org/doi/10.1103/PhysRevE.71.041609.

[104] Renpin Liu et al. "Dual carbon decorated germanium-carbon composite as a stable anode for sodium/potassium-ion batteries". In: *Journal of Colloid and Interface Science* 584 (2021), pp. 372–381. ISSN: 0021-9797. DOI: https://doi.org/10.1016/j.jcis.2020.09.083. URL: https://www.sciencedirect.com/science/article/pii/S0021979720312728.

[105] W. Blake Hawley and Jianlin Li. "Electrode manufacturing for lithium-ion batteries—Analysis of current and next generation processing". In: *Journal of Energy Storage* 25 (2019), p. 100862. ISSN: 2352-152X. DOI: https://doi.org/10.1016/j.est.2019.100862. URL: https://www.sciencedirect.com/science/article/pii/S2352152X19304840.

[106] Carl D. Reynolds et al. "A review of metrology in lithium-ion electrode coating processes". In: *Materials Design* 209 (2021), p. 109971. ISSN: 0264-1275. DOI: https://doi.org/10.1016/j.matdes.2021.109971. URL: https://www.sciencedirect.com/science/article/pii/S0264127521005256.

[107] Thangavelu Palaniselvam et al. "Sodium Storage and Electrode Dynamics of Tin–Carbon Composite Electrodes from Bulk Precursors for Sodium-Ion Batteries". In: *Advanced Functional Materials* 29.18 (2019), p. 1900790. DOI: https://doi.org/10.1002/adfm.201900790.

[108] Yusuke Abe et al. "Role of SiOx in rice-husk-derived anodes for Li-ion batteries". In: *Scientific Reports* 12.1 (2022), p. 975. DOI: 10.1038/s41598-022-04979-5. URL: https://doi.org/10.1038/s41598-022-04979-5.

[109] Héctor Gómez et al. "Isogeometric analysis of the Cahn–Hilliard phase-field model". In: *Computer Methods in Applied Mechanics and Engineering* 197.49 (2008), pp. 4333–4352. ISSN: 0045-7825. DOI: https://doi.org/10.1016/j.cma.2008.05.003. URL: https://www.sciencedirect.com/science/article/pii/S0045782508001953.

[110] Ingo Steinbach. "Phase-field models in materials science". In: *Modelling and Simulation in Materials Science and Engineering* 17.7 (2009), p. 073001. DOI: 10.1088/0965-0393/17/7/073001. URL: https://dx.doi.org/10.1088/0965-0393/17/7/073001.

[111] Morton E. Gurtin. "A gradient theory of single-crystal viscoplasticity that accounts for geometrically necessary dislocations". In: *Journal of the Mechanics and Physics of Solids* 50.1 (2002), pp. 5–32. ISSN: 0022-5096. DOI: https://doi.org/10.1016/S0022-5096(01)00104-1. URL: https://www.sciencedirect.com/science/article/pii/S0022509601001041.

[112] C. Di Leo, E. Rejovitzky, and L. Anand. "A Cahn-Hilliard-type phase-field theory for species diffusion coupled with large elastic deformations: Application to phase-separating Li-ion electrode materials". In: *J MECH PHYS SOLIDS* 70 (2014), pp. 1–29.

[113] R.L.J.M. Ubachs, P.J.G. Schreurs, and M.G.D. Geers. "A nonlocal diffuse interface model for microstructure evolution of tin–lead solder". In: *Journal of the Mechanics and Physics of Solids* 52.8 (2004), pp. 1763–1792. ISSN: 0022-5096. DOI: https://doi.org/10.1016/j.jmps.2004.02.002. URL: https://www.sciencedirect.com/science/article/pii/S0022509604000262.

[114] P. Areias, E. Samaniego, and T. Rabczuk. "A staggered approach for the coupling of Cahn–Hilliard type diffusion and finite strain elasticity". In: *Computational Mechanics* 57.2 (2016), pp. 339–351. ISSN: 1432-0924. DOI: 10.1007/s00466-015-1235-1. URL: https://doi.org/10.1007/s00466-015-1235-1.

[115] M.E. Gurtin, E. Fried, and L. Anand. *The Mechanics and Thermodynamics of Continua*. Cambridge University Press, 2010.

[116] Gyula I. Tóth, Mojdeh Zarifi, and Bjørn Kvamme. "Phase-field theory of multicomponent incompressible Cahn-Hilliard liquids". In: *Phys. Rev. E* 93 (1 2016), p. 013126. DOI: 10.1103/PhysRevE.93.013126. URL: https://link.aps.org/doi/10.1103/PhysRevE.93.013126.

[117] Ziyang Huang, Guang Lin, and Arezoo M. Ardekani. "A consistent and conservative volume distribution algorithm and its applications to multiphase flows using Phase-Field models". In: *International Journal of Multiphase Flow* 142 (2021), p. 103727. ISSN: 0301-9322. DOI: https://doi.org/10.1016/j.ijmultiphaseflow.2021.103727. URL: https://www.sciencedirect.com/science/article/pii/S0301932221001750.

[118] Meng Li et al. “Low-temperature performance of Na-ion batteries”. In: *Carbon Energy* 6.10 (2024), e546. DOI: https://doi.org/10.1002/cey2.546. eprint: https://onlinelibrary.wiley.com/doi/pdf/10.1002/cey2.546. URL: https://onlinelibrary.wiley.com/doi/abs/10.1002/cey2.546.

[119] S.R. De Groot and P. Mazur. *Non-Equilibrium Thermodynamics*. Dover, 1984.

[120] F.C. Larché and J.W. Cahn. “Overview no. 41 The interactions of composition and stress in crystalline solids”. In: *Acta Metallurgica* 33.3 (1985), pp. 331–357. ISSN: 0001-6160. DOI: https://doi.org/10.1016/0001-6160(85)90077-X. URL: https://www.sciencedirect.com/science/article/pii/000161608590077X.

[121] Julia Kundin et al. “Modeling vacancy-induced porosity in compositionally-graded complex alloys”. In: *Acta Materialia* 271 (2024), p. 119905. ISSN: 1359-6454. DOI: https://doi.org/10.1016/j.actamat.2024.119905. URL: https://www.sciencedirect.com/science/article/pii/S1359645424002581.

[122] Ruqing Fang et al. “Modeling the electro-chemo-mechanical failure at the lithium-solid electrolyte interface: Void evolution and lithium penetration”. In: *Journal of the Mechanics and Physics of Solids* 192 (2024), p. 105799. ISSN: 0022-5096. DOI: https://doi.org/10.1016/j.jmps.2024.105799. URL: https://www.sciencedirect.com/science/article/pii/S0022509624002655.

[123] Kenneth Antonio Connors. *Chemical Kinetics: The Study of Reaction Rates in Solution*. New York: John Wiley & Sons, 1990, p. 480.

[124] F. Larche and J.W. Cahn. “A linear theory of thermochemical equilibrium under stress”. In: *ACTA METALL MATER* 21 (1973), pp. 1051–1063.

[125] F. Larche and J.W. Cahn. “Non linear theory of thermochemical equilibrium under stress”. In: *ACTA METALL MATER* 26 (1978), pp. 53–60.

[126] L.S. García-Colín, S.M.T. de la Selva, and E. Piña. “The mass action law in extended irreversible thermodynamics”. In: *Physics Letters A* 110.7 (1985), pp. 363–365. ISSN: 0375-9601. DOI: https://doi.org/10.1016/0375-9601(85)90055-6. URL: https://www.sciencedirect.com/science/article/pii/0375960185900556.

[127] Bin Wu and Wei Lu. "A consistently coupled multiscale mechanical–electrochemical battery model with particle interaction and its validation". In: *Journal of the Mechanics and Physics of Solids* 125 (2019), pp. 89–111. ISSN: 0022-5096. DOI: https://doi.org/10.1016/j.jmps.2018.12.005. URL: https://www.sciencedirect.com/science/article/pii/S0022509618309141.

[128] A. Salvadori et al. "A coupled model of transport-reaction-mechanics with trapping. Part I - small strain analysis." In: *J MECH PHYS SOLIDS* 114 (2018), pp. 1–30.

[129] Yuzhang Liu et al. "Insight into the Critical Role of Exchange Current Density on Electrodeposition Behavior of Lithium Metal". In: *Advanced Science* 8.5 (2021). Published 2021-01-06, p. 2003301. DOI: 10.1002/advs.202003301.

[130] Axel Durdel et al. "Modeling Silicon-Dominant Anodes: Parametrization, Discussion, and Validation of a Newman-Type Model". In: *Batteries* 9.11 (2023). ISSN: 2313-0105. DOI: 10.3390/batteries9110558. URL: https://www.mdpi.com/2313-0105/9/11/558.